



## Durham E-Theses

---

### *Insights into mafic enclave crystallisation at Soufriere Hills Volcano from groundmass crystal shape-size relationships*

HUGHES, REBECCA,ROSE

#### How to cite:

---

HUGHES, REBECCA,ROSE (2025) *Insights into mafic enclave crystallisation at Soufriere Hills Volcano from groundmass crystal shape-size relationships*, Durham theses, Durham University. Available at Durham E-Theses Online: <http://etheses.dur.ac.uk/16113/>

#### Use policy

---

The full-text may be used and/or reproduced, and given to third parties in any format or medium, without prior permission or charge, for personal research or study, educational, or not-for-profit purposes provided that:

- a full bibliographic reference is made to the original source
- a [link](#) is made to the metadata record in Durham E-Theses
- the full-text is not changed in any way

The full-text must not be sold in any format or medium without the formal permission of the copyright holders.

Please consult the [full Durham E-Theses policy](#) for further details.

# Insights into mafic enclave crystallisation at Soufrière Hills Volcano from groundmass crystal shape-size relationships

Rebecca R. Hughes

## Abstract

Crystal size and shape in igneous rocks reflects the magmatic conditions experienced during their nucleation and growth. Whilst crystal size distributions are widely used in textural studies, crystal shape variability and its petrogenetic significance is not as well understood. Recent work has demonstrated that plagioclase nucleates as a prism and only develops its typical tabular shape during subsequent overgrowth (Mangler et al., 2022; 2023). It is yet unclear whether other phases besides plagioclase display a systematic evolution of shape with size.

Here, we reconstruct groundmass crystal 3D shape-size relationships in mafic enclaves from Soufrière Hills Volcano (SHV), Montserrat. Mafic enclaves preserve evidence of magma mixing events, a potential eruption trigger at SHV. Cooling of mafic enclaves in-situ provides a simple groundmass crystallisation scenario in which to explore new concepts of how crystal shape evolves with size.

Plagioclase evolves from prismatic to tabular with increasing size. Orthopyroxene potentially evolves from equant to bladed, with statistical validation being inconclusive. Amphibole does not show a systematic change in shape with size. Crystal growth modelling can reproduce the plagioclase shape-size relationships by modelling the growth of an initial prism to a range of overgrowth shapes. Overgrowth shape has been demonstrated experimentally to vary with melt composition, from higher relative growth rates in crystals grown in basaltic melts to lower relative growth rates in crystals grown in silicic melts (Mangler et al., 2023). Here, changing plagioclase shape with size is interpreted to reflect changing melt chemistry as successive populations nucleate and grow. The first plagioclase nucleate in basaltic melt and overgrow to tabular shapes. The melt becomes increasingly silicic with cooling and crystallisation. Successive populations nucleate in increasingly silicic melt, overgrowing to progressively more prismatic shapes. This is reflected in the plagioclase shape-size distributions in the mafic enclave, demonstrating the petrogenetic significance of crystal shape.

# Insights into mafic enclave crystallisation at Soufrière Hills Volcano from groundmass crystal shape-size relationships

Rebecca R. Hughes

Thesis submitted in fulfilment of the requirements for the degree of Master of Science

Department of Earth Sciences, Durham University

2025



# Contents

<b>1</b>	<b>Introduction</b>	<b>1</b>
1.1	Background . . . . .	1
1.1.1	Crystal nucleation and growth . . . . .	1
1.1.2	Crystal Size Distributions . . . . .	2
1.1.3	Crystal shape . . . . .	4
1.2	Crystal shape-size relationships in mafic enclaves . . . . .	6
1.3	Geological history and petrology of Soufrière Hills Volcano . . . . .	8
<b>2</b>	<b>Methods</b>	<b>12</b>
2.1	2D intersection data to 3D size-shape estimates . . . . .	12
2.1.1	ShapeCalc . . . . .	12
2.1.2	Crystal Size Distributions . . . . .	14
2.1.3	Binning method . . . . .	14
2.2	SEM data acquisition . . . . .	17
2.2.1	BSE maps . . . . .	17
2.2.2	Chemical maps . . . . .	17
2.2.3	Representative geochemistry . . . . .	19
2.3	2D size-shape data collection . . . . .	19
2.3.1	Intersection measurement approaches . . . . .	19
2.3.2	Measurement comparison tests . . . . .	23
2.4	Crystal outlining approach . . . . .	32
2.4.1	Automated outlining . . . . .	34
2.4.2	Manual outlining . . . . .	36
2.5	Statistical validation . . . . .	46
2.5.1	CrystalSlice . . . . .	47
2.5.2	Model 2D Intersection Data . . . . .	48
<b>3</b>	<b>Mafic Enclave Sample Petrology</b>	<b>50</b>
3.1	MVO-1591A . . . . .	50
3.2	BEL1B-A . . . . .	50
3.3	TRA10A . . . . .	53
<b>4</b>	<b>3D Size-Shape Results</b>	<b>55</b>
4.1	Tabulated results . . . . .	55
4.2	Plagioclase . . . . .	56
4.2.1	MVO-1591A . . . . .	56
4.2.2	BEL1B-A . . . . .	61
4.2.3	TRA10A . . . . .	65
4.3	Orthopyroxene . . . . .	69
4.3.1	BEL1B-A . . . . .	69
4.4	Amphibole . . . . .	72
4.4.1	TRA10A . . . . .	72

<b>5</b>	<b>Statistical Validation</b>	<b>75</b>
5.1	Plagioclase: MVO-1591A . . . . .	78
5.1.1	CrystalSlice: for plagioclase in MVO-1591A . . . . .	78
5.1.2	Validating the smallest plagioclase population for MVO-1591A . . . . .	79
5.2	Plagioclase: BEL1B-A . . . . .	80
5.2.1	CrystalSlice: plagioclase in BEL1B-A . . . . .	80
5.2.2	Validating the smallest plagioclase population for BEL1B-A . . . . .	81
5.3	Plagioclase: TRA10A . . . . .	83
5.3.1	CrystalSlice: plagioclase in TRA10A . . . . .	83
5.4	Orthopyroxene: BEL1B-A . . . . .	84
5.4.1	CrystalSlice: orthopyroxene in BEL1B-A . . . . .	84
5.4.2	Validating the smallest orthopyroxene population for BEL1B-A . . . . .	85
5.5	Amphibole: TRA10A . . . . .	87
5.5.1	CrystalSlice: amphibole in MVO-1591A . . . . .	87
5.5.2	Summary . . . . .	88
<b>6</b>	<b>Discussion</b>	<b>89</b>
6.1	Crystal growth modelling . . . . .	89
6.1.1	The crystal growth model . . . . .	89
6.1.2	Application to groundmass plagioclase . . . . .	91
6.1.3	Limitations of the crystal growth model . . . . .	100
6.2	Groundmass crystal shapes in TRA10A . . . . .	101
6.2.1	Plagioclase . . . . .	101
6.2.2	Amphibole . . . . .	106
6.3	Orthopyroxene . . . . .	106
6.4	Mafic enclave crystallisation at SHV . . . . .	109
<b>7</b>	<b>Conclusions</b>	<b>112</b>
<b>8</b>	<b>References</b>	<b>115</b>
<b>A</b>	<b>Appendix A: crystal growth model code</b>	<b>123</b>
A.1	Crystal growth modelling MatLab code . . . . .	123
A.2	Textural characteristics . . . . .	128

## List of Figures

1.1	Crystal nucleation and growth in magmatic systems . . . . .	2
1.2	Example Crystal Size Distribution . . . . .	3
1.3	Evolution in plagioclase shape . . . . .	5
1.4	Montserrat map . . . . .	8
1.5	SHV plumbing system . . . . .	9
2.1	Example ShapeCalc output and Zingg diagram . . . . .	13
2.2	Binning method: CSD approach . . . . .	15
2.3	Binning method: counterparts approach . . . . .	16
2.4	Chemical map and BSE map comparison . . . . .	18
2.5	Intersection measurement approach comparison . . . . .	23
2.6	MVO-1591A measurement tests, $w/l$ distribution. . . . .	25
2.7	MVO-1591A: $w:l$ deviation (%) between test measurement approaches . . . . .	26
2.8	TRA10A measurement tests, $w/l$ distribution. . . . .	28
2.9	TRA10A: $w:l$ deviation (%) between test measurement approaches . . . . .	29
2.10	Explanation of the shape descriptor ‘solidity’ . . . . .	30
2.11	Comparison of outlining approaches . . . . .	34
2.12	Comparison of outlining approaches, detailed . . . . .	35
2.13	Comparison of outlining using ‘maximum’ and ‘minimum’ approach . . . . .	39
2.14	$w/l$ distribution of the ‘maximum’ and ‘minimum’ approach. . . . .	40
2.15	CSD test . . . . .	41
2.16	Comparison of outlining around intergrowths or extrapolating through them . . . . .	43
2.17	$w/l$ distribution of the outlining intergrown crystals versus extrapolating through them . . . . .	44
2.18	Overlapping intersections . . . . .	45
2.19	Inclusions in TRA10A . . . . .	46
2.20	CrystalSlice output . . . . .	48
2.21	2D model crystal scaling approach . . . . .	49
3.1	Petrology of host andesite and MVO-1591A . . . . .	51
3.2	Petrology of BEL1B-A and TRA10A . . . . .	52
3.3	Mafic enclave sample geochemistry . . . . .	53
4.1	MVO-1591A intersection outlines . . . . .	57
4.2	MVO-1591A Crystal Size Distribution . . . . .	58
4.3	MVO-1591A plagioclase 3D shape estimate . . . . .	59
4.4	MVO-1591A $w/l$ distributions . . . . .	60
4.5	BEL1B-A plagioclase intersection outlines . . . . .	61
4.6	BEL1B-A Crystal Size Distribution . . . . .	62
4.7	BEL1B-A plagioclase 3D shape estimate . . . . .	63
4.8	BEL1B-A plagioclase $w/l$ distributions . . . . .	64
4.9	TRA10A intersection outlines . . . . .	65
4.10	TRA10A Crystal Size Distribution . . . . .	66
4.11	TRA10A plagioclase 3D shape estimate . . . . .	67

4.12	TRA10A plagioclase <i>w/l</i> distributions . . . . .	68
4.13	BEL1B-A orthopyroxene intersection outlines . . . . .	69
4.14	BEL1B-A orthopyroxene Crystal Size Distribution . . . . .	70
4.15	BEL1B-A orthopyroxene 3D shape estimate . . . . .	71
4.16	BEL1B-A orthopyroxene <i>w/l</i> distributions . . . . .	72
4.17	TRA10A amphibole intersection outlines . . . . .	73
4.18	TRA10A amphibole Crystal Size Distribution . . . . .	74
4.19	TRA10A amphibole 3D shape estimate . . . . .	74
5.1	Statistical validation approach schematic . . . . .	77
5.2	MVO-1591A plagioclase: CrystalSlice results . . . . .	78
5.3	MVO-1519A plagioclase: validation of the smallest size fraction . . . . .	79
5.4	BEL1B-A plagioclase CrystalSlice results . . . . .	81
5.5	BEL1B-A plagioclase: validation of the smallest size fraction . . . . .	82
5.6	TRA10A plagioclase: CrystalSlice results . . . . .	84
5.7	BEL1B-A orthopyroxene CrystalSlice results . . . . .	85
5.8	BEL1B-A plagioclase: validation of the smallest size fraction . . . . .	86
5.9	TRA10A amphibole: CrystalSlice results . . . . .	87
6.1	Crystal growth model schematic . . . . .	90
6.2	Plagioclase growth modelling, Approach 1 . . . . .	93
6.3	Plagioclase growth modelling, Approach 2 . . . . .	95
6.4	Plagioclase growth modelling, Approach 3 . . . . .	96
6.5	Comparison of experimentally grown plagioclase to mafic enclave populations . . . . .	97
6.6	Proposed plagioclase growth scenario in mafic enclaves . . . . .	98
6.7	Growth modelling: 100 $\mu\text{m}^3$ initial prism . . . . .	100
6.8	Mafic enclave cooling model . . . . .	102
6.9	Textural complexity of groundmass plagioclase in TRA10A . . . . .	104
6.10	Textural complexity of groundmass amphibole in TRA10A . . . . .	105
6.11	Orthopyroxene growth modelling, Approach 1 . . . . .	107
6.12	Orthopyroxene growth modelling, Approach 2 . . . . .	107
6.13	3D shape estimates of orthopyroxene populations . . . . .	109
6.14	Mafic enclave crystallisation at SHV . . . . .	110

## List of Tables

2.1	Standards analysis . . . . .	19
2.2	Intersection measurement approach comparison . . . . .	21
2.3	3D shape estimates for test measurement approaches . . . . .	24
2.4	$w:l$ deviation (%) between test measurement approaches . . . . .	24
2.5	Crystal intersection outlining approaches . . . . .	33
2.6	Outlining tests: 2D size-shape data . . . . .	37
2.7	3D shape estimates from 2D intersection width and length measurement for different outlining approaches. . . . .	38
3.1	Mafic enclave sample chemistry . . . . .	54
4.1	2D intersection size-shape data . . . . .	55
4.2	Crystal Size Distribution slope, intercept and inputs . . . . .	56
4.3	Intersection & 3D shape data for all phases . . . . .	56
5.1	CrystalSlice model inputs and results . . . . .	75
5.2	MVO-1591A plagioclase: Model cuboid scaling . . . . .	76
6.1	Plagioclase growth modelling inputs . . . . .	91
6.2	Orthopyroxene growth modelling inputs . . . . .	106
A.1	3D textural characteristics of MVO-1591A . . . . .	128
A.2	3D textural characteristics of BEL1B-A . . . . .	128

## **Declaration**

I declare that this thesis, submitted for the degree of Master of Science at Durham University, is my own work and does not contain material previously submitted for a degree in this or any other institution.

## **Statement of Copyright**

The copyright of this thesis (including any appendices or supplementary materials to this thesis) rests with the author, unless otherwise stated.

## **Acknowledgements**

Foremost, a great deal of thanks is extended to my supervisors Madeleine Humphreys and Martin Mangler for their expert guidance, feedback and encouragement over the last year and a half. It has been a privilege to work with them, and I am extremely grateful for their support. I would like to thank Amando Lindoo for many helpful discussions on all things plagioclase, and Ceri Allgood for kindly providing her wonderful code. Leon Bowen is thanked for his assistance with SEM-EDS imaging and analysis.

Thank you to the Volcanology group at Durham for fostering such a vibrant, welcoming space in which I felt empowered to participate, learn from others, ask for help, share my thoughts and consume many caterpillar cakes. I am more confident in my abilities now than when I first started at Durham, and that is in no small part due to the support of the wider Volcanology group.

In particular, I am grateful to the officemates of Chaos Corner for their friendship, inspiration and coffee runs; it was a pleasure to be a part of the madness for a year. Finally, I would like to thank Hakan for his kindness, endless support and Tuesday lunches.

# 1 Introduction

## 1.1 Background

Crystals in igneous rocks are recorders of the magmatic conditions experienced during their nucleation and growth. When combined with geochemical information, characterising the textural features of the crystal cargo such as crystal size, shape, number density, and the zonation within individual crystals can inform on magmatic processes. This includes insights into storage and assembly of melts (Zellmer et al., 2024; Blundy & Cashman, 2008; Streck, 2008; Bennett et al., 2019; Salisbury et al., 2008) or ascent and eruptive processes (Brugger & Hammer, 2010; Rutherford & Hill, 1993; Browne & Gardner, 2006).

### 1.1.1 Crystal nucleation and growth

The petrogenetic significance of crystal size is both well-understood, and a well-established parameter in textural studies. Crystal size is a function of nucleation and growth rate, where both have a dependency on the degree of undercooling (Kirkpatrick, 1975; Marsh, 1998). Undercooling can be defined as the difference between the actual melt temperature and the temperature at which a crystal phase saturates in the melt (Mollo & Hammer, 2017; Kirkpatrick, 1981). Undercooling can refer to either a decrease in the actual temperature of a melt, or an increase in the liquidus temperature of a melt due to compositional change induced by crystallisation or volatile exsolution (Mollo & Hammer, 2017).

In crystal nucleation, the nucleus is required to reach a critical size by addition of atoms or molecules in order to grow spontaneously (Swanson, 1977; Kirkpatrick, 1981; Hammer, 2008). This critical size varies from very high near liquidus temperatures to smaller sizes as the degree of undercooling increases. At higher degrees of undercooling, a smaller size of nucleus is required to become stable and grow, making nucleation more likely to occur in these conditions. Therefore, higher degrees of undercooling promote a higher nucleation rate, resulting in a high number density of small crystals (Figure 1.1a). Conversely, relatively lower undercooling promotes a lower nucleation rate, producing a low number density of larger crystals (Figure 1.1; Marsh, 1998; Cashman, 1990).

Growth rate is also integral to the development of crystal textures. Crystal growth is characterised as either interface-controlled or diffusion-limited, the transition between which is controlled by the degree of undercooling (Kirkpatrick, 1975; Lofgren, 1974; Muncill & Lasaga, 1987). Low degrees of undercooling promote interface-controlled growth, where the rate-limiting process is the attachment of atoms to the advancing crystal face. High undercooling promotes diffusion-limited growth, where the rate-limiting process is the movement of components through the melt to and from the advancing crystal face. The balance between interface-controlled and diffusion-limited growth exerts control on crystal morphology, discussed in Chapter 1.1.3 and illustrated in Figure 1.1b. Likewise to nucleation rates, growth rates increase to a maximum at some degree of undercooling and then decrease (Figure 1.1a), with the exact position of the curves and their maxima being specific to both the crystallising phase and magmatic system in question (Mollo & Hammer, 2017).

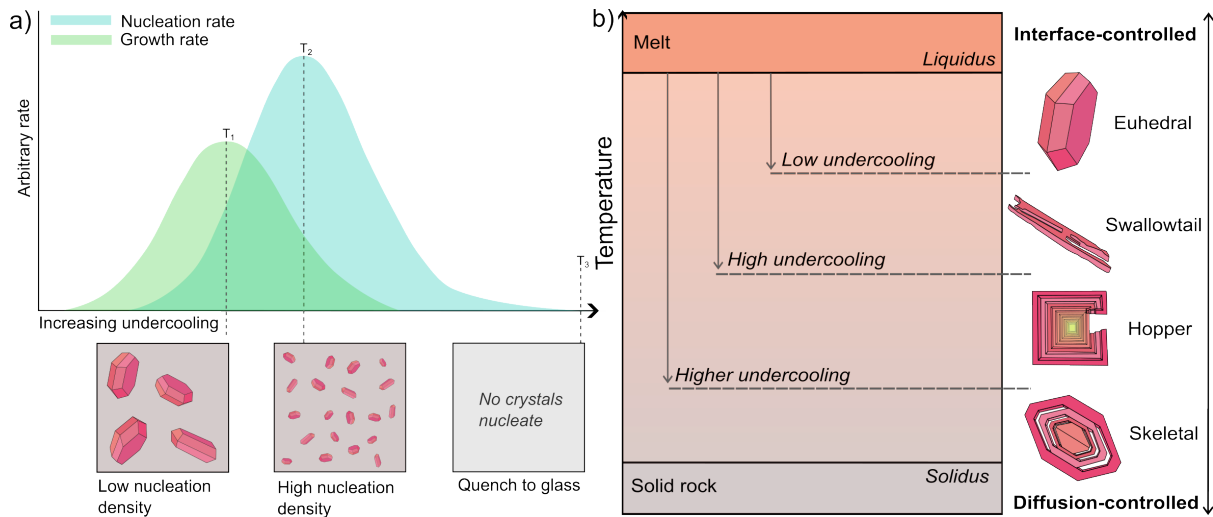


**Figure 1.1:** Crystal nucleation and growth in magmatic systems. **a)** Nucleation rates peak at a higher degree of undercooling than growth rates. Undercooling a melt to  $T_1$  below the liquidus promotes crystal formation in the growth-dominated regime, producing a low number density of large crystals. A higher degree of undercooling to  $T_2$  promotes crystal formation in the nucleation-dominated regime, producing a higher number density of small crystals. A very high degree of undercooling to  $T_3$  causes the melt to quench to glass before nucleation can occur. **b)** Low undercooling promotes the formation of euhedral crystals, with greater undercooling producing increasingly anhedral morphologies.

Continuous nucleation and growth in a melt will produce multiple crystal size populations. This is because undercooling is a dynamic property that changes over time in natural magmatic scenarios, imparting different nucleation and growth rates to different crystal populations formed through time. For example, a magma could experience a relatively low cooling rate upon intrusion into the crust, reflected in a low number density of large euhedral crystals. A second undercooling event upon rapid ascent in eruption would impart a high degree of undercooling, producing a high number density of small crystals, possibly with anhedral morphology (after Figure 1.1). Complexity in the overall crystal assemblage can be added by the addition of crystals from elsewhere, including antecrysts from magma mixing or xenocrysts from incorporation of wall-rock.

### 1.1.2 Crystal Size Distributions

The presence of multiple size populations is utilised in Crystal Size Distribution (CSD) analysis, an approach to quantitatively characterise the crystallinity of a rock as a function of crystal size (see Cashman (2020) for an in-depth review). Initially developed for industrial crystallisation scenarios (Randolph & Larsen, 1971), CSD theory was adapted by Marsh (1988) for application to magmatic systems. CSDs are a plot of the natural logarithm of population density against size, the interpretation of which can be used to derive timescales of crystal nucleation and growth (Figure 1.2). Nucleation rate can be estimated from the y-intercept, characteristic crystal size can be estimated from the slope, and where residence times are known, growth rate can be calculated (Marsh, 1988). These inferences require the assumption of a single, constant growth rate for all phenocrysts measured. This is problematic given that crystal populations can have

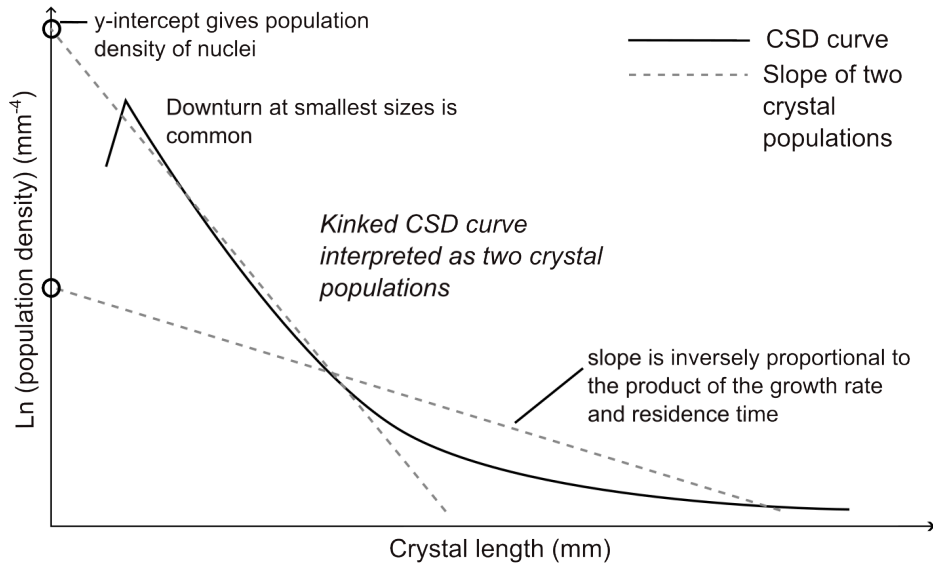


**Figure 1.2:** Example CSD showing a kinked plot with two crystal populations, often inferred to occur by addition of antecrysts by magma mixing (Higgins, 1996b), two nucleation events within a melt (Marsh, 1998) or aggregation of smaller crystals to form larger forms (Marsh, 1998). A downturn at the smallest crystal sizes is common, and often attributed to a lack of smaller crystals imaged due to low resolution (Marsh, 1998; Hammer et al., 1999), coarsening of the smallest crystals to larger forms (Higgins & Roberge, 2003), or intersection probability effects (Brugger & Hammer, 2010). The y-intercept can be used to calculate the nucleation rate, and the slope can be used to calculate growth rate if residence time is known.

diverse origins, experiencing different growth rates as magmatic conditions change over time (Cashman, 2020; Brugger & Hammer, 2010). CSDs have been used to constrain crystallisation histories of igneous rocks, by inferring residence times of storage prior to eruption (Cashman & Marsh, 1988; Cashman, 1992; Mangan, 1990; Salisbury et al., 2008; Higgins, 2002), identifying magma mixing events (Higgins, 1996) and informing on ascent rate dynamics, degassing and microlite crystallisation (Brugger & Hammer, 2010; Hammer et al., 1999).

In practice, CSDs are commonly constructed using the software CSDCorrections (Higgins, 2000). This programme converts 2D crystal intersection measurements into a 3D crystal size distribution by complex stereological corrections. There are two key problems, outlined by Higgins (2000). The cut-section effect describes that a particle is rarely ever intersected in the centre. Therefore, even in a homogenous, single shape-size population of crystals, the resulting intersections will cover a wide range of sizes. Many small intersections may result from the intersection of the edge of a much larger crystal, here referred to as corner-cuts. Moreover, the intersection probability effect describes that for a population of multiple sizes, larger crystals are much more likely to be intersected than smaller ones. Crystal shape will also affect the CSD reconstruction, but usually is assumed to be constant. Any reconstruction of 3D size or shape from 2D intersection measurements must therefore account for these issues in stereological corrections.

### 1.1.3 Crystal shape

In contrast to crystal size, the petrogenetic significance of crystal shape is less well understood and applied in textural studies. Crystal growth is characterised as either interface-controlled or diffusion-limited, the transition between which is controlled by the degree of undercooling. (Kirkpatrick 1975; Lofgren, 1974; Muncill & Lasaga, 1987). The growth regime exerts control on the crystal morphology. A low degree of undercooling promotes interface-controlled growth, where the rate-limiting process is the attachment of atoms to the advancing crystal face. This produces euhedral morphologies with well-formed crystal facets (Figure 1.1b), with the exact habit being determined by the relative growth rates of individual crystal faces (Kirkpatrick, 1975). A high degree of undercooling promotes diffusion-limited growth, where the rate-limiting process is the movement of components through the melt to and from the advancing crystal face. This produces cellular morphologies such as skeletal, dendritic and spherulitic forms (Figure 1.1b; Lofgren, 1974; Kirkpatrick, 1975; Shea & Hammer, 2013). Undercooling therefore exerts control on crystal shape as well as size. The transition from euhedral to cellular morphologies has been investigated extensively in both isobaric cooling experiments (Lofgren, 1974; Lofgren, 1973; Muncill & Lasaga, 1987; Shea & Hammer, 2013; Arzilli et al., 2022) and isothermal decompression experiments (Shea & Hammer, 2013; Hammer & Rutherford, 2002; Martel, 2012). Most studies have been concerned with high degrees of undercooling, focusing on the development of cellular morphologies. However, what is missing is a comprehensive understanding of the conditions that produce variation in euhedral crystal shapes.

Recent work has sought to address this gap. Duchene et al. (2008) reconstructed the 3D shape of plagioclase crystals grown experimentally, by applying a geomodelling software to photographs of 2D sections. Whilst most plagioclase were tabular, with a constant intermediate/long ( $I/L$ ) axes ratio, there was significant variability in short/intermediate ( $S/I$ ) axes ratio. This variability in euhedral shape developed in an isobaric thermal experiment where cooling rate was constant during crystallisation. It was suggested that plagioclase shapes reflected distinct episodes of crystal growth as melt conditions changed over the course of the experiment, possibly due to changing melt diffusivity with cooling affecting growth rates on individual crystal faces. Another explanation for the morphological variation was crystal attachment by synneusis. Holness (2014) explored variation in plagioclase aspect ratio (AR, 2D intersection long and short axes ratio) in natural sills. Plagioclase AR was found to vary systematically through the sills, the average AR being higher in thin sills inferred to experience higher cooling rates than thicker sills, with lower AR and slower cooling rates. This demonstration of the dependence of plagioclase shape on cooling rate illustrated how euhedral crystal shape has petrogenetic significance, and can be applied to understand magmatic conditions.

More recently, Mangler et al. (2022) recognised that since crystal shape is sensitive to magmatic conditions, this should be reflected in the presence of different shape populations produced by continuous nucleation and growth of crystals through changing magmatic conditions - much the same as the presence of multiple size populations that has been so successfully exploited in CSD analysis. Reconstructing 3D shape-size relationships for plagioclase in natural samples, where 'habit' describes the ratio of the Short:Intermediate:Long axis ( $S:I:L$ ), Mangler et al. (2022)

demonstrated that plagioclase undergoes a systematic evolution in shape with size as it grows. Plagioclase nucleates as a prism (high  $S/I$ ) and preferentially overgrows in the intermediate dimension ( $I$ ) to evolve into a steady-state tab (lower  $S/I$ ) (Figure 1.3). Plagioclase rapidly attain the shape defined by their relative growth rates after nucleation, attaining ‘steady-state shape’ with a small volume increase. For the overgrowth of a  $0.1 \mu\text{m}^3$  prism, steady-state shape was achieved with a  $\sim 100 \mu\text{m}^3$  increase in crystal volume; the absolute value will depend on the initial crystal size, shape, overgrowth shape and number density (Mangler et al., 2022).

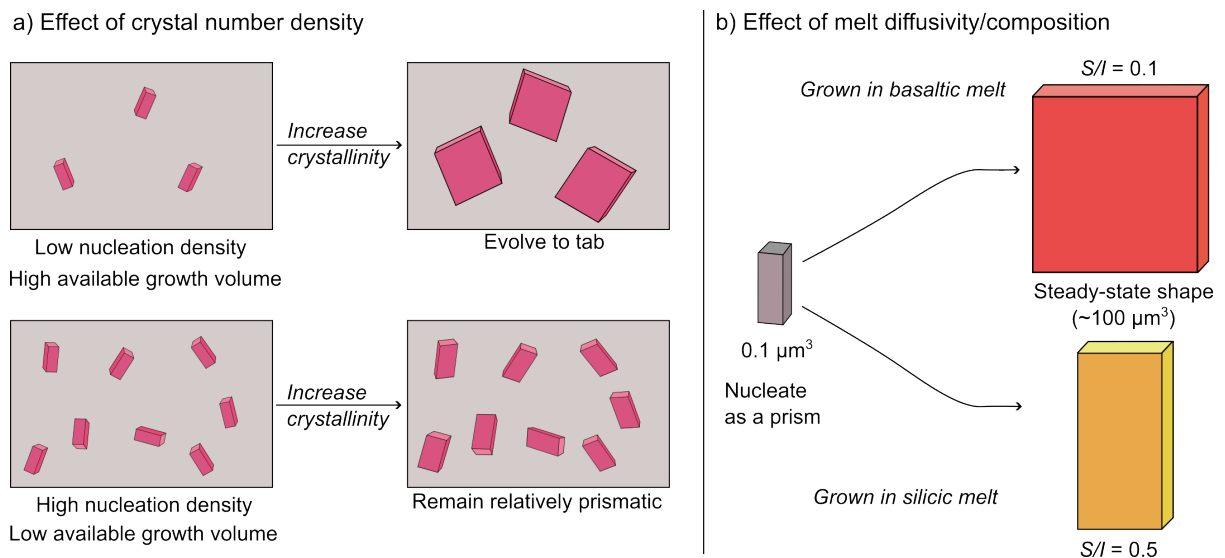


**Figure 1.3:** Evolution in plagioclase shape with size. **a)** Effect of number density (after Mangler et al., 2022). A low number density associated with low degrees of undercooling means there is large available growth volume for crystals to evolve from prisms to steady-state tabs. A high number density reduces the available growth volume, so crystals remain relatively prismatic with growth. **b)** Effect of melt composition/diffusivity (after Mangler et al., 2023). Plagioclase experimentally grown in basaltic melt (red) have a lower  $S/I$  (i.e., more tabular) steady-state overgrowth shape than those grown in more silicic melt (yellow). Steady-state shape is reached with a relatively small volume increase (i.e. from an initial volume of  $0.1 \mu\text{m}^3$  to  $100 \mu\text{m}^3$  with growth).

The systematic evolution in crystal shape is affected by undercooling. A high degree of undercooling imparts a high nucleation rate, producing a large number of small crystals with low ‘available growth volume’, meaning that crystals remain relatively prismatic (Figure 1.3). Lower undercooling produces a lower crystal number density, such that the few crystals have greater available growth volume and therefore can evolve in size to tabular shapes. Mangler et al. (2022) linked these concepts to magmatic ascent rates, demonstrating the petrogenetic significance of euhedral plagioclase shape. Mangler et al. (2023) explored these concepts further, showing that when interface reactions occur at a similar rate to diffusion processes, plagioclase growth can occur in an intermediate growth-regime where different growth-limitations act on different advancing crystal faces. This manifests as variation in euhedral plagioclase morphology. The morphology of experimentally-grown plagioclase populations displayed a dependency on the melt composition/diffusivity, with plagioclase grown from basaltic melts having a lower

$S/I$  (i.e., more tabular) shape than those grown from more silicic melts, due to differences in relative growth rates between populations.

It is not yet clear whether other silicate phases undergo a similar systematic evolution in shape with size that can be linked to magmatic conditions. Recent work (Okumura et al., 2022; 2024) has explored pyroxene ‘tracht’, a term similar to habit but that specifically describes the combination of crystallographic faces (Sunagawa, 2006). Decompression-induced crystallisation experiments demonstrated that pyroxene tracht evolves from octagonal at low effective undercooling to hexagonal at higher undercooling (Okumura et al., 2022), with the threshold undercooling at which transition occurs influenced by melt composition (Okumura et al., 2024). Whilst this did not show a systematic change in 3D aspect ratio as is inferred for plagioclase, this did demonstrate the sensitivity of pyroxene morphology to changing magmatic conditions. This could suggest that there is a underlying process controlling crystal shape, that may be common across all silicates; however, a demonstration of this is currently missing in the literature.

Crystal shape in igneous rocks has petrogenetic significance, with the sensitivity of crystals to changing magmatic conditions reflected in systematic variations in euhedral morphology (Mangler et al., 2022; 2023; Okumura et al., 2022; 2024). Characterising crystal shape-size relationships can therefore provide insights into magmatic processes at depth and upon ascent. As well as this, CSD analysis requires an estimate of crystal shape for stereological corrections, which is usually assumed to be constant across crystal sizes (Higgins, 2002; Higgins & Roberge, 2003; Mangan, 1990; Armienti et al., 1994). Accurately constraining the 3D shape of each crystal size population is therefore important to produce useful CSDs for better interpretation of nucleation and growth dynamics.

Further, crystal shape is an important property to consider in understanding the development and remobilisation of crystal mushes, as the shape of crystals within a melt affects the rheology of the magma (Moitra & Gonnermann, 2015). ‘Maximum packing fraction’ describes the crystallinity at which a suspension is considered rheologically immobile, and is strongly dependent on particle aspect ratio (Mueller et al., 2010; 2011). The fraction of particles a melt can hold before becoming ‘locked’ as a mush is greatest for equant ( $S \approx I$ ) crystals, decreasing for increasingly tabular ( $S \ll I \ll L$ ) crystals (Mueller et al., 2011). Bretagne et al. (2023) found that crystal shape not only affects the maximum packing fraction, but also changes the permeability of a mush at a given melt fraction. The permeability of a maximally packed mush consisting of prolate (needle-like habit) crystals is higher than that consisting of oblate (platy habit) crystals. Constraining crystal shape and how it may systematically evolve in response to changing magmatic conditions is therefore crucial to understand the dynamics and timescales of processes in crystal mushes, as well as volcanic processes.

## 1.2 Crystal shape-size relationships in mafic enclaves

Characterising crystal shapes under different crystallisation conditions is important to better understand the petrogenetic significance of crystal morphology. Different conditions include decompression-induced crystallisation upon magmatic ascent, crystallisation at depth prior to eruption, and cooling of intrusions. Here, we explore crystallisation upon intrusion prior to

eruption by examining groundmass crystal shape-size relationships in magmatic enclaves. Magmatic enclaves form upon the mingling of two melts that are thermo-mechanically inhibited from mixing fully due to a significant contrast in viscosity, caused by the different temperature, composition or crystallinity of the magmas (Bacon, 1986; Sparks & Marshall, 1986; Eichelberger, 1980). Magma mingling typically occurs when a more mafic magma replenishes a long-lived silicic mush reservoir, and is a significant process in arc volcanism (Laumonier et al., 2014; Coombs et al., 2003; Tepley et al., 2000; Clynne, 1999; Browne et al., 2006; Pallister et al., 1992, 1996; Kent et al., 2010). The addition of heat, mass and volatiles from the intruding magma to the silicic reservoir has the potential to remobilise melt, with magma mixing having been recognised to be a potential eruption trigger (Sparks et al., 1977; Eichelberger, 1980; Pallister et al., 1996; Larsen et al., 2006). Mafic enclaves therefore preserve a snapshot of these mingling dynamics. Enclaves with diktytaxitic groundmass texture are thought to form by rapid quench crystallisation (Bacon, 1986), and therefore provide a relatively simple crystallisation scenario in which to explore the petrogenetic significance of crystal shape.

This study examines 3D crystal shape-size relationships in three mafic enclaves from SHV. The aims of this study are as follows:

- Characterise the mafic enclaves texturally and geochemically (Chapter 3).

The thin sections were examined and imaged using optical microscopy and Scanning Electron Microscopy (SEM) to characterise crystal textures. Electron Dispersive Spectroscopy (SEM-EDS) was used to analyse crystal chemistry.

- Characterise the 3D shape-size relationships of groundmass plagioclase, orthopyroxene and amphibole. (Chapter 4).

Groundmass crystals were outlined and measured to obtain 2D intersection data. Crystal size distributions were then reconstructed using CSDCorrections (Higgins 2000) and 3D crystal shape estimated using ShapeCalc (Mangler et al., 2022). This was carried out to investigate if groundmass plagioclase displays the same systematic evolution in shape (from prismatic to tabular with increasing size) observed in Mangler et al. (2022). Whereas that study examined plagioclase microlites formed by decompression-induced crystallisation upon magmatic ascent, here we examine groundmass plagioclase formed by quench crystallisation upon magma mixing. Amphibole and orthopyroxene shape-size relationships were also constrained in order to investigate whether other key rock-forming silicate phases display a similar systematic evolution in shape with size. If so, this possibly suggests a common underlying process in silicate mineral growth, which could be exploited to infer crystallisation conditions.

- Verify that the 3D shape-size relationships are true textural features rather than statistical artefacts (Chapter 5).

Statistical testing of the 3D shape-size results was conducted to assess whether the suggested 3D shape-size relationships are true textural features, or whether they could be explained as statistical artefacts. For example, the smallest crystal populations might

possibly be corner-cuts of a larger population (i.e., the previously described 'cut-section effect').

- Explore how varying steady-state overgrowth shape can reproduce the observed shape-size relationships in the mafic enclaves (Chapter 6).

An adapted crystal growth model (c.f. Mangler et al., 2022) is used to model crystal growth. Comparing the model evolution in crystal shape and size to the observed shape-size relationships enables comment on the crystallisation conditions under which the groundmass crystal populations could have formed.

- Interpret the petrogenetic significance of crystal shape in enclave crystallisation in terms of the wider context of mingling dynamics at SHV (Chapter 6)

### 1.3 Geological history and petrology of Soufrière Hills Volcano

Soufrière Hills Volcano, Montserrat is part of the Lesser Antilles volcanic island arc (Figure 1.4), formed by the oceanic Atlantic Plate subducting underneath the Caribbean Plate. Of the five volcanic centres on Montserrat, SHV is the only active centre, with activity from  $\sim 300$  ka to present (Rea, 1974). The volcano is a composite of at least five andesitic lava domes, with the flanks composed of pyroclastic deposits (Zellmer et al., 2003a; Murphy et al., 2000). The most recent eruption lasted 15 years, from July 1995 to February 2010, encompassing five phases of activity (see Wadge et al. (2014) for a detailed eruption chronology). The eruptive activity was characterised by episodic dome growth and collapse alongside Vulcanian explosions, interrupted by repose in lava extrusion (Wadge et al., 2014; Sparks & Young, 2002; Ryan et al., 2010).

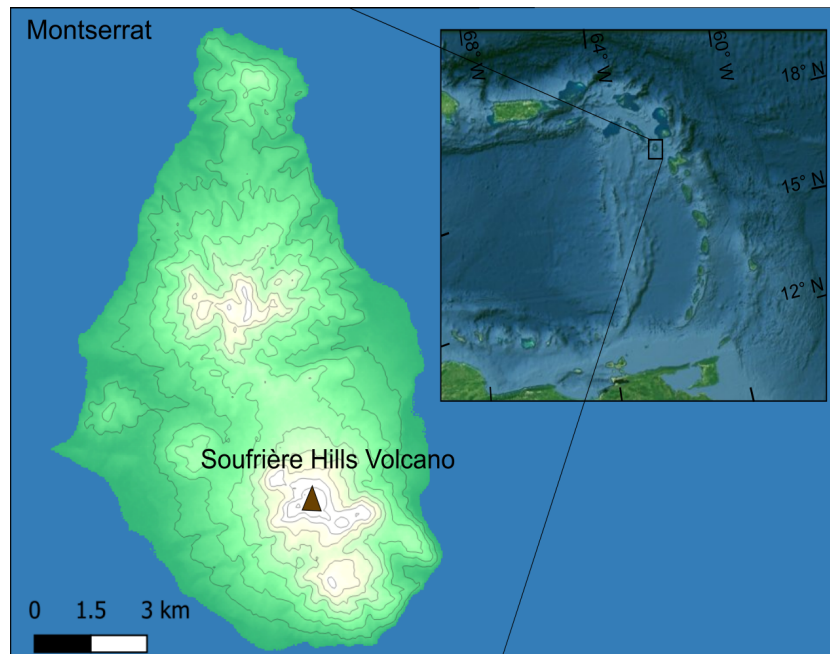


**Figure 1.4:** Location of SHV, Montserrat in the Lesser Antilles volcanic island arc (ASTGTM v003 DEM, USGS, 2025).

The SHV plumbing system is thought to consist of a long-lived andesitic reservoir at shallow depth, that is periodically recharged by influxes of mafic magma (Figure 1.5). Earlier work suggested that the depth of the reservoir was  $\sim 5\text{-}6$  km (110-130 MPa) constrained by experimental and petrological work (Barclay et al., 1998; Devine et al., 1998) and seismic studies (Aspinall et al., 1998). More recent work (Edmonds et al., 2016) has suggested deeper storage depths of 8-14 km and the presence of a vertically protracted crystal mush underlying south Soufrière Hills. Prior to eruption, the andesite was stored at 820-840 °C, constrained by the stability fields of amphibole and quartz, which are both present in the phenocryst assemblage (Barclay et al., 1998). The extended history of the andesite reservoir includes multiple cycles of reheating and recrystallisation on a millennial scale ( $10^3\text{-}10^4$  years), evident from textural disequilibrium features in phenocrysts including complex zonation, reaction rims and resorption features (Zellmer et al., 2003a) and an inferred wide range of crystal residence times (Zellmer et al., 2003b). Periodic recharge of the silicic reservoir by basaltic melt from a deeper region ( $\sim 12$  km depth, Elsworth et al., 2008) drives these reheating cycles and was inferred to have occurred prior to the most recent eruption, acting as an eruption trigger (Murphy et al., 2000; Murphy et al., 1998). The intrusion of hotter (1050 °C, Murphy et al. (2000)), less crystalline basalt provides heat and volatiles as the driver for eruption (Devine et al., 2003; Murphy et al., 2000; Edmonds et al., 2014). Mafic enclaves are present throughout the eruption (Murphy et al., 2000; Barclay et al., 2010; Plail et al., 2014) but additional evidence for mixing is abundant, including

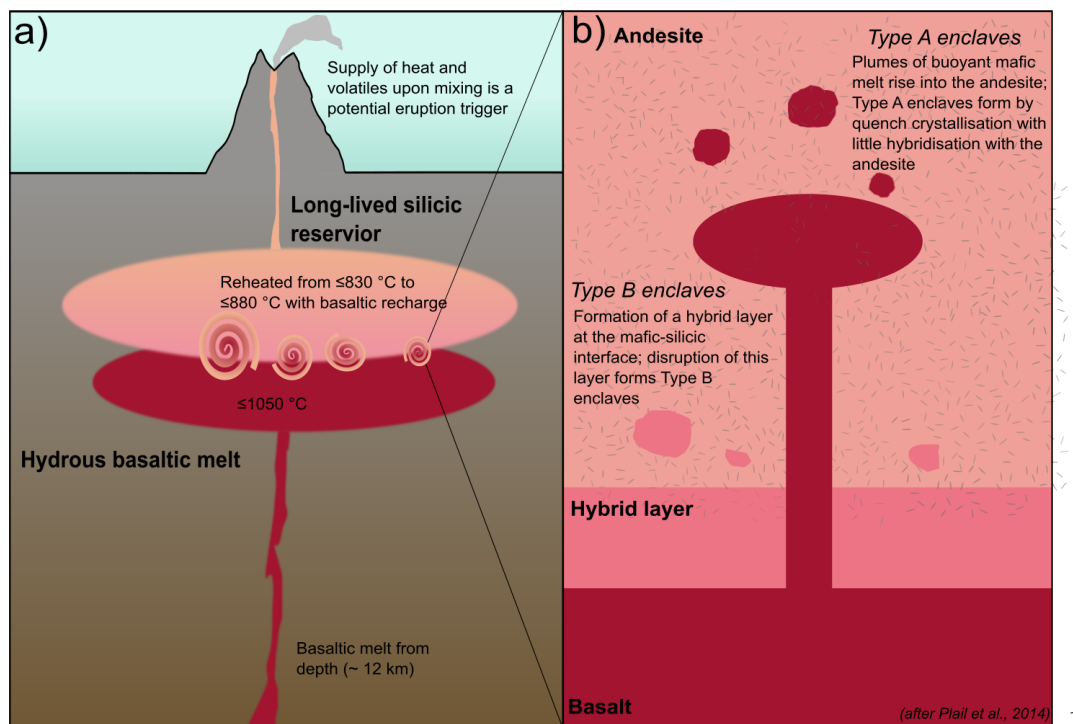


**Figure 1.5:** **a)** The SHV plumbing system involves a long-lived silicic reservoir that is periodically recharged by basaltic magma from depth. **b)** After Plail et al. (2014; 2018), mafic magma rises as buoyant plumes into the andesite. Type A enclaves form by quench crystallisation, likely at plume margins. A hybrid layer develops at the mafic-silicic interface, from which Type B enclaves form.

disequilibrium textures in the andesite phenocryst assemblage (Murphy et al., 2000; Devine et al., 1998), excess volatile emissions (Edmonds et al., 2010; Christopher et al., 2010) and the presence of microlites grown in basaltic melt transferred to the host andesite (Humphreys et al., 2009). Mafic enclaves notably increased in abundance across the five phases of the eruption (Barclay et al., 2010). In Phase I, mafic enclaves constituted <1 % of erupted material, rising to 5-7 % in Phase III, and finally 3-8 % in Phase IV-V (Murphy et al., 2000; Plail et al., 2014; Barclay et al., 2010; Didonna et al., 2022).

The petrology of the andesitic rocks has been extensively characterised (Murphy et al., 2000; Barclay et al., 1998; Devine et al., 1998; Humphreys et al., 2009) and remained relatively constant over the course of the eruption, despite changes in eruptive style (Murphy et al., 2000; Humphreys et al., 2009; Christopher et al., 2014). The andesite is 57-61 wt.% SiO<sub>2</sub>, highly crystalline and porphyritic, with 33-66 vol.% phenocrysts (Murphy et al., 1998; Didonna et al., 2022; Devine et al., 1998; Barclay et al., 1998; Humphreys et al., 2009; Murphy et al., 2000). The phenocryst assemblage, in order of abundance, consists of plagioclase + amphibole + orthopyroxene + Fe-Ti oxides, with minor quartz, apatite and clinopyroxene. The groundmass assemblage lacks amphibole, instead consisting of plagioclase + orthopyroxene + clinopyroxene + Fe-Ti oxides + interstitial glass ± quartz. Glass abundance varies from 5-25 %, and is high-Si rhyolite of 75-79 wt.% SiO<sub>2</sub> (Murphy et al., 2000; Humphreys et al., 2010). Phenocrysts of plagioclase, orthopyroxene, amphibole and quartz display varied and complex textures indicative of disequilibrium, categorised in detail by Murphy et al. (2000) and Humphreys et al. (2009). These textures have been used to infer the repeated reheating of the shallow silicic body and have been linked to magmatic ascent by decompression-induced breakdown rims in amphiboles (Rutherford & Devine, 2003).

Mafic enclaves comprise a minor but ubiquitous component of the eruptive material (Barclay et al., 2010), with their petrology also having been extensively characterised (Murphy et al., 2000; Plail et al., 2014; Christopher et al., 2014). The whole rock composition is basaltic to basaltic-andesitic, ranging in SiO<sub>2</sub> from 49 - 57 wt.% (Plail et al., 2014; Christopher et al., 2014). The enclaves have a diktytaxitic groundmass texture of framework plagioclase. This is indicative of rapid cooling by quench crystallisation (Bacon, 1986). The groundmass assemblage consists of plagioclase ± amphibole ± orthopyroxene ± clinopyroxene + Fe-Ti oxides + trace amounts of apatite + interstitial glass. Glass abundance is variable, and is high-Si rhyolite of 71-78 wt.% silica (Plail et al., 2014; Humphreys et al., 2010). Enclaves contain large (2-3 cm) crystals of plagioclase, amphibole and orthopyroxene, interpreted as inherited phenocrysts from the host andesite (Plail et al., 2014; Humphreys et al., 2009). These crystals typically display a range of disequilibrium textures attributed to both reheating episodes experienced when resident in the silicic reservoir, and then disequilibrium induced by transferring into the hotter, basaltic melt of the enclave. This includes plagioclase with sieved cores indicative of pervasive resorption, rounded interiors from surficial resorption, orthopyroxene overgrown by clinopyroxene at the rim, and reacted amphiboles with a range of breakdown textures (Humphreys et al., 2009). Plail et al. (2014) designed a classification for enclaves from Phase IV-V as Type A, B or C based on their textural features, which are linked to the differences in mingling dynamics in their

formation (Figure 1.5). Type A enclaves are typified by a high-Al amphibole-bearing groundmass, chilled margins at the contact between the enclave and host andesite, high vesicularity (32 vol.% mean) and the most primitive compositions (49-52 wt.% SiO<sub>2</sub>). They are suggested to form at plume margins by rapid quench crystallisation, with little hybridisation between the mingling magmas. Type B enclaves lack groundmass amphibole and chilled margins, are of lower vesicularity (13 vol.% mean), are more evolved (53-57 wt.% SiO<sub>2</sub>), and they are thought to have formed from a 'hybrid layer' that develops between the silicic and mafic magmas. Type C enclaves are composite, with at minimum two distinct textural zones, proposed to form from mingling between the mafic melt with the hybrid layer.

## 2 Methods

Here we present the methods used to produce and validate the 3D crystal shape estimates. First, conversion of 2D crystal intersection data to 3D shape and size estimates will be discussed, explaining the use of the programs ShapeCalc (Mangler et al., 2022) and CSDCorrections (Higgins, 2000). Then, the method of collecting BSE maps, chemical maps and geochemical data of crystal phases using SEM-EDS will be discussed. Approaches to crystal intersection measurement will be considered, with three methods tested and recommendations given. Different approaches to crystal intersection outlining will then be tested to establish an accurate, consistent and reproducible method used to collect 2D size-shape measurements. This data is then used to produce 3D shape estimates of crystals. Finally, statistical validation tests are outlined to explore whether the suggested shape-size relationships in groundmass crystals could be explained by statistical artefacts.

### 2.1 2D intersection data to 3D size-shape estimates

#### 2.1.1 ShapeCalc

Crystal intersections in thin section are a 2D expression of 3D crystals. 2D intersection width and length ( $w$  and  $l$ ) can be used to constrain 3D shape (Short:Intermediate:Long dimensions;  $S:I:L$ ) using stereological conversion (Higgins, 1994; Higgins, 2000; Higgins, 1996). It was established that for a crystal population that is randomly oriented, the same shape and the same size:

- Modal 2D length ( $l$ ) approximates the intermediate dimension ( $I$ );
- Modal 2D width ( $w$ ) approximates the short dimension ( $S$ );
  - Therefore the mode of the 2D intersection  $w/l$  distribution provides the 3D  $S/I$  of the crystal.
- Skewness of the  $w/l$  distribution (+ 0.5) can provide an estimate of intermediate/long dimension ( $I/L$ );
  - Long dimension ( $L$ ) alone is challenging to constrain, due to the lack of intersections along the long axis in thin section.

The requirements to enable conversion of 2D intersection data to 3D shape measurements are therefore:

- Understanding of crystal orientation;
- Understanding of 3D crystal size;
- Robust 2D  $w/l$  measurements, obtained by measuring a sufficient number of 2D intersections with an accurate, consistent and reproducible method.

The program ShapeCalc (Mangler et al., 2022) was used to constrain 3D crystal shape from 2D intersection  $w$  and  $l$ . 200 intersections is the minimum sufficient number for analysis (Mangler

et al., 2022; Mock & Jerram, 2005). ShapeCalc compares the  $w/l$  distribution of input sample data to 2618 model  $w/l$  distributions, spanning  $S:I:L$  between 1:1:1 to 20:20:20. The best-fit 3D shape is calculated by maximising  $R_c^2$ , the cumulative measure of the goodness-of-fit between the sample and model distributions.  $R_c^2 \geq 0.975$  indicates satisfactory model fits.  $R_c^2 < 0.975$  indicates a larger discrepancy between sample and model  $w/l$  distributions than reasonably expected for a natural sample (Mangler et al., 2022). Model  $w/l$  distributions are derived from the program CSDCorrections (Higgins, 2000; Chapter 2.1.2). In this program, an orthogonal solid is randomly sectioned 50,000 times to create a representative  $w/l$  distribution. The ShapeCalc database includes 20,000 intersections per model shape distribution.

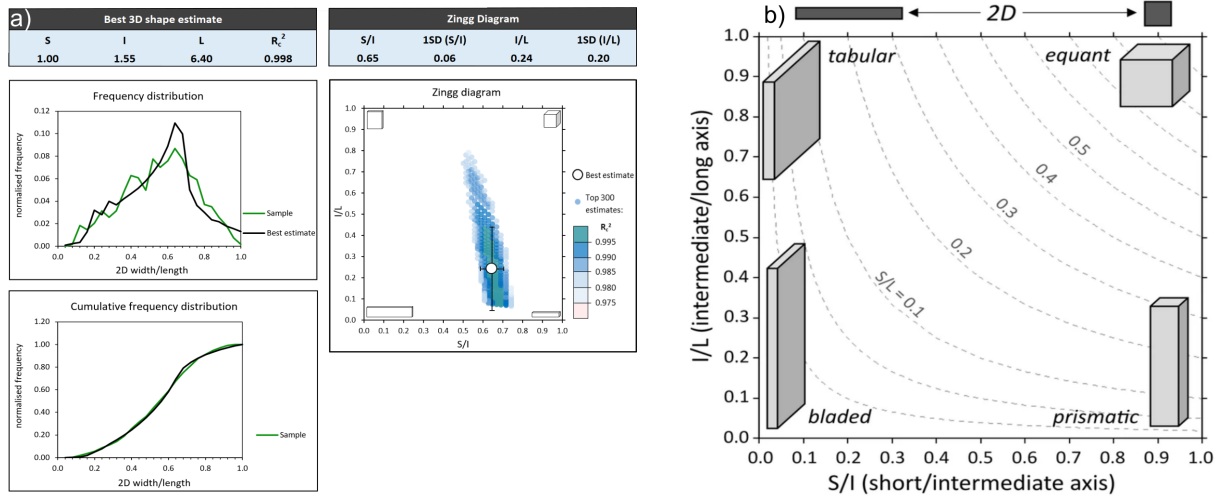


**Figure 2.1:** a) ShapeCalc output featuring the best-fit 3D shape estimate illustrated on a Zingg diagram, alongside a comparisons of the  $w/l$  distributions and the cumulative frequency distributions of the natural sample intersection data and the best-fit model shape. In this example, the natural sample data has a best-fit 3D shape of 1.00:1.55:6.40. The high  $R_c^2$  suggests a good fit of the sample data to the model shape, illustrated by the comparison of  $w/l$  distributions. b) Example Zingg diagram from Mangler et al. (2022). This plot visualises 3D shape by plotting  $S/I$  against  $I/L$ . The dominant 2D intersection shape of equant and prismatic 3D shapes has  $S=I$ . The dominant 2D intersection shape of tabular and bladed 3D shapes has  $I>S$ . Contours of equal  $S/L$  become more closely spaced towards equant shapes.

Figure 2.1a illustrates a ShapeCalc output for a good sample-model fit. The best-fit  $S:I:L$  and  $R_c^2$  are presented alongside the ratio of  $S/I$  and  $I/L$ . Uncertainty is given as one standard deviation (1 SD) of the 300 best model fits. Uncertainty for  $I/L$  is typically large, reflecting the difficulty in constraining the  $L$  dimension. The best-fit 3D shape estimate is plotted on a Zingg diagram of  $S/I$  against  $I/L$ . The 300 best-ranked  $S:I:L$  estimates are plotted, colour-coded to their  $R_c^2$  value. Figure 2.1b presents a blank Zingg diagram. Each corner defines a shape:  $S \approx I \approx L$ , ‘equant’;  $S \approx I < L$ , ‘prismatic’;  $S < I \approx L$ , ‘tabular’; and  $S < I < L$ , ‘bladed’. 3D shape estimates of groundmass crystals in the enclave samples will be described using this terminology. In Figure 2.1a, a comparison of the  $w/l$  distributions and cumulative frequency distributions illustrate goodness-of-fit between the natural sample data and the best-fit model shape. The sharpness of the peaks in the model  $w/l$  distributions is unlikely to be replicated

by the natural sample  $w/l$  distributions. This occurs for two reasons (Higgins, 1994). Natural crystals are much more ‘irregular’ in shape than model orthogonal solids; model shapes will have sharp corners, whilst natural crystals usually have rounded or multi-faceted corners. Also, there is a much smaller number of natural sample intersections (typically a few hundred) than the 20,000 model intersections..

### 2.1.2 Crystal Size Distributions

3D crystal size was constrained using CSD analysis. As discussed in Chapter 1.1.2, CSD Corrections (Higgins, 2000) was used, with the required inputs as follows.

- Intersection  $w$  and  $l$  measurements. At minimum a few hundred intersections are required for accurate results. Intersection measurement will be discussed in Chapter 2.3.
- A *3D shape estimate* for the entire crystal population in the form  $S:I:L$ . This was calculated using ShapeCalc.
- The *measured area* ( $\text{mm}^2$ ) of the sample, i.e. the area of the BSE map minus the crystals of the phase of interest that intersect the image edge. The area of the BSE map was calculated using the dimensions of the image as reported in Fiji. Crystals of the phase of interest that intersect the image edge were outlined, their total area calculated, which was then subtracted from the area of the BSE map to give measured area of the sample.
- *Volumetric Phase Abundance* (VPA), i.e. the combined area of all measured intersections expressed as a percentage of the total measured area. All CSDs are therefore corrected to phase abundance. In a sample with crystals of no preferred orientation (‘massive’), the crystal area fraction is equivalent to the crystal volume fraction (Higgins, 2002; Delesse, 1847).
- The average intersection ‘*roundness*’, measured on a scale of 1.0 - 0.0 in 0.1 increments, where 0.0 = block and 1.0 = ellipsoid. Roundness ranged between 0.1-0.3 for different crystal phases.
- The *fabric* of the sample, from the options ‘massive’, ‘foliated’ or ‘lineated’. All samples had ‘massive’ fabric.
- An estimate of *vesicularity* expressed as percentage of the total measured area. This was estimated using thresholding in Fiji. Vesicularity ranged between  $\sim 15\%$  -  $\sim 40\%$ .
- A chosen number of *bins per decade* in the size distribution plot. CSDs were consistently reported using 5 bins per decade. More bins can introduce error due to the lower number of intersections per bin, and the greater number of corrections necessary during stereological conversion (Higgins, 2000).

### 2.1.3 Binning method

To explore how crystal shape changes with size, 2D intersection data were binned by size fraction. The width and length measurements in each size fraction were input into ShapeCalc

to produce best-fit 3D shape estimates. Two approaches were used to define size bins.

Initially, intersection populations were binned according to breaks in slope at certain sizes (lengths) on their CSD (Figure 2.2). As CSDCorrections uses a singular 3D shape estimate of the entire crystal population, it was thought that if shape did change with size in a population, this might be reflected in the CSD by breaks in slope of the distribution curve. Whilst CSDs were consistently reported in Chapter 4 with 5 bins per decade, CSDs with up to 8 bins per decade were created to show any minor breaks in slope present in the smallest sizes that may be obscured using only 5 bins per decade. Identifying breaks in slope helped suggest some size bins in the plagioclase populations. However, this approach proved unhelpful for binning the mafic phases; no breaks in slope correlating with change in shape were identified in the orthopyroxene and amphibole cases. Also, many factors have been attributed to causing breaks in slope in CSDs, for example a sequence of two nucleation events (Marsh, 1998). It cannot be certain that a change in shape with size is what produced breaks in slope in this case.

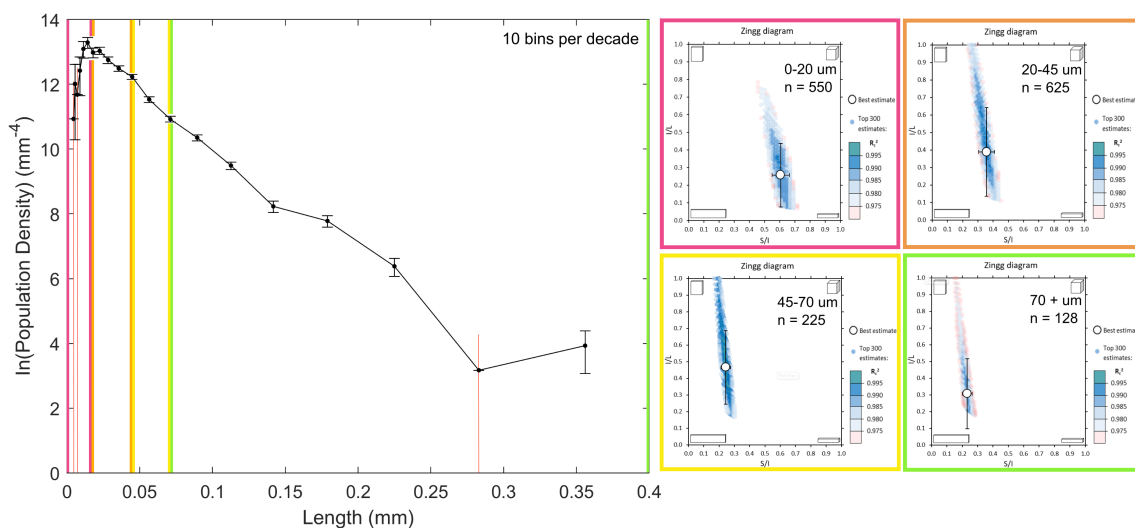


**Figure 2.2:** BEL1B-A plagioclase CSD, using 10 bins per decade. Breaks in slope used to suggest lengths to bin 2D intersection data are marked on the curve, alongside corresponding ShapeCalc outputs for binned intersection data.

A second approach to define bins was to split each intersection population into two sub-populations, either side of a threshold length, i.e., ‘intersections greater than a certain length’ and ‘intersections below a certain length’. Figure 2.3 illustrates this process. Here, a crystal population of 1500 crystals was split into counterpart sub-populations, the first being the ‘200 largest intersections’, with the rest constituting the ‘1300 smallest intersections’. The population was then systematically split into counterparts every hundred intersections: the ‘300 largest intersections’ paired with the ‘1200 smallest intersections’, the ‘400 largest intersections’ paired with the ‘1100 smallest intersections’. This process continued until counterparts reached the ‘1300 largest intersections’ paired with the ‘200 smallest intersections’. Each counterpart

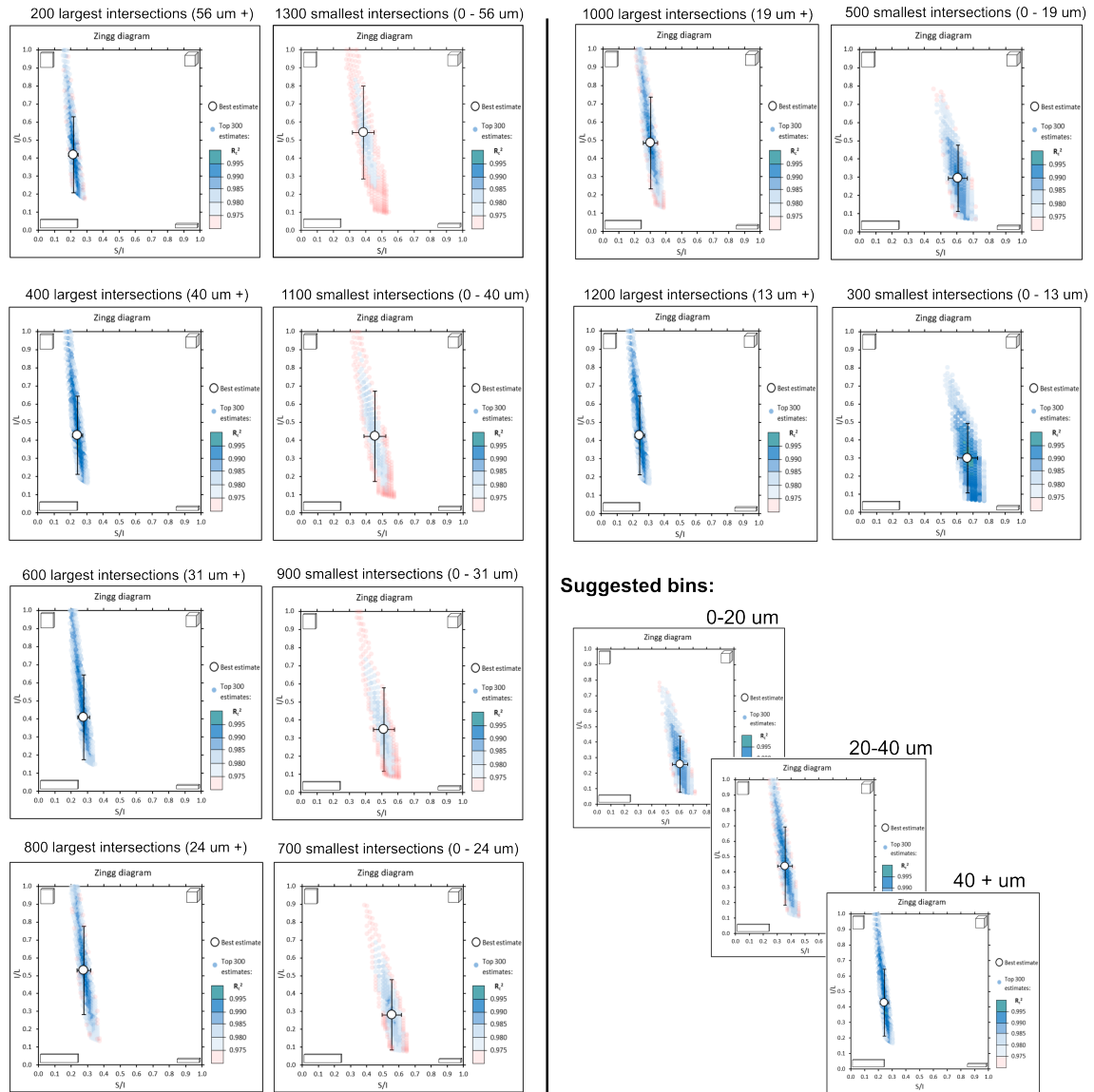


**Figure 2.3:** Example of counterpart sub-population approach for plagioclase in MVO-1591A, illustrated with ShapeCalc Zingg diagram outputs. The population of 1500 crystals was split into counterpart sub-populations, starting with the ‘200 largest intersections’ and the ‘1300 smallest intersections’. Whilst splitting into sub-populations was carried out in hundred crystal increments, here the results are shown for every other increment. The suggested size bins are shown.

sub-population was input into ShapeCalc to produce a best-fit 3D shape estimate (Figure 2.3). The 3D shape estimates were used to examine if, and if so, how, shape changed with size fraction.

Both approaches were applied to all intersection data sets to identify if there was any change in shape with size within a population. Where bins could be identified, it was aimed to have at minimum 200 intersections per bin in order to have a sufficient number of crystal intersections for analysis (Chapter 2.1.2). This was not always achievable for the largest size bins as there is a lower abundance of the largest crystals in all samples, except for plagioclase in TRA10A.

## 2.2 SEM data acquisition

### 2.2.1 BSE maps

Back-scattered electron (BSE) maps were acquired with a Hitachi SU-70 field emission Scanning Electron Microscope (SEM) at Durham University (UK), using 15 kV accelerating voltage and 15 mm working distance. Representative areas of groundmass texture in each thin section of a sample were identified under an optical microscope. The specific area selected to be mapped needed to include an easily identifiable feature, such as a distinctive large phenocryst, that would allow the chosen area to be located using optical microscopy, marked on a flatscan of the thin section, and then located again using the SEM.

The purpose of acquiring BSE maps was to outline and measure groundmass crystal phases of plagioclase, orthopyroxene and amphibole. The requirements of the maps were therefore:

1. Images were taken at sufficient magnification and resolution so that crystals were clear enough to outline accurately, with a minimum size of  $\sim 1 \mu\text{m}$  ;
2. Greyscale values of each crystal phase (a function of mean atomic number of each phase, and brightness and contrast settings of the image) were distinct enough that phases could be distinguished from each other;
3. Images included a sufficient number of crystal intersections for analysis across all crystal lengths (minimum  $\sim$  a few hundred crystal intersections per size fraction (Mangler et al., 2022; Mock & Jerram, 2005)).

To achieve this, test images were taken in the imaging and EDS analysis software Aztec to establish optical image properties by varying magnification, image resolution, pixel dwell time and brightness and contrast. Test images were acquired using two thin sections representing end-member cases of groundmass crystal size: BEL1B-A for the finest-grained samples, and TRA10A for the coarsest-grained. BSE maps were acquired using the decided optimal properties of 2048 x 2048 pixel resolution, 45  $\mu\text{s}$  dwell time, at x 300 magnification for the coarsest-grained samples and x 500 magnification for finer-grained samples. Mapped areas ranged between 2.5  $\text{mm}^2$  - 17  $\text{mm}^2$ , consisting of 150-250 individual BSE images stitched together in Aztec in order to image a sufficient number of crystal intersections. The largest areas were required for the coarsest-grained samples. The minimum crystal intersection length that could be imaged in high enough resolution to measure was  $\sim 1 \mu\text{m}$ . The maximum intersection length that was imaged ranged from  $\sim 250 \mu\text{m}$  in the finest-grained sample to  $\sim 750 \mu\text{m}$  in the coarsest-grained sample.

### 2.2.2 Chemical maps

Chemical maps were acquired with an Oxford Instruments Xmax<sup>50</sup> EDS analyser using 15 kV accelerating voltage, 15 mm working distance, 400 s dwell time per frame, process time 4, 1048 x 1048 pixel resolution, at x 300 magnification for all samples. Using lower resolution than the BSE maps was appropriate as the purpose of the chemical maps was only to visually differentiate the mafic phases of orthopyroxene, clinopyroxene, amphibole and apatite. These phases have

extremely similar greyscale values in BSE due to their similar mean atomic number relative to the rest of the sample. A chemical map of calcium, magnesium and phosphorus content allows these phases to be distinguished from each other (Figure 2.4). Orthopyroxene contains high MgO (24-25 wt.%) and low CaO (1-2 wt.%) relative to low MgO (13-15 wt.%) and high CaO (17-20 wt.%) in clinopyroxene. Amphibole contains intermediate MgO (13-16 wt.%) and CaO (11-12 wt.%).

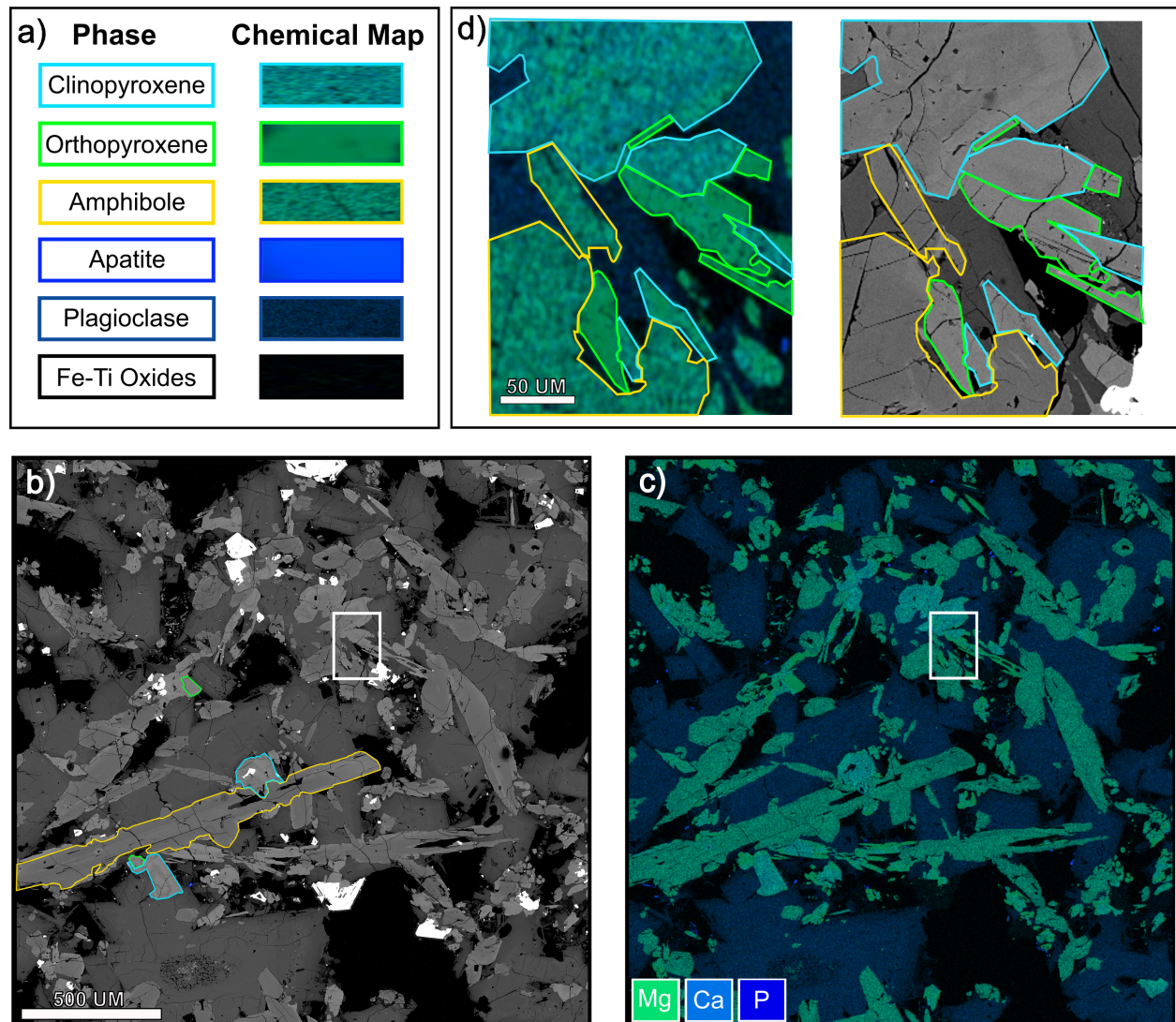


**Figure 2.4:** Comparison of a BSE map and chemical map for the same area. **a)** Key showing the highlight colour and chemical map colour associated with each phase. **b)** BSE map where the brightness and contrast has been adjusted to create the maximum disparity in greyscale values possible between the mafic phases, highlighting the difficulty in distinguishing them using BSE intensity alone. Examples of each of the mafic phases have been outlined. **c)** Chemical map of the same area for calcium, magnesium and phosphorus. The mafic phases are more clearly distinguished by colour. **d)** Area with a complex intergrowth of mafic phases, outlined in both BSE and chemical map, located in the white rectangle in (b) and (c).

### 2.2.3 Representative geochemistry

Representative geochemistry of phases was acquired using SEM-EDS point analyses. A Hitachi SU-70 field emission Scanning Electron Microscope (SEM) with an Oxford Instruments Xmax<sup>50</sup> EDS analyser was used to collect data in Aztec. Conditions used were 15 kV accelerating voltage, 15.0 mm working distance, acquisition time of 60 s and process time 4. 3-5 point analyses were taken for each crystal analysed, and then averaged.

Analysis of standards was conducted to estimate uncertainty in geochemical data, presented in Table 2.1. 5 point analyses were taken of each standard, reported in Table 2.1 as the mean value for each standard. The % difference between the mean value and the standard accepted value provides a measure of accuracy. Standard deviation provides a measure of precision. The analytical uncertainty is the 1 sigma error as reported in Aztec.

**Table 2.1:** Analysis of standards to estimate error in geochemical analyses. 5 point analyses were taken of each standard and averaged to give a mean value in oxide wt. %.

Standards	Reference	Label	NaO	MgO	Al <sub>2</sub> O <sub>3</sub>	SiO <sub>2</sub>	K <sub>2</sub> O	CaO	TiO <sub>2</sub>	Cr <sub>2</sub> O <sub>3</sub>	MnO	FeO <sub>total</sub>	Total	
Labradorite	NMNH 115900	Mean	3.68	0.18	30.42	52.04	0.15	13.07	0.04			0.42	100.00	
		Accepted value	3.45	0.15	30.91	51.25	0.18	13.64	0.05		0.01	0.49	100.13	
		% difference	6.7	22.7	-1.6	1.5	-18.9	-4.2	-20.0				-14.3	
		Standard deviation	0.02	0.01	0.04	0.06	0.02	0.06	0.02				0.02	
		Analytical uncertainty	0.03	0.02	0.06	0.08	0.01	0.04	0.03				0.03	
Anorthite	NMNH 137041	Mean	0.48	0.08	35.76	44.37	0.02	18.83	0.01			0.46	100.00	
		Accepted value	0.53	<0.02	36.03	44.00	0.03	19.09	0.03			0.62	100.33	
		% difference	-9.1	280.0	-0.7	0.8	-46.7	-1.4	-80.0				-25.5	
		Standard deviation	0.01	0.01	0.04	0.12	0.01	0.09	0.01				0.02	
		Analytical uncertainty	0.02	0.02	0.06	0.08	0.01	0.05	0.03				0.03	
Anorthoclase	NMNH 133868	Mean	7.53	0.05	20.42	68.68	2.57	0.60				0.15	100.00	
		Accepted value	9.31		20.12	66.44	2.35	0.87				0.2	99.29	
		% difference	-19.1		1.5	3.4	9.4	-30.6					-23.0	
		Standard deviation	0.03	0	0.03	0.02	0.03	0.02					0.02	
		Analytical uncertainty	0.03	0.02	0.05	0.09	0.02	0.02					0.03	
Augite	NMNH 164905	Mean	0.85	17.18	7.74	50.90	0.02	17.24	0.48	0.87	0.13	4.59	100.00	
		Accepted value	0.84	17.32	8.03	50.48	0.01	17.3	0.51	0.85	0.12	4.81	100.26	
		% difference	1.2	-0.8	-3.7	0.8	120.0	-0.4	-6.3	2.6	10.0		-4.6	
		Standard deviation	0.01	0.02	0.03	0.05	0.01	0.06	0.02	0.02	0.03	0.04	0.04	
		Analytical uncertainty	0.02	0.05	0.04	0.08	0.01	0.05	0.03	0.03	0.03	0.03	0.05	
Diopside	NMNH 117733	Mean	0.27	18.16	0.35	55.76		25.26				0.20	100.00	
		Accepted value	0.25	17.79	0.11	55.81		25.28			0.04	0.25	99.53	
		% difference	8.8	2.1	214.5	-0.1		-0.1					-20.0	
		Standard deviation	0.06	0.03	0.1	0.08		0.13					0.04	
		Analytical uncertainty	0.02	0.06	0.03	0.09	0.01	0.02	0.03	0.03	0.03	0.03	0.07	
Hypersthene	USNM 746	Mean	0.07	27.53	1.10	55.44	0.01	1.23	0.10	0.67	0.45	13.41	100.00	
		Accepted value	0.05	26.79	1.23	54.09	0.05	1.52	0.16	0.75	0.49	15.22	100.25	
		% difference	44.0	2.8	-10.7	2.5	-72.0	-19.2	-35.0	-10.9	-8.6	-11.9		
		Standard deviation	0.02	0.2	0.1	0.09	0.01	0.1	0.02	0.02	0.02	0.01	0.14	
		Analytical uncertainty	0.02	0.06	0.03	0.09	0.01	0.02	0.03	0.03	0.03	0.03	0.07	
Hornblende	NMNH 143965	Mean	2.51	13.04	14.78	41.74	2.06	10.28	5.00			0.11	10.48	100.00
		Accepted value	2.6	12.8	14.9	40.37	2.05	10.3	4.72			0.09	11.25	100.02
		% difference	-3.5	1.8	-0.8	3.4	0.7	-0.2	5.8				24.4	-6.8
		Standard deviation	0.07	0.14	0.17	0.24	0.03	0.19	0.11				0.02	0.06
		Analytical uncertainty	0.03	0.04	0.05	0.08	0.02	0.04	0.04				0.03	0.06

## 2.3 2D size-shape data collection

### 2.3.1 Intersection measurement approaches

2D intersection length and width are required to estimate 3D shape using ShapeCalc (Mangler et al., 2022). Potential approaches to constrain length and width include best-fit ellipse, direct line measurements and minimum bounding rectangles (Table 2.2; Figure 2.5). Measurements were collected using Fiji, a version of image processing software ImageJ (Schindelin et al.,

2012). Best-fit ellipse and bounding rectangle require the intersections to be outlined. In Fiji, an overlay is a layer of outlines from which size-shape data can be extracted.

### *Best-Fit Ellipse*

The most common approach is best-fit ellipse, typically used in the construction of Crystal Size Distributions (e.g., Higgins, 2000). In Fiji, this can be achieved by outlining each intersection to create an overlay, and then fitting an ellipse of the same area, orientation and centroid to each intersection in the overlay, with major and minor axes measurements equating to length and width. The program can automate fitting an ellipse to each intersection, meaning data collection is straightforward and time-efficient as measurements can be extracted directly from the overlay without extra work additional to outlining. Length and width measurements are collected simultaneously but are in separate columns in the output, removing the need to manually sort data. However, the process of outlining intersections can be time-consuming. It can be complicated to distinguish individual intersections if crystals are intergrown (Chapter 2.4), as they are in these enclave samples. Further difficulties arise in defining full outlines if the thin section used to acquire the BSE maps is of poor quality, with fractured crystals. If the extent of an intersection has to be estimated, this can introduce random error into measurements. However, since fitting ellipses is automated by Fiji, it is a consistent and reproducible approach between and within samples.

Holness (2014) notes that for rectangular intersections (i.e., a pair of orthogonal lines), the best-fit ellipse fitted to the rectangular outline by Fiji consistently results in an aspect ratio (length/width) higher than the intersection outline aspect ratio by an exponent of 1.5. This is because the area of the ellipse has to be equal to the area of the intersection outline, and thus for rectangular intersections the ellipse has a greater length than the intersection outline. This is illustrated in Figure 2.5a, where the length of the best-fit ellipse is visually slightly longer than the length of the outline. The w:l ratio for the best-fit ellipse approach (0.31) is slightly lower than both the direct line (0.34) and bounding rectangle (0.36) approaches. Holness (2014) argues there is an absolute offset between best-fit ellipse measurements for rectangular intersections and the length of the intersection outline, and there is a need to account for this uniform scaling. This argument is relevant to the enclave samples as they contain many crystals with rectangular intersections. This point is given further consideration in Chapter 2.3.2.

### *Direct Line Measurements*

Another common approach is direct line measurements (Cashman, 1992; Mangler et al., 2022). Intersection length and width are measured manually, using a line tool in Fiji. Outlines of intersections are not required. For ‘regular’ shapes, direct line measurements follow the obvious crystallographic axes and are perpendicular, as illustrated in Figure 2.5a. For ‘irregular’ shapes (Figure 2.5b and 2.5c), a better approximation of length and width is to take measurements at certain points on the intersection boundary (personal communication, Mangler, 2024). In ‘irregular’ shapes such as Figure 2.5b, the crystallographic axis is not

**Table 2.2:** Comparison of intersection measurement approaches: best-fit ellipse, direct line measurements, and minimum bounding rectangles.

Measurement Approach	Function	Advantages	Disadvantages
<i>Best-fit Ellipse</i>	Fits an ellipse of the same area, centroid and orientation to each intersection. Major and minor axes measurements equate to intersection length and width.	<ul style="list-style-type: none"> <li>• Can be semi-automated, with no need for data sorting.</li> <li>• Ensures consistent and reproducible approach between samples because fitting ellipses is automated by Fiji.</li> </ul>	<ul style="list-style-type: none"> <li>• Requires an overlay of outlined intersections which can be time-consuming to generate and may introduce random error if outlines have to be estimated.</li> </ul>
<i>Direct Line Measurements</i>	Intersection length and width are measured manually using a line tool.	<ul style="list-style-type: none"> <li>• Does not require outlines to collect measurements, which may be conceptually more robust for intergrown crystals.</li> </ul>	<ul style="list-style-type: none"> <li>• Manual measurements may introduce error in ensuring length and width are always perpendicular and in the correct order, introducing the need for data sorting.</li> <li>• Deciding how to measure complex, 'irregular' shapes can undermine how consistent and reproducible this approach is.</li> </ul>
<i>Minimum Bounding Rectangle</i>	Fits a bounding box that describes the maximum extent of the intersection. Height and width equates to intersection length and width.	<ul style="list-style-type: none"> <li>• Can be semi-automated, with hundreds of length and width measurements collected in minutes, without the need for data sorting.</li> </ul>	<ul style="list-style-type: none"> <li>• Requires an overlay of outlined intersections which can be time-consuming to generate and may introduce random error if outlines have to be estimated.</li> </ul>

perpendicular, and therefore length and width will not be taken perpendicular to each other. Assessing whether intersections are ‘regular’ or ‘irregular’ shapes, and therefore deciding the appropriate place to take length and width measurements, takes time and consideration. Direct line measurements have been suggested to be conceptually more robust for measuring intergrown crystals (Mangler et al., 2022). This is because measurements can be taken without defining full outlines, the process of which may introduce random errors if intersection shape has to be estimated.

This method requires taking twice as many measurements as there are intersections. If length and width are taken concurrently for each intersection, extracted data must be sorted to separate length and width measurements, in order to calculate aspect ratio. The need to sort data can be avoided by taking all length measurements first, followed by width. This requires that each intersection is measured in the exact same order twice, which is susceptible to human error. For the most square intersections, where length and width are of similar value, it is sometimes challenging to ensure the longest axis is attributed to length and the shorter to width; confusing these values necessitates additional manual data sorting. Ensuring that measurements are taken exactly perpendicular to each other for shapes where the crystallographic axes are perpendicular (i.e. ‘regular’ shapes, Figure 2.5a) can be difficult. This is required to ensure accurate measurements are taken in a consistent and reproducible way between rectangular intersections.

#### *Minimum Bounding Rectangle*

Using a ‘minimum bounding rectangle’, the program fits a bounding box that describes the maximum extent of the intersection. The width and height of the box describes the measured width and length of the intersection (Figure 2.5). This approach is not as time-efficient as best-fit ellipse as it cannot be automated to the same extent, i.e. extracted directly from the outline overlay. Instead, bounding rectangles must be fit to each intersection in the overlay, which can be semi-automated and achieved relatively quickly (bounding rectangles fit to hundreds of intersections in minutes). However, the process of outlining intersections is time-consuming.

In theory, the bounding rectangle approach addresses some of the issues with direct line measurements. Width and length of the intersection are measured simultaneously, removing the need to sort data to separate measurements. It removes human error in ensuring that width and length measurements are taken exactly perpendicular for rectangular intersections (Figure 2.5a). Unlike best-fit ellipse measurements, bounding rectangle length measurements for rectangular intersections do not have an absolute offset greater than the intersection outline length (Figure 2.5a). It is a much quicker data collection process than taking individual direct line measurements. It was thought that minimum bounding rectangle might be a good approximation of direct line measurements for ‘regular’ shapes (Figure 2.5a) as rectangle measurements usually follow the crystallographic axes. Rectangle measurements are unlikely to be a good match to direct line measurements for ‘irregular’ shapes (Figure 2.5b).

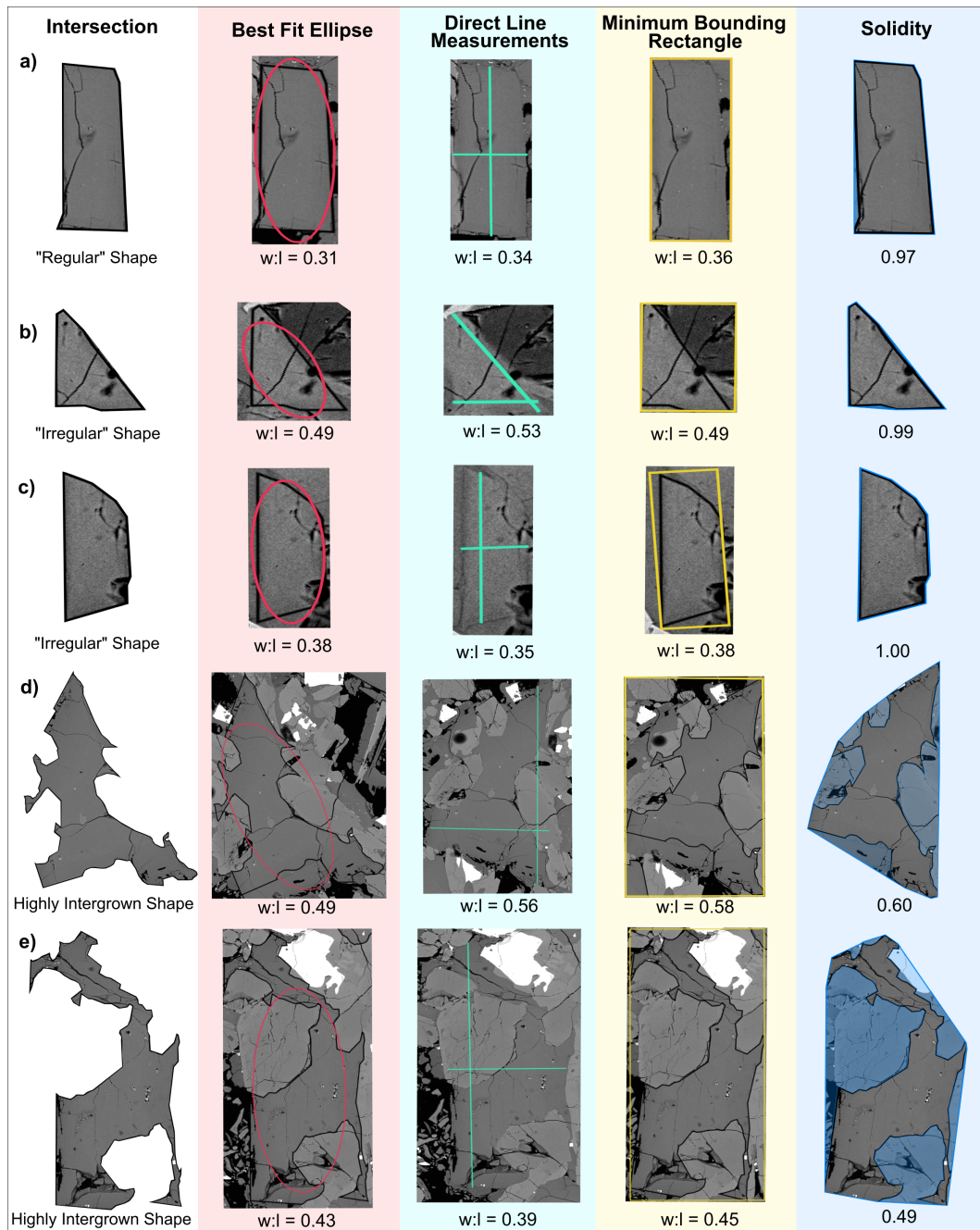


**Figure 2.5:** A comparison of intersection shapes illustrating how different approaches would measure the same shape, the resulting  $w:l$  value, how solidity is measured (see Chapter 2.3.1 for further detail) and the resulting solidity value. **a)** A 'regular' shape. **b)** An 'irregular' shape. **c)** An 'irregular' shape. **d)** A highly intergrown shape with relatively low solidity. **e)** A highly intergrown shape with relatively low solidity.

### 2.3.2 Measurement comparison tests

Tests of the measurement approaches were run to decide which would be most appropriate for the enclave material. Plagioclase crystals were outlined in two end-member samples of ground-mass crystal size: MVO-1591A for the least intergrown, finest-grained sample, and TRA10A for the most intergrown, coarsest-grained sample. 300 intersections and 200 intersections were outlined and measured in MVO-1591A and TRA10A respectively. 2D width and length mea-

measurements were taken using best-fit ellipse, direct line measurements and minimum bounding rectangle approaches. 2D intersection measurements were converted to 3D shapes estimates using ShapeCalc (Table 2.3).

The percentage deviation of the  $w:l$  ratios estimated for the same intersection using different approaches was calculated to compare how each approach measures individual intersections (Table 2.4, Figure 2.7 and 2.9). For example, Figure 2.7a presents the percentage deviation of the  $w:l$  ratio of direct line measurements relative to best-fit ellipse measurements. 0 % deviation means that there is no difference in the  $w:l$  ratio between the two approaches for a particular intersection. A positive deviation means that direct line measurements overestimate the  $w:l$  ratio relative to the best-fit ellipse approach, and a negative deviation means that the direct line measurements underestimate the  $w:l$  ratio relative to the best-fit ellipse approach.

Percentage deviation is plotted against solidity. Solidity describes the density of a shape. It is defined as the area of an object divided by the area of a convex hull drawn around the object, illustrated in Figure 2.10 and Figure 2.5. A value of 1 indicates a solid shape, and a value of  $<1$  indicates a shape with an uneven outline. Intergrown crystals tend to have more uneven intersection outlines, and therefore lower solidity values, than non-intergrown crystals (Figure 2.5d and Figure 2.5e).

**Table 2.3:** 3D shape estimates from 2D intersection width and length measurements for each different measurement approach.

Sample	Measurement Approach	$n^a$	$S$	$I$	$L$	$R_c^2$	$S/I$	$\pm$	1SD <sup>b</sup>	$I/L$	$\pm$	1SD <sup>b</sup>
MVO-1591A	Best-fit ellipse	300	1.00	2.80	5.60	0.967	0.36	$\pm$	0.06	0.50	$\pm$	0.25
	Direct line measurements	300	1.00	2.70	4.80	0.947	0.37	$\pm$	0.07	0.56	$\pm$	0.25
	Bounding rectangle	300	1.00	3.00	5.20	0.967	0.33	$\pm$	0.06	0.58	$\pm$	0.24
TRA10A	Best-fit ellipse	200	1.00	2.30	4.80	0.989	0.43	$\pm$	0.07	0.48	$\pm$	0.25
	Direct line measurements	200	1.00	1.80	6.40	0.974	0.56	$\pm$	0.07	0.28	$\pm$	0.24
	Bounding rectangle	200	1.00	2.30	3.80	0.981	0.43	$\pm$	0.07	0.61	$\pm$	0.25

<sup>a</sup>Number of intersections outlined and measured.

<sup>b</sup>One standard deviation of the 300 best model fits in ShapeCalc (Mangler et al., 2022).

**Table 2.4:**  $w:l$  percentage deviation between each test measurement approach.

Sample	Measurement Comparison	$n$	w:l % deviation		
			Mean	$\pm 10$ % <sup>a</sup>	$\pm 20$ % <sup>b</sup>
MVO-1591A	Direct line measurements relative to best-fit ellipse	300	8.8	59.7	82.3
	Bounding rectangle relative to direct line measurements	300	4.2	64.7	89.7
	Best-fit ellipse relative to bounding rectangle	300	2.5	73.7	92.7
TRA10A	Direct line measurements relative to best-fit ellipse	200	12.9	53.5	78.5
	Bounding rectangle relative to direct line measurements	200	-1.6	52.0	79.5
	Best-fit ellipse relative to bounding rectangle	200	7.1	59.5	82.5

<sup>a</sup>The percentage of the total number of intersections that lie between  $\pm 10$  % deviation.

<sup>b</sup>The percentage of the total amount of intersections that lie between  $\pm 20$  % deviation.

### MVO-1591A

There is no significant difference in the 3D shape estimate between any of the three approaches in the least intergrown, finest-grained sample (Table 2.3). Best-fit ellipse produces a 3D shape estimate with  $S/I$  and  $I/L$  of  $0.36 \pm 0.06$  and  $0.50 \pm 0.25$ . Direct line measurements produce a 3D shape estimate with  $S/I$  and  $I/L$  of  $0.37 \pm 0.07$  and  $0.56 \pm 0.25$ . Bounding rectangle

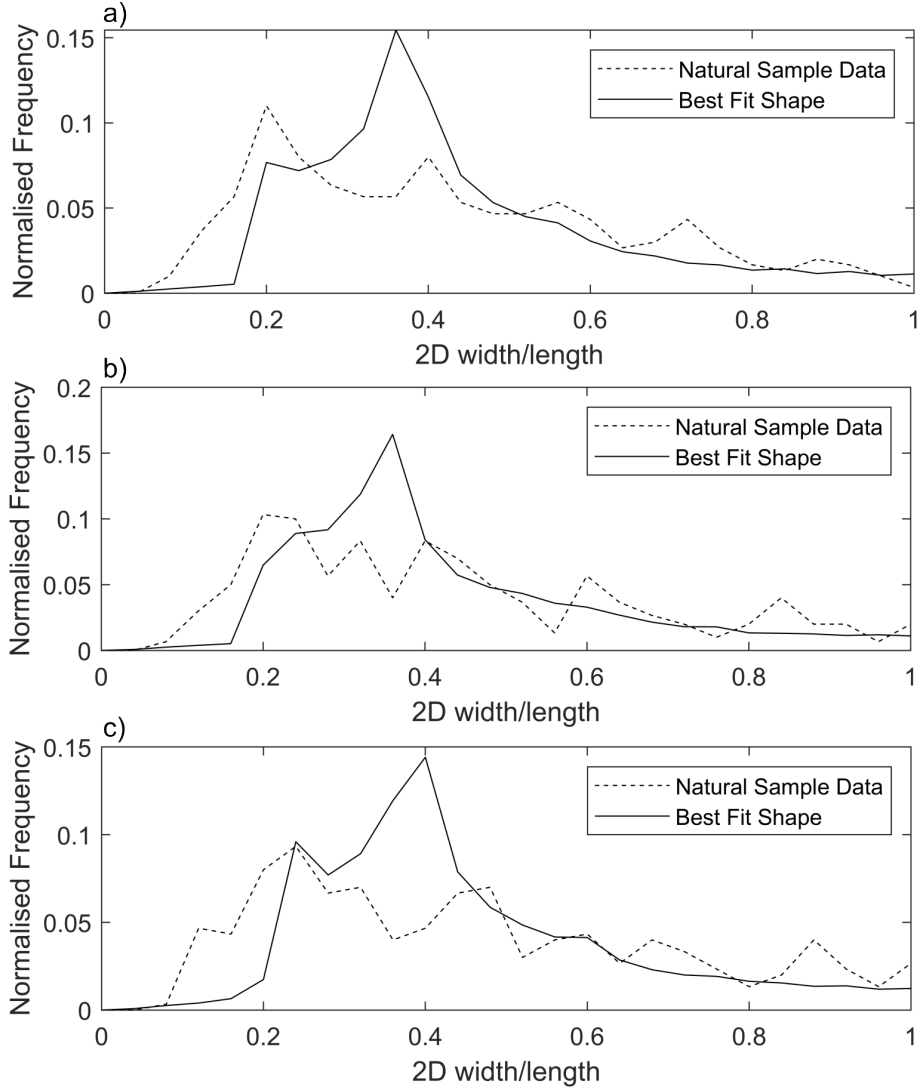


**Figure 2.6:** 2D  $w/l$  distributions of the best-fit model shape compared to the  $w/l$  distribution of the measured intersections for **a)** best-fit ellipse, **b)** bounding rectangle and **c)** direct line measurements.

produces a 3D shape estimate with  $S/I$  and  $I/L$  of  $0.33 \pm 0.06$  and  $0.58 \pm 0.24$ . All best-fit shape estimates are within uncertainty.  $R_c^2$  values agree within 2 %. Direct line measurements produce a slightly greater uncertainty, of 0.947 compared to 0.967 for both best-fit ellipse and bounding rectangle. There is no significant difference in 3D shape estimate because the  $w/l$  distributions of the intersections for each approach are so similar, and so have a similar best-fit model shape (Figure 2.6). The lower  $R_c^2$  for direct line measurements could be due to random error introduced when measuring complex, intergrown shapes without the use of outlines.

Figure 2.7a compares the percentage deviation of the  $w:l$  ratios of direct line measurements relative to best-fit ellipse. There is no clear trend with solidity. Direct line measurements tend to overestimate relative to best-fit ellipse, on average by  $\sim 9\%$  (Table 2.4; dashed line in Figure 2.7a).  $\sim 82\%$  of direct line measurements fall within  $\pm 20\%$  deviation. This suggests that the  $w:l$  ratios produced by direct line measurements and best-fit ellipse are a good fit to each other in this sample.

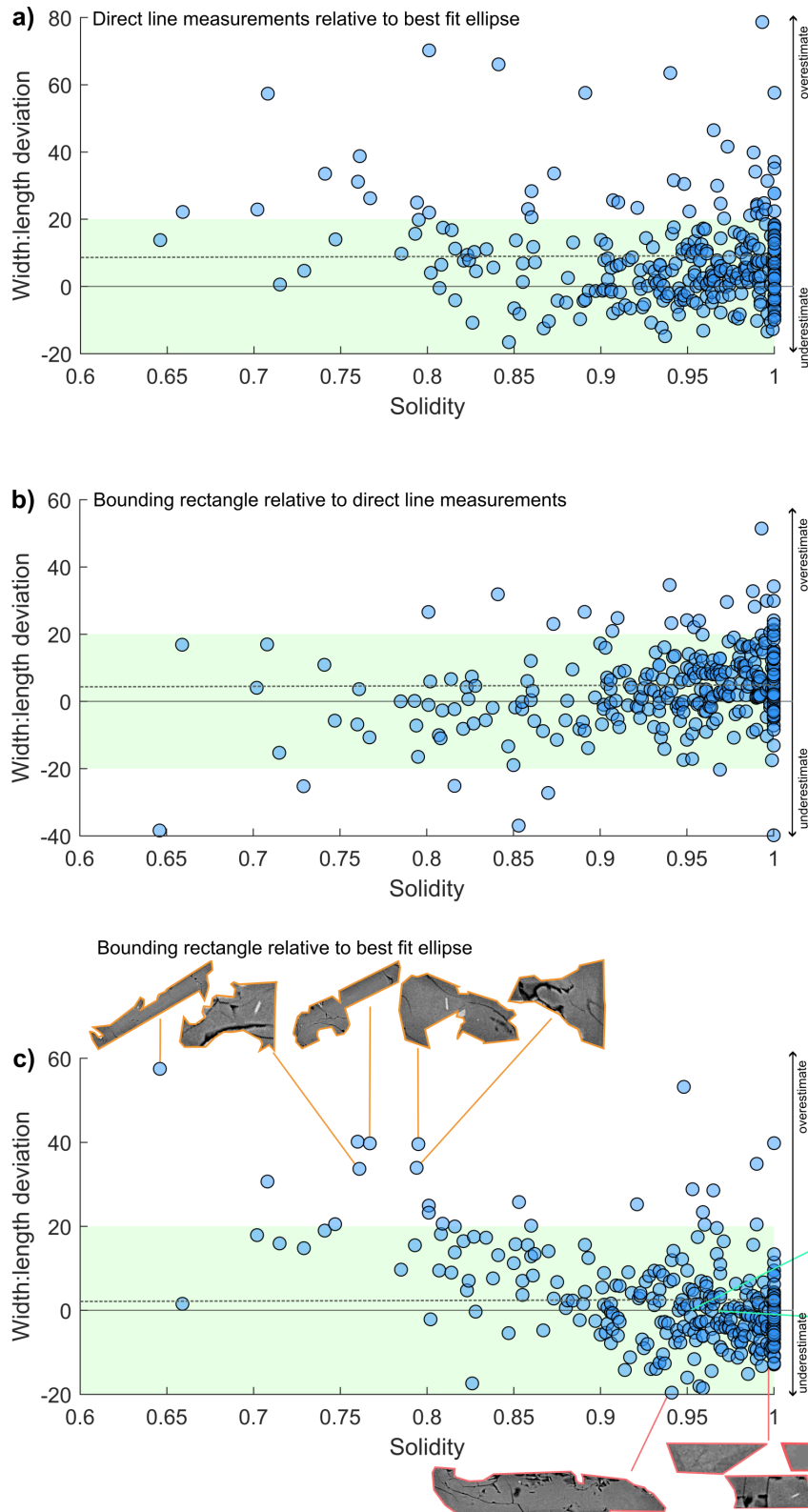


**Figure 2.7:** The percentage deviation of  $w:l$  ratio measured for each intersection using different approaches, against solidity, for sample 1591A. This sample is representative of the finest-grained and least intergrown groundmass. Each point is an individual intersection. The green box delineates  $\pm 20\%$  deviation from 0%. **a)** Direct line measurements relative to best-fit ellipse. **b)** Bounding rectangle relative to direct line measurements. **c)** Bounding rectangle relative to best-fit ellipse. Representative intersection shapes of the greatest negative deviations (underestimations, pink), 0% deviations (green), and the greatest positive deviations (overestimations, orange).

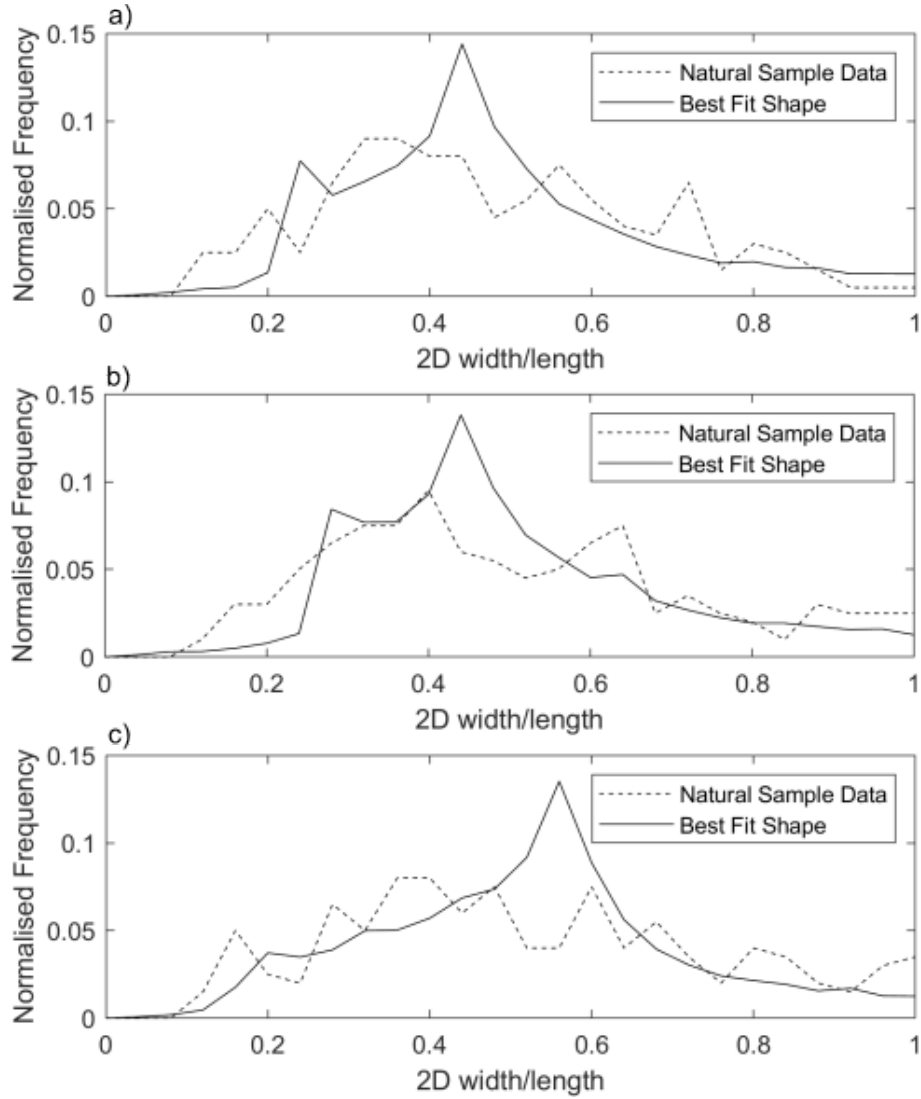
Figure 2.7b compares the percentage deviation of the  $w:l$  ratios of bounding rectangle measurements relative to direct line measurements. There is no clear trend with solidity. Direct line measurements tend to overestimate relative to bounding rectangle, on average by  $\sim 4\%$  (Table 2.4; dashed line in Figure 2.7b).  $\sim 90\%$  of direct line measurements fall within  $\pm 20\%$  deviation. Bounding rectangle and direct line measurements are a good fit to one another regardless of solidity in this sample. This suggests that bounding rectangles could be used as an approximation of direct line measurements in samples with less intergrown groundmass.

Figure 2.7c compares the percentage deviation of the  $w:l$  ratios of bounding rectangle measurements relative to best-fit ellipse measurements. There is a trend with solidity, in that bounding rectangle measurements tend to underestimate  $w:l$  ratio relative to best-fit ellipse for intersections with high solidity, and tend to overestimate for intersections with low solidity. This is illustrated with representative examples of intersection shapes for the greatest negative deviations, the greatest positive deviations and  $0\%$  deviations. The  $0\%$  deviations and greatest negative deviations tend to be intersections with higher solidity and clear crystallographic axes. The negative deviations are always within  $\pm 20\%$ . Low solidity shapes with high positive deviations lack clear crystallographic axes, have uneven outlines, and exceed  $+20\%$  deviation (orange intersection shapes in Figure 2.7c). Overall, bounding rectangle measurements tend to overestimate relative to best-fit ellipse, on average by  $\sim 3\%$  (dashed line in Figure 2.7c).  $\sim 93\%$  of intersections fall within  $\pm 20\%$  deviation. This suggests that the bounding rectangle and best-fit ellipse approach are generally a good fit to each other. However, low solidity shapes with high positive deviations exceeding  $20\%$  (orange intersection shapes in Figure 2.7c) show that bounding rectangle and best-fit ellipse do not produce a good match in  $w:l$  ratio.

### TRA10A

TRA10A is the coarsest-grained and most intergrown sample. The greater range of solidity and lower mean solidity in TRA10A compared to 1591A (minimum solidity of  $\sim 0.45$  versus  $\sim 0.65$  respectively) reflects the more intergrown groundmass and more complex intersection shapes in TRA10A. There is no significant difference in the 3D shape estimate produced by the best-fit ellipse and bounding rectangle approach in the most intergrown, coarsest-grained sample (Table 2.3). Best-fit ellipse and bounding rectangle produces a 3D shape estimate with  $S/I = 0.43 \pm 0.07$  and  $I/L = 0.48 \pm 0.25$ . There is a significant difference between these estimates and the 3D shape estimate provided by direct line measurements ( $S/I = 0.56 \pm 0.07$  and  $I/L = 0.28 \pm 0.24$ ). The significant difference in 3D shape estimate is because the  $w/l$  distribution of the intersections measured using direct line measurements is different to that collected by the other two approaches, and so direct line measurements have a different best-fit model shape. Figure 2.8 shows that for direct line measurements, the peak of the best-fit model shape distribution is shifted towards the more equant intersection shape compared to that of the other two approaches.

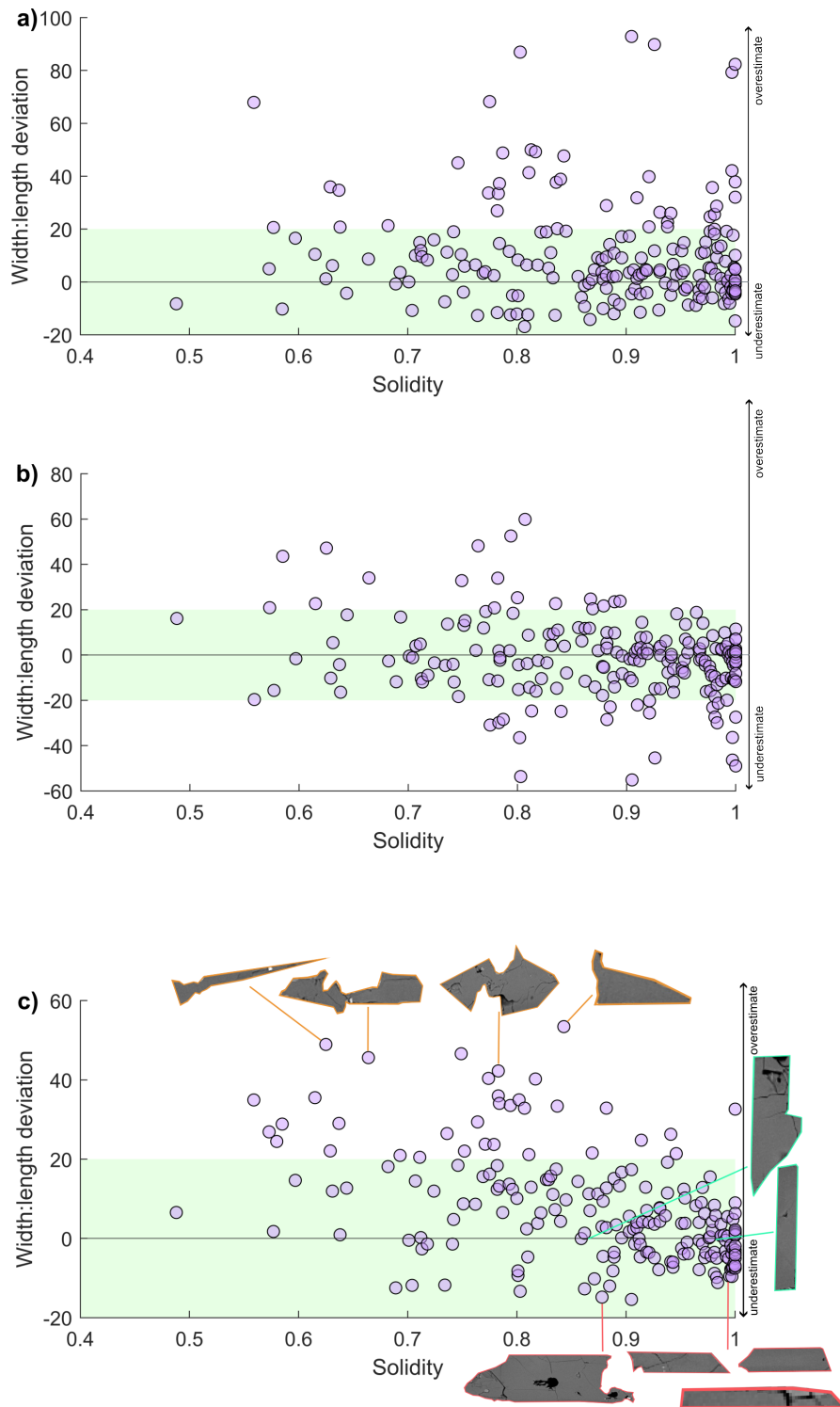
Figure 2.9a compares the percentage deviation of the  $w:l$  ratios of direct line measurements relative to best-fit ellipse. There is no clear trend with solidity, similar to that of MVO-1591A. Direct line measurements tend to overestimate relative to best-fit ellipse, on average by  $\sim 13\%$  (Table 2.4).  $\sim 79\%$  of direct line measurements fall within  $\pm 20\%$  deviation. Whilst



**Figure 2.8:** 2D  $w/l$  distributions of the best-fit model shape compared to the  $w/l$  distribution of the measured intersections for **a)** best-fit ellipse, **b)** bounding rectangle and **c)** direct line measurements.

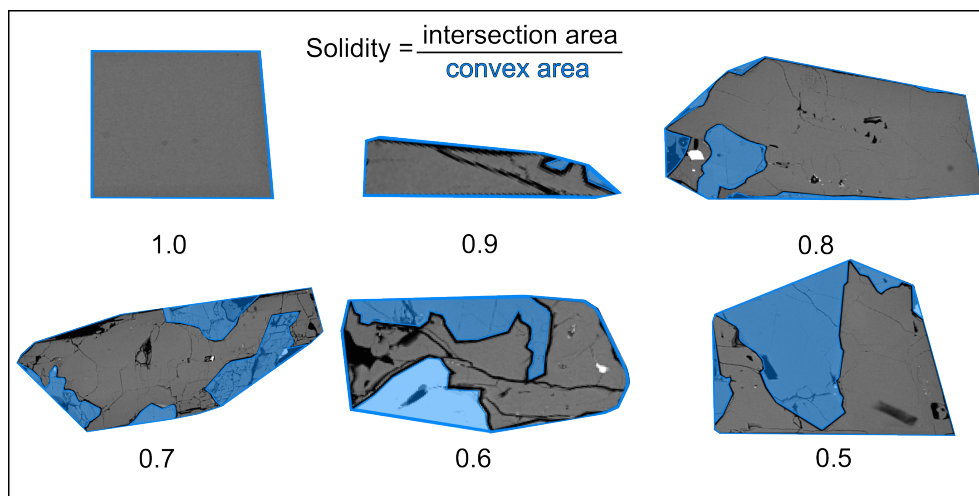
this suggests that these approaches are generally a good fit to each other, the greatest positive deviations range to  $>90\%$ . For intersections with greatest positive deviations, the best-fit ellipse and direct line measurements produce  $w:l$  ratios that are not a good match.

Figure 2.9b compares the percentage deviation of the  $w:l$  ratios of bounding rectangle measurements relative to direct line measurements. There is a trend with solidity, in that bounding rectangle measurements tend to underestimate  $w:l$  ratio relative to direct line measurements for intersections with high solidity, and tend to overestimate for intersections with low solidity. Overall, bounding rectangles tend to underestimate intersection  $w:l$  ratio relative to direct line measurements, on average by  $\sim -1.6\%$  (Table 2.4).  $\sim 80\%$  of direct line measurements fall within  $\pm 20\%$  deviation. Bounding rectangle and direct line measurements are generally a good fit to each other in this sample, suggesting that bounding rectangles maybe could be used as an approximation of direct line measurements. However, as the greatest deviations range  $\pm 80\%$  and the overall 3D shape estimates are significantly different, this suggests that



**Figure 2.9:** The percentage deviation of  $w:l$  ratio measured for each intersection using different approaches, against solidity, for sample TRA10A. This sample is representative of the coarsest-grained and most intergrown groundmass. Each point is an individual intersection. The green box delineates  $\pm 20\%$  deviation from  $0\%$ . a) Direct line measurements relative to best-fit ellipse. b) Bounding rectangle relative to direct line measurements. c) Bounding rectangle relative to best-fit ellipse. Representative intersection shapes of the greatest negative deviations (underestimations, pink),  $0\%$  deviations (green), and the greatest positive deviations (overestimations, orange).

bounding rectangles are not as reliable as an approximation of direct line measurements in this coarse-grained, more intergrown sample than in MVO-1591A, a less intergrown sample.



**Figure 2.10:** Illustration of the shape descriptor ‘solidity’ using representative intersection shapes from the enclave samples. The dark blue outline defines the convex hull. An intersection with a solidity value of 1.0 is a ‘solid’ shape, where the intersection area is equivalent to the area of the convex hull. Solidity values decrease as intersection outlines become increasingly complex due to intergrowth with other crystals, and the intersection area decreases relative to the area of the convex hull.

Figure 2.9c compares the percentage deviation of the  $w:l$  ratios of bounding rectangle measurements relative to best-fit ellipse measurements. There is a trend with solidity, in that bounding rectangle measurements tend to underestimate  $w:l$  ratio relative to best-fit ellipse for intersections with high solidity, and tend to overestimate for intersections with low solidity. This is illustrated with representative examples of intersection shapes for the greatest negative deviations, the greatest positive deviations and 0 % deviations. Similarly to MVO-1591A, the 0 % deviations and greatest negative deviations (the negative deviations are always within  $\pm 20$  %), tend to be intersections with higher solidity and clear crystallographic axes. Low solidity shapes with high positive deviations lack clear crystallographic axes, have uneven outlines, and are often irregular shapes (similar to Figure 2.5b). Overall, bounding rectangle measurements tend to overestimate relative to best-fit ellipse, on average by  $\sim 7$  %.  $\sim 83$  % of intersections fall within  $\pm 20$  % deviation. This suggests that these approaches are a good fit for the majority of intersections measured, but not as reliable for highly intergrown shapes.

### *Summary & Recommendations*

Tests of best-fit ellipse, direct line measurements and bounding rectangles for the less intergrown, finer-grained sample MV0-1591A reveal that all three approaches produce similar results. All three produce the same 3D shape estimate with similar uncertainty. When comparing the percentage deviation of  $w:l$  ratios between two approaches, the majority ( $\sim 80$ - $90$  %) of intersections lie within  $\pm 20$  % deviation, indicating a good fit between approaches. Bounding rectangle measurements appear to generally be a good approximation of direct line measurements. This suggests that bounding rectangle measurements could be used in place of direct

line measurements in samples with less intergrown groundmass that have intersections with relatively high solidity. This is beneficial as fitting bounding rectangles is quicker than taking individual direct line measurements, are less susceptible to human error in data collection and do not require manual data sorting (Table 2.2).

In the coarser-grained, more intergrown sample of TRA10A, not all approaches produce similar results. Best-fit ellipse and bounding rectangle produce the same 3D shape estimate with similar uncertainty, however, direct line measurements produce a significantly different estimate. Whilst the majority ( $\sim 80\%$ ) of intersections lie within  $\pm 20\%$  deviation when examining percentage deviation of  $w:l$  ratios, suggesting a good fit between approaches, the range in deviation contradicts this. Direct line measurements can overestimate best-fit ellipse by up to  $\sim 90\%$ , bounding rectangles can overestimate direct line measurements by up to  $\sim 70\%$  and bounding rectangles can overestimate best-fit ellipse measurements by up to  $\sim 60\%$  (Figure 2.9). The largest deviations tend to be for lower solidity intersections with complex outlines, or ‘irregular’ shapes. Best-fit ellipse may underestimate width and length in absolute terms for elongate, low solidity intersections, such as Figure 2.5d and 2.5e. This is because the area of the ellipse has to equal the area of the intersection outline, and so for elongate shapes with complex outlines, the ellipse visually underestimate length and width. Bounding rectangle always takes length and width perpendicular, even for ‘irregular’ intersections where the crystallographic axes is not perpendicular to one another. It can be a challenge to take direct line measurements in an accurate, consistent and reproducible way in a highly intergrown sample with complex intersections.

Having considered the results of these tests, it was decided to use best-fit ellipse to measure intersections. It is an appropriate approach for both end-member cases of groundmass size and degree of intergrowth. Whilst outlines are required, and take time to fit, they are necessary to yield areal information crucial for further analyses, including to construct Crystal Size Distributions. Data collection of length and width is time-efficient as fitting ellipses is automated by Fiji, with no manual data sorting required. As the majority of published data uses best-fit ellipse, the use of best-fit ellipse in this study enables comparison with existing work.

As mentioned in Chapter 2.3.1, Holness (2014) notes that for rectangular intersections (i.e., a pair of orthogonal lines), the best-fit ellipse fitted to the rectangular outline by Fiji consistently results in an aspect ratio (length/width) higher than the intersection outline aspect ratio. For these rectangular intersections, arguably bounding rectangle provides a more accurate measure of width and length without an offset, visually seen in Figure 2.5a. Figure 2.7c and Figure 2.9c illustrate the percentage deviation in  $w:l$  ratio between the best-fit ellipse and bounding rectangle approaches in both samples. Rectangular intersections are illustrated, outlined in blue. For rectangular intersections, the deviations are typically  $\sim 0\%$ . This suggests that despite an absolute offset in length and width using best-fit ellipse, the resulting  $w:l$  ratio does not need correcting for to obtain 3D shape estimates using ShapeCalc.

## 2.4 Crystal outlining approach

Crystal intersections in the BSE maps of each sample were outlined in order to use best-fit ellipse to extract size-shape measurements and visualise intersect shape. Outlining was carried out using Fiji. Accurate outlining requires that different crystal phases are distinguishable from each other, distinguishable from surrounding glass and vesicles, and that crystals of the same phase can be identified as individuals. Three different approaches were attempted, summarised in Table 2.5. The test results of each displayed in Figure 2.11.

**Table 2.5:** Summary of approaches to crystal intersection outlining: simple thresholding, segmentation and manual outlining.

<b>Outlining Approach</b>	<b>Description</b>	<b>Advantages</b>	<b>Disadvantages</b>	<b>Decision</b>
<i>Simple Thresholding</i>	Divides an image into two classes of pixels based on greyscale value.	Automated and easy to apply, therefore time-efficient.	Unable to differentiate between compositional phases with overlapping greyscale values. Unable to identify contacts between intersections in intergrown groundmass.	Unsuitable for enclave samples (too intergrown, presence of overlap in greyscale values between phases).
<i>Trainable Weka Segmentation</i>	Segmentation tool that combines machine learning algorithms with user-selected features that trains a classifier to divide an image into features of interest and background.	Some manual outlining and time required to train classifier, but once trained can be applied to other images without user-input (automated, time-efficient). May be able to identify intersection contacts in intergrown samples where simple thresholding fails.	May be unable to distinguish the phase of interest from the background if they are not distinctly different in greyscale and geometry.	Unsuitable for enclave samples (too intergrown, overlap in greyscale values between phases).
<i>Manual Outlining</i>	Drawing crystal intersection outlines by hand.	Allows confidence in accuracy of crystal outlines as they are user-generated.	Time-consuming; requires manually drawing around 1000s of crystal intersections, with decisions in outlining approach needing to be consistent between and within samples.	Suitable approach for enclave material.

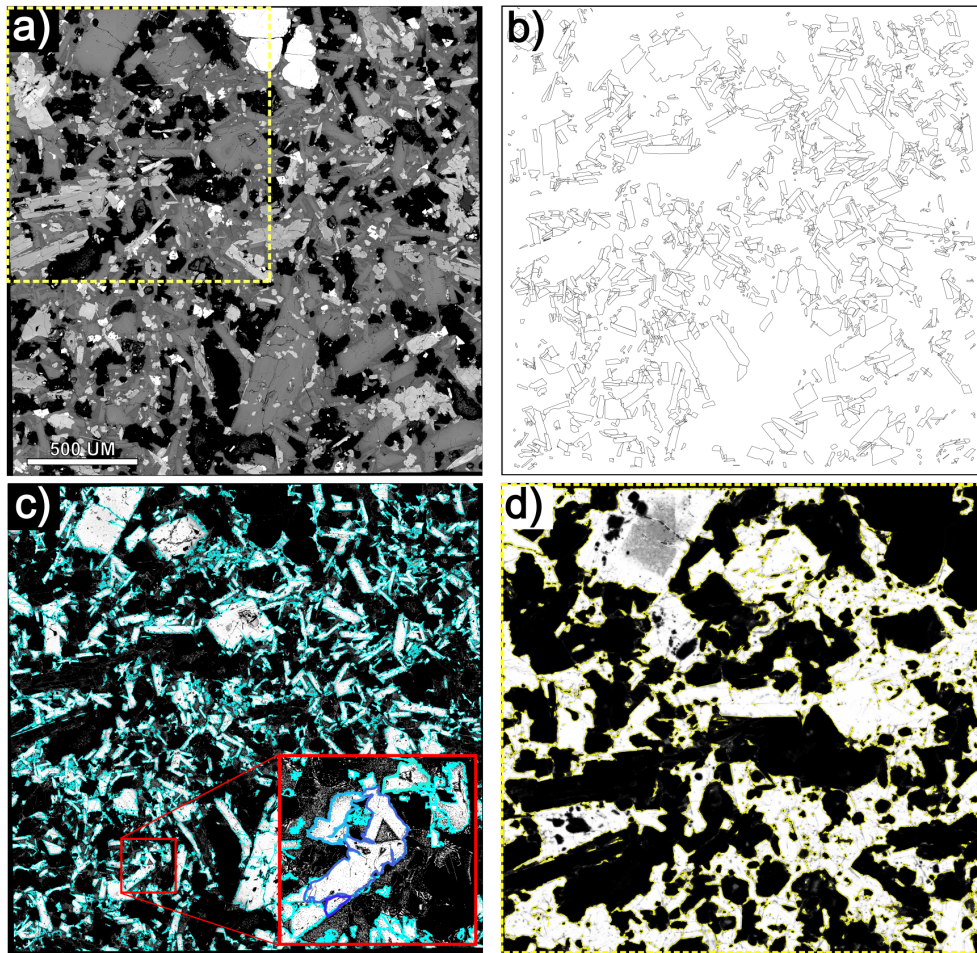


**Figure 2.11:** Comparison of result of different crystal intersection outlining approaches, attempting to isolate plagioclase groundmass crystals. **a)** Unprocessed BSE map; **b)** Manual Outlining; **c)** Simple thresholding; **d)** Trainable Weka Segmentation (Arganda-Carreras et al. 2017).

#### 2.4.1 Automated outlining

**Simple thresholding** is the most straightforward approach to create an overlay of measurable crystal intersections. This technique divides an image into two classes of pixels based on greyscale value, effectively a ‘foreground’ and ‘background’. It can be applied to BSE images to isolate features of a certain greyscale value (foreground), for example a certain crystal phase, from everything else in the image (background). As it is an automated technique, it is a very time-efficient approach, therefore it was attempted on a BSE map to test its suitability.

Simple thresholding was unsuitable to outline the enclave material. The plagioclase crystals are too similar in atomic weight, and therefore greyscale value, to glass and thus cannot be distinguished from it using simple thresholding (Figure 2.11c and 2.12c). The presence of compositional zoning within individual crystals complicates this further. For plagioclase, greyscale value in a BSE image correlates well with anorthite content because variation in CaAl-NaSi has a dominant effect on atomic number (Ginibre et al., 2002). Strong compositional zoning within the groundmass plagioclase therefore hinders the ability of simple thresholding

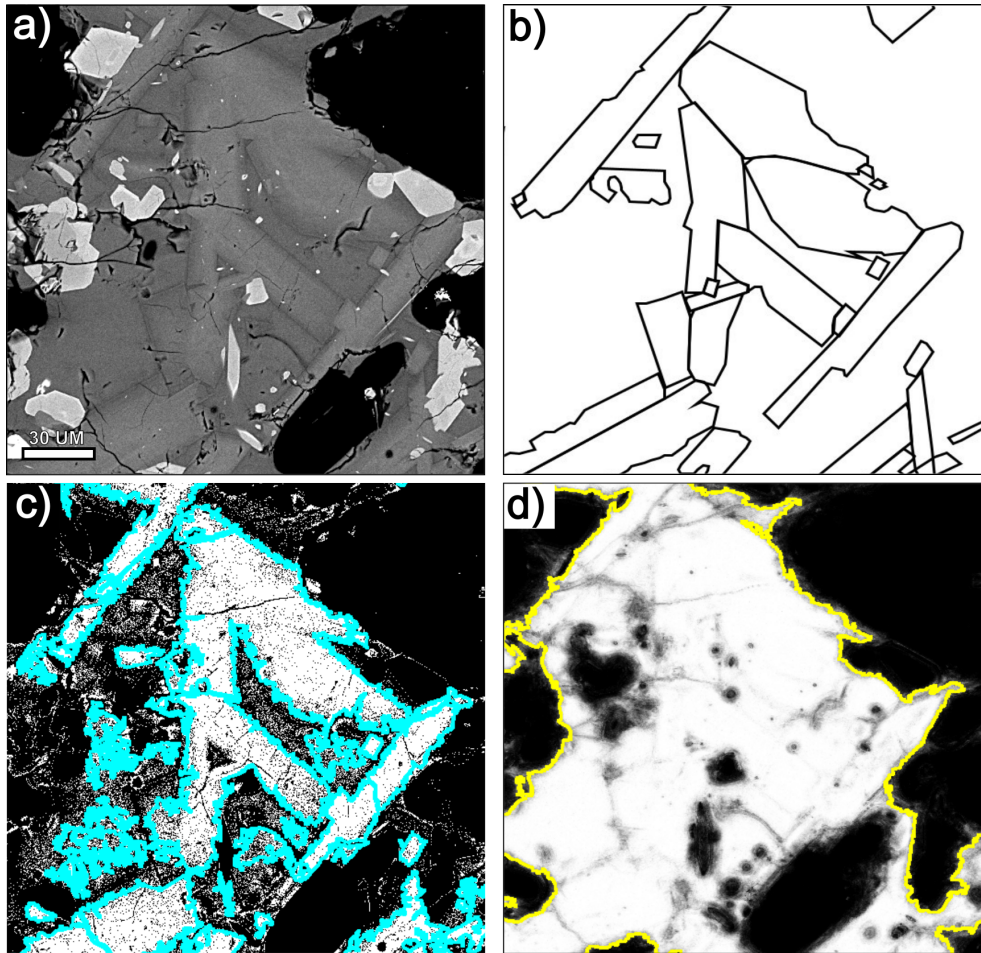


**Figure 2.12:** Comparison of different outlining approaches for a smaller area of Figure 2.11. **a)** Unprocessed BSE map; **b)** Manual Outlining; **c)** Simple thresholding; **d)** Trainable Weka Segmentation (Arganda-Carreras et al., 2017).

to outline intersections accurately, as it splits whole crystals with brighter, more anorthite-rich cores and darker, less-calcic rims into those two components. The effect of compositional zoning on BSE intensity is so pronounced that this feature has been exploited to correlate greyscale values with anorthite contents in plagioclase crystals with complex zoning (Ginibre et al., 2022; Humphreys et al., 2013). Whilst the plagioclase in these samples is easily distinguished from the mafic phases, the mafic phases are not easily distinguished from each other (Figure 2.4). The greyscale values of orthopyroxene, clinopyroxene and amphibole are too similar, further complicated by compositional zoning creating overlapping greyscale values between different phases (Figure 2.4d). Clinopyroxene sometimes forms thin reaction rims on groundmass amphibole. The reaction rims are incorrectly included in outlines produced by simple thresholding. This approach is also incapable of separating intergrown crystals from each other (Figure 2.12c), a necessity due to the highly intergrown nature of the groundmass in all samples. Simple thresholding is therefore not a suitable approach to outlining crystal intersection in these samples, and demonstrates the challenges in accurate outlining.

**Segmentation** is a more complex approach to automated outlining. ‘Trainable Weka Segmentation’ is a Fiji plugin (Arganda-Carreras et al., 2017) that combines machine learning

algorithms with user-selected image features to divide an image into ‘foreground’ and ‘background’. The user trains the plugin to classify areas of an image by manually outlining both features of interest and areas of disinterest, from which the program will attempt to classify the whole image. This approach was attempted as it is time-efficient relative to manually outlining an entire image, and if successful, the classifier can be used on multiple successive images. Unfortunately, segmentation was unsuitable to outline the enclave material broadly for the same reasons simple thresholding failed: inability to distinguish between phases with similar greyscale value, and poor ability to identify and separate individual crystal intersections in an intergrown groundmass (Figure 2.11 and Figure 2.12).

#### 2.4.2 Manual outlining

**Manual outlining** of groundmass crystal intersections was the only viable approach to generate a measurable overlay, to account for both the intergrown nature of the groundmass and the similarities in greyscale between phases. Outlines were drawn onto the BSE maps for each sample using the polygon tool in Fiji. Resources used to aid in differentiating phases and to identify crystal intersection edges and contacts included:

- *Chemical maps* of calcium, magnesium and phosphorus content were used to distinguish mafic phases from each other.
- *False colour image* versions of the BSE maps, created using Look-Up Tables in Fiji. Pseudo-colouring of images enhanced contrast and thus illustrated compositional difference between and within phases.
- The *individual BSE images* that were stitched together to create the map. They have slightly better resolution than the stitched map, and thus sometimes better illustrated crystal zoning and contacts.
- *Optical microscopy* was used to verify outlines for the coarsest-grained samples; this was not possible for the finer grained samples.

Fractured crystals and crystals intersecting the image edge were discarded from analysis as any size-shape data extracted would not be accurate. It is common practice in crystal size-shape analyses to discard such crystals. For crystals intersecting the image edge, there is no way to determine the true length and width of their 2D intersection. Including the ‘incomplete’ intersections in analysis would contribute to error in 3D shape reconstruction and could bias the results of a CSD towards smaller crystals. Discarding crystals that intersect the image edge could also arguably bias size-shape results, potentially by underestimating the total crystal volume which could affect the CSD. However, as such large BSE maps were constructed (Chapter 2.2), there are only a few edge-intersecting crystals relative to ‘whole’ crystal intersections; for plagioclase, ~50-100 edge-intersecting crystals discarded for 500-1500 whole crystal intersections measured and analysed. Therefore, it is suggested that discarding fractured crystals is unlikely to bias size-shape analyses, and that the inclusion of edge-intersecting crystals would negatively impact the 3D shape estimate more than their exclusion. Likewise, fractured crystals are also discarded from being measured. This is also because their 2D intersection dimensions may not

be accurate. Again, discarding such crystals could potentially bias size-shape results, especially if a particular size of crystal is prone to fracturing during sample preparation. However, there are very few fractured crystals within a BSE map (at most  $\sim 10$ ). Discarding this many crystals relative to the number of crystals measured (a few hundred minimum) is therefore unlikely to bias subsequent size-shape analyses.

Crystals interpreted as ‘inherited’ from the host andesite were discarded (Chapter 3). Inherited plagioclase crystals were identified by their large size, sieve textures, and often complex zoning patterns (Murphy et al., 2000; Humphreys et al., 2009). Inherited mafic phases were identified by large size and evidence of alteration.

Manual outlining requires establishing a set of rules to follow on how to draw outlines. A consistent, accurate approach must be followed that is reproducible within and between samples. The intergrown nature of the groundmass in all samples introduces complexity in outlining. Factors to consider were:

- 2.4.2.1 How should outlines be drawn when it is not completely clear whether a crystal is a single crystal, or two crystals intergrown?
- 2.4.2.2 Should twinned crystals be outlined together, or as a single crystal?
- 2.4.2.3 Should outlines be drawn around intergrowths, or extrapolated through them?
- 2.4.2.4 How should outlines be drawn when crystals completely overlap?
- 2.4.2.5 Should inclusions of other crystals within a groundmass crystal be included in the outline?

These factors were each tested by outlining the same area in a sample in different ways. 2D size-shape measurements were extracted from the overlay and used to produce a 3D shape estimate in ShapeCalc. The 2D and 3D size-shape data was compared between approaches. A minimum number of  $\sim 300$  crystal intersections in each test run were outlined in order to produce statistically significant results.

**Table 2.6:** 2D size-shape data extracted from intersection outlines for different outlining tests.

Approach	n	Intersection area <sup>a</sup> (mm <sup>2</sup> )	% difference in intersection area <sup>b</sup>	Mean				
				Intersection area (μm <sup>2</sup> )	l (μm)	w (μm)	w:l (μm)	Solidity
Maximum	540	0.50		930	45.7	15.7	0.42	0.94
Minimum	302	0.51	1.53	1690	63.6	23.3	0.41	0.88
Outlining around intergrowths	300	0.21		730	43.7	14.1	0.41	0.94
Extrapolating through	300	0.23	5.10	770	44.4	14.5	0.41	0.96
Include overlapping	1510	1.20		780	42.5	14.7	0.42	0.95
Discard overlapping	1500	1.20	-0.27	780	42.6	14.7	0.42	0.95

<sup>a</sup>Total intersection area.

<sup>b</sup>% difference in intersection area between two approaches, i.e., ‘maximum’ and ‘minimum’, etc.

Approach	Intersections	$S$	$I$	$L$	Rc2	$S/I$	$\pm$	1SD	$I/L$	$\pm$	1SD
Maximum	540	1.00	2.70	5.60	0.972	0.37	$\pm$	0.06	0.48	$\pm$	0.25
Minimum	302	1.00	2.80	5.60	0.982	0.36	$\pm$	0.06	0.50	$\pm$	0.25
Outlining around intergrowths	300	1.00	2.80	5.60	0.967	0.36	$\pm$	0.06	0.50	$\pm$	0.25
Extrapolating through	300	1.00	2.80	5.60	0.969	0.36	$\pm$	0.06	0.50	$\pm$	0.25
Include overlapping	1510	1.00	2.70	5.60	0.974	0.37	$\pm$	0.06	0.48	$\pm$	0.25
Discard overlapping	1500	1.00	2.70	5.60	0.974	0.37	$\pm$	0.06	0.48	$\pm$	0.25

**Table 2.7:** 3D shape estimates from 2D intersection width and length measurement for different outlining approaches.

#### 2.4.2.1 How should outlines be drawn when it is not completely clear whether a crystal is a single crystal, or two crystals intergrown?

The factor thought most likely to have a significant impact on how intersection outlines were drawn, and thus an influence on size-shape data, was how outlines would be drawn when it was not completely clear whether a crystal is a single crystal, or multiple intergrown. Figure 2.12a and 2.13 illustrates the complexity in intergrown groundmass texture, and therefore difficulty in accurate outlining. To evaluate the most suitable approach, the same area in a sample was manually outlined twice: once where all crystals that could possibly be multiple intergrown were split into the maximum number of crystals possible (a ‘maximum intersections’ approach), and once where all crystals that could possibly be multiple intergrown were treated as single crystals (a ‘minimum intersections’ approach). Figure 2.13 provides comparative examples. In the ‘maximum’ approach, multiple intersections were outlined if there were multiple cores or different zoning patterns, if there was a visible suture between crystals, or if contiguous crystals had different orientations. In the ‘minimum’ approach, these cases were treated as singular crystals and thus fewer were outlined in the same overall area. These decisions were based on the work of Mangler (2024) and Brugger & Hammer (2015).

In order to test this, 302 intersections were outlined in the ‘minimum’ approach and 540 intersections were outlined in the ‘maximum’ approach, covering the same total crystal area. Intersections were measured using a best-fit ellipse to extract size-shape data (Table 2.6). The width-length data were input into ShapeCalc to assess whether the different measurement approaches produce significantly different estimates of 3D shape (Table 2.7).

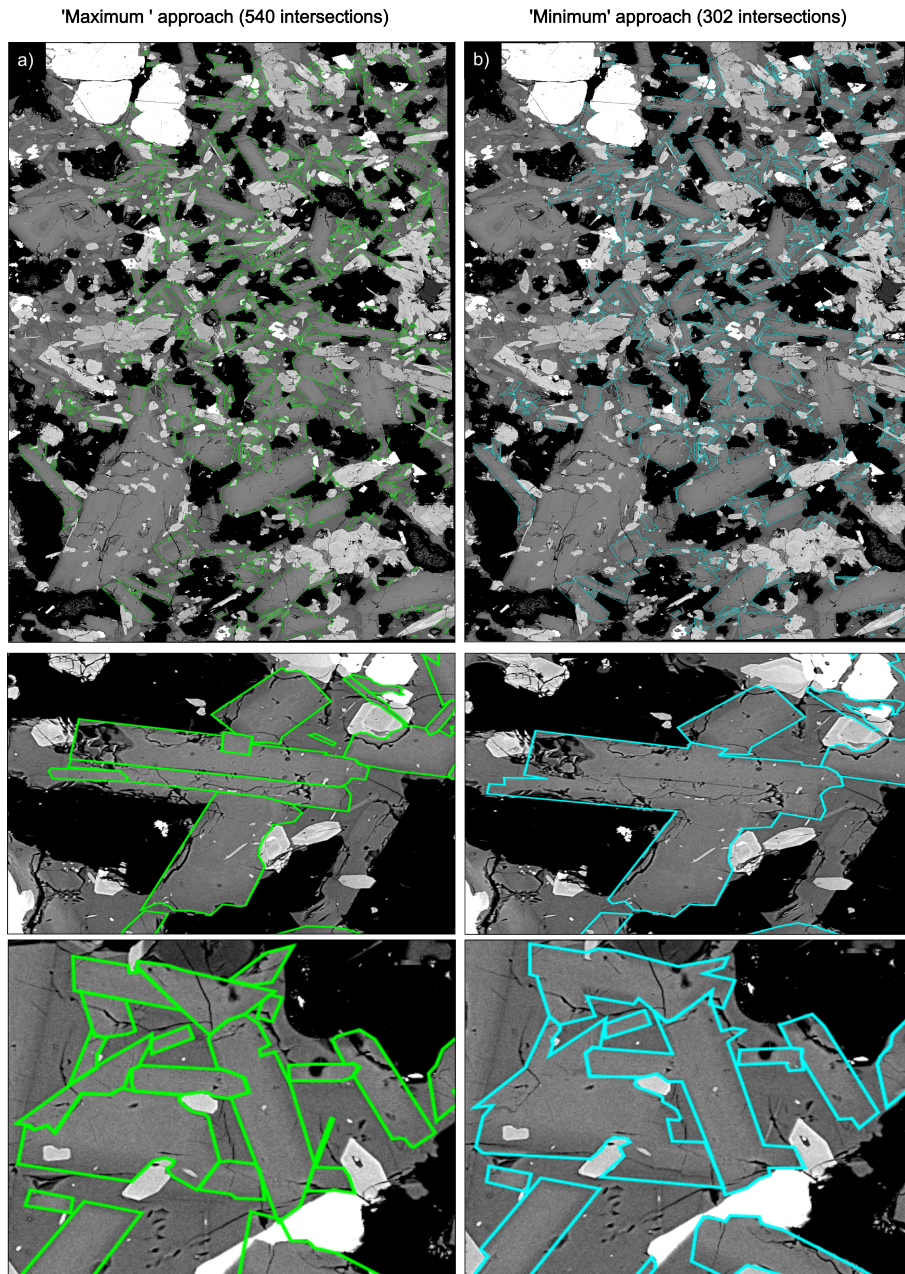


**Figure 2.13:** Comparison of outlines for 'maximum' and 'minimum' approach. **a)** 'Maximum' approach. **b)** 'Minimum' approach.

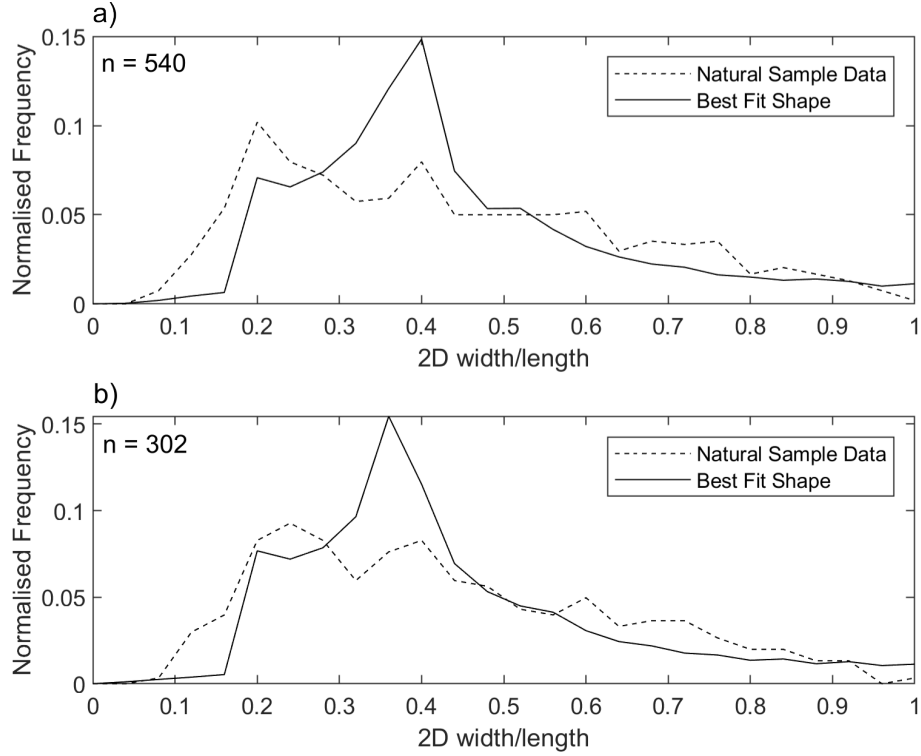


**Figure 2.14:** 2D  $w/l$  distributions for intersection populations produced through **a)** the ‘maximum’ approach and **b)** the ‘minimum’ approach. There is no significant difference between the 3D shape estimates of the two approaches.

There is no significant difference between the two approaches for the 3D shape estimate (Table 2.7). The ‘maximum’ approach results in a best-fit shape with  $S/I$  of  $0.37 (\pm 0.06)$  and  $I/L$  of  $0.48 (\pm 0.25)$ . The ‘minimum’ approach results in a best-fit shape with  $S/I$  of  $0.36 (\pm 0.06)$  and  $I/L$  of  $0.50 (\pm 0.25)$ . The lack of a significant difference is due to the 2D  $w/l$  distributions of the intersections being so similar that they do not have a significantly different best-fit model shape (Figure 2.14). The minor difference in  $R_c^2$  of 0.972 for the ‘maximum’ approach and 0.982 for the ‘minimum’ approach could be due to the discrepancy in the number of crystal intersections per approach, with the ‘maximum’ approach resulting in nearly twice the number of intersections in the same area as the ‘minimum’ approach.

The average area per intersection is much larger in the ‘minimum’ approach compared to the ‘maximum’, with values of  $1690 \mu\text{m}^2$  and  $930 \mu\text{m}^2$  respectively (Table 2.6). The total intersection area outlined is  $\sim 1.5\%$  higher in the ‘minimum’ approach. As both approaches outline the same crystals and therefore attempt to outline the same area, the difference of  $\sim 1.5\%$  reflects human error in outlining the same areas accurately. The average width and length for the ‘minimum’ approach is  $23 \mu\text{m}$  and  $64 \mu\text{m}$ , which again is larger than the average width and length for the ‘maximum’ approach of  $16 \mu\text{m}$  and  $46 \mu\text{m}$  (Table 2.6). The  $w:l$  ratios are the same for both approaches ( $0.42$  for ‘maximum’ and  $0.41$  for ‘minimum’).

Whilst there is no significant difference in 3D shape estimate, the ‘maximum’ approach is thought to be conceptually more robust. Due to the intergrown nature of the groundmass, a large proportion ( $\sim 70\%$ ) of the crystals are contiguous. The ‘minimum’ approach does not

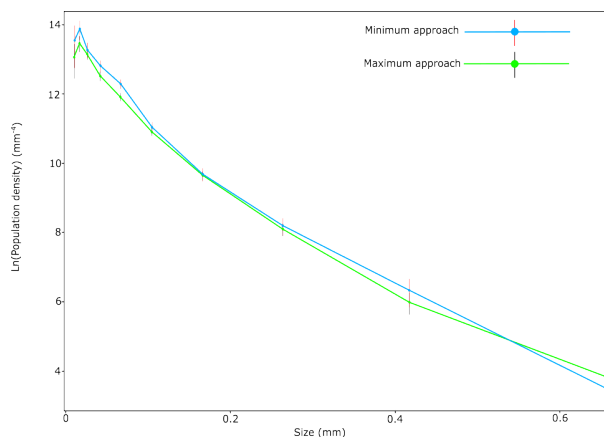


**Figure 2.15:** CSDs constructed using the ‘maximum’ and ‘minimum’ approach are not significantly different. The size distribution for the ‘minimum’ approach is slightly more abundant in the smallest crystal sizes than the ‘maximum’ approach, but is still within error.

split up contiguous crystals, and therefore areas outlined as a singular crystal intersection that are in reality multiple contiguous crystals will create irregular outlines, as seen in Figure 2.13b & c.

The irregularity of outlines is reflected in the average solidity values (Table 2.6). The average solidity of an intersection outlined in the ‘maximum’ approach is 0.94 compared to the lower 0.88 in the ‘minimum’ approach. The ‘minimum’ approach produces more irregular outlines on average. This can be seen in the outlines themselves (Figure 2.13). Some of the outlines produced through the minimum approach do not reflect normal plagioclase crystal morphologies in any growth conditions. Reasons why the individual crystal intersections may not be evident in a contiguous mass could be the quality of the BSE map in terms of resolution or the greyscale (Chapter 2.2.1), or that the sample may not have been cut optimally to show individual crystals, as a thin section is a random 2D intersection of 3D shapes. The ‘maximum’ approach is therefore a better approach based on the accuracy of outlining on an individual crystal intersection basis. This approach also enables the greatest number of crystal intersections to be outlined and measured in a certain area. This is valuable as it maximises the data that can be extracted from a single BSE map, and a high number of intersection measurements is beneficial to accurately constrain a 3D shape estimate in ShapeCalc. This test provides reassurance that if a contiguous mass of intergrown crystals was misidentified as a singular crystal, this will not have a significant impact on overall results. Likewise, if a singular crystal was misidentified as multiple intergrown, this will not have a significant impact on overall results. In both scenarios, this is provided a sufficient number of intersects are measured (a few hundred at minimum).

Presumably, there could be a significant difference in CSDs constructed from a ‘maximum’ and ‘minimum’ approach. To test this, the data collected using both approaches was input into CSDCorrections. There is no significant difference between the CSDs, both following a similar shape of curve, and with individual data points on the curve being within error of each other (Figure 2.15). Therefore, taking forward the ‘minimum’ approach for analyses is unlikely to produce significantly different size results to a ‘maximum’ approach.

#### **2.4.2.2 Should twinned crystals be outlined individually, or as a single crystal?**

The established rule when outlining intersections was not to split intersections into twins. This was because it is difficult to be certain when identifying twins using just the BSE maps. An analytical method like Electron Backscatter Diffraction (EBSD) would have been necessary to correctly identify all simple twins present (Brugger & Hammer, 2015). The use of optical microscopy to check for optical continuity would only have been possible for the coarsest-grained samples, meaning the outlining approach would not have been consistent across all samples. Therefore it was decided to not split intersections into twins to ensure a more consistent and accurate approach to outlining across all samples. As established in Chapter 2.4.2.1, even if few crystals were split into twins, this is unlikely to have a significant effect on 3D shape estimate results.

#### **2.4.2.3 Should outlines be drawn around intergrowths, or extrapolate through them?**

Another factor to consider is whether to draw outlines exactly around intergrown crystals (Figure 2.16a), or to extrapolate through intergrowths, approximating how the crystal boundary may look if it had grown unimpinged (Figure 2.16b). It was thought that due to the highly intergrown nature of the groundmass, perhaps extrapolating the outline would produce a more accurate 3D-shape estimate. To test these approaches, the same 300 crystals were outlined twice: once drawing lines exactly around intergrown crystals, and another time extrapolating through boundaries (Figure 2.16).

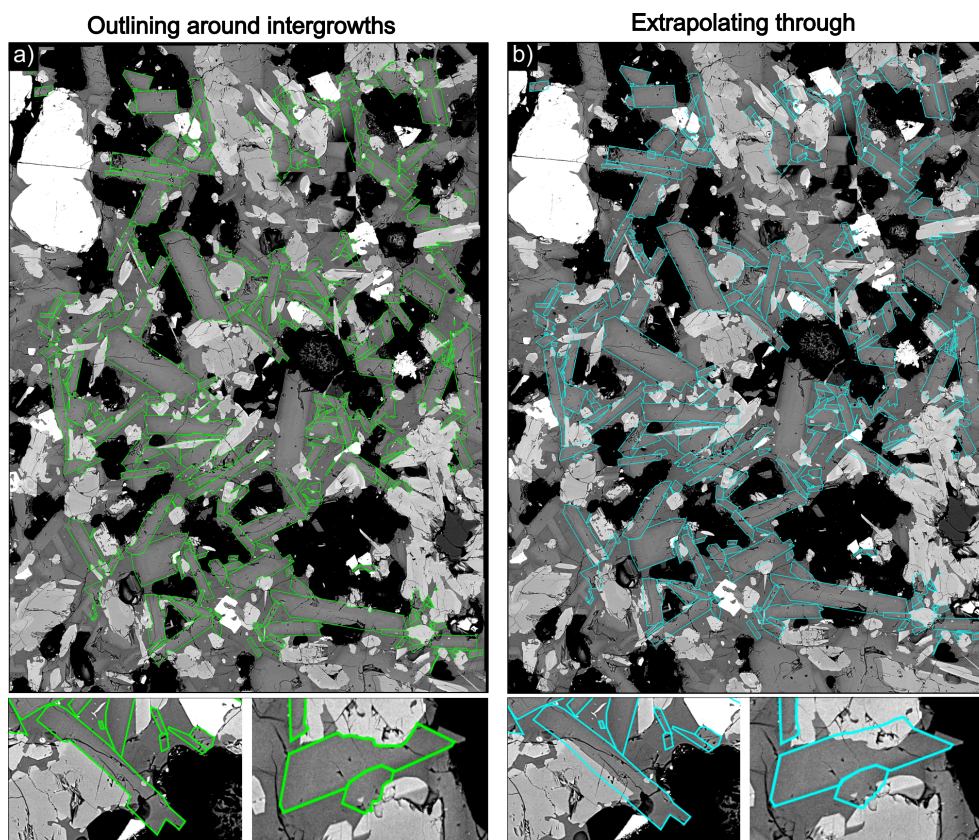


**Figure 2.16:** Comparison of outlining around intergrowths or extrapolating through them. **a)** Outlining around intergrowths. **b)** Extrapolating through intergrowths.

There is no significant difference in 3D shape estimate (Table 2.7). Outlining around intergrowths results in a best-fit shape with  $S/I$  of  $0.36 (\pm 0.06)$  and  $I/L$  of  $0.50 (\pm 0.25)$ , the exact same values as for extrapolating through intergrowths. The  $R_c^2$  values are within 0.02%, with 0.967 for outlining around intergrowths and 0.969 for extrapolating through intergrowths. The 3D shape estimate is identical because both approaches produce intersection population with the same  $w/l$  distribution (Figure 2.17).

Both approaches yield similar 2D size-shape values (Table 2.6.) Outlining around intergrowths results in mean intersection length of  $44 \mu\text{m}$ , a mean intersection width of  $14 \mu\text{m}$ , a mean  $w:l$  ratio of 0.41, and a mean solidity of 0.94. Extrapolating through intergrowths results in mean intersection length of  $44 \mu\text{m}$ , a mean intersection width of  $15 \mu\text{m}$ , a mean  $w:l$  ratio of 0.41, and a mean solidity of 0.96.

Extrapolating through intergrowths results in a greater total area outlined and a higher average intersection area, by  $\sim 5 \%$  (Table 2.6). This is greater than the estimated error in outlining of  $\sim 1.5 \%$ , as established in Section 1.4.2.1, and is therefore interpreted as a significant difference in area measurements. Extrapolating through intergrowths arguably overestimates total intersection area, which is a crucial measurement to produce accurate Crystal Size

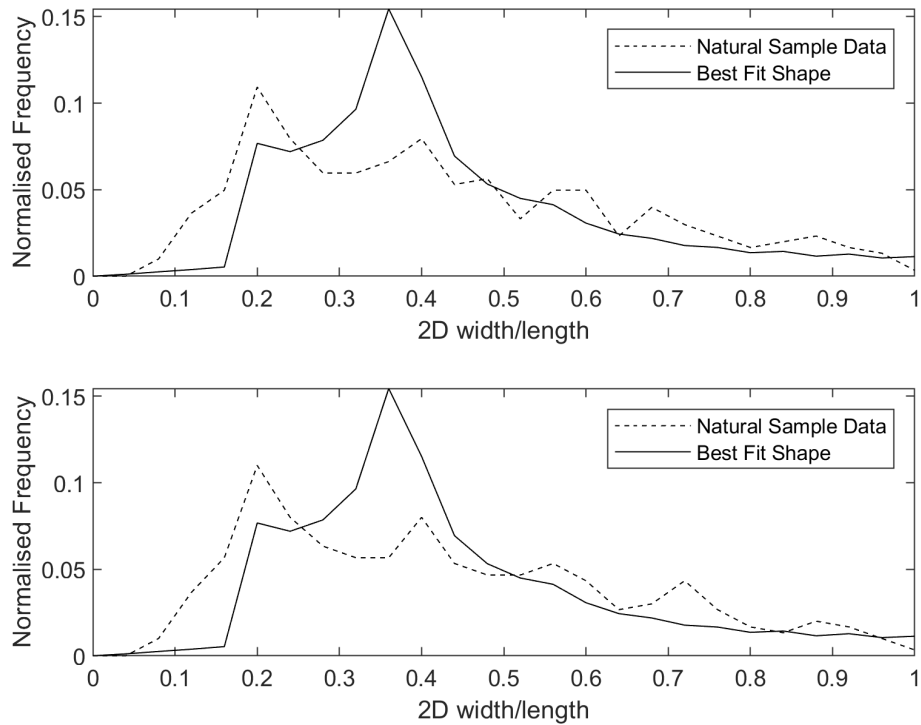


**Figure 2.17:** 2D  $w/l$  distributions for intersection populations produced through a) outlining around intergrown crystals b) extrapolating through intergrown crystals. There is no significant difference between the 3D shape estimates of the two approaches.

Distributions (Chapter 2.1.2). The decision was made to outline around intergrown crystals rather than extrapolate through. The former is conceptually a better representation of actual crystal intersect shape in these very intergrown samples, provides a more accurate estimate of crystal intersection area and subsequently volume, and is a simpler approach to reproduce between samples.

#### 2.4.2.4 How should outlines be drawn when crystals completely overlap?

There are instances in which crystal intersections appear to overlap, or “cut through” each other (Figure 2.18). The overlapping crystal has been intersected twice, producing two separate intersections in the BSE map. Evidence that supports this is the geometry of the intersections, i.e. the boundaries line up, and the presence of identical zoning in the same orientation. Two outlining approaches were tested: once outlining overlapping crystals by extrapolating through the crystals they intersect, and again by discarding overlapping intersections.

Of the 1510 intersections measured in sample 1591A, there were 10 instances of overlapping crystals. Instances of overlapping therefore occur once every 150 outlines. There is no significant difference in 3D shape estimate (Table 2.7) or 2D size-shape data (Table 2.6). This is expected as there are so few instances of overlapping crystals, and therefore only 10 out of 1510 intersections had to be discarded. The difference in total area between the approaches is negligible: outlining the overlapping crystals adds 0.27 % total area, well below the outlining error estimate of 1.5 % (Chapter 2.4.2.3.). As the instances of overlapping crystals are so rare, including them does not have a detrimental effect on the accuracy of the total area estimate, whilst providing more

intersections within an area for analysis. The decision was made to include them in further analyses by outlining overlapping crystals as in Figure 2.18a.

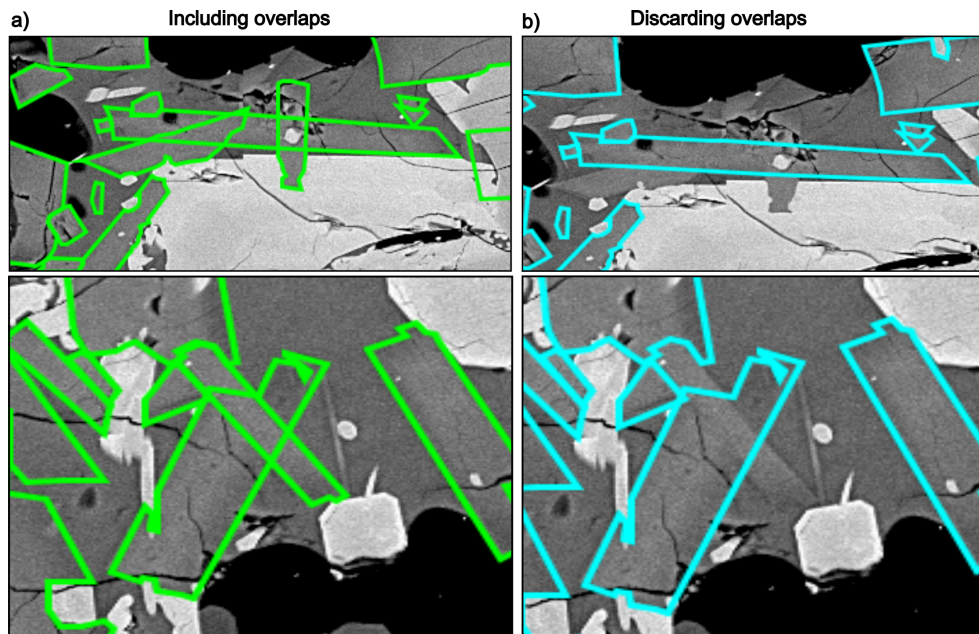


**Figure 2.18:** Comparison of outlining for a) Including overlapping intersections, and b) discarding overlaps.

#### 2.4.2.5 Should inclusions of other crystals be removed from outlines?

Some larger groundmass plagioclase and amphibole crystals contain small inclusions of other phases. As outlines were drawn around the host crystals, these inclusions are included within the outlines and consequently contribute to the estimates of crystal area and volume. If the area of inclusions is large, this could lead to an overestimate of host crystal area and volume. To test whether inclusions significantly contribute to estimates of plagioclase area, inclusions in plagioclase groundmass crystals in one sample were outlined, and their area measured. The sample chosen visually contains the largest amount of inclusions compared to other samples, meaning this test could act as a maximum estimate of the contribution of inclusions to the estimated area of host crystals (Figure 2.19). In this sample, inclusions constitute only 0.78 % of the total groundmass plagioclase area. As inclusions are only a minor contribution to area estimates (at maximum  $\sim 0.8\%$ ), it was decided to outline groundmass crystals regardless of whether they hosted inclusions.

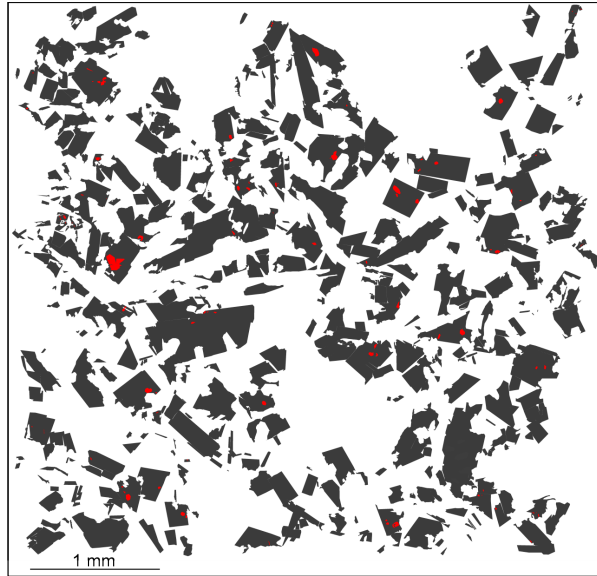


**Figure 2.19:** Outlined plagioclase groundmass crystals in TRA10A in grey, with inclusions in red. Inclusions make up 0.78 % of estimated groundmass plagioclase crystal area in this sample. It is the most inclusion-abundant sample, and therefore gives an upper estimate for inclusion contribution to host crystal total area.

### Manual Outlining Rules:

Having considered a range of factors affecting how best to outline crystal intersections, the following set of rules was established as an accurate, reproducible and consistent approach.

- Discard (do not measure intersections, or include intersections in area measurements):
  - Crystals of the phase of interest that intersect the image edge;
  - Broken or fractured crystals;
  - Crystals affected by misaligned stitching in the BSE map;
  - ‘Inherited’ crystals.
- Use the ‘Maximum’ approach: as many crystals as are petrographically reasonable are outlined and measured. Intergrown crystals are distinguished using compositional zoning, the presence of cores, and geometry of intersections.
- Draw around intergrowths as opposed to extrapolating through crystals.
- Do not split crystals into twins.
- Rare instances of overlapping crystals are outlined individually, extrapolating through each other.

## 2.5 Statistical validation

2D size-shape data collected by outlining and measuring 2D intersections was binned by length and input into ShapeCalc to produce 3D shape estimates (Chapter 2.1). Statistical tests were

conducted to validate the 3D shape-size results.

### 2.5.1 CrystalSlice

The program CrystalSlice (Allgood, in preparation) was used to generate  $w/l$  distributions of model crystal populations. The CrystalSlice algorithm is compatible with the CSDCorrections algorithm (Higgins, 2000), which was used to create the database of shapes in ShapeCalc (Mangler et al., 2022). In CrystalSlice, model cuboids are randomly sectioned to create a representative  $w/l$  distribution. 10,000 sections are attempted, resulting in 5500-7500 successful intersections of the model cuboid. The model crystal population can contain up to four sub-populations ( $P_1 - P_4$ ). The user defines the 3D shape ( $S:I:L$ ) and the relative proportions of each sub-population. Relative crystal size between sub-populations can be varied by scaling the  $S:I:L$  ( $x:y:z$ ) to a chosen length. The ability to vary 3D shape, size and proportions allows the generation of model populations representing different crystal shape-size scenarios.

Two types of model crystal population were created:

- Multiple shapes, one size;
- One shape, one size.

The  $w/l$  distribution of each model population was compared to the  $w/l$  distribution of the natural sample population, with goodness-of-fit quantified by  $R_c^2$ . Comparing the results of different models indicates whether the natural sample population is better fit to a model population of multiple shapes, or a model population of a singular shape.

Figure 2.20a illustrates the method for a model crystal population of multiple shapes, one size. Here, plagioclase intersection data in a natural sample was binned into four size fractions of 0-20  $\mu\text{m}$ , 20-40  $\mu\text{m}$ , 40-100  $\mu\text{m}$  and 100 +  $\mu\text{m}$ , with 3D shape estimates produced for each bin ( $S:I:L$ ). The proportion of the total intersections in each bin was 31.3 %, 29.9 %, 31.5 % and 7.2 % respectively. The 3D shape estimates and their relative proportions were input into CrystalSlice to generate a model  $w/l$  distribution. Goodness-of-fit ( $R_c^2$ ) between the model  $w/l$  distribution and the natural sample  $w/l$  distribution suggests how well the model of multiple shape populations matches the natural sample population.

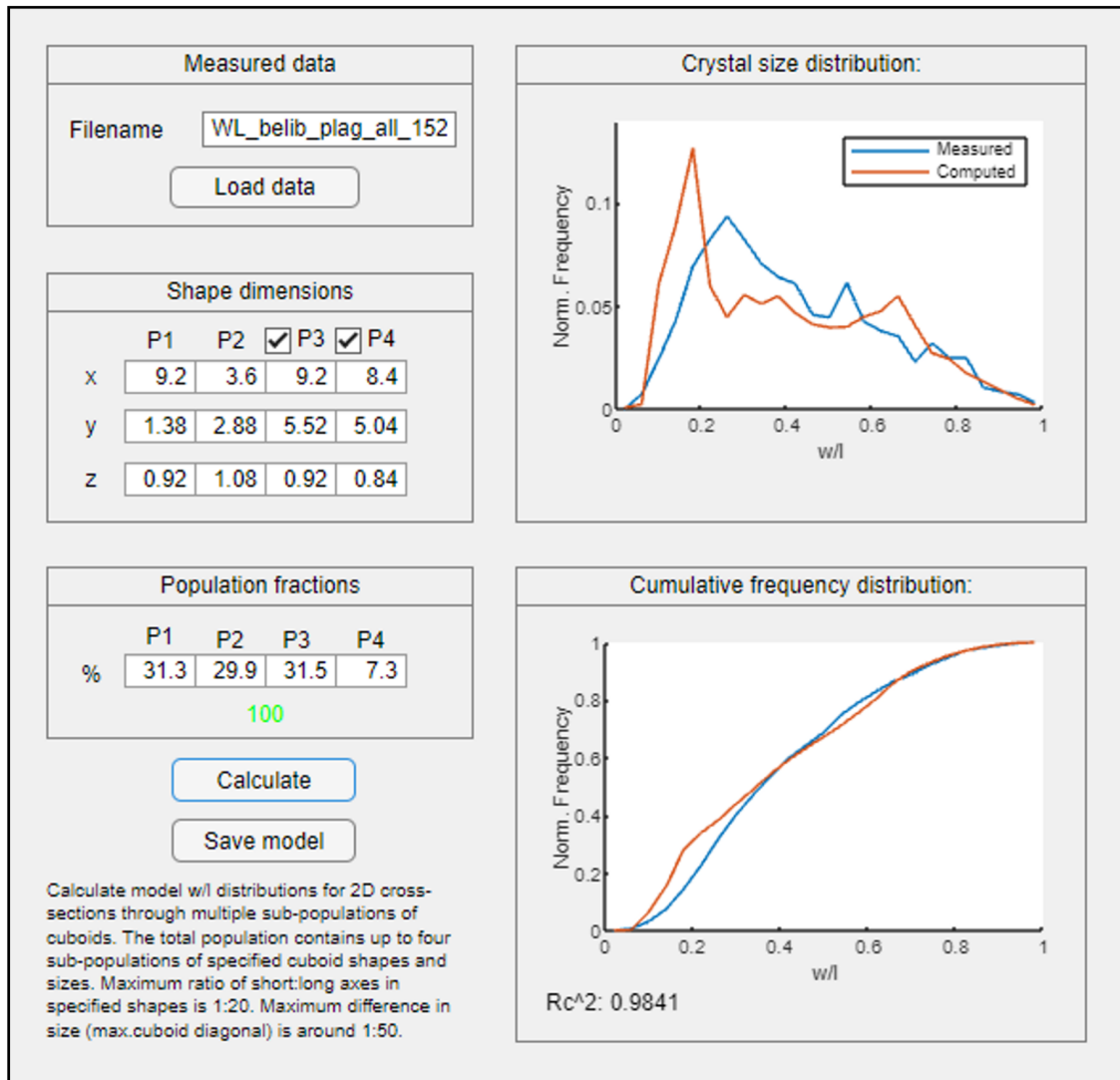


**Figure 2.20:** Example CrystalSlice (Allgood, in preparation) outputs different model crystal populations. The  $w/l$  distribution of plagioclase intersections in an unbinned, natural sample is compared to the  $w/l$  distribution of model intersections for multiple shapes model.

### 2.5.2 Model 2D Intersection Data

The natural sample data were binned by 2D intersection length to identify size fractions with different 3D shapes (Chapter 2.1.3). For example, plagioclase intersection data in a natural sample were binned into four size fractions of 0-20  $\mu\text{m}$ , 20-40  $\mu\text{m}$ , 40-100  $\mu\text{m}$  and 100 +  $\mu\text{m}$ . The intersections that comprise the smallest size fraction (0-20  $\mu\text{m}$ ) may have been produced by sectioning through the corner of a crystal much larger than 20  $\mu\text{m}$  (cut-section effect). A number of the smallest intersections observed in the natural sample are expected to be corner-cuts of a larger crystal, and are likely to be triangular. If the majority of the smallest intersections (0-20  $\mu\text{m}$ ) are produced in this way, then the smallest size fraction does not represent a “real” crystal population of significantly different shape.

To address this problem, CrystalSlice was used to create model 2D intersection data by sectioning a cuboid with the  $S:I:L$  of the complete unbinned population, generating intersection

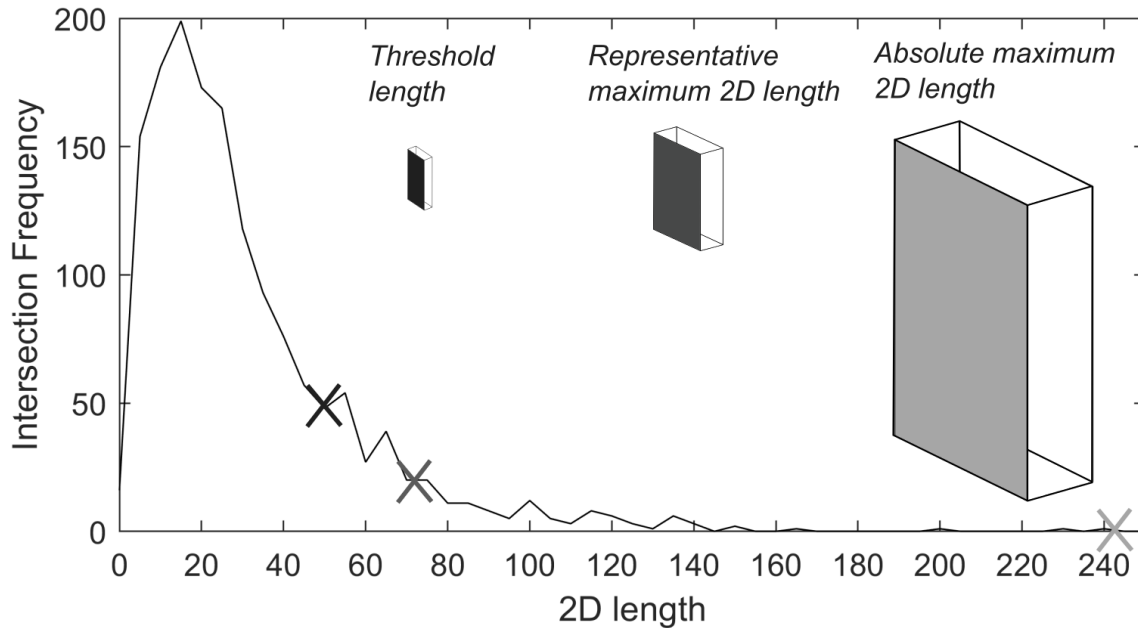


**Figure 2.21:** Scaling approach for 2D model intersection data. 2D model length measurements are scaled to a representative maximum 2D length (around the base of the frequency curve). Absolute maximum 2D length is not thought to be representative because there are so few very large crystals. Scaling to different lengths was tested to establish a threshold length where the proportion of the smallest size fraction in the model data and sample data matches.

width, length and shape data. The measurements were scaled to a representative maximum intersection length, here based on the base of the frequency curve (Figure 2.21). The scaled model 2D intersection data was then proportioned into each size bin, i.e., the number of model intersections between 0-20  $\mu\text{m}$  and the number of model intersections larger than 0-20  $\mu\text{m}$  (Figure 2.21). If sectioning a model cuboid can recreate the proportion of intersections in the smallest size fraction (i.e., 0-20  $\mu\text{m}$  length) in the natural samples, this suggests that the smallest crystal population is likely corner-cuts of a large crystal population, and is therefore not a distinct shape-size population.

The proportion of each intersection shape within the size bins is also compared. Corner-cuts of the model cuboid will produce triangular intersections. If the model smallest fraction contains more 3-point intersections than the sample smallest fraction, this suggests that the sample smallest fraction is not just corner-cuts of larger crystals. There is a limitation in that natural crystals are more irregular than model cuboids, and will often have rounded or multi-faceted corners (Higgins, 1994). Some intersections that are corner-cuts of larger crystals will therefore not appear triangular and will be missed in analysis.

### 3 Mafic Enclave Sample Petrology

In this thesis, crystal textures were studied in three mafic enclaves erupted during Phase V, the final eruptive phase lasting from October 2009 to February 2010: MVO-1591A, BEL1B-A and TRA10A. Here, we characterise them in terms of texture (Figure 3.1 and Figure 3.2) and chemistry (Table 3.1; Figure 3.3). The enclaves preserve a snapshot of the mingling dynamics at SHV, where periodic basaltic recharge of the shallow mush reservoir is thought to be a potential eruption trigger (Murphy et al., 2000; Murphy et al., 1998). The diktytaxitic groundmass texture of the enclaves suggests they formed by rapid quench crystallisation (Bacon 1986; Plail et al. 2014), and therefore provide a relatively simple crystallisation scenario in which to explore the petrogenetic significance of crystal shape.

#### 3.1 MVO-1591A

MVO-1591A is a fine-grained enclave with relatively high vesicularity (28.5 %) and a groundmass assemblage of plagioclase + amphibole + orthopyroxene + clinopyroxene + apatite + iron oxides + rhyolitic interstitial glass (Figure 3.1d-e). Framework plagioclase makes up the diktytaxitic groundmass texture. Plagioclase has high-An cores ( $An_{75-85}$ ) and thin, more calcic rims ( $An_{40-75}$ ). High-Al amphibole occurs alongside orthopyroxene, sometimes with darker cores (1.2-2.4 wt.% CaO) and lighter rims (1.3-1.6 wt.% CaO), with the overlapping values likely due to the difficulty in sampling very thin rims on small crystals in SEM-EDS (Figure 3.3b-c). Large (2-3 cm) inherited phenocrysts from the andesite include plagioclase, which often displays sieved cores, orthopyroxene, often with reaction rims of clinopyroxene, and amphibole, with individual crystal textures ranging from euhedral to nearly entirely opacitised (Figure 3.1d). MVO-1591A is categorised as a Type A enclave according to the system of Plail et al. (2014), owing to the presence of groundmass amphibole, high vesicularity, and presence of a chilled margin. Taken together, these observations suggest that this enclave formed by quench crystallisation (Bacon, 1986).

#### 3.2 BEL1B-A

BEL1B-A is similar to MVO-1591A, again being a fine-grained enclave with the same groundmass assemblage and an inherited phenocryst population of plagioclase, orthopyroxene and amphibole, which in this sample is accompanied by rare quartz hosting a clinopyroxene reaction rim (Figure 3.2a). There is a similar amount of intergrowth between groundmass phases, with notably complex interactions between amphibole and pyroxenes (Figure 3.2b-c). Groundmass plagioclase compositions are similar to MVO-1591A, with high-An cores ( $An_{70-90}$ ) and thin rims ( $An_{15-45}$ ). Orthopyroxene nearly always appears with at least one zonation, usually a darker core (1.7-2.3 wt.% CaO) and lighter rim (0.8-1.6 wt.% CaO). Low-Al amphibole does not represent typical enclave compositions, instead resembling compositions of amphibole phenocrysts in the host andesite, showing the complexity in enclaves erupted even within the Phase V. A chilled margin (Figure 3.2e) between the host andesite and enclave suggests the enclave formed by quench crystallisation. This, combined with the presence of groundmass amphibole, categorises this enclave as Type A despite the relatively lower vesicularity (~14 %).

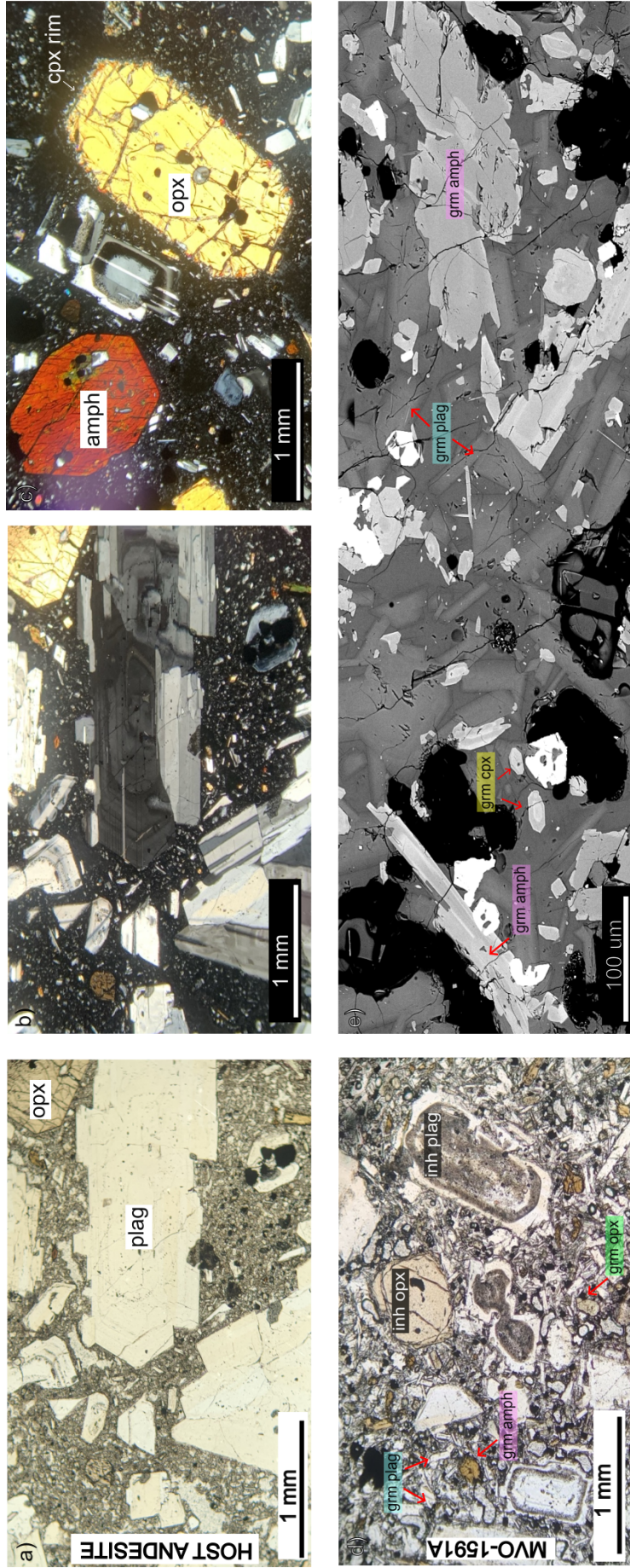


**Figure 3.1:** Petrology of host andesite (a-c) and mafic enclave MVO-1591A (d-e). The host andesite has a fine-grained groundmass (grm), with phenocrysts of plagioclase (plag) (a), orthopyroxene (opx) and amphibole (amph) (b-c). MVO-1591A has a fine-grained groundmass (d-e) with the most abundant phases being plagioclase + pyroxene (both clinopyroxene (cpx) and orthopyroxene (opx)). Inherited plagioclase phenocrysts show pervasive resorption.

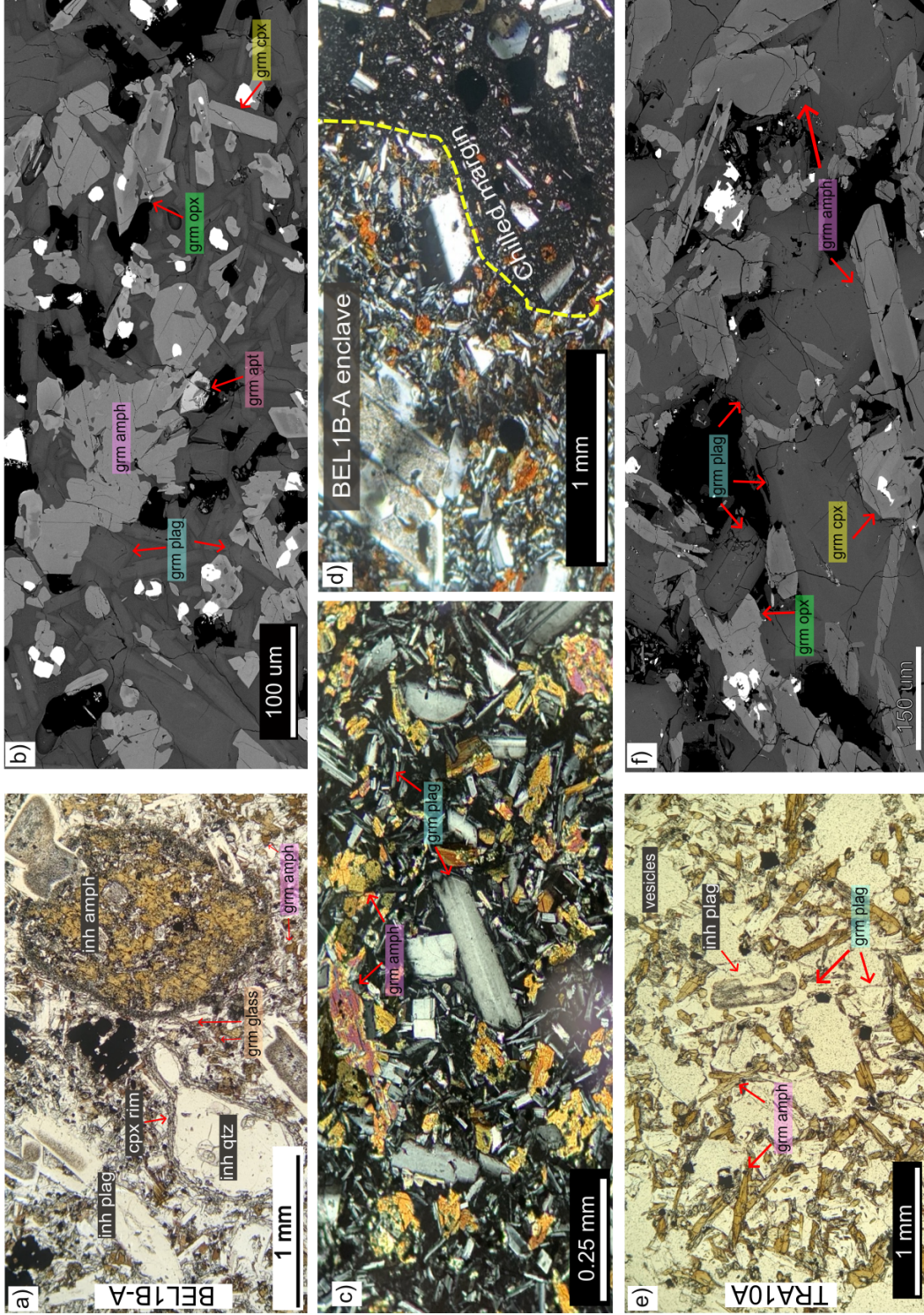


**Figure 3.2:** Petrology of BEL1B-A (a-d) and TRA10A (e-f). BEL1B-A is fine-grained (a), with complex intergrowths of groundmass amphibole and pyroxene (b-c), and a clear chilled margin between the enclave and host andesite (d). TRA10A is coarse-grained (e), with a highly intergrown groundmass of plagioclase + amphibole + pyroxene (f).

### 3.3 TRA10A

TRA10A is highly vesicular ( $\sim 30\%$ ) and coarse-grained, with the same groundmass assemblage as previous. The groundmass is highly intergrown with little interstitial glass (Figure 3.2e-f). Groundmass plagioclase is not significantly different to the other enclaves, with high-An cores ( $An_{75+}$ ). Plagioclase is the only inherited phenocryst, typically with dusty sieved cores pervading the whole crystal interior, bounded by a calcic overgrowth rim. Groundmass amphibole is low-Al, similar to that of MVO-1519A, as is groundmass orthopyroxene (cores, 1.6-2.6 wt.% CaO). TRA10A is categorised as a Type A enclave, due to the presence of groundmass amphibole and high vesicularity.

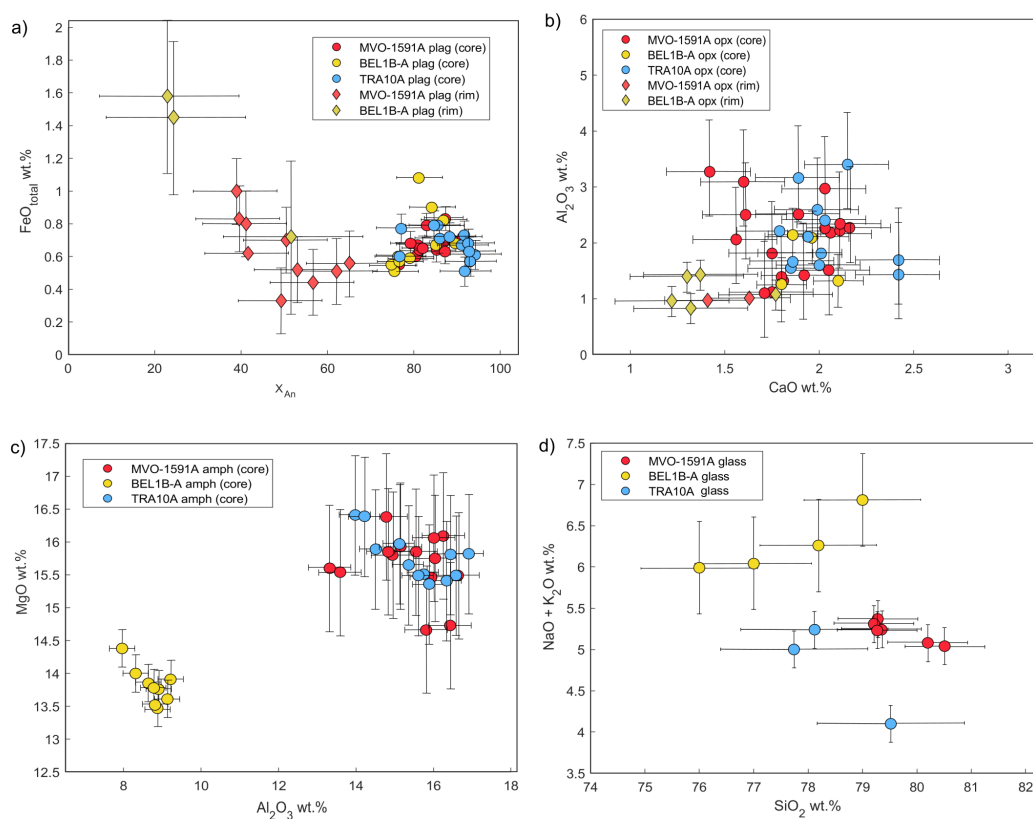


**Figure 3.3:** Compositions of key groundmass phases analysed in the three enclaves.  $X_{An}$  is calculated as  $\frac{CaO \text{ wt.}\%}{CaO \text{ wt.}\% + NaO \text{ wt.}\%} \times 100$ . **a)** Groundmass plagioclase have high-anorthite cores and more calcic rims, with no significant difference in composition between enclaves. **b)** Groundmass orthopyroxene have no significant difference in composition between enclaves, with slightly less calcic rims than cores. **c)** Groundmass amphibole in MVO-1519A and TRA10A is high-Al, whereas amphibole in BEL1B-A is low-Al, similar in composition to amphibole phenocrysts in the host andesite. **d)** Interstitial glass is rhyolitic, ranging from  $\sim 75$ - $82\%$   $SiO_2$ .

**Table 3.1:** Average compositions of groundmass plagioclase, orthopyroxene, amphibole and interstitial glass of the three studied enclaves.

	MVO-1591A		MVO-1591A		BEL1B-A		BEL1B-A		TRA10A	
Groundmass plagioclase	Core	$\pm 1\sigma$	Rim	$\pm 1\sigma$	Core	$\pm 1\sigma$	Rim	$\pm 1\sigma$	Core	$\pm 1\sigma$
SiO <sub>2</sub>	49.51	1.62	64.40	6.77	50.56	1.96	75.57	5.18	47.81	2.25
Al <sub>2</sub> O <sub>3</sub>	31.99	1.12	22.13	4.54	31.19	1.27	13.95	4.04	33.02	1.58
FeO <sub>total</sub>	0.68	0.07	0.63	0.20	0.70	0.18	1.25	0.46	0.68	0.09
MgO	0.09	0.04	0.06	0.04	0.06	0.02	0.13	0.08	0.11	0.04
CaO	14.56	1.22	5.88	2.56	13.79	1.48	2.28	1.90	15.96	1.76
Na <sub>2</sub> O	3.03	0.70	6.01	0.95	3.55	0.85	4.36	0.28	2.33	1.01
K <sub>2</sub> O	0.09	0.04	0.78	0.62	0.08	0.03	2.17	0.66	0.04	0.03
Total	100.13		100.10		100.07		100.04		100.07	
X <sub>An</sub>	84.20	4.18	49.80	9.47	80.90	5.24	32.97	16.12	88.08	5.86
	<b>MVO-1591A</b>		<b>MVO-1591A</b>		<b>BEL1B-A</b>		<b>BEL1B-A</b>		<b>TRA10A</b>	
Groundmass orthopyroxene	Core	$\pm 1\sigma$	Rim	$\pm 1\sigma$	Core	$\pm 1\sigma$	Rim	$\pm 1\sigma$	Core	$\pm 1\sigma$
SiO <sub>2</sub>	53.12	0.91	52.63	0.1	53.22	1.13	52.76	0.48	52.51	0.69
Al <sub>2</sub> O <sub>3</sub>	2.09	0.65	0.99	0.03	1.70	0.48	1.14	0.27	2.13	0.65
FeO <sub>total</sub>	16.82	1.57	21.74	0.25	17.37	2.14	21.58	1.61	18.37	1.49
MgO	25.25	1.26	21.66	0.16	24.77	1.57	21.96	1.17	23.84	1.12
CaO	1.85	0.22	1.52	0.16	1.93	0.13	1.40	0.22	2.03	0.21
Na <sub>2</sub> O	0.08	0.03	0.07	0.06	0.13	0.05	0.11	0.03	2.10	0.05
K <sub>2</sub> O	0		0		0		0.06	0.01	0	
TiO <sub>2</sub>	0.22	0.08	0.20	0.02	0.27	0.12	0.16	0.08	0.31	0.1
MnO	0.55	0.14	1.18	0.23	0.62	0.17	0.94	0.13	0.7	0
Total	99.98		100.01		100.0		100.01		102.02	
	<b>MVO-1591A</b>		<b>BEL1B-A</b>		<b>TRA10A</b>					
Groundmass amphibole		$\pm 1\sigma$		$\pm 1\sigma$		$\pm 1\sigma$				
SiO <sub>2</sub>	42.33	0.71	46.66	0.58	41.99	0.67				
Al <sub>2</sub> O <sub>3</sub>	15.38	1.01	8.73	0.39	15.56	0.95				
FeO <sub>total</sub>	9.89	0.74	15.09	0.41	9.78	0.24				
MgO	15.66	0.48	13.81	0.28	15.77	0.36				
CaO	11.93	0.21	11.03	0.10	12.03	0.24				
Na <sub>2</sub> O	2.43	0.07	1.85	0.10	2.48	0.08				
K <sub>2</sub> O	0.27	0.03	0.28	0.03	0.25	0.03				
TiO <sub>2</sub>	1.98	0.18	2.15	0.22	1.99	0.12				
MnO	0.16	0.06	0.39	0.07	0.16	0.06				
Total	100.01		100.05		100.00					
	<b>MVO-1591A</b>		<b>BEL1B-A</b>		<b>TRA10A</b>					
Interstitial glass		$\pm 1\sigma$		$\pm 1\sigma$		$\pm 1\sigma$				
SiO <sub>2</sub>	79.64	0.57	77.55	1.32	78.46	0.94				
Al <sub>2</sub> O <sub>3</sub>	11.91	0.38	10.28	0.73	12.86	0.66				
FeO <sub>total</sub>	1.56	0.05	1.98	0.12	0.56	0.07				
MgO	0.12	0.04	0.97	0.12	0					
CaO	1.01	0.07	2.10	0.18	1.79	0.29				
Na <sub>2</sub> O	2.46	0.11	3.10	0.35	4.61	0.22				
K <sub>2</sub> O	2.76	0.02	1.75	0.35	1.49	0.12				
TiO <sub>2</sub>	0.48	0.12	0.38	0.08	0.15	0.03				
MnO	0.11	0.05	0.07	0.02	0.08	0.06				
Total	100.04		98.7		100.04					
NaO + K <sub>2</sub> O	5.21	0.13	4.85	0.51	6.10	0.14				

## 4 3D Size-Shape Results

Here, we present the results of the outlining, measurement and 3D shape estimation of ground-mass crystals in the enclave samples. The results are organised by crystal phase: starting with plagioclase, followed by the mafic phases of orthopyroxene and amphibole. First, the overlay of intersection outlines will be presented alongside the extracted 2D size-shape data. Then, the Crystal Size Distribution (CSD) will be presented, with size bins marked on if the sample could successfully be binned by size to show change in shape. Finally, the results of the 3D shape estimation will be presented, including the best-fit 3D shape estimate to both the binned fractions and the complete unbinned intersection population for each sample.

### 4.1 Tabulated results

Table 4.1 presents the 2D size-shape data extracted from each overlay of outlined intersections according to the method detailed in Chapter 2.3.1. Table 4.2 details the textural parameters used to construct the CSDs. Table 4.3 presents the best-fit 3D shape estimates produced in ShapeCalc for each phase in each sample. Plagioclase intersections were binned into four size fractions: 0-20  $\mu\text{m}$ , 20-40  $\mu\text{m}$ , 40-100  $\mu\text{m}$  and 100 +  $\mu\text{m}$ . The same bins were used consistently to enable comparison between different samples for the same phase. Groundmass plagioclase was outlined in all samples. Groundmass orthopyroxene was outlined in one sample, BEL1B-A. Groundmass amphibole was outlined in one sample, TRA10A.

#### *2D intersection measurements*

**Table 4.1:** 2D size-shape data extracted from the overlays of outlined intersections.

Sample	Phase	n <sup>a</sup>	Measured area <sup>b</sup> (mm <sup>2</sup> )	$\varphi^c$ (%)	Mean Area <sup>d</sup> ( $\mu\text{m}^2)$	l <sub>max</sub> <sup>e</sup> ( $\mu\text{m}$ )	l <sub>min</sub> <sup>f</sup> ( $\mu\text{m}$ )	l <sub>mean</sub> <sup>g</sup> ( $\mu\text{m}$ )	w/l <sub>mean</sub> <sup>h</sup>	Solidity		
										Mean	Range	Mode
MVO-1591A	Plagioclase	1510	4.39	25.9	780	299	4	42.5	0.38	0.95	0.6 - 1.0	1.00
BEL1B-A	Plagioclase	1528	2.49	27.5	449	241	3	33.6	0.42	0.96	0.6 - 1.0	1.00
	Orthopyroxene	1317	9.80	5.2	385	248	4	28.3	0.55	0.94	0.6 - 1.0	1.00
TRA10A	Plagioclase	534	15.98	32.2	9634	736	8	131.7	0.46	0.88	0.4 - 1.0	1.00
	Amphibole	542	16.92	13.5	4200	1298	9	97.7	0.54	0.90	0.4 - 1.0	1.00

<sup>a</sup>Number of crystal intersections measured.

<sup>b</sup>The area of the BSE map minus the area of edge-intersecting crystals of the phase of interest (Chapter 2.1.2).

<sup>c</sup>Crystallinity of phase as a percentage of measured area (including vesicularity).

<sup>d</sup>Mean intersection area.

<sup>e</sup>Maximum intersection length.

<sup>f</sup>Minimum intersection length.

<sup>g</sup>Mean intersection length.

<sup>h</sup>Mean intersection width:length ratio.

## Crystal Size Distributions

**Table 4.2:** Crystal Size Distribution (CSD) results and inputs.  $S:I:L$  is the best-fit 3D shape estimate for the complete unbinned intersection population. Slope and intercept are calculated in CSDCorrections (Higgins, 2000) using a linear least squares regression. The largest amphibole crystal measured in TRA10A is an outlier, as it is twice as large as the second largest crystal measured, and so has been removed from this analysis.

Sample	Phase	$n$	Slope	$\pm$	Error	Intercept	$\pm$	Error	CSD Inputs							
									Measured area (mm <sup>2</sup> )	VPA <sup>a</sup> (%)	$S$	$I$	$L$	Fabric	Roundness	Vesicularity (%)
MVO-1591A	Plagioclase	1510	-28.6	$\pm$	0.50	12.7	$\pm$	0.04	4.39	25.91	1.00	2.70	5.60	Massive	0.1	28.50
BEL1B-A	Plagioclase	1528	-34.8	$\pm$	0.60	13.61	$\pm$	0.05	2.49	27.50	1.00	2.70	5.60	Massive	0.1	14.65
	Orthopyroxene	1317	-29.7	$\pm$	0.60	11.77	$\pm$	0.05	9.80	5.17	1.00	1.50	5.20	Massive	0.1	13.25
TRA10A	Plagioclase	534	-6.38	$\pm$	0.21	7.57	$\pm$	0.08	15.98	32.91	1.00	2.10	6.00	Massive	0.3	31.81
	Amphibole	541	-7.58	$\pm$	0.24	7.77	$\pm$	0.08	16.80	12.86	1.00	1.55	6.40	Massive	0.2	30.25

<sup>a</sup>Volumetric Phase Abundance: the combined area of all measured intersections expressed as a percentage of the total measured area (Chapter 2.1.2)

### 3D shape estimate results

**Table 4.3:** Best-fit 3D shape estimates for complete unbinned intersection data and binned size fractions. Starred (\*) bins have fewer than 200 intersections (considered the minimum sufficient number for analysis).

Sample	Phase	Fraction ( $\mu\text{m}$ )	$n$	% Total	$S$	$I$	$L$	$R_c^2$	$S/I$	$\pm$	1 SD*	$I/L$	$\pm$	1 SD*
MVO-1591A	Plagioclase	Unbinned	1510	100	1.00	2.70	5.60	0.974	0.37	$\pm$	0.06	0.48	$\pm$	0.25
		0-20	474	31.4	1.00	1.45	9.20	0.996	0.69	$\pm$	0.06	0.16	$\pm$	0.18
		20-40	451	29.9	1.00	2.80	5.60	0.982	0.36	$\pm$	0.06	0.50	$\pm$	0.25
		40-100	476	31.5	1.00	3.60	9.20	0.994	0.28	$\pm$	0.04	0.39	$\pm$	0.23
		100 + *	109	7.2	1.00	5.00	8.40	0.996	0.20	$\pm$	0.03	0.60	$\pm$	0.22
BEL1B-A	Plagioclase	Unbinned	1528	100	1.00	2.70	5.60	0.981	0.37	$\pm$	0.06	0.48	$\pm$	0.25
		0-20	550	36.0	1.00	1.70	6.40	0.991	0.61	$\pm$	0.06	0.26	$\pm$	0.18
		20-40	549	35.9	1.00	2.80	6.40	0.993	0.36	$\pm$	0.05	0.44	$\pm$	0.25
		40-100	376	24.6	1.00	4.10	9.60	0.997	0.24	$\pm$	0.03	0.43	$\pm$	0.22
		100 + *	53	3.5	1.00	4.90	12.00	0.990	0.20	$\pm$	0.03	0.41	$\pm$	0.22
	Orthopyroxene	Unbinned	1317	100	1.00	1.50	5.20	0.997	0.67	$\pm$	0.06	0.29	$\pm$	0.20
		0-35	1012	76.8	1.00	1.40	2.60	0.998	0.71	$\pm$	0.08	0.54	$\pm$	0.27
		35 +	305	23.2	1.00	3.00	6.80	0.989	0.33	$\pm$	0.05	0.44	$\pm$	0.25
TRA10A	Plagioclase	Unbinned	534	100	1.00	2.10	6.00	0.989	0.48	$\pm$	0.07	0.35	$\pm$	0.25
		0-20 *	15	2.8	1.00	2.80	3.60	0.989	0.36	$\pm$	0.07	0.78	$\pm$	0.26
		20-40 *	47	8.8	1.00	2.20	4.80	0.992	0.45	$\pm$	0.06	0.46	$\pm$	0.24
		40-100	190	35.8	1.00	2.10	6.00	0.987	0.48	$\pm$	0.07	0.35	$\pm$	0.24
		100 +	281	52.6	1.00	2.10	6.00	0.988	0.48	$\pm$	0.06	0.35	$\pm$	0.24
	Amphibole	Unbinned	542	100	1.00	1.55	6.40	0.998	0.65	$\pm$	0.06	0.24	$\pm$	0.20

## 4.2 Plagioclase

### 4.2.1 MVO-1591A

Figure 4.1a presents the overlay of outlined plagioclase crystal intersections produced by the method detailed in Section 2.4.2. Figure 4.1b illustrates the binning process (Chapter 2.1.3), with outlines differentiated by size fractions of 0-20  $\mu\text{m}$ , 20-40  $\mu\text{m}$ , 40-100  $\mu\text{m}$  and 100 +  $\mu\text{m}$ . It is a representative area of the proportion of intersections per size fraction, with the proportions presented in Table 4.3. Intersections in the smallest bin generally have equant shapes, and intersections become increasingly elongate with larger bins.

MVO-1591A has fine-grained groundmass, dominated by plagioclase. It is an end-member sample for groundmass crystal size, being one of the finest-grained and least intergrown enclave samples (Chapter 3). 26 % of the measured area is groundmass plagioclase (Table 4.1).

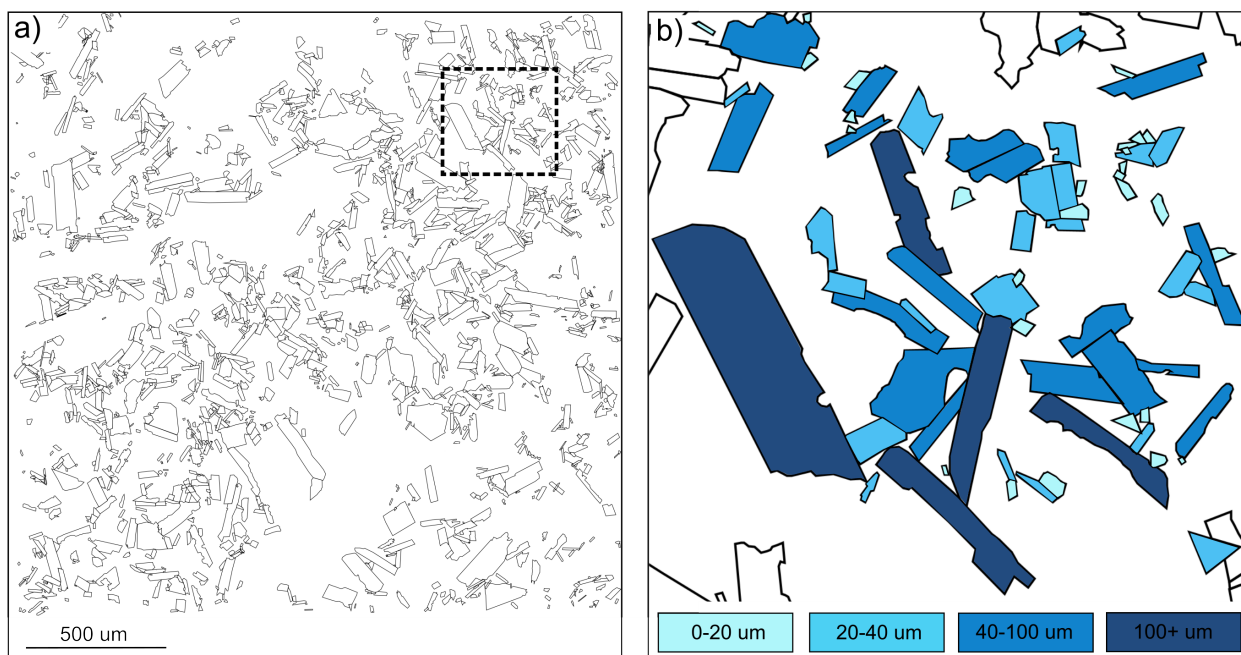


**Figure 4.1:** Overlay of groundmass plagioclase intersection outlines in MVO-1591A. **a)** Overlay of 1510 intersection outlines. Dashed area defines **b)**. **b)** Intersection outlines colour-coded to illustrate the binning process and relative proportions of intersections in each bin.

The maximum intersection length is 299  $\mu\text{m}$ , with the minimum length being 4  $\mu\text{m}$ . The mean intersection length is 43  $\mu\text{m}$ . The minimum width is 1  $\mu\text{m}$ , representing the minimum resolvable width from the quality of the BSE maps (Chapter 2.2). Solidity ranges from 0.6 - 1.0, with an average solidity value of 0.95 and a modal solidity of 1.00. This suggests that crystal intersections generally have quite even boundaries and regular shapes. This can be visually seen in the overlay (Figure 4.1).

Figure 4.2 presents the CSD for the groundmass plagioclase. The 2D size-shape data and textural data used as inputs are detailed in Table 4.2. The CSD is a curved slope, with a slope of  $-28.6 (\pm 0.5)$  and an intercept of  $12.7 (\pm 0.04)$ . The lower limit of crystal size is 7  $\mu\text{m}$ . The downturn of the slope is due to the lower abundance of resolvable crystals at the smallest sizes.

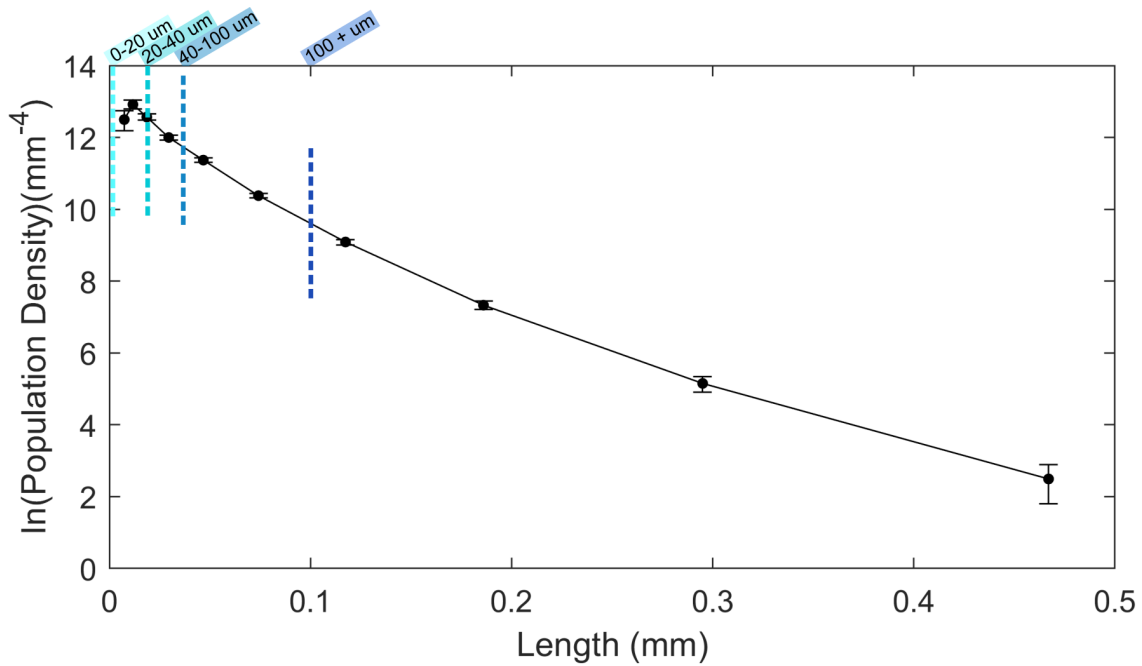


**Figure 4.2:** Crystal size distribution of groundmass plagioclase in MVO-1591A. The resulting size fractions from binning the intersection data are marked on the slope.

The groundmass plagioclase intersection data were binned by size fraction to investigate change in shape. Each binned fraction, as well as the complete unbinned data, were input into ShapeCalc to produce a best-fit 3D shape estimate (Table 4.3). Figure 4.3 illustrates the 3D shape estimates and the suggested change in shape with size. There is a decrease in  $S/I$  with increasing crystal size. Crystals approach more tabular shapes with increasing size. The smallest crystals (0-20  $\mu\text{m}$ ) have a prismatic shape ( $S/I = 0.69 \pm 0.06$ ,  $I/L = 0.16 \pm 0.18$ ). Crystals in the 20-40  $\mu\text{m}$  fraction are a significantly different shape, moving towards more tabular with a decrease in  $S/I$  and increase in  $I/L$  ( $S/I = 0.36 \pm 0.06$ ,  $I/L = 0.50 \pm 0.25$ ). Crystals in the 40-100  $\mu\text{m}$  fraction are not a significantly different shape in terms of  $S/I$  to the 20-40  $\mu\text{m}$  fraction ( $S/I = 0.28 \pm 0.04$ ,  $I/L = 0.39 \pm 0.23$ ). Crystals in the 100+  $\mu\text{m}$  fraction are significantly different to the smaller fractions, with the most tabular shape estimate ( $S/I = 0.20 \pm 0.03$ ,  $I/L = 0.60 \pm 0.22$ ). It should be noted that this size fraction includes only 109 crystals, below the minimum sufficient number required for analysis (Chapter 2.2.1). However, the high  $R_c^2$  value of 0.996 (Table 4.3) for this fraction indicates that despite the low number of intersections, there is a good match between the natural sample data and the best-fit model shape in ShapeCalc.

Figure 4.4 compares the  $w/l$  distributions for each binned fraction in the natural sample data against the best-fit model shape. The  $R_c^2$  values (Table 4.3) for the binned fractions are 0.996 (0-20  $\mu\text{m}$ ), 0.982 (20-40  $\mu\text{m}$ ), 0.994 (40-100  $\mu\text{m}$ ) and 0.996 (100+  $\mu\text{m}$ ). All four  $R_c^2$  values are above 0.980, three are above 0.990, and two are above 0.995. This goodness-of-fit is illustrated in Figure 4.4. Again, despite the 100+  $\mu\text{m}$  bin having fewer than 200 intersections, there is a close match in  $w/l$  distribution between the natural sample data and the best-fit model shape (Figure 4.4d). As established in Chapter 2.1.1, the sharpness

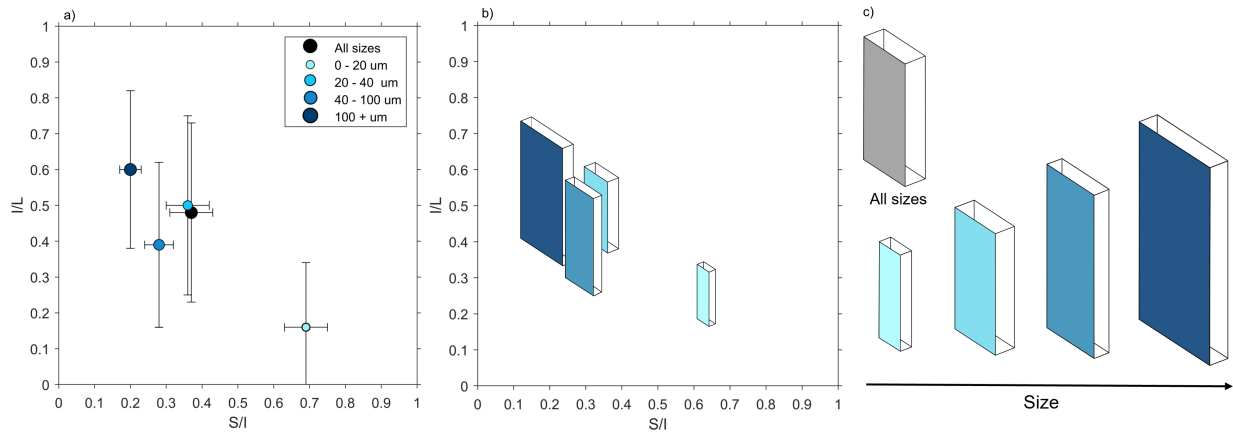


**Figure 4.3:** 3D shape estimates for groundmass plagioclase in MVO-1591A. **a)** Zingg diagram showing the  $S/I$  and  $I/L$  estimates for each binned size fraction and the complete unbinned data. There is a decrease in  $S/I$  with increasing size, and general trend of shapes moving from prismatic to tabular. **b)** Zingg diagram with the 3D shape estimates for each binned fraction visualised. **c)** The suggested change in shape with size visualised alongside the singular shape estimate for the unbinned intersection data. Shape evolves from prismatic to tabular with size.

of the peaks in the model  $w/l$  distributions is unlikely to be replicated by the natural sample  $w/l$  distributions (Higgins, 1994).

The best-fit 3D shape estimate for the complete, unbinned data is  $S/I = 0.37 \pm 0.06$ ,  $I/L = 0.48 \pm 0.25$ . This overlaps with the shape estimate for the 20-40  $\mu\text{m}$  bin. The  $R_c^2$  value for the complete, unbinned data is 0.974, a lower confidence value than any of the binned size fractions. The lower goodness-of-fit between the unbinned data and the best-fit model shape is illustrated in Figure 4.4e.

The intersection outlines (Figure 4.1) provide a qualitative confirmation of the change in shape with size fraction. The intersections in the 0-20  $\mu\text{m}$  bin are generally equant shapes. Intersections become increasingly elongate in larger bins, reflecting the progression from prismatic to tabular shapes with size.

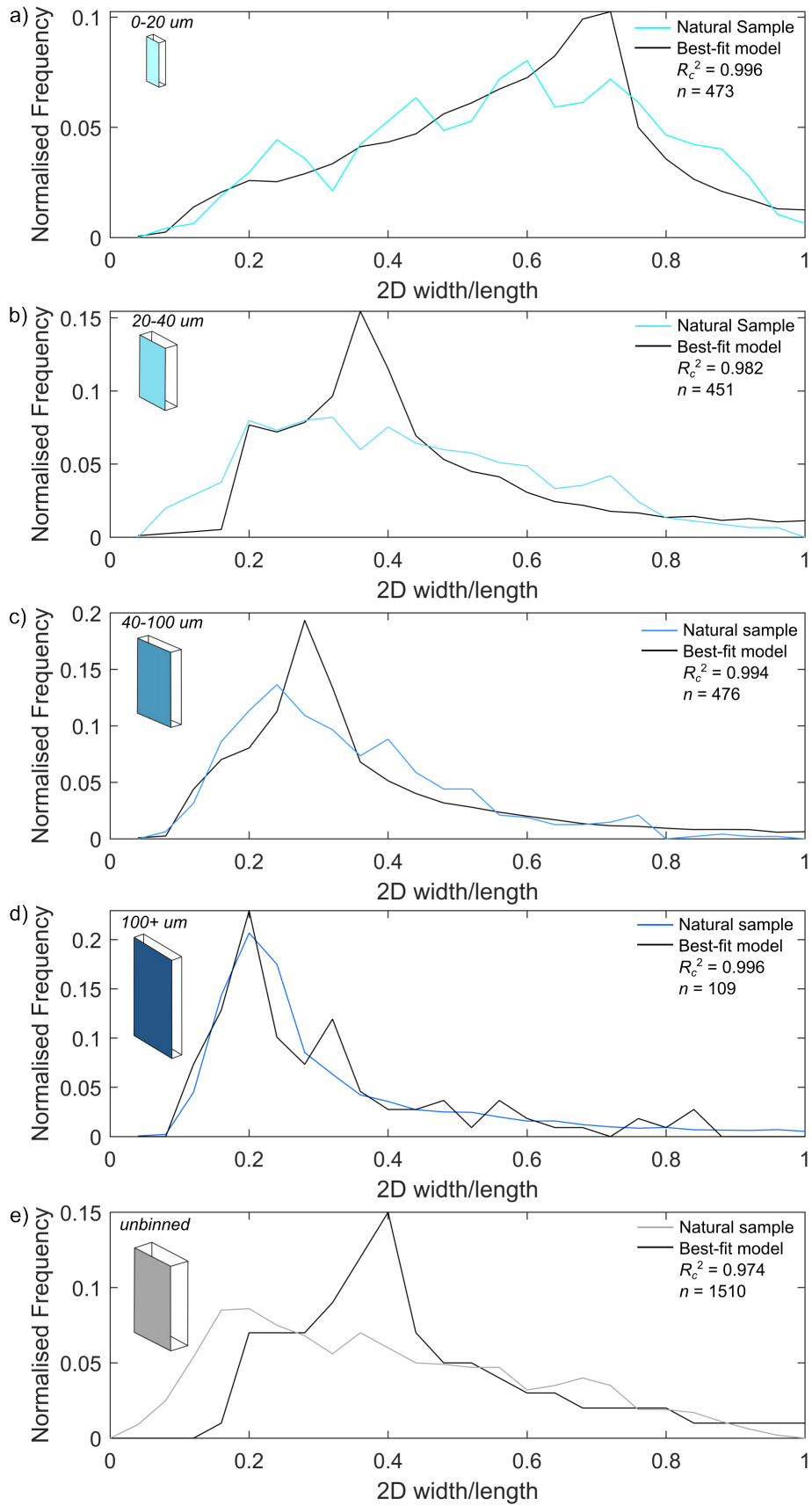
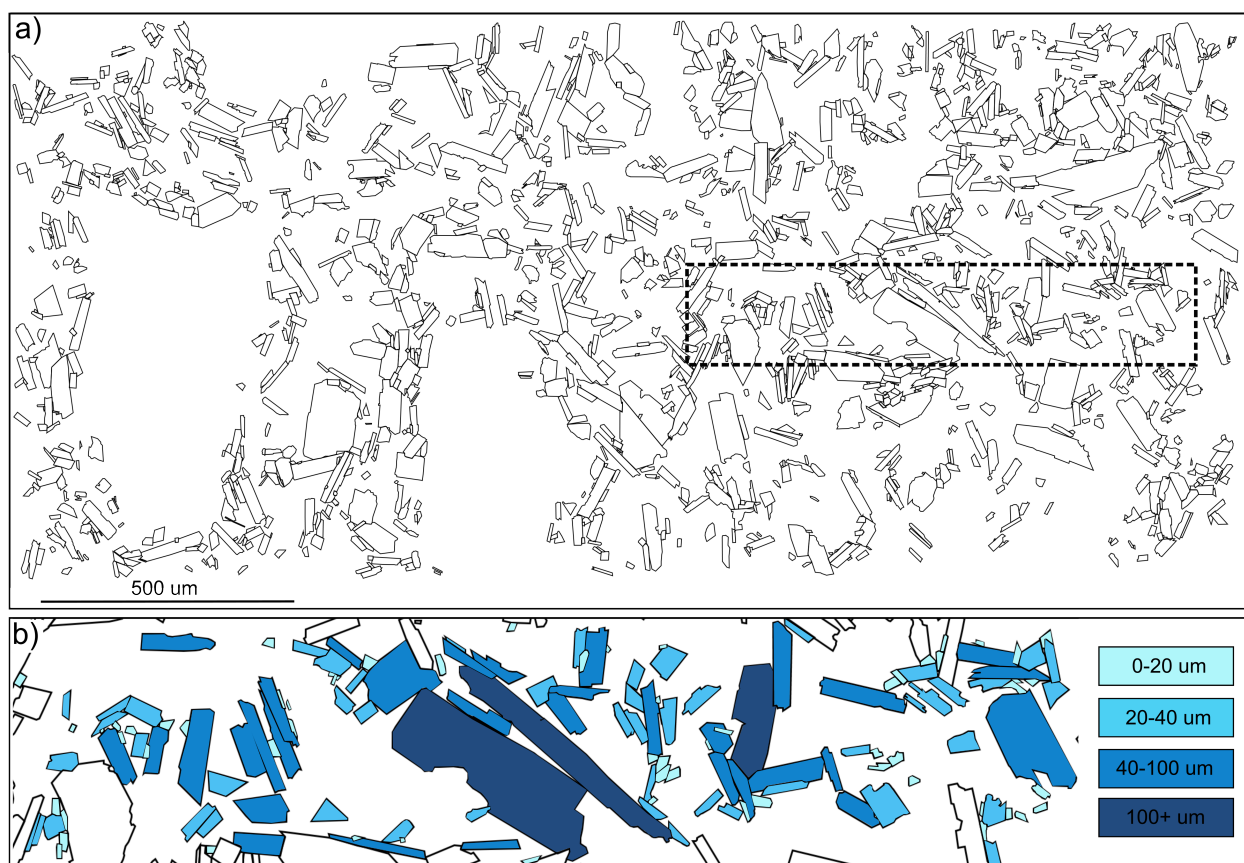


**Figure 4.4:**  $w/l$  distributions of the natural sample data in each binned fraction against the model best fit shape distribution for groundmass plagioclase intersections in MVO-1591A. **a)** 0-20  $\mu\text{m}$ . **b)** 20-40  $\mu\text{m}$ . **c)** 40-100  $\mu\text{m}$ . **d)** 100 +  $\mu\text{m}$ . **e)** Complete unbinned data.

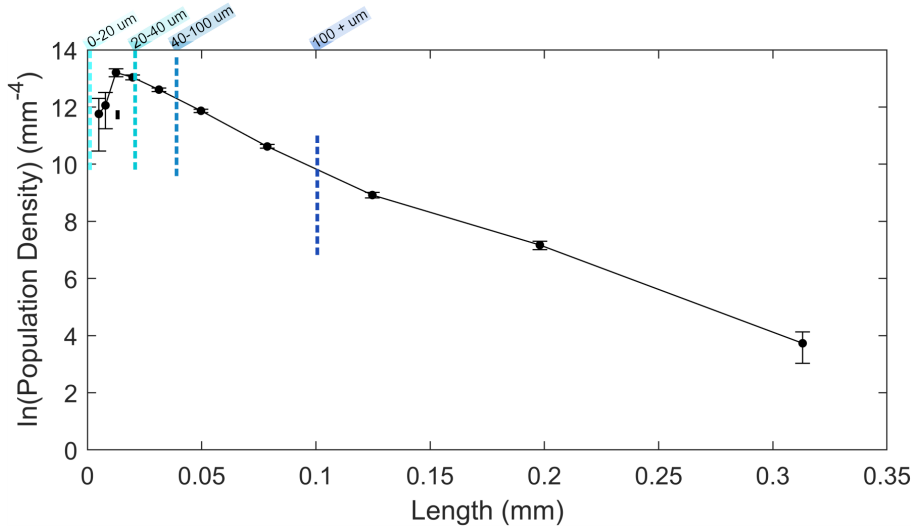
#### 4.2.2 BEL1B-A

Figure 4.5a presents the overlay of outlined plagioclase crystal intersections. Figure 4.5b illustrates the binning process, with outlines differentiated by size fractions of 0-20  $\mu\text{m}$ , 20-40  $\mu\text{m}$ , 40-100  $\mu\text{m}$  and 100 +  $\mu\text{m}$ . It is a representative area of the proportion of intersections per size fraction, with the proportions presented in Table 4.3. Like plagioclase in MVO-1591A, intersections in the smallest bin generally have equant shapes, and intersections become increasingly elongate with larger bins.

Like MVO-1591A, BEL1B-A has fine-grained groundmass, dominated by plagioclase. It is an end-member sample for groundmass crystal size, being the finest-grained and least intergrown enclave sample (Chapter 3). 28 % of the measured area is groundmass plagioclase (Table 4.1). The maximum intersection length is 241  $\mu\text{m}$ , with the minimum length being 3  $\mu\text{m}$ . The mean intersection length is  $\sim 34$   $\mu\text{m}$ . The minimum width is 1  $\mu\text{m}$ , representing the minimum resolvable width from the quality of the BSE maps. Solidity ranges from 0.6-1.0, with an average solidity value of 0.96 and a modal solidity of 1.00. This suggests that crystal intersections generally have quite even boundaries and regular shapes. This can be visually seen in the overlay (Figure 4.5).



**Figure 4.5:** Overlay of groundmass plagioclase intersection outlines in BEL1B-A. **a)** Overlay of 1528 intersection outlines. Dashed area defines **b)**. **b)** Intersection outlines colour-coded to illustrate binning process and relative proportions of intersections in each bin.

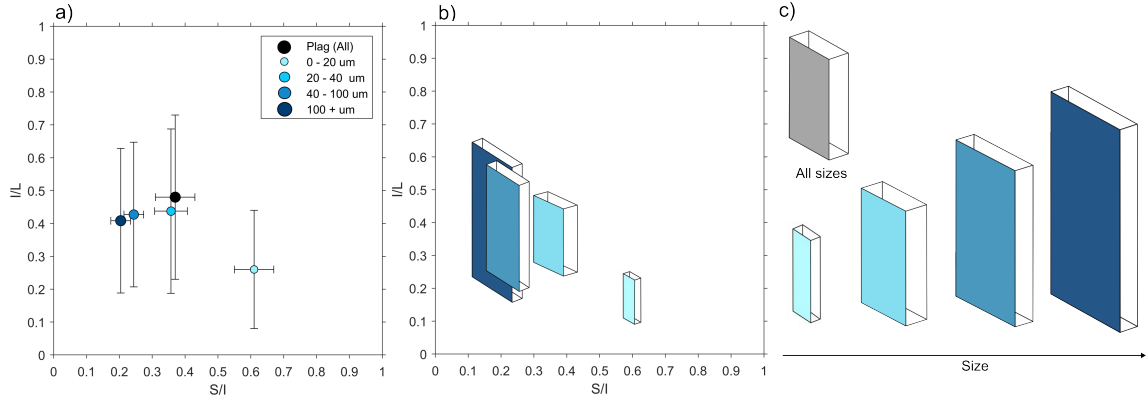


**Figure 4.6:** Crystal size distribution of groundmass plagioclase in BEL1B-A. The resulting size fractions from binning the intersection data are marked on the slope.

Figure 4.6 presents the CSD for the groundmass plagioclase. The 2D size-shape data and textural data used as inputs are detailed in Table 4.2. The CSD is a curved slope, with a slope of  $-34.8 (\pm 0.6)$  and an intercept of  $13.61 (\pm 0.05)$  (Table 4.2). The lower limit of crystal size is  $5 \mu\text{m}$ . The downturn of the slope is due to the lower abundance of resolvable crystals at the smallest sizes.

The groundmass plagioclase intersection data were binned by size fraction to investigate change in shape. Each binned fraction, as well as the complete unbinned data, were input into ShapeCalc to produce a best-fit 3D shape estimate (Table 4.3). Figure 4.7 illustrates the 3D shape estimates and the suggested change in shape with size. There is a decrease in  $S/I$  with increasing crystal size. Crystals approach more tabular shapes with increasing size. The smallest crystals ( $0\text{-}20 \mu\text{m}$ ) have a prismatic shape ( $S/I = 0.61 \pm 0.06$ ,  $I/L = 0.26 \pm 0.18$ ). Crystals in the  $20\text{-}40 \mu\text{m}$  fraction are a significantly different shape, moving towards more tabular with a decrease in  $S/I$  and increase in  $I/L$  ( $S/I = 0.36 \pm 0.05$ ,  $I/L = 0.44 \pm 0.25$ ). Crystals in the  $40\text{-}100 \mu\text{m}$  fraction again move closer to tabular shapes, with a decrease in  $S/I$  and no change in  $I/L$  ( $S/I = 0.24 \pm 0.03$ ,  $I/L = 0.43 \pm 0.22$ ). There is no significant difference in 3D shape estimate for the  $40\text{-}100 \mu\text{m}$  fraction and the  $100 + \mu\text{m}$  fraction, which has  $S/I = 0.20 \pm 0.03$ ,  $I/L = 0.41 \pm 0.22$ .

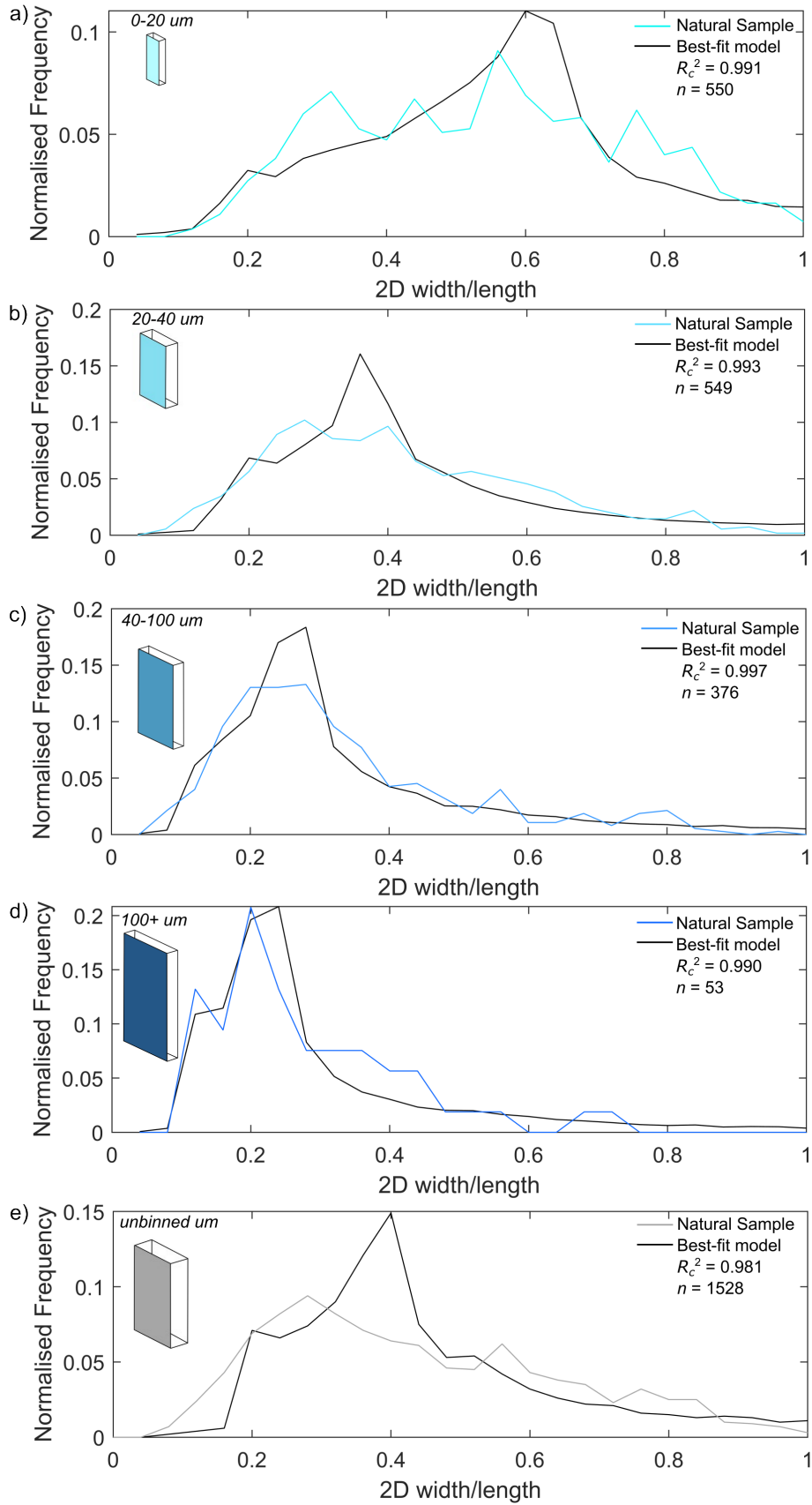
Figure 4.8 compares the  $w/l$  distributions for each binned fraction of the natural sample data against the best-fit model shape. The  $R_c^2$  values (Table 4.3) for the binned fractions are 0.991 ( $0\text{-}20 \mu\text{m}$ ), 0.993 ( $20\text{-}40 \mu\text{m}$ ), 0.997 ( $40\text{-}100 \mu\text{m}$ ) and 0.990 ( $100 + \mu\text{m}$ ). All four  $R_c^2$  values are above 0.990. This goodness-of-fit is illustrated in Figure 4.8. The  $100 + \mu\text{m}$  size fraction includes only 53 crystals, below the minimum sufficient number required for analysis (Chapter 2.2.1). However, the high  $R_c^2$  value of 0.990 (Table 4.3) for this fraction indicates that despite the low number of intersections, there is a good match between the natural sample data and the best-fit model shape in ShapeCalc. This is illustrated by Figure 4.8d, with the close match in  $w/l$  distribution between the natural sample data and the best-fit model shape.



**Figure 4.7:** 3D shape estimates for groundmass plagioclase in BEL1B-A. **a)** Zingg diagram showing the  $S/I$  and  $I/L$  estimates for each binned size fraction and the complete unbinned data. There is a decrease in  $S/I$  with increasing size, and general trend of shapes moving from prismatic to tabular. **b)** Zingg diagram with the 3D shape estimates for each binned fraction visualised. **c)** The suggested change in shape with size visualised alongside the singular shape estimate for the unbinned intersection population. Shape evolves from prismatic to tabular with size.

The best-fit 3D shape estimate for the complete, unbinned data is  $S/I = 0.37 \pm 0.06$ ,  $I/L = 0.48 \pm 0.25$ . This overlaps with the shape estimate for the 20-40  $\mu\text{m}$  bin (Figure 4.7a). The  $R_c^2$  value 3D shape estimate for the complete, unbinned data is 0.981, a lower confidence value than any of the binned size fractions. The lower goodness-of-fit between the unbinned data and the best-fit model shape is illustrated in Figure 4.8e. Whilst the  $I/L$  value for the complete unbinned data is higher than the  $I/L$  values for each binned data, the  $I/L$  values are not significantly different in terms of error. The large error in  $I/L$  occurs due to the difficulty in constraining  $L$  in stereological correction (Chapter 2.1).

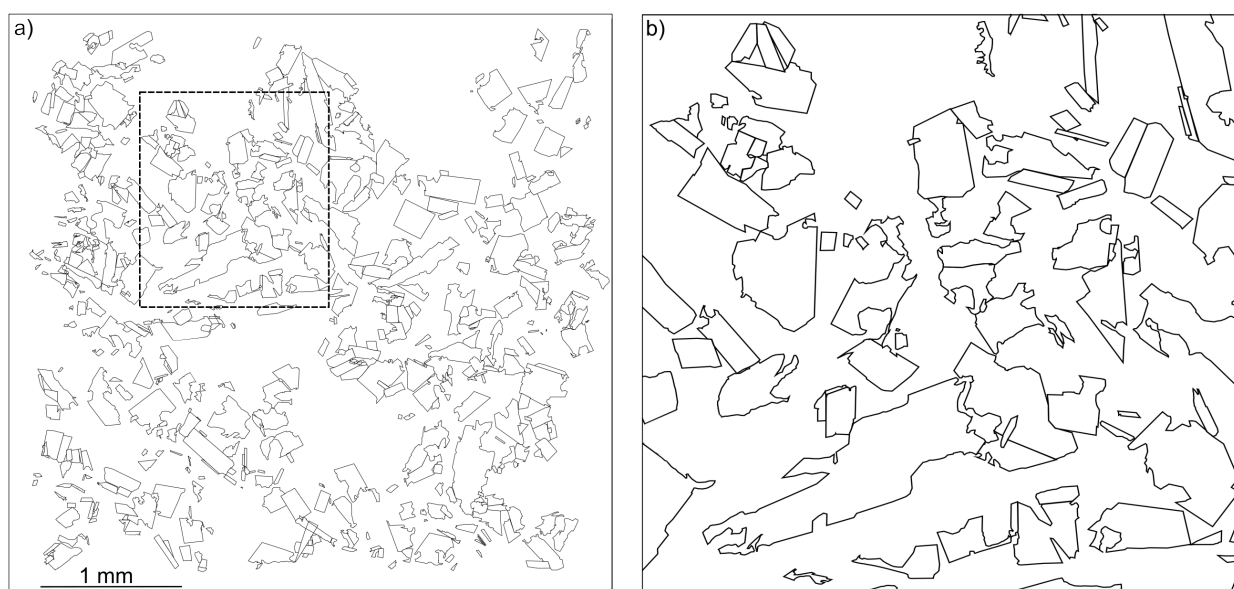
The intersection outlines (Figure 4.5) provide a qualitative confirmation of the change in shape with size fraction. The intersections in the 0-20  $\mu\text{m}$  bin are generally equant shapes. Intersections become increasingly elongate in larger bins, reflecting the progression from prismatic to tabular shapes with size.



**Figure 4.8:**  $w/l$  distributions of the natural sample data in each binned fraction against the model best-fit shape distribution for groundmass plagioclase intersections in BEL1B-A. **a)** 0-20  $\mu\text{m}$ . **b)** 20-40  $\mu\text{m}$ . **c)** 40-100  $\mu\text{m}$ . **d)** 100 +  $\mu\text{m}$ . **e)** Complete unbinned data.

### 4.2.3 TRA10A

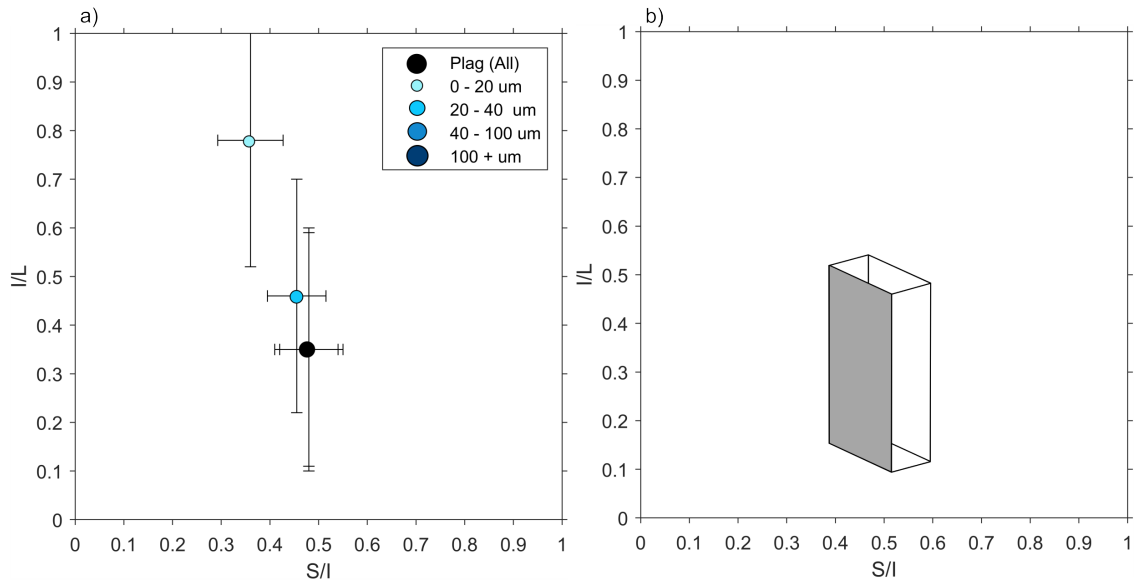
Figure 4.9 presents the overlay of outlined plagioclase crystal intersections. Whilst binning was attempted, no change in shape with size was identified. TRA10A has coarse-grained groundmass, dominated by plagioclase. It is an end-member sample for groundmass crystal size, being the coarsest-grained and most intergrown enclave sample (Chapter 3). 32 % of the measured area is groundmass plagioclase (Table 4.1). The maximum intersection length is 736  $\mu\text{m}$ , with the minimum being 8  $\mu\text{m}$ . The mean intersection length is 132  $\mu\text{m}$ . The minimum width is 3  $\mu\text{m}$ , above the minimum resolvable width from the BSE maps. Solidity ranges from 0.4-1.0, with an average solidity value of 0.88 and a modal solidity of 1.00. The wider range in solidity and lower average solidity than MVO-1591A and BEL1B-A reflects the more intergrown groundmass with complex crystal intersection shapes. This can be visually seen in the overlay (Figure 4.9).



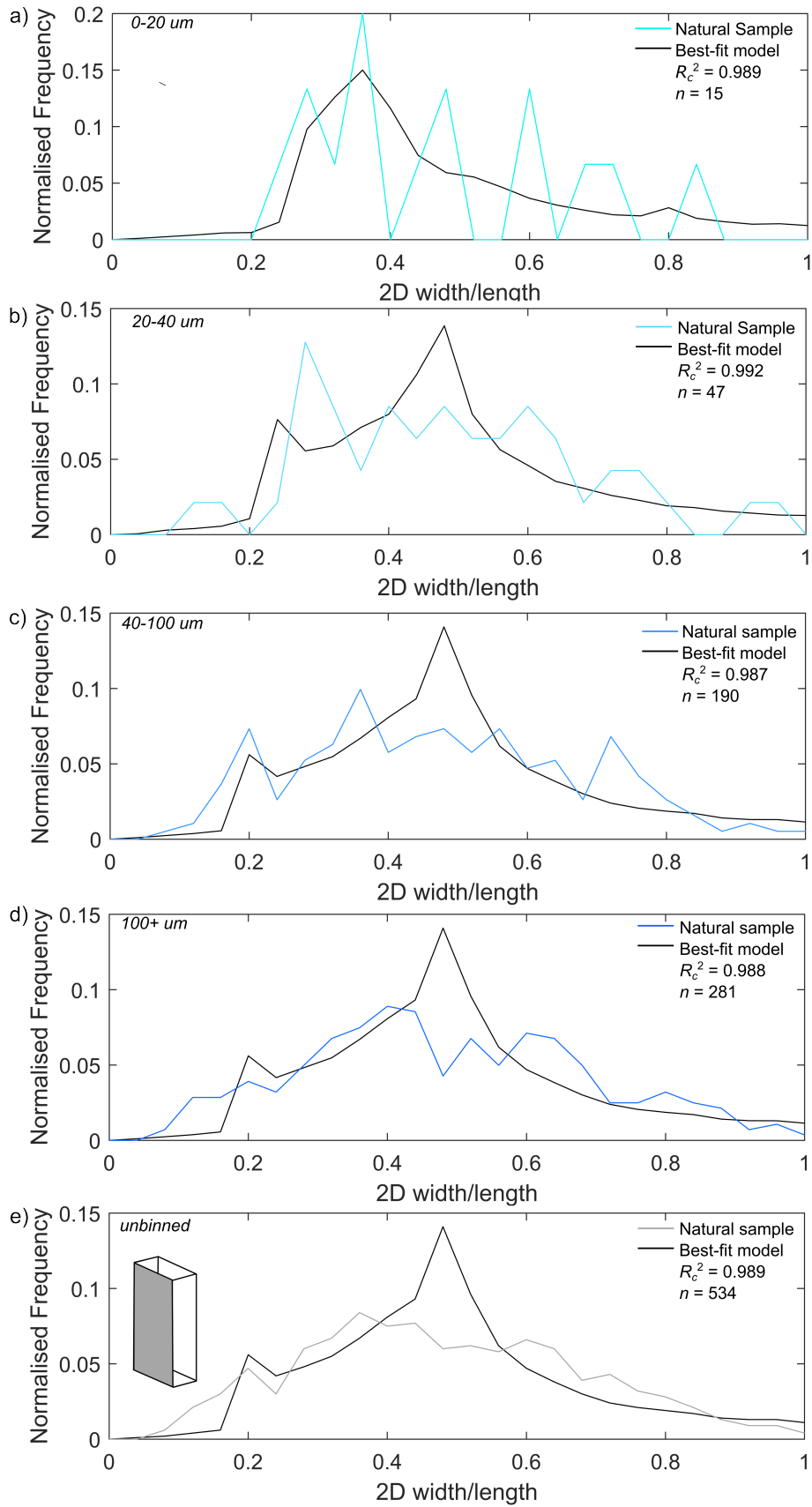
**Figure 4.9:** Overlay of groundmass plagioclase intersection outlines in TRA10A. **a)** Overlay of 534 intersection outlines. Dashed area defines **b)**. **b)** Closer view of intersection outlines. Binning was attempted, but no change in shape with size was identified.

Figure 4.10 presents the CSD for the groundmass plagioclase. The 2D size-shape data and textural data used as inputs are detailed in Table 4.2. The CSD is a curved slope, with a slope of  $-6.38 (\pm 0.21)$  and an intercept of  $7.57 (\pm 0.08)$  (Table 4.2). The lower limit of crystal size is 20  $\mu\text{m}$ .





**Figure 4.11:** 3D shape estimates for groundmass plagioclase in TRA10A. **a)** Zingg diagram showing the  $S/I$  and  $I/L$  estimates for each binned size fraction and the complete unbinned data. The 40-100  $\mu\text{m}$  fraction, the 100 +  $\mu\text{m}$  fraction and the unbinned data have the same best-fit 3D shape estimate. The 0-20  $\mu\text{m}$  and 20 - 40  $\mu\text{m}$  bins have only 15 and 47 intersections respectively. **b)** Zingg diagram with the 3D shape estimate for the complete unbinned fraction visualised.



**Figure 4.12:**  $w/l$  distributions of the natural sample data in each binned fraction against the model best fit shape distribution for plagioclase in TRA10A. **a)** 0-20  $\mu\text{m}$ . **b)** 20-40  $\mu\text{m}$ . **c)** 40-100  $\mu\text{m}$ . **d)** 100 +  $\mu\text{m}$ . **e)** Complete unbinned data.

### 4.3 Orthopyroxene

#### 4.3.1 BEL1B-A

Figure 4.13a presents the overlay of outlined orthopyroxene crystal intersections. Figure 4.13b illustrates the binning process, with outlines differentiated by size fractions of 0-35  $\mu\text{m}$  and 35 +  $\mu\text{m}$ . It is a representative area of the proportion of intersections per size fraction. The smallest intersections tend to have equant shapes, approximating octagonal or hexagonal. Intersections become increasingly elongate at larger sizes.

In BEL1B-A,  $\sim 5\%$  of the measured area is groundmass orthopyroxene (Table 4.1). The maximum intersection length is 248  $\mu\text{m}$ , with the minimum length being 4  $\mu\text{m}$ . The mean intersection length is  $\sim 28$   $\mu\text{m}$ . The minimum width is 2.6  $\mu\text{m}$ , above the minimum resolvable width from the quality of the BSE maps. Solidity ranges from 0.6-1.0, with an average solidity value of 0.94 and a modal solidity of 1.00. This suggests that crystal intersections generally have quite even boundaries, as can be visually seen in the overlay (Figure 4.13), and is expected as BEL1B-A has one of the least intergrown groundmass out of the samples.

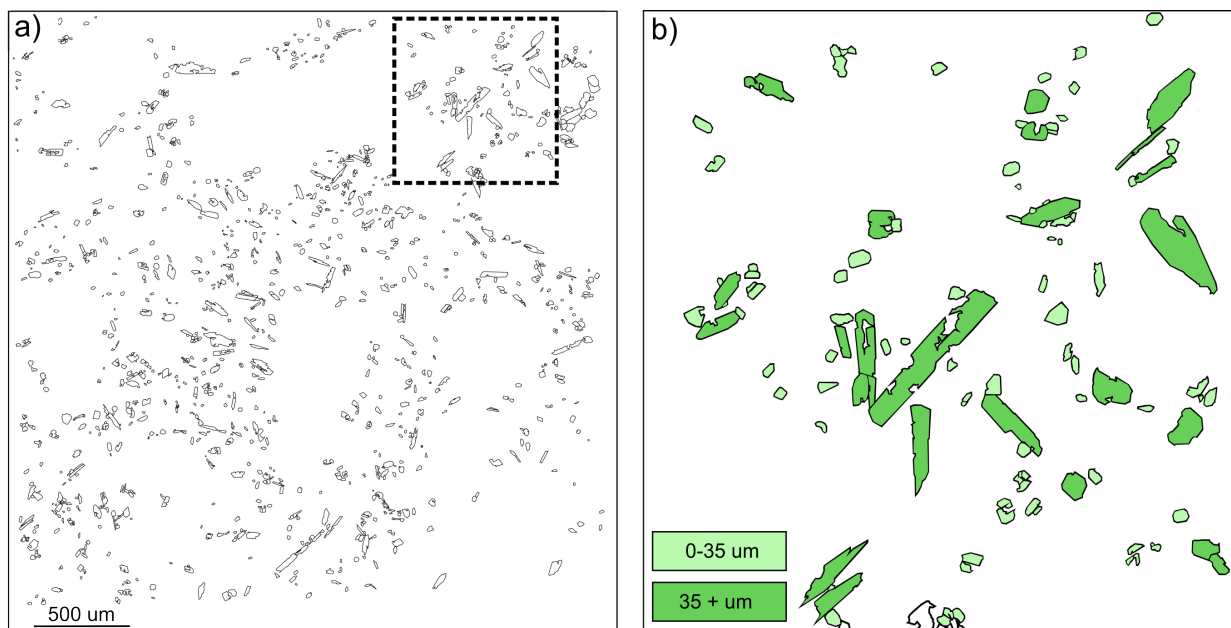


**Figure 4.13:** Overlay of groundmass orthopyroxene intersection outlines in BEL1B-A. **a)** Overlay of 1317 intersection outlines. Dashed area defines **b)**. **b)** Intersection outlines colour-coded to illustrate binning process and relative proportions of intersections in each bin.

Figure 4.14 presents the CSD for the groundmass orthopyroxene. The 2D size-shape data and textural data used as inputs are detailed in Table 4.2. The CSD is a curved slope, with a slope of  $-29.7 (\pm 0.6)$  and an intercept of  $11.77 (\pm 0.05)$ . The lower limit of crystal size is 10  $\mu\text{m}$ . The downturn of the slope is due to the lower abundance of resolvable crystals at the smallest sizes. The intersection population was binned into two size fractions, 0-35  $\mu\text{m}$  and 35 +  $\mu\text{m}$ . The bins are marked on the slope.

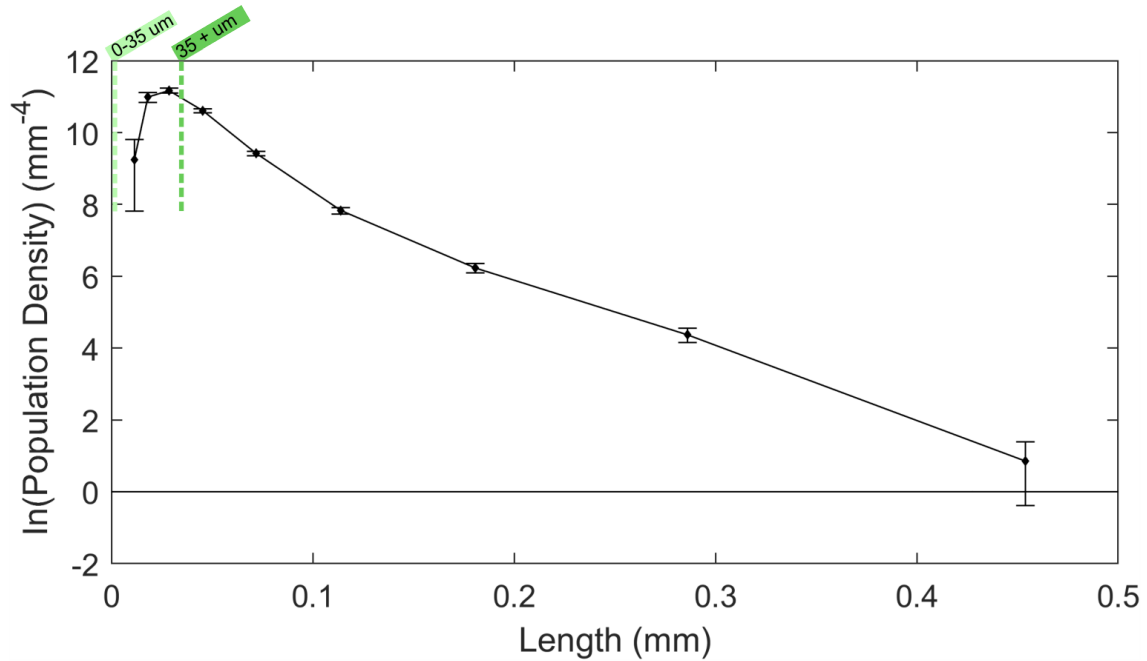
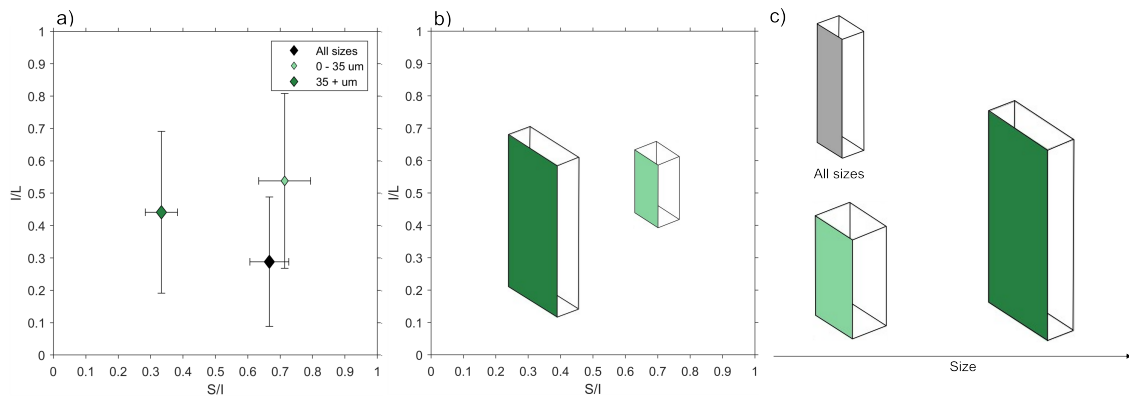


**Figure 4.14:** Crystal size distribution of groundmass orthopyroxene in BEL1B-A. The resulting size fractions from binning the intersection data are marked on the slope.

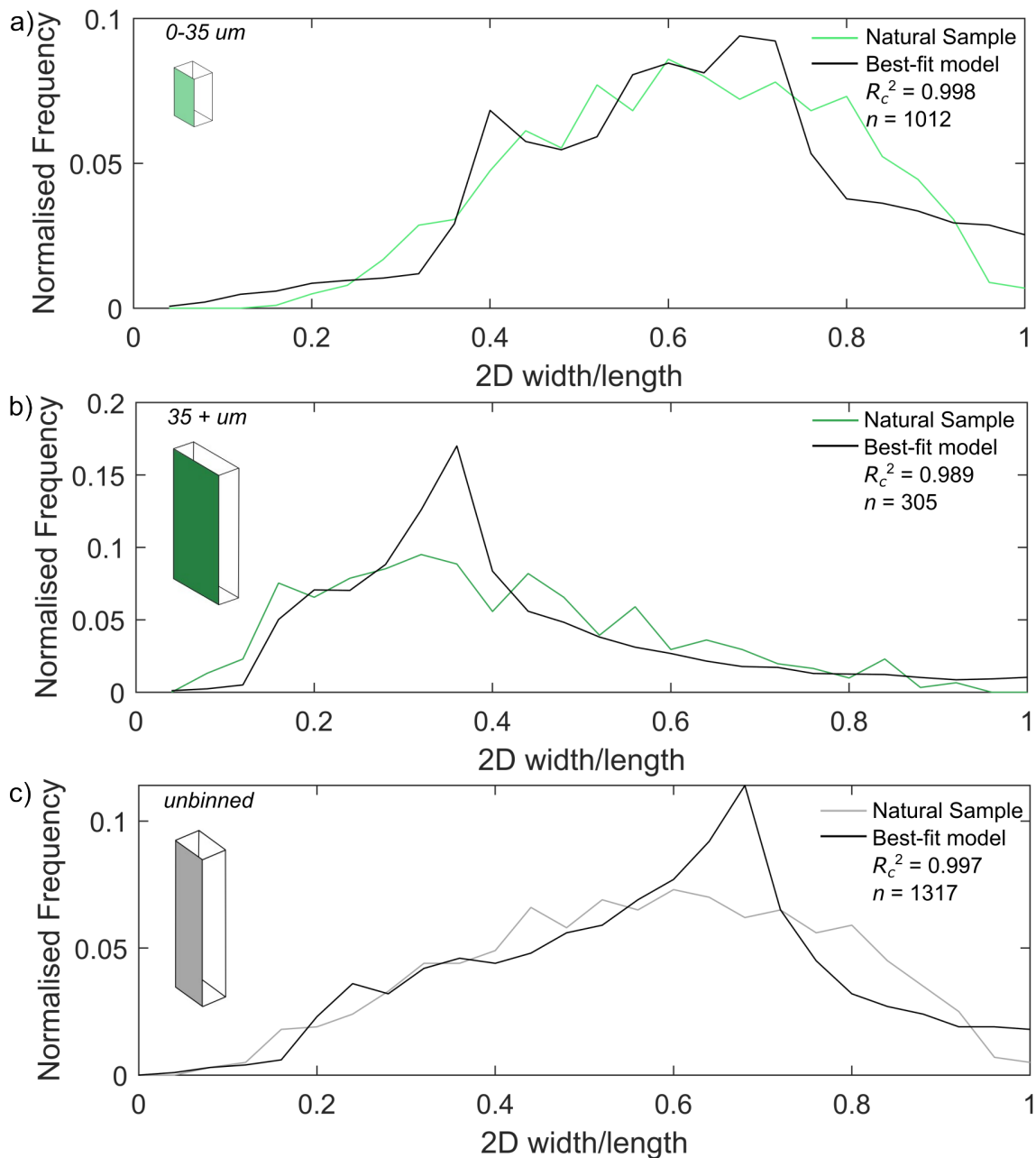
Groundmass orthopyroxene intersection data were binned by size fraction to investigate change in shape. Both binned fractions, as well as the complete unbinned data, was input into ShapeCalc to produce a best-fit 3D shape estimate (Table 4.3). Figure 4.15 illustrates the 3D shape estimates and the suggested change in shape with size.  $S/I$  decreases with increasing size. Crystals in the smallest bin (0-35  $\mu\text{m}$ ) have an equant best-fit shape ( $S/I = 0.71 \pm 0.08$ ,  $I/L = 0.54 \pm 0.27$ ). Crystals in the larger bin (35 +  $\mu\text{m}$ ) have a significantly different best-fit shape, moving towards bladed ( $S/I = 0.33 \pm 0.05$ ,  $I/L = 0.44 \pm 0.25$ ).

Figure 4.16 compares the  $w/l$  distributions for each binned fraction against the best-fit model shape. The  $R_c^2$  values (Table 4.3) for the binned fractions are 0.998 (0-35  $\mu\text{m}$ ) and 0.989 (35 +  $\mu\text{m}$ ). Both fractions contain a sufficient number of crystals for analysis using ShapeCalc: 1012 intersections for 0-35  $\mu\text{m}$ , and 305 intersections for 35 +  $\mu\text{m}$ . The goodness-of-fit is illustrated in Figure 4.16. The intersection outlines (Figure 4.13) provide a qualitative confirmation of the suggested change in shape with size fraction. The intersections in the 0-35  $\mu\text{m}$  bin are generally equant shapes, approximating octagons. Intersections tend to be more elongate in the larger 35  $\mu\text{m}$  bin, possibly reflecting the progression from equant to more bladed shapes with size.

Whilst the binning approach yields two size fractions of significantly different shapes with a good fit to model 3D shapes, the complete unbinned data also produces a strong fit to model shape data. The 3D shape estimate for the complete, unbinned data is  $S/I = 0.67 \pm 0.06$ ,  $I/L = 0.29 \pm 0.20$ . This overlaps with the shape estimate for the 0-35  $\mu\text{m}$  bin. The  $R_c^2$  value for the complete, unbinned data is 0.997, a similar (within 1 %) confidence value to the 0-35  $\mu\text{m}$  bin and a higher value (by 8 %) than the 35 +  $\mu\text{m}$  bin. The goodness-of-fit between the unbinned data and the best-fit model shape is illustrated in Figure 4.16c.



**Figure 4.15:** 3D shape estimates for groundmass orthopyroxene in BEL1B-A. **a)** Zingg diagram showing the  $S/I$  and  $I/L$  estimates for each binned size fraction and the complete unbinned data. **b)** Zingg diagram with the 3D shape estimates for each binned fraction visualised. **c)** The suggested change in shape with size visualised alongside the singular shape estimate for the unbinned intersection population. Best-fit shapes of the binned fractions move from a more equant shape towards more bladed.



**Figure 4.16:**  $w/l$  distributions of the natural sample data in each binned fraction against the model best fit shape distribution of orthopyroxene in BEL1B-A. **a)** 0-35  $\mu\text{m}$ . **b)** 35 +  $\mu\text{m}$ . **c)** Complete unbinned data.

## 4.4 Amphibole

### 4.4.1 TRA10A

Figure 4.17 presents the overlay of outlined amphibole crystal intersections. Whilst binning was attempted, no change in shape with size was identified. TRA10A is an end-member sample for groundmass crystal size, being the coarsest-grained and most intergrown enclave sample (Chapter 3). 13.5 % of the measured area is groundmass amphibole (Table 4.1). The maximum intersection length is 1298  $\mu\text{m}$ . The largest amphibole crystal measured in TRA10A

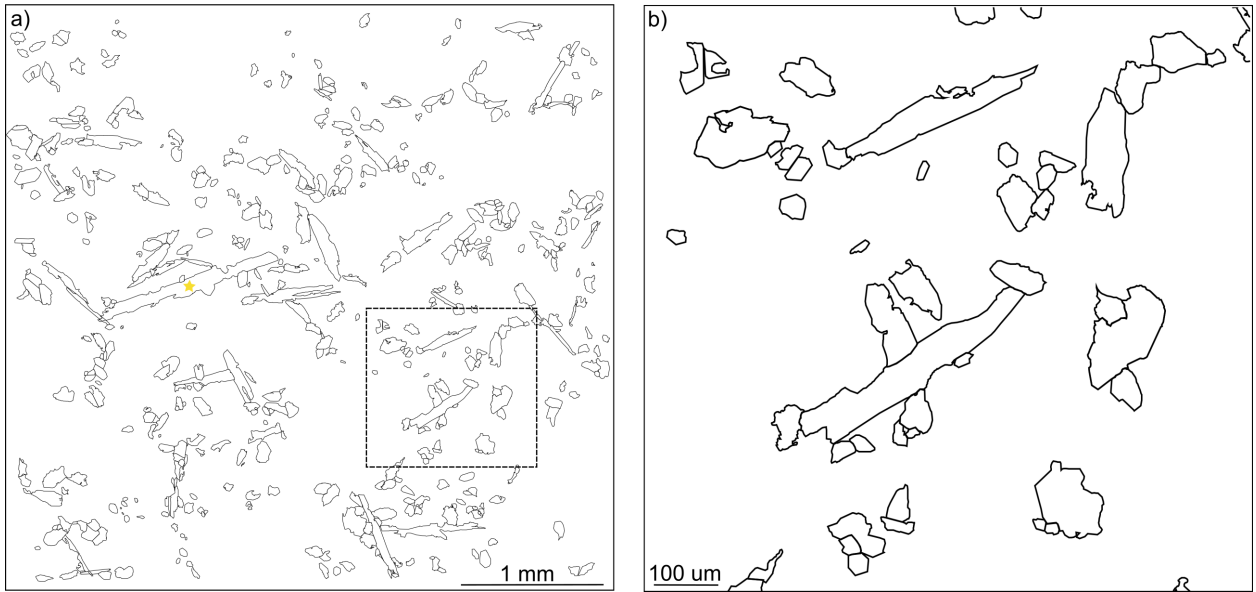
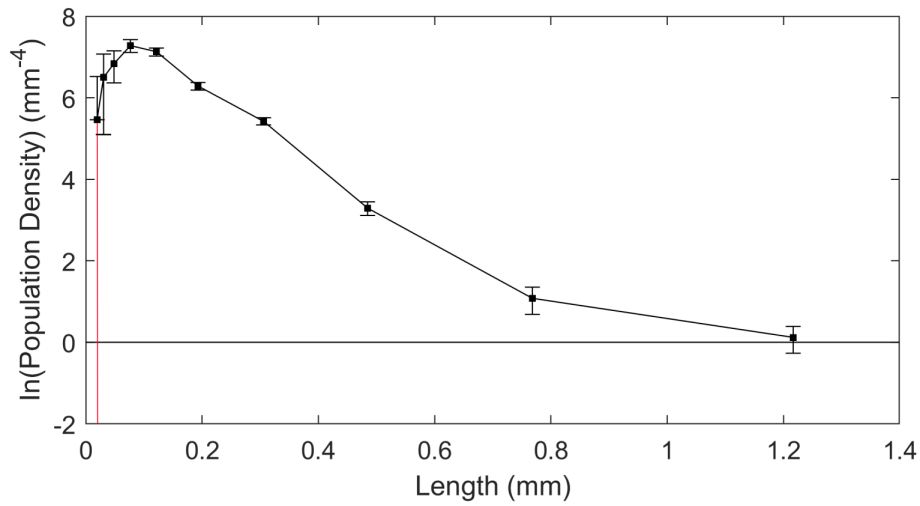


**Figure 4.17:** Overlay of groundmass amphibole intersection outlines in TRA10A. **a)** Overlay of 542 intersection outlines. Dashed area defines **b)**. Yellow star marks intersection with largest length, that was discarded from CSD creation. **b)** Close look at intersection outlines. Binning was attempted, but no change in shape with size was identified.

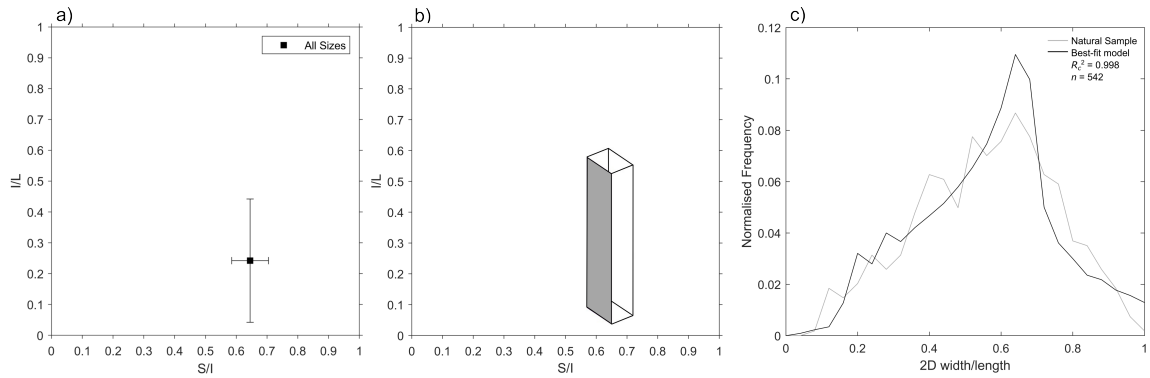
is an outlier (starred in Figure 4.17a). It is twice as large as the second largest crystal measured, which has a maximum length of 624  $\mu\text{m}$ . The minimum intersection length is 9  $\mu\text{m}$ . The mean intersection length is 98  $\mu\text{m}$ . The minimum width is 5  $\mu\text{m}$ , above the minimum resolvable width (1  $\mu\text{m}$ ). Solidity ranges from 0.4-1.0, with an average solidity value of 0.90 and a modal solidity of 1.00. The wider range in solidity and lower average solidity than the plagioclase in MVO-1591A and plagioclase and orthopyroxene in BEL1B-A reflects the more intergrown groundmass with complex crystal intersection shapes. This can be visually seen in the overlay (Figure 4.5).

Figure 4.18 presents the CSD for the groundmass amphibole. The 2D size-shape data and textural data used as inputs are detailed in Table 4.2. The CSD is a curved slope, with a slope of  $-7.58 (\pm 0.24)$  and an intercept of  $7.77 (\pm 0.08)$ . The lower limit of crystal size is 20  $\mu\text{m}$ . The downturn of the slope is due to the lower abundance of resolvable crystals at the smallest sizes.

Binning of the intersection data was attempted to investigate potential change in shape with size. No change in shape with size was identified. The best-fit 3D shape estimate for the complete unbinned data is  $S/I = 0.65 \pm 0.06$ ,  $I/L = 0.24 \pm 0.20$  (Table 4.1). Figure 4.19b illustrates the 3D shape estimate. The  $R_c^2$  value is high at 0.998. This strong goodness-of-fit is illustrated in Figure 4.19c, where the  $w/l$  distribution of the unbinned intersection data is compared to the best-fit model shape.



**Figure 4.18:** Crystal size distribution of groundmass amphibole in TRA10A. Binning was attempted, but no change in shape with size was identified. Red error bar means "infinite" error.



**Figure 4.19:** 3D shape estimate for groundmass amphibole in TRA10A. **a)** Zingg diagram showing the  $S/I$  and  $I/L$  estimate for the complete unbinned data. No change in shape with size was identified. **b)** Zingg diagram with the 3D shape estimate for the unbinned data **c)**  $w/l$  distribution of the unbinned natural sample data against the model best-fit shape distribution.

## 5 Statistical Validation

Chapter 4 presented 3D shape and size estimates for groundmass crystals in the mafic enclaves. Here, we test the 2D intersection data to assess if the 3D shape-size results are true, distinct crystal populations, or if they can be explained by sectioning effects producing statistical artefacts. Two approaches are taken, framed as questions below. The null hypothesis is that the groundmass crystals are a single shape-size population.

- CrystalSlice: can a single shape-size model population reproduce the natural crystal shape-size relationships?

Here, we use the numerical model CrystalSlice (Allgood, in prep) to model the 2D intersection  $w/l$  distributions resulting from sectioning (1) a single shape-size population and (2) multiple shape populations (Figure 5.1b). If the  $w/l$  distribution of the single shape model matches that of the groundmass crystals better than that of the multiple shapes model, this suggests that the mafic enclave crystals are a single shape population. Table 5.1 presents the CrystalSlice inputs. Single shape model distributions are produced from sectioning one model crystal population ( $P_1$ ) with one shape ( $S:I:L$ ). Multiple shape model distributions combine the  $w/l$  intersection data from sectioning multiple cuboids of distinct shape, with their  $S:I:L$  defined by the 3D shape estimate of the groundmass crystal populations for that sample.  $R_c^2$  compares the similarity between the modelled  $w/l$  distribution and the observed groundmass crystal  $w/l$  distribution.

**Table 5.1:** CrystalSlice inputs to create model 2D intersection  $w/l$  distributions.

Sample	Phase	Model	$R_c^2$	$P_n$	Fraction ( $\mu\text{m}$ )	%	$S$	$I$	$L$
MVO-1591A	Plagioclase	Single shape	0.953	$P_1$	Unbinned	100.0	1.00	2.70	5.60
		Multiple shapes	0.998	$P_1$	0-20	31.4	1.00	1.45	9.20
				$P_2$	20-40	29.9	1.00	2.80	5.60
				$P_3$	40-100	31.5	1.00	3.60	9.20
				$P_4$	100+	7.2	1.00	5.00	8.40
BEL1B-A	Plagioclase	Single shape	0.961	$P_1$	Unbinned	100.0	1.00	2.70	5.60
		Multiple shapes	0.996	$P_1$	0-20	36.0	1.00	1.70	6.40
				$P_2$	20-40	35.9	1.00	2.80	6.40
				$P_3$	40-100	24.6	1.00	4.10	9.60
				$P_4$	100+	3.5	1.00	4.90	12.00
TRA10A	Plagioclase	Single shape	0.986	$P_1$	Unbinned	100.0	1.00	2.10	6.00
		Multiple shapes	0.987	$P_1$	0-20	2.8	1.00	2.80	3.60
				$P_2$	20-40	8.8	1.00	2.20	4.80
				$P_3$	40-100	35.8	1.00	2.10	6.00
				$P_4$	100+	52.6	1.00	2.10	6.00
BEL1B-A	Orthopyroxene	Single shape	0.89	$P_1$	Unbinned	100	1.00	1.50	5.20
		Multiple shapes	0.990	$P_1$	0-35	76.8	1.00	1.40	2.60
				$P_2$	35+	23.2	1.00	3.00	6.80
TRA10A	Amphibole	Single shape	0.997	$P_1$	Unbinned	100	1.00	1.55	6.40

- Validating the smallest crystal population: can sectioning a single shape-size population reproduce the smallest crystal population observed in the groundmass crystals?

Sectioning a single shape-size population of large crystals will produce ‘corner-cuts’, which are small intersections through the crystal edge. It is therefore important to test whether the

smallest shape population in the groundmass crystals can be explained by simply being corner-cuts of a larger crystal population, i.e., the cut-section effect (Chapter 1.1.2). To address this, we use the same modelled 2D intersections from the previous approach/question and scale these modelled 2D intersection data to a size representative of the groundmass crystal population observed for each sample (scaling method described in Chapter 2.5.2). We then compare the proportion and shapes of intersections that fit in the smallest size bin between the model and groundmass crystals to ascertain if the smallest population in each mafic enclave is likely to be corner-cuts, or a distinct shape-size population (Figure 5.1c). Table 5.2 presents the scaling inputs and results for testing each sample. ‘Proportion’ shows what percentage of the scaled model intersections falls within the size fraction. ‘Corner-cuts’ shows what percentage of the scaled model intersections that are 0-20  $\mu\text{m}$  in length are triangular, and are interpreted as corner-cuts of the model cuboid.

**Table 5.2:** Validating the smallest population: details of the model cuboid shape and how the model intersection data was scaled.

Sample	Phase	<i>S</i>	<i>I</i>	<i>L</i>	Scaling approach	Scaling ( $\mu\text{m}$ )	Proportion %	Corner-cuts (%)
MVO-1591A	Plagioclase	1.00	2.70	5.60	Representative maximum	145	7.3	100
MVO-1591A	Plagioclase	1.00	2.70	5.60	Threshold value	50.0	31.3	48.2
BEL1B-A	Plagioclase	1.00	2.70	5.60	Representative maximum	70.0	21.3	59.6
BEL1B-A	Plagioclase	1.00	2.70	5.60	Threshold value	45.9	36.0	42.4
BEL1B-A	Orthopyroxene	1.00	1.50	5.20	Representative maximum	60.0	86.8	17.8
BEL1B-A	Orthopyroxene	1.00	1.50	5.20	Threshold value	81	76.8	19.5

Below, we address these two questions systematically in turn for each phase in a sample that displayed a change in shape with size: the plagioclase in MVO-1591A and BEL1B-A, and the orthopyroxene in BEL1B-A. We address the first question for the phases that did not display a change in shape with size: plagioclase and amphibole in TRA10A.

Key terms used throughout are defined here for clarity. The *observed/natural sample* refers to the measured crystals in the mafic enclaves. A comparison of observed versus modelled data is therefore a comparison of measurements from real groundmass crystals in the mafic enclaves with model data. The *smallest crystal population* refers to the shape population generated by the smallest size intersections in Chapter 4. For plagioclase in MVO-1591A and BEL1B-A, the smallest crystal population is prismatic and generated by the 0-20  $\mu\text{m}$  intersections. For orthopyroxene in BEL1B-A, the smallest crystal population is equant and is generated by the 0-35  $\mu\text{m}$  intersections. Reference to the 0-20  $\mu\text{m}$  fraction and 0-35  $\mu\text{m}$  fraction therefore describes the *w/l* measurements of the intersections of this size in the natural groundmass crystals. The *modelled intersection data* is the *w/l* measurements and shapes of 2D intersections generated from sectioning a model cuboid in CrystalSlice. *Scaled model intersection data* are the widths and lengths of the model intersections when scaled to a certain  $\mu\text{m}$  value so that they can be compared to the natural intersection data.

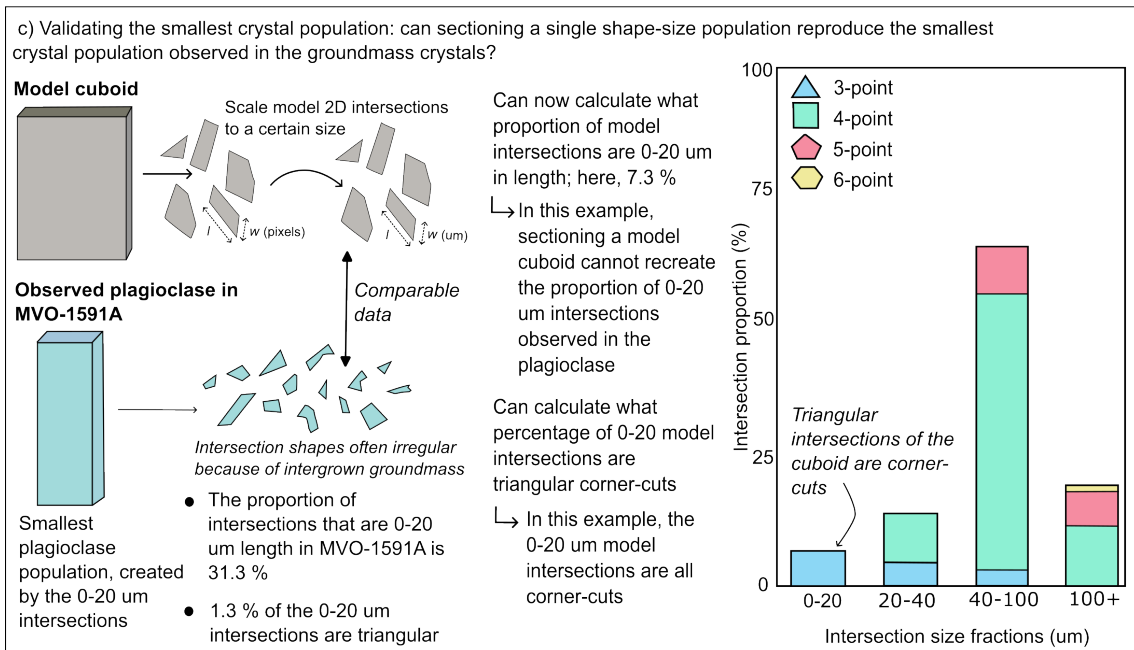
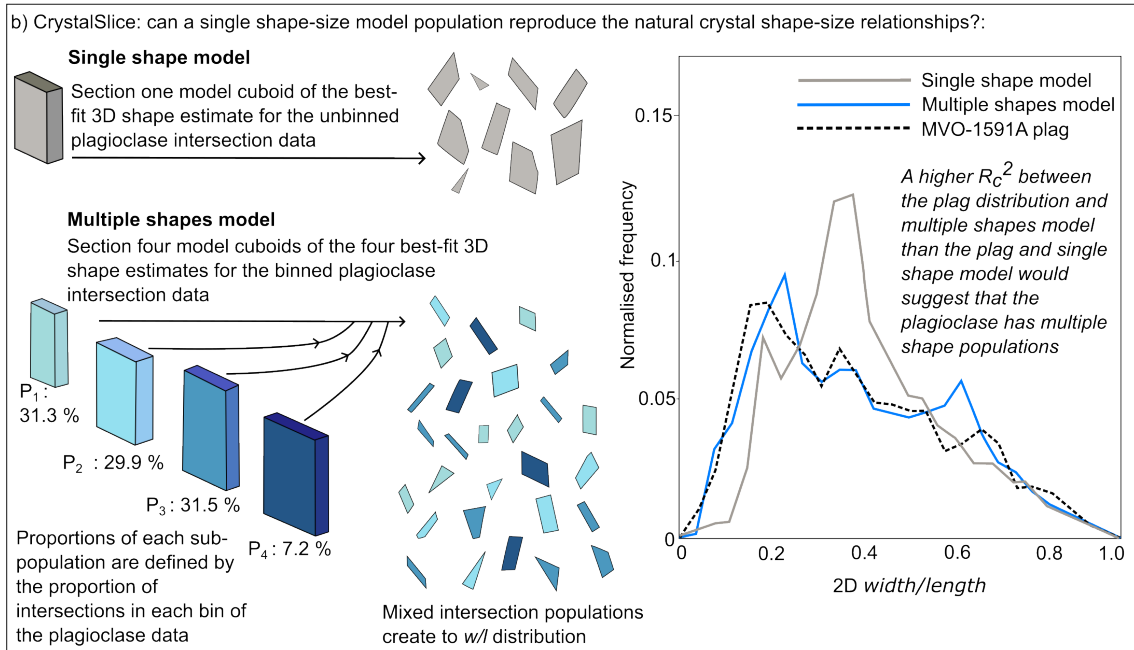
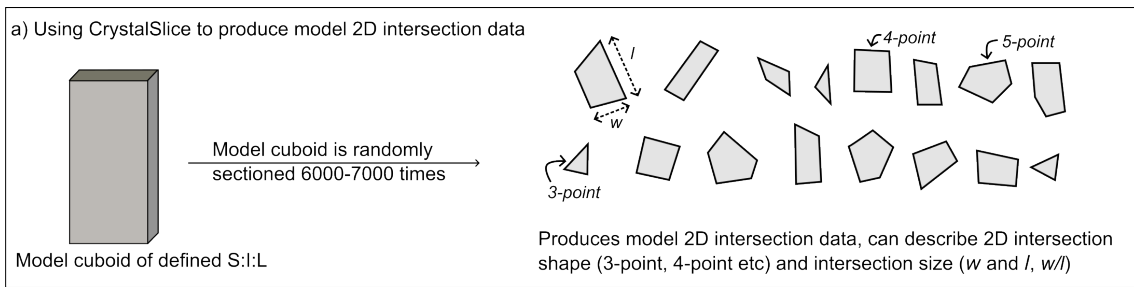


**Figure 5.1:** a) CrystalSlice is used to section a cuboid to generate model 2D intersection data for a known 3D shape. b) CrystalSlice is used to test if a single shape-size model population can reproduce the natural crystal shape-size relationships. c) Model intersection data is compared to the natural sample data to test if the smallest size fraction of natural crystals can be explained as corner-cuts of large, single shape-size crystal population.

## 5.1 Plagioclase: MVO-1591A

Groundmass plagioclase in MVO-1591A showed change in shape with size (Section 4.2.1). 2D intersection data were binned into four size fractions of 0-20  $\mu\text{m}$ , 20-40  $\mu\text{m}$ , 40-100  $\mu\text{m}$  and 100 +  $\mu\text{m}$ . 3D shape estimates suggest evolution from prismatic to tabular ( $S/I$  decreases) with increasing size (Figure 4.3). In this section, comparisons of natural and model  $w/l$  distributions, and comparisons of natural and model 2D intersection data are used to explore the validity of the shape-size result.

### 5.1.1 CrystalSlice: for plagioclase in MVO-1591A

CrystalSlice (Allgood, in preparation) was used to generate model  $w/l$  distributions of random 2D intersections through a population of crystals with a single size and single shape (the ‘single shape, single size’ population, Figure 5.2b) and a combined population of crystals that are binned into four size fractions, each with a distinct shape (the ‘multiple shapes’ population, Figure 5.2a) defined by the 3D shape estimates of each size fraction in the groundmass plagioclase (Table 5.1). This is illustrated in Figure 5.1a and b.

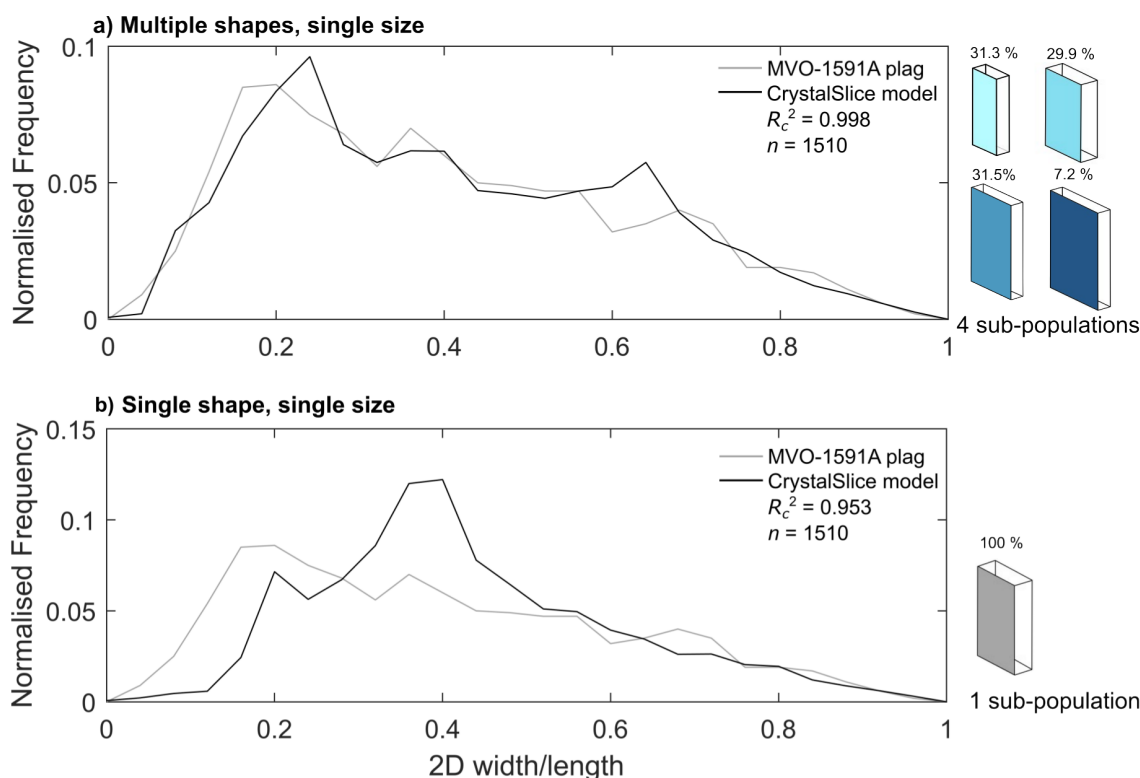


**Figure 5.2:** Comparison of the unbinned plagioclase  $w/l$  distribution in MVO-1591A against the  $w/l$  distribution of: **a)** a model  $w/l$  distribution of four shape sub-populations, defined by the 3D shape estimates of each size plagioclase size fraction; **b)** a model  $w/l$  distribution for a single shape population.

The  $w/l$  distribution of the multiple shape population closely matches the  $w/l$  distribution of the plagioclase, with  $R_c^2 = 0.998$  and a good visual fit between the peaks, both at  $\sim 0.2$  (Figure 5.2a). The  $w/l$  distribution of the single shape population is a poorer match to that of the

plagioclase, with an  $R_c^2 = 0.953$ , 4.5 % lower than the multiple shapes estimate. Mangler et al. (2022) established that an  $R_c^2 < 0.975$  was a poor fit (Chapter 2.1). There is a poorer visual fit with the peak of the model curve sitting at higher  $w/l$  value of  $\sim 0.4$  than the plagioclase peak at  $\sim 0.2$ . (Figure 5.2b). This suggests that the groundmass plagioclase does contain multiple shape populations, validating the 3D shape-size result. Of note is that the  $R_c^2$  for the best-fit 3D shape estimate of the unbinned plagioclase intersections in ShapeCalc was 0.974. The lower goodness-of-fit (0.953) for the single shape model population in CrystalSlice is likely due to a lower number of successful intersections in this program (5500-7500 successful intersections in CrystalSlice; 20,000 intersections in ShapeCalc).

### 5.1.2 Validating the smallest plagioclase population for MVO-1591A

The 0-20  $\mu\text{m}$  intersections were interpreted as the smallest, most prismatic plagioclase population (Chapter 4.2.1). However, it is possible that this small population could be corner-cuts of larger crystals, not a true plagioclase population. Therefore, using CrystalSlice, model 2D intersection data were generated to assess whether sectioning a single shape-size population of crystals could reproduce the 0-20  $\mu\text{m}$  plagioclase intersection proportions and shapes.

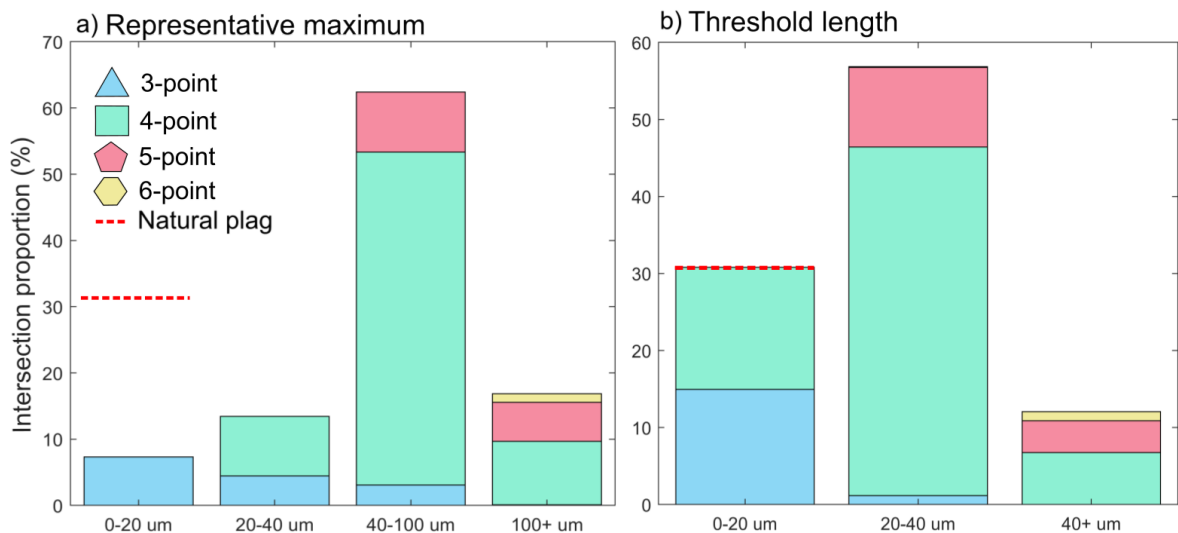


**Figure 5.3:** **a)** Sectioning a model cuboid of 1:2.7:5.6, scaled to a representative maximum length of 145  $\mu\text{m}$  cannot reproduce the proportion or shapes of the 0-20  $\mu\text{m}$  plagioclase population observed in MVO-1591A. **b)** The threshold scaling length to reproduce the proportion of plagioclase intersections is  $\sim 50 \mu\text{m}$ , but cannot reproduce intersection shapes. See text for explanation.

A model cuboid of 1:2.7:5.6 (which is the estimated 3D shape for the unbinned plagioclase, 4.2.1) was sectioned to generate 2D intersection  $w/l$  data (Figure 5.3). These measurements were scaled to a representative maximum 2D intersection length measured in the plagioclase, 145  $\mu\text{m}$ , estimated from the 2D length distribution (Chapter 2.5.2; Figure 5.3). This was done to make the model 2D intersection data comparable to the natural plagioclase intersection data. Only 7.3 % of the model intersections are 0-20  $\mu\text{m}$ , far less than the 31.4 % (red dashes) constituted by the 0-20  $\mu\text{m}$  fraction in the plagioclase (Table 5.2; Figure 5.3a). Furthermore, 100

% of the model smallest intersections are triangles, indicating that they are all corner-cuts of the model cuboid. In contrast, only 6 (1.3 %) of the smallest plagioclase intersections are triangles, clear corner-cuts. Sectioning a single model population of crystals with the same shape and size therefore cannot reproduce the proportion or shapes of the 0-20  $\mu\text{m}$  plagioclase fraction, indicating that the smallest, most prismatic population in MVO-1591A is a true distinct shape population (Figure 5.3).

The threshold length to which scaling the 2D model intersection data will reproduce the observed proportion (31.4 %) of 0-20  $\mu\text{m}$  intersections was found to be  $\sim 50 \mu\text{m}$  (Table 5.2; Figure 5.3b). In this case, 48.2 % of model 0-20  $\mu\text{m}$  intersections are triangular corner-cuts of the model cuboid, much greater than the 1.3 % of plagioclase intersections which are observed to be triangular in MVO-1591A. Moreover, the model intersection widths and lengths produce a 3D shape estimate of  $S/I = 0.63 \pm 0.07$ ,  $I/L = 0.70 \pm 0.28$  using ShapeCalc ( $R_c^2 = 0.998$ ). This is significantly different in terms of  $I/L$  to the best-fit 3D shape estimate for the plagioclase 0-20  $\mu\text{m}$  fraction,  $S/I = 0.69 \pm 0.06$  and  $I/L = 0.16 \pm 0.18$  (Table 4.3). Therefore, whilst sectioning this single shape-size model population can reproduce the proportion of 0-20  $\mu\text{m}$  plagioclase intersections, it cannot reproduce the proportion of corner-cuts or the 3D shape estimate for the 0-20  $\mu\text{m}$  intersections. This suggests that the smallest, most prismatic plagioclase crystals in MVO-1591A represent a true, distinct population, rather than a statistical artefact.

## 5.2 Plagioclase: BEL1B-A

Like MVO-1519A, the 2D intersection measurements of groundmass plagioclase in BEL1B-A were binned into four size fractions of 0-20  $\mu\text{m}$ , 20-40  $\mu\text{m}$ , 40-100  $\mu\text{m}$  and 100 +  $\mu\text{m}$ , suggesting that plagioclase evolves from prismatic to tabular with increasing size ( $S/I$  decreases,  $I/L$  increases) (Chapter 4.2.2). Again, we compare natural and model  $w/l$  distributions, and compare natural and model 2D intersection data to explore the validity of this shape-size result.

### 5.2.1 CrystalSlice: plagioclase in BEL1B-A

CrystalSlice (Allgood, in preparation) was used in the same way as MVO-1519A, to generate model  $w/l$  distributions of random 2D intersections through a population of crystals with a single size and single shape (the ‘single shape, single size’ population, Figure 5.4b) and a combined population of crystals that are binned into four size fractions, each with a distinct shape (the ‘multiple shapes’ population, Figure 5.4a) defined by the 3D shape estimates of each size fraction in the groundmass plagioclase (Table 5.1).

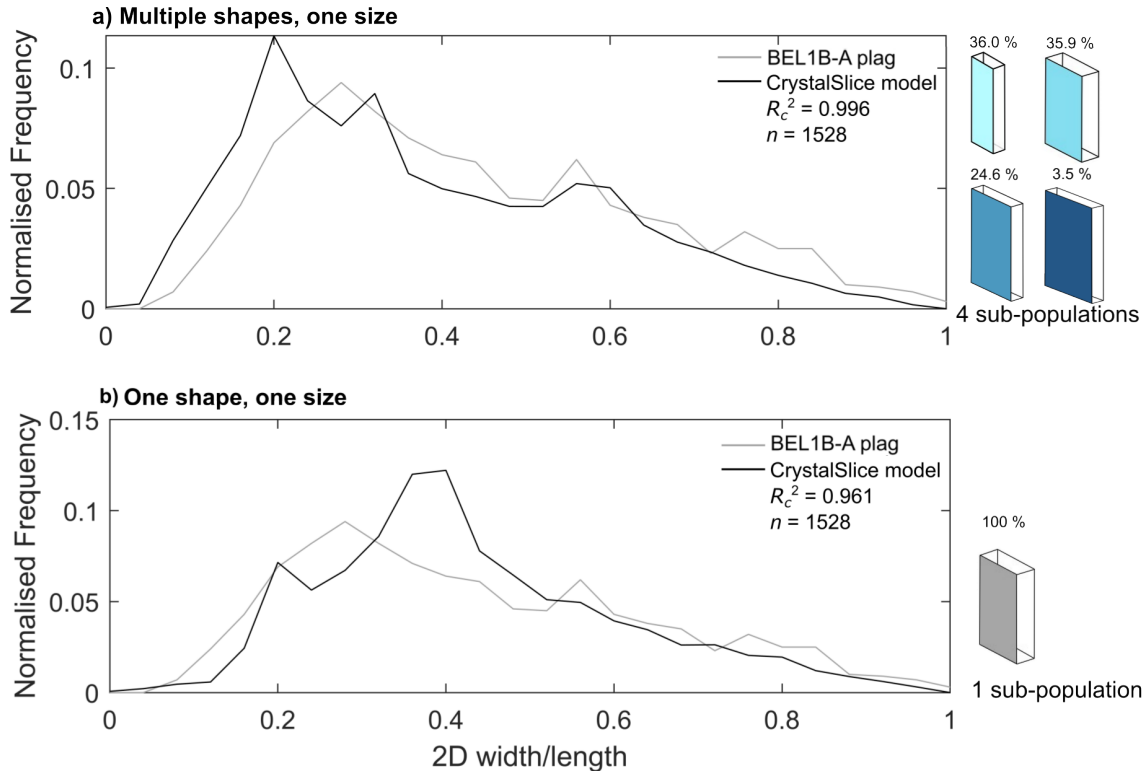


**Figure 5.4:** Comparison of the unbinned plagioclase  $w/l$  distribution in BEL1B-A against the  $w/l$  distribution of: **a)** a model  $w/l$  distribution of four shape sub-populations, defined by the 3D shape estimates of each size plagioclase size fraction; **b)** a model  $w/l$  distribution for a single shape population.

For BEL1B-A, the  $w/l$  distribution of the multiple shape population closely matches the  $w/l$  distribution of the plagioclase, with  $R_c^2 = 0.996$  and a good visual match between the distribution peaks ( $w/l \approx 0.2-0.25$ ) (Figure 5.4a). The  $w/l$  distribution of the modelled single shape population is again a poorer match to that of the plagioclase, with an  $R_c^2 = 0.961$ , which is 3.7 % lower than the multiple shape estimate. This is also below 0.975, where an  $R_c^2 < 0.975$  was established by Mangler et al. (2022) to mean a poor fit. There is a poorer visual fit between the distribution peaks (Figure 5.4b). The stronger goodness-of-fit between the  $w/l$  distributions of the multiple shape model and the observed plagioclase indicates that BEL1B-A does contain multiple distinct shape populations of plagioclase, validating the 3D shape-size result.

### 5.2.2 Validating the smallest plagioclase population for BEL1B-A

The 0-20  $\mu\text{m}$  plagioclase intersections were interpreted as the smallest, most prismatic population (Chapter 4.2.2). However, it is possible that these intersections could be corner-cuts of a larger crystal. CrystalSlice was therefore used to generate model 2D intersection data for a model cuboid to assess whether sectioning a modelled single shape-size population of crystals could reproduce the 0-20  $\mu\text{m}$  plagioclase intersection proportions and shapes in BEL1B-A.

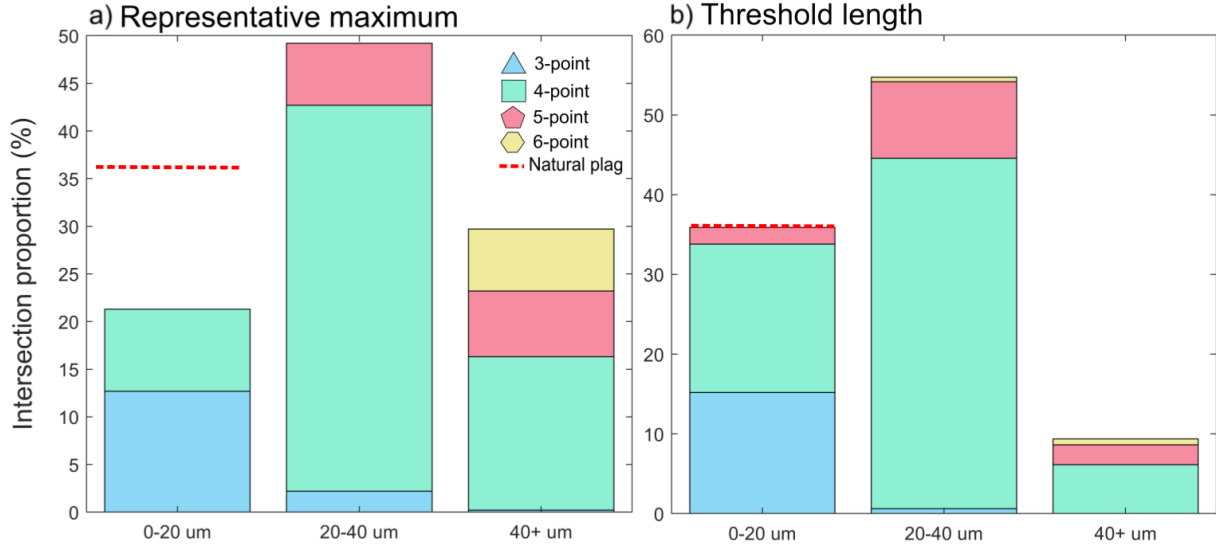


**Figure 5.5:** a) Sectioning a model cuboid of 1:2.7:5.6, scaled to a representative maximum length of 70  $\mu\text{m}$  cannot reproduce the proportion or shapes of 0-20  $\mu\text{m}$  plagioclase intersections. b) The threshold scaling length to reproduce the proportion of plagioclase intersections is  $\sim 45.9$   $\mu\text{m}$ , but cannot reproduce intersection shapes. See text for explanation.

A model cuboid of 1:2.7:5.6 (which is the estimated 3D shape for the unbinned plagioclase, Chapter 4.2.2) was sectioned to generate model 2D intersection measurements (Figure 5.5). These model intersections were scaled to a representative maximum 2D length measured in the plagioclase, 70  $\mu\text{m}$  (after Chapter 2.5.2). 21.3 % of the model intersections are 0-20  $\mu\text{m}$  in length, which is  $\sim 41$  % less than the 36.0 % constituted by the 0-20  $\mu\text{m}$  fraction in the plagioclase (Table 5.2; Figure 5.5a). 59.6 % of the 0-20  $\mu\text{m}$  model intersections are triangular corner-cuts, compared to only 6 (1.1 %) of the 0-20  $\mu\text{m}$  intersections of plagioclase being clear corner-cuts. Sectioning this model single shape-size population therefore cannot reproduce the observed proportion or shapes of the 0-20  $\mu\text{m}$  plagioclase fraction, indicating that the smallest, most prismatic population in BEL1B-A is a true distinct shape population.

The threshold length at which scaling the model 2D intersection data will reproduce the observed proportion (36.0 %) of 0-20  $\mu\text{m}$  intersections in the groundmass of BEL1B-A was found to be  $\sim 45.9$   $\mu\text{m}$  (Table 5.2; Figure 5.5b). In this case, 42.4 % of the model 0-20  $\mu\text{m}$  intersections are triangular corner-cuts of the model cuboid, much greater than the 1.1 % of 0-20  $\mu\text{m}$  plagioclase intersections that are observed to be triangular in BEL1B-A. Again, the 0-20  $\mu\text{m}$  model intersection measurements generate a best-fit 3D shape estimate is  $S/I = 0.63 \pm 0.06$  and  $I/L = 0.44 \pm 0.25$ , with an  $R_c^2 = 0.999$  using ShapeCalc. This is not significantly different than the best-fit 3D shape estimate for the observed plagioclase 0-20  $\mu\text{m}$  fraction,  $S/I = 0.61 \pm 0.06$  and  $I/L = 0.26 \pm 0.18$  (Table 4.3). Sectioning this single shape-size population can therefore reproduce the proportion of 0-20  $\mu\text{m}$  intersections, and can reproduce the prismatic 3D shape estimate. However, the proportion of model intersections that are corner-cuts is much greater than what is observed in the plagioclase intersections, so sectioning this single shape-size population cannot fully reproduce the smallest plagioclase population. This suggests that the smallest, most prismatic plagioclase in BEL1B-A are a true distinct population, not a statistical

artefact.

### 5.3 Plagioclase: TRA10A

Groundmass plagioclase in TRA10A was not found to exhibit change in shape with size, being a single shape population (Section 4.2.3). A comparison of the plagioclase  $w/l$  distribution and model  $w/l$  distributions is used to explore the validity of this result.

#### 5.3.1 CrystalSlice: plagioclase in TRA10A

CrystalSlice was used to generate a model single shape-size population representative of the TRA10A plagioclase shape estimate, 1:2.1:6 (Table 2.5.1). The  $w/l$  distribution of the plagioclase is a good match to that of the single shape model, with an  $R_c^2 = 0.986$  (Figure 5.6a).

A multiple shapes model was generated (Table 2.5.1), where the four sub-populations were defined by the respective best-fit 3D shape estimates and 2D intersection proportions of the binned fractions in TRA10A (Table 2.5.1, after Chapter 4.2.3). The 0-20  $\mu\text{m}$  and 20-40  $\mu\text{m}$  fractions do not have sufficient intersections for reliable analysis with ShapeCalc (15 and 47 intersections respectively, Table 4.3) and have poor sample-model fits, as can be seen visually in Figure 4.12.

The  $w/l$  distribution of the multiple shape model is a good fit to the observed plagioclase  $w/l$  distribution in TRA10A, with an  $R_c^2 = 0.987$  (Figure 5.6b). This sample-model fit is just as good of a sample-model fit as between the observed plagioclase and the modelled single shape population, with the  $R_c^2$  of both sample-model fits being within 0.1 % of each other. Likewise, there is visually little difference between the  $w/l$  distributions of the single shape model (Figure 5.6a) and the multiple shapes model (Figure 5.6b). Only 2.8 % of cuboids in the multiple shapes model population are a significantly different 3D shape to the remaining 97.2 % (Table 2.5.1 and cuboid shapes in Figure 5.6b). The 2.8 % is defined by  $P_1$ , representing the 0-20  $\mu\text{m}$  fraction. This population is so small that it does not have a significant impact on the resulting  $w/l$  distribution. The sample 0-20  $\mu\text{m}$  fraction is thought to be off-cuts of larger crystals, and not a true crystal sub-population. The multiple shapes approach demonstrates that even if the 0-20  $\mu\text{m}$  fraction is treated as a true crystal sub-population, the resulting model  $w/l$  distribution is not significantly different to the single shape model  $w/l$  distribution. This supports the conclusion that the observed plagioclase in TRA10A has no change in shape with size, and is a single shape population.

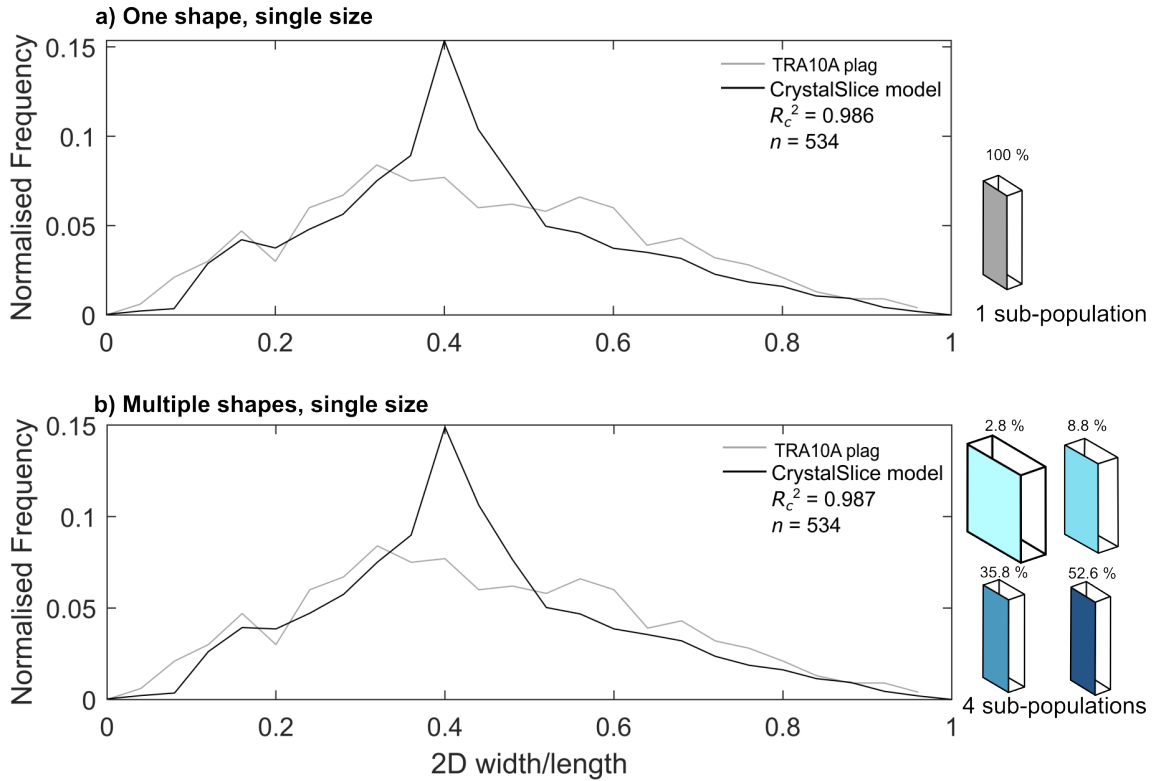


**Figure 5.6:** Comparison of the unbinned plagioclase  $w/l$  distribution in TRA10A against the  $w/l$  distribution of: **a)** a model  $w/l$  distribution for a single shape population. **b)** a model  $w/l$  distribution of four shape sub-populations, defined by the 3D shape estimates of each size plagioclase size fraction. See text for explanation.

## 5.4 Orthopyroxene: BEL1B-A

Groundmass orthopyroxene in BEL1B-A was found to exhibit apparent changes in shape with size (Chapter 4.3.1). 2D intersection measurements were binned into two size fractions of 0-35  $\mu\text{m}$  and 35+  $\mu\text{m}$ . 3D shape estimates suggest evolution from a higher  $S/I$  shape to a lower  $S/I$  shape with increasing size (Chapter 4.3.1). As with the statistical validation of the plagioclase populations, we compared the observed orthopyroxene  $w/l$  distribution and 2D intersection shapes to model  $w/l$  distributions and intersection shapes, to explore the validity of the shape-size result.

### 5.4.1 CrystalSlice: orthopyroxene in BEL1B-A

CrystalSlice (Allgood, in preparation) was used to generate model  $w/l$  distributions of random 2D intersections through a population of crystals with a single size and single shape (the ‘single shape, single size’ population, Figure 5.7b) and a combined population of crystals that are binned into two size fractions, each with a distinct shape (the ‘multiple shapes’ population, Figure 5.7a) defined by the 3D shape estimates of each size fraction in the orthopyroxene (Table 5.1). The  $w/l$  distribution of the multiple shapes model is a strong match to that of the orthopyroxene, with  $R_c^2 = 0.990$  (Figure 5.7a). The  $w/l$  distribution of the single shape model is an equally good fit to the model data, with an  $R_c^2 = 0.989$ , within 0.1 % of the multiple shapes model. Examining the shapes of the model distribution curves, the multiple

shapes model (Figure 5.7a) has two peaks, centred on  $w/l \approx 0.3$  and  $0.75$ . The orthopyroxene distribution does not match these peaks, particularly that at  $w/l \approx 0.3$ . The single shape population (Figure 5.7b) has a clear peak at  $w/l \approx 0.65$ .

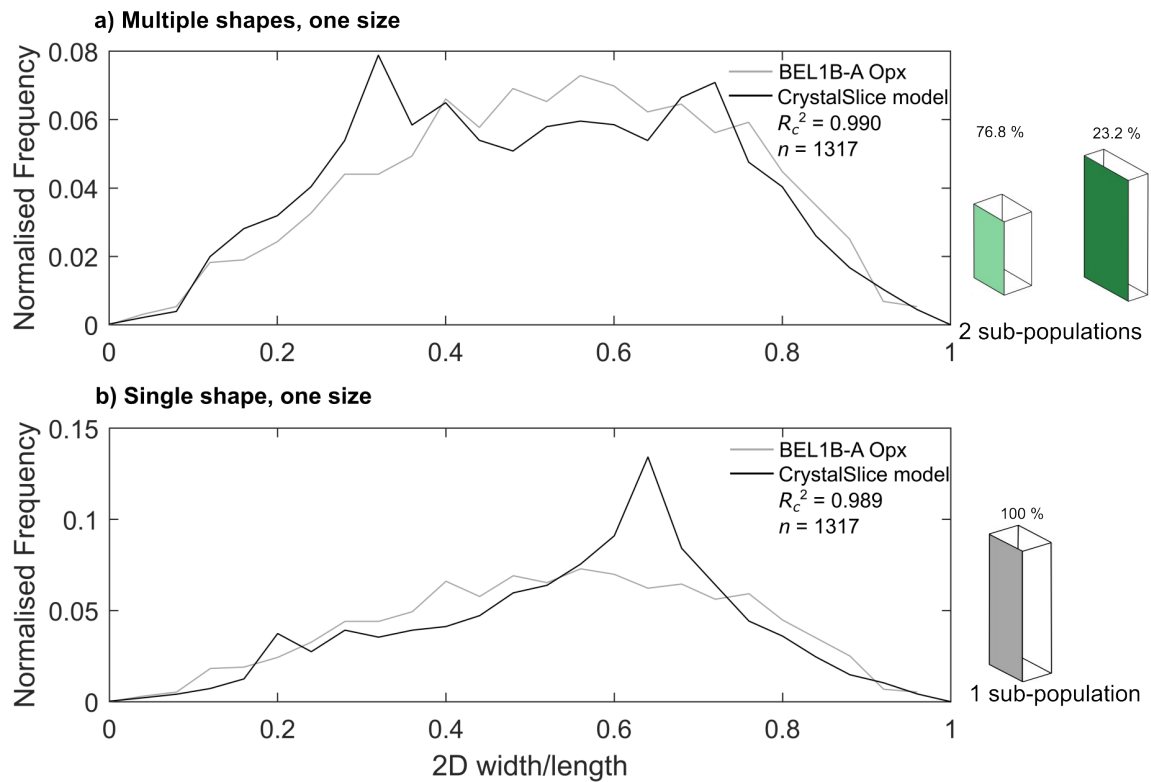


**Figure 5.7:** Comparison of the unbinned plagioclase  $w/l$  distribution in BEL1B-A against the  $w/l$  distribution of: **a)** a model  $w/l$  distribution of four shape sub-populations, defined by the 3D shape estimates of each size plagioclase size fraction; **b)** a model  $w/l$  distribution for a single shape population.

The  $w/l$  distribution of the observed orthopyroxene in BEL1B-A lacks this peak, but this is not unexpected. The sharpness of most peaks in model data are unlikely to be observed in natural crystals, due to the irregular form of natural crystals as opposed to perfect model cuboids, and because of the much smaller number of intersections in natural data (here, 534 orthopyroxene measured) compared to model data (6000-7000 intersections) (Higgins, 1994). The  $w/l$  distribution curve shape in Figure 5.7b is therefore typical of a single shape, prismatic population. This would suggest that the two distinct shape populations identified in Chapter 4.3.1 is a statistical artefact. However, as the  $R_c^2$  values are virtually identical, it is inconclusive as to whether the orthopyroxene in BEL1B-A is a single shape-size population, or does indeed contain two distinct shape populations.

#### 5.4.2 Validating the smallest orthopyroxene population for BEL1B-A

The 0-35  $\mu\text{m}$  observed orthopyroxene intersections were interpreted as the smallest, most equant population of crystals in BEL1B-A (Chapter 4.3.1). From above, it is inconclusive as to whether this population does exist. To test whether the smallest population could be reproduced by

sectioning a model single shape-size population, model 2D intersection data was generated for a model cuboid and compared to the observed orthopyroxene data.

A model cuboid of 1:1.5:5.2 (the 3D shape estimate for the unbinned orthopyroxene intersections, Chapter 4.3.1) was sectioned to generate model 2D intersection  $w/l$  data that was then scaled to a representative maximum 2D intersection length, 60.0  $\mu\text{m}$  (Table 5.2). The 0-35  $\mu\text{m}$  fraction constitutes 86.8 % of the total model intersections, exceeding by 10 % the 76.8 % constituted by

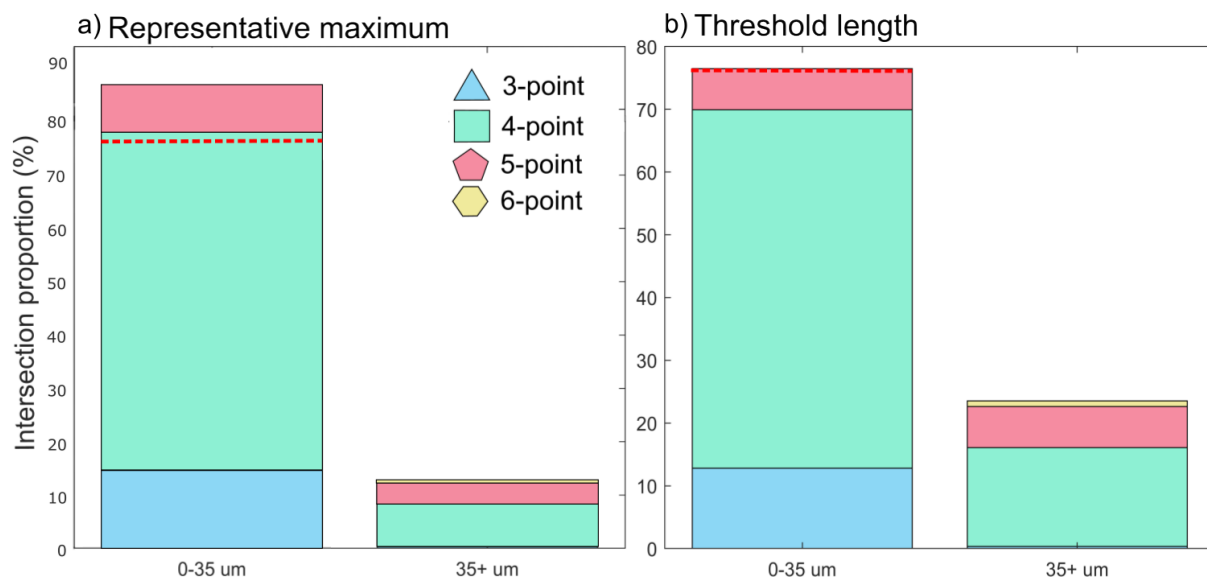


**Figure 5.8:** Sectioning a model cuboid of 1:1.5:5.2, scaled to a representative maximum length of 60.0  $\mu\text{m}$  can reproduce the proportion or shapes of 0-35  $\mu\text{m}$  orthopyroxene intersections. **b)** The threshold scaling length to reproduce the proportion of orthopyroxene intersections is  $\sim 81.0$   $\mu\text{m}$ .

the 0-35  $\mu\text{m}$  fraction in the orthopyroxene (Figure 5.8a). Sectioning this modelled single shape population can therefore reproduce the proportion of the smallest orthopyroxene population. The majority of the model 0-35  $\mu\text{m}$  intersections are 4- or 5-point shapes, matching the observed orthopyroxene intersections being quads or above in outline. However, 17.8 % of model intersections in the 0-35  $\mu\text{m}$  fraction are triangular, indicating that nearly a fifth of the model 0-35  $\mu\text{m}$  fraction are corner-cuts of the model cuboid population, whereas none of the orthopyroxene intersections measured in BEL1B-A were triangular. Moreover, the best-fit 3D shape estimate of the model 0-35  $\mu\text{m}$  fraction is  $S/I = 0.53 \pm 0.06$  and  $I/L = 0.66 \pm 0.25$  using ShapeCalc, with an  $R_c^2 = 0.998$ . This is significantly different than the best-fit 3D shape estimate for the 0-35  $\mu\text{m}$  fraction of the observed orthopyroxene,  $S/I = 0.71 \pm 0.08$  and  $I/L = 0.54 \pm 0.27$  (Table 4.3). Sectioning a single shape-size model population can reproduce the proportion of 0-35  $\mu\text{m}$  intersections observed in BEL1B-A and can partially reproduce the intersection shapes, but cannot recreate the lack of triangular corner-cuts or the 3D shape estimate.

The threshold length at which scaling the model 2D intersection data will reproduce the proportion (76.8 %) of 0-35  $\mu\text{m}$  intersections observed in BEL1B-A was found to be  $\sim 81$   $\mu\text{m}$  (Table

5.2). Similar to the previous scaling approach, the majority of the intersections are quads or above- matching that observed in the orthopyroxene intersections, even though 19.5 % of model 0-35  $\mu\text{m}$  intersections are triangular. The best-fit 3D shape estimate of the model 0-35  $\mu\text{m}$  fraction is  $S/I = 0.69 \pm 0.08$  and  $I/L = 0.73 \pm 0.26$  using ShapeCalc, with an  $R_c^2 = 0.990$ . Sectioning a model single shape-size population can therefore broadly reproduce the proportion of 0-35  $\mu\text{m}$  intersections as well as their 3D shape estimate, and, albeit to a lesser extent, the intersection shapes. Despite not seeing any clear triangular corner-cuts in the orthopyroxene intersections, it is not necessarily expected that corner cuts of a pyroxene would be triangular, as pyroxenes are not perfect cuboids; as they often have octagonal or hexagonal tracht, their corner-cuts could have more complex shapes with more than 3 points.

In summary, whilst these tests cannot unambiguously prove either one of two orthopyroxene shape populations in BEL1B-A, the results point towards the groundmass orthopyroxene is a single shape population, and that the two distinct populations are a statistical artefact.

## 5.5 Amphibole: TRA10A

Like groundmass plagioclase in TRA10A, groundmass amphibole was not found to exhibit change in shape with size (Chapter 4.4.1). A comparison of the amohibole  $w/l$  distribution and a model  $w/l$  distribution is used to explore the validity of this single shape population result.

### 5.5.1 CrystalSlice: amphibole in MVO-1591A

CrystalSlice was used to generate a single shape-size population representative of the TRA10A amphibole shape estimate, 1:1.55:6.4 (Table 2.5.1). The  $w/l$  distribution of the observed amphibole in TRA10A is a good match to the  $w/l$  distribution of the single shape model, with an  $R_c^2 = 0.997$  (Figure 5.6a). This is within 0.1 % of the  $R_c^2 = 0.998$  best-fit shape estimate using ShapeCalc. There is no multiple shapes model  $w/l$  distribution for comparison. The high goodness-of-fit between the amphibole and single-shape model distributions supports the result that there is no change in shape with size in the groundmass amphibole of TRA10A, it is a single shape population.

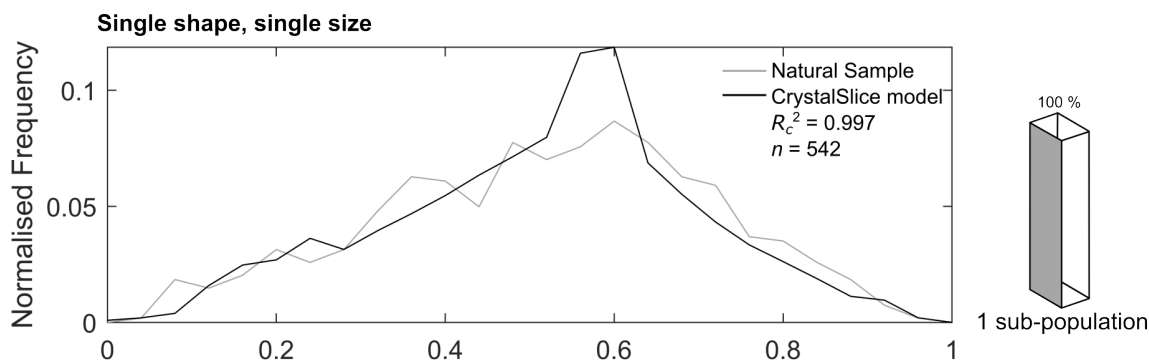


**Figure 5.9:** There is a strong goodness-of-fit between the single shape model population and the TRA10A amphibole population.

### 5.5.2 Summary

Groundmass plagioclase in MVO-1591A and BEL1B-A both showed change in shape from prismatic to tabular with increasing size, and the statistical tests indicate that these mafic enclaves contain true, distinct shape populations. TRA10A plagioclase does not show change in shape with size, and statistical tests support that there is a single shape population. Groundmass orthopyroxene in BEL1B-A possibly contained two shape populations, with a smaller, higher  $S/I$  population and a larger, lower  $S/I$  population. However, statistical tests suggest that the orthopyroxene is likely a single prismatic shape population, and that the smaller, more equant population suggested to occur is likely a statistical artefact. Groundmass amphibole in TRA10A did not show change in shape with size, and like the plagioclase in this mafic enclave, the statistical tests support that the amphibole is a single shape population.

## 6 Discussion

In this chapter, we use crystal growth modelling to explore how the observed groundmass crystal shape-size relationships could have been produced in the mafic enclaves. First, we apply the model to the plagioclase results, informing discussion of the processes that could have contributed to the development of multiple plagioclase shape-size populations in BEL1B-A and MVO-1591A. We then explore why we observe only one shape-size population in the groundmass plagioclase and amphibole of TRA10A. Following this, we apply the growth model to the orthopyroxene shape-size populations in BEL1B-A, and discuss these results with regard to recent studies exploring variation in pyroxene morphology (Okumura et al., 2022; 2024). Finally, we use the derived petrogenetic significance of groundmass crystal shape in the mafic enclaves to comment on magmatic processes occurring at SHV.

### 6.1 Crystal growth modelling

We present an adapted crystal growth model that attempts to reproduce the groundmass shape-size populations. Exploration of how varying steady-state overgrowth shape affects crystal evolution and comparing these results with recent experimental work (Mangler et al., 2023) enables comment on the crystallisation history of the mafic enclaves.

#### 6.1.1 The crystal growth model

Mangler et al. (2022) presented a growth model that calculates the change in shape of a crystal for a given initial shape and size, crystal volume increase, and defined overgrowth shape. The magmatic process modelled is the growth of a single isolated crystal in the melt. The steady-state overgrowth shape imparts relative growth rates on crystal faces that determine how the crystal shape evolves with increasing volume. Mangler et al. (2022) found that, at a given crystallisation interval, the shapes of crystal populations depend on their number density and initial crystal size (Figure 6.1). A further application of the model has been to establish relative growth rates ( $\delta S/\delta I$ ) for experimentally grown plagioclase populations in basaltic and rhyolitic melts by characterising plagioclase shape as a function of size (Mangler et al., 2023).

The growth model is a valuable tool to explore the effects of initial size, shape, number density and overgrowth shape on crystal shape-size evolution. However, a functional limitation exists in that the user is required to manually adjust the ‘k factor’, which is a value that is necessary to calculate the correct model crystal volume, necessitating a trial-and-error approach. Only a singular ‘point’ in shape evolution can be calculated at a time; the complete shape-size evolution must be manually plotted. Regarding geological applications, the model does not account for the initial crystallinity of the melt volume. The initial population of proto-prisms will constitute a small (typically  $\leq 1\%$ ) volume, which is not taken into account when calculating the volume increase required per crystal to achieve the desired increase in total crystallinity.

To address these issues, the Excel sheet model of Mangler et al. (2022) was converted to a MatLab script (Appendix A). The core difference is that the code iteratively solves for the ‘k factor’ for a range of shapes between the initial and overgrowth shape, plotting the complete

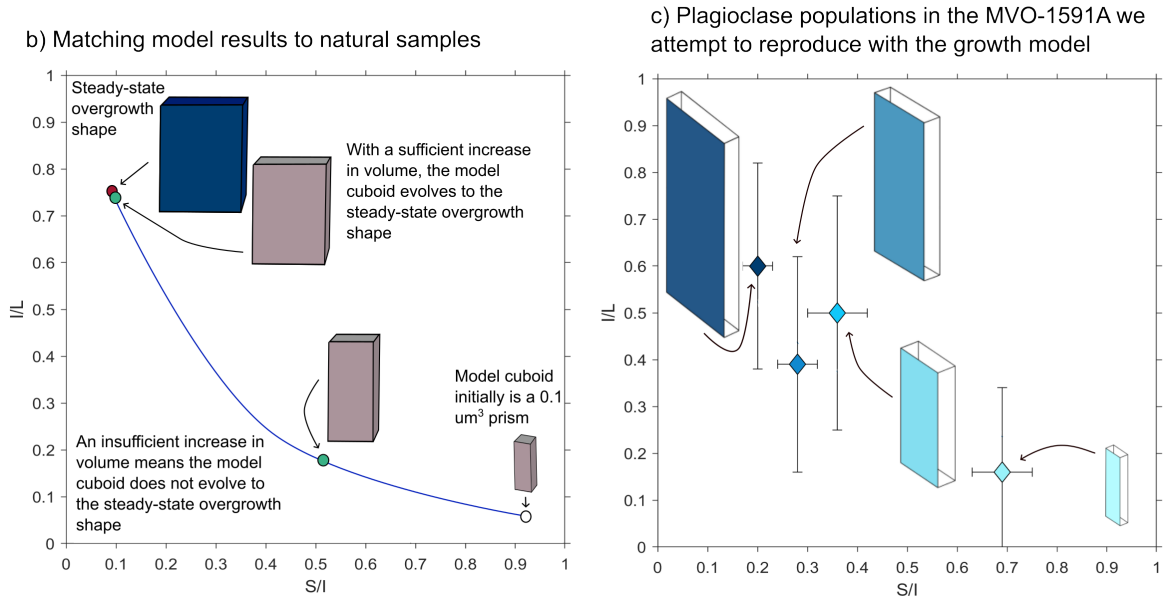
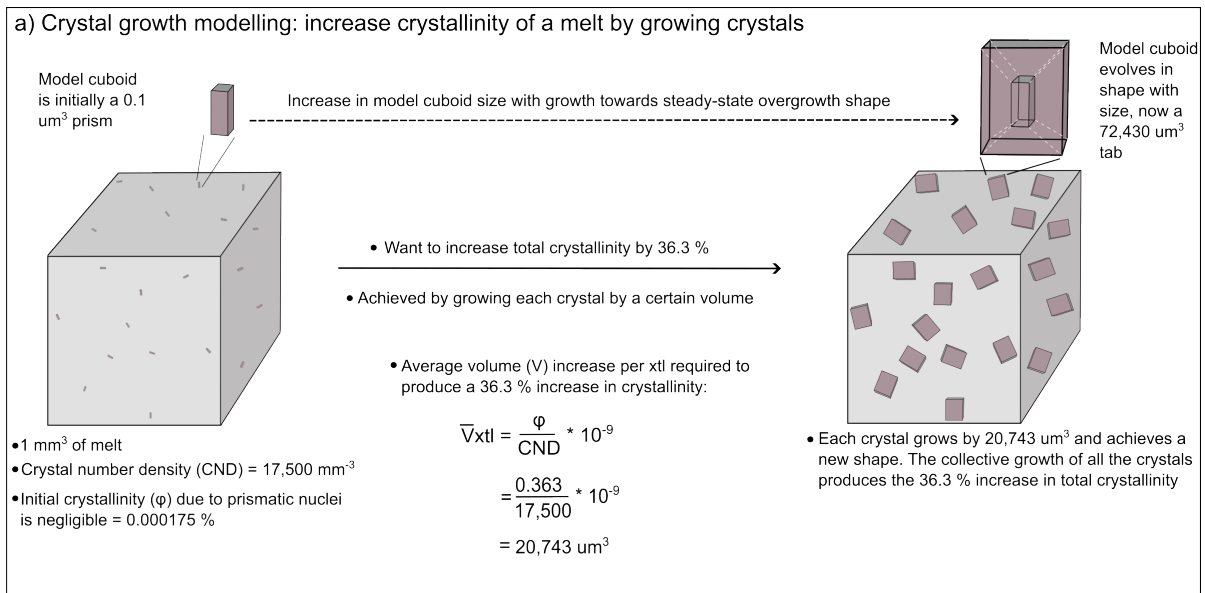


**Figure 6.1:** Schematic of the crystal growth model. **a)** The model grows a cuboid of a specified initial shape (prism) and size (here, 0.1  $\mu\text{m}^3$ ) by a certain volume depending on the initial crystal number density (here, 17,500  $\text{mm}^{-3}$ ) and desired increase in total crystallinity (here, 36.3 %, the estimated crystallinity of groundmass plagioclase in MVO-1591A). For a melt of initially 0 % crystallinity, to increase the total crystallinity by 36.3 %, each cuboid must increase in volume by 20,743  $\mu\text{m}^3$ . As the volume increases, the cuboid evolves in shape towards the steady-state overgrowth shape. **b)** How model cuboid shape evolves with size from an initial prism towards the steady-state overgrowth shape. The steady-state overgrowth shape will be one of the plagioclase populations in MVO-1591A (**c**). A sufficient increase in volume will evolve the model cuboid to the overgrowth shape, successfully reproducing the plagioclase population. Conversely, an insufficient increase in volume means the model cuboid cannot reach the overgrowth shape, failing to reproduce the plagioclase population.

evolution in individual crystal shape and volume, and total crystallinity of a volume of melt (here, 1  $\text{mm}^3$ ). The initial crystallinity constituted by the volume of the initial crystal population is accounted for (after Equation (1)). This conceptually improves the applicability of the

model to real magmatic scenarios by accounting for the initial crystallinity based on the crystal number density.

(1) Initial crystallinity = (100 / melt volume) \* (initial crystal volume \* crystal number density).

An example output of this revised growth model output (Figure 6.2) presents the shape-size evolution of the model crystal (red/yellow curves) from the initial shape and size (white circle) to the overgrowth shape (black circle). The green circle shows the model shape-size when the desired increase in total crystallinity (here, 36.3 %) has been achieved by the collective volume increase of growing the initial crystal population (here, each individually by 20,743  $\mu\text{m}^3$ ). The volume increase in each individual crystal is therefore 207,000 %.

### 6.1.2 Application to groundmass plagioclase

The revised crystal growth model is applied to the mafic enclave samples to try to reproduce the groundmass plagioclase size-shape relationships. The model was applied in three approaches. Approach 1 models the evolution of a prism to different overgrowth shapes, following Mangler et al. (2022). However, shape-size evolution of a singular crystal is not reflective of continuous nucleation and growth in magmatic scenarios. Approach 2 attempts to address this through a step-wise crystallisation approach to grow successive distinct shape-size populations observed in the mafic enclaves. Following this, Approach 3 then varies steady-state overgrowth shape to grow successive populations, as it was observed in Mangler et al. 2023 that steady-state shape can evolve with changing melt composition/diffusivity.

The textural characteristics of BEL1B-A and MVO-1591A are similar, with the latter used as model inputs (Table 6.1). The CSDs (Figure 4.6 and Figure 4.2 respectively) show that groundmass crystals exponentially decrease in number density with increasing size. Four shape-size populations were identified (Chapter 4) and verified to be real textural characteristics as opposed to an analytical artefact (Chapter 5). The smallest crystal population is prismatic with an  $S/I \sim 0.7$ , evolving to increasingly tabular crystals ( $S/I \approx 0.50, 0.35, 0.20$ ) with increasing size. The modelling approaches attempt to reproduce these populations in succession.

**Table 6.1:** Growth model inputs for each approach. Total crystallinity increase ( $\varphi_{\text{inc}}$ ) and volumetric number density ( $N_v$ ) after the textural characteristics of shape populations in MVO-1591A. Constant parameters in all model runs include initial melt volume = 1  $\text{mm}^3$ , initial crystal volume = 0.1  $\mu\text{m}^3$  and initial crystal shape = 1:1.3:6.0.  $\delta S/\delta I$  describe the relative growth rates of the Short to Intermediate faces.

Approach	Step	Population	$\varphi_{\text{inc}}$ (%)	$N_v$ ( $\text{mm}^{-3}$ )	$V_{\text{inc}}$ ( $\mu\text{m}^3$ )	Overgrowth shape	$\delta S/\delta I$
<b>Approach 1</b>	Run 1	n/a	36.3	17,500	20,743	1:20:24	0.05
	Run 2	n/a	36.3	17,500	20,743	1:5:8	0.2
<b>Approach 2</b>	Step 1	100 + $\mu\text{m}$	18.4	480	383,333	1:10:12	0.1
	Step 2	40-100 $\mu\text{m}$	14.8	4900	30,204	1:10:12	0.1
	Step 3	20-40 $\mu\text{m}$	3.5	9200	3804	1:10:12	0.1
	Step 4	0-20 $\mu\text{m}$	0.9	20,000	450	1:10:12	0.1
<b>Approach 3</b>	Step 1	100 + $\mu\text{m}$	18.4	480	383,333	1:5:8	0.2
	Step 2	40-100 $\mu\text{m}$	14.8	4900	30,204	1:4:7.5	0.25
	Step 3	20-40 $\mu\text{m}$	3.5	9200	3804	1:3:7	0.33
	Step 4	0-20 $\mu\text{m}$	0.9	20,000	450	1:1.5:6.5	0.66

## Approach 1

Approach 1 treats the groundmass plagioclase crystals as a single population nucleated instantaneously. Following Mangler et al. (2022), a  $0.1 \mu\text{m}^3$  prism (1:1.3:6) was overgrown to two steady-state shapes: 1:20:24 ( $\delta S/\delta I = 0.05$ , relative growth rate on Short to Intermediate faces) and 1:5:8 ( $\delta S/\delta I = 0.2$ ). These are endmembers of shapes observed in plagioclase grown experimentally (Mangler et al., 2023). In each model run,  $1 \text{ mm}^3$  of melt was crystallised by 36.3 %, which is the estimated groundmass plagioclase crystallinity of MVO-1591A (Table 6.1). Overgrowth of the initial prism to either steady-state shape can reproduce the observed plagioclase shape populations, given the uncertainties, as the model cuboid evolves from prismatic to tabular with increasing volume (Figure 6.2a). This agrees with Mangler et al. (2022), where overgrowth of a 1:1.3:6 prism to a 1:10:12 tab was able to produce the range of plagioclase microcline shapes observed in natural samples from intermediate arc volcanoes. The growth model shape results here are therefore consistent with each plagioclase size fraction in the mafic enclave evolving towards the same steady-state shape. The later nucleating crystals do not reach the steady-state shape because the increasing cumulative crystal number density causes a reduction in available growth volume with time. However, Approach 1 fails to reproduce the crystal size. The average volumes of the observed plagioclase populations are orders of magnitude greater than the model cuboid at the same  $S/I$  (Figure 6.2b-c). This is because evolution in model shape occurs at small volumes ( $10^{-1}$ - $10^2 \mu\text{m}^3$ , equivalent melt crystallinity  $\approx 0.1$ -1 %), reaching steady-state shape at  $\sim 100 \mu\text{m}^3$ . The plagioclase populations therefore cannot be linked by the shape evolution of a single crystal with progressive overgrowth (cf Mangler et al., 2022).

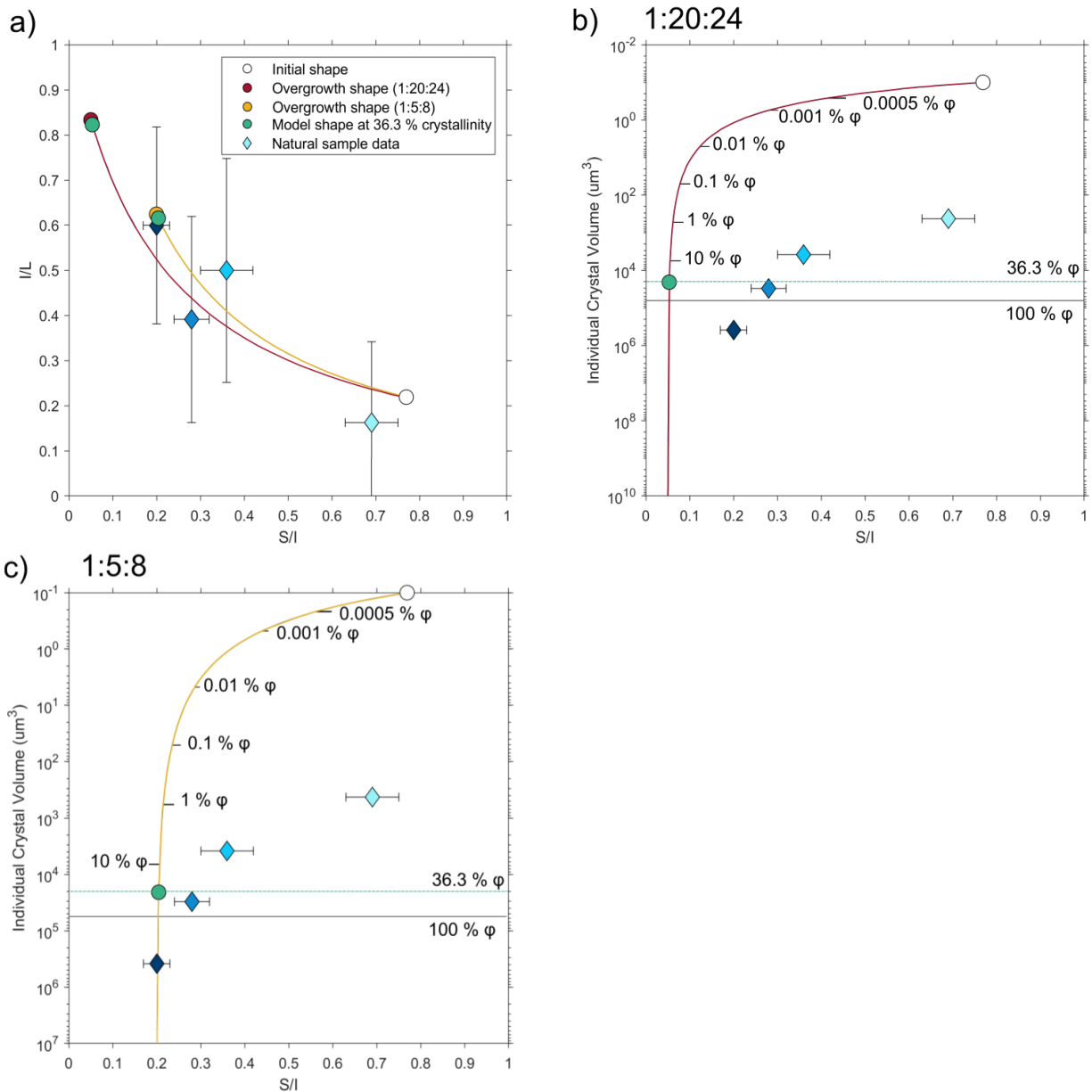


**Figure 6.2:** Approach 1: overgrowth of a prism to two steady-state shapes: 1:20:24 (red) and 1:5:8 (yellow). Natural plagioclase data are from MVO-1591A and represent four size fractions as reported in Table 4.3. The evolution of the model crystal in shape and size with growth follows the coloured lines, from initial shape to overgrowth shape. The model evolves through the shapes of the plagioclase populations (a)), but cannot reproduce the averages sizes (b) and c)). See text for further explanation.

### Approach 2: Step-wise crystallisation

In natural scenarios, crystallinity of the melt increases incrementally with continuous crystal nucleation and growth, producing multiple shape-size populations. Approach 2 approximates this by modelling four ‘steps’ of crystallisation, aiming to reproduce the groundmass crystallinity and number density of each plagioclase population (Table 6.1). For example, Step 1 attempts to reproduce the largest, most tabular population using an 18.4 % crystallinity increase and a

480 mm<sup>-3</sup> number density, as observed for the >100 μm size fraction. Using the groundmass crystallinity of each plagioclase population as the input for the total crystallinity increase means that the model crystal will have the correct average volume to match the observations. Therefore, this approach aims to see if the correct shape can also be reproduced. This approach was run for two steady-state overgrowth shapes: 1:10:12 and 1:5:8. The first, 1:10:12 was used as it is a typical plagioclase shape for groundmass in intermediate arc volcanoes (i.e. Mangler et al., 2022). The second, 1:5:8 was shown in Approach 1 (Figure 6.2) to produce a range of shapes with high S/I, and is therefore an alternative that may better reproduce the plagioclase shape populations.

Neither overgrowth shape with this approach can reproduce the plagioclase shapes (Figure 6.3a and 6.3c) with the correct average crystal volume (Figure 6.3b and 6.3d). In both cases, the model shape at the desired crystallinity is much more tabular than the observed plagioclase shape populations, the only exception being that an overgrowth shape of 1:5:8 (Figure 6.3c and d) can reproduce both the size and shape of the largest, most tabular plagioclase population. Failure to reproduce the plagioclase shapes is again because the model crystal evolves quickly to the overgrowth shape with a small increase in volume, reaching  $\sim 0.15$  S/I with only a  $\sim 1$  % increase in total crystallinity (Step 4). This is because the number density is relatively low, which means that each crystal has a relatively high available growth volume, a concept explained in Figure 1.3.

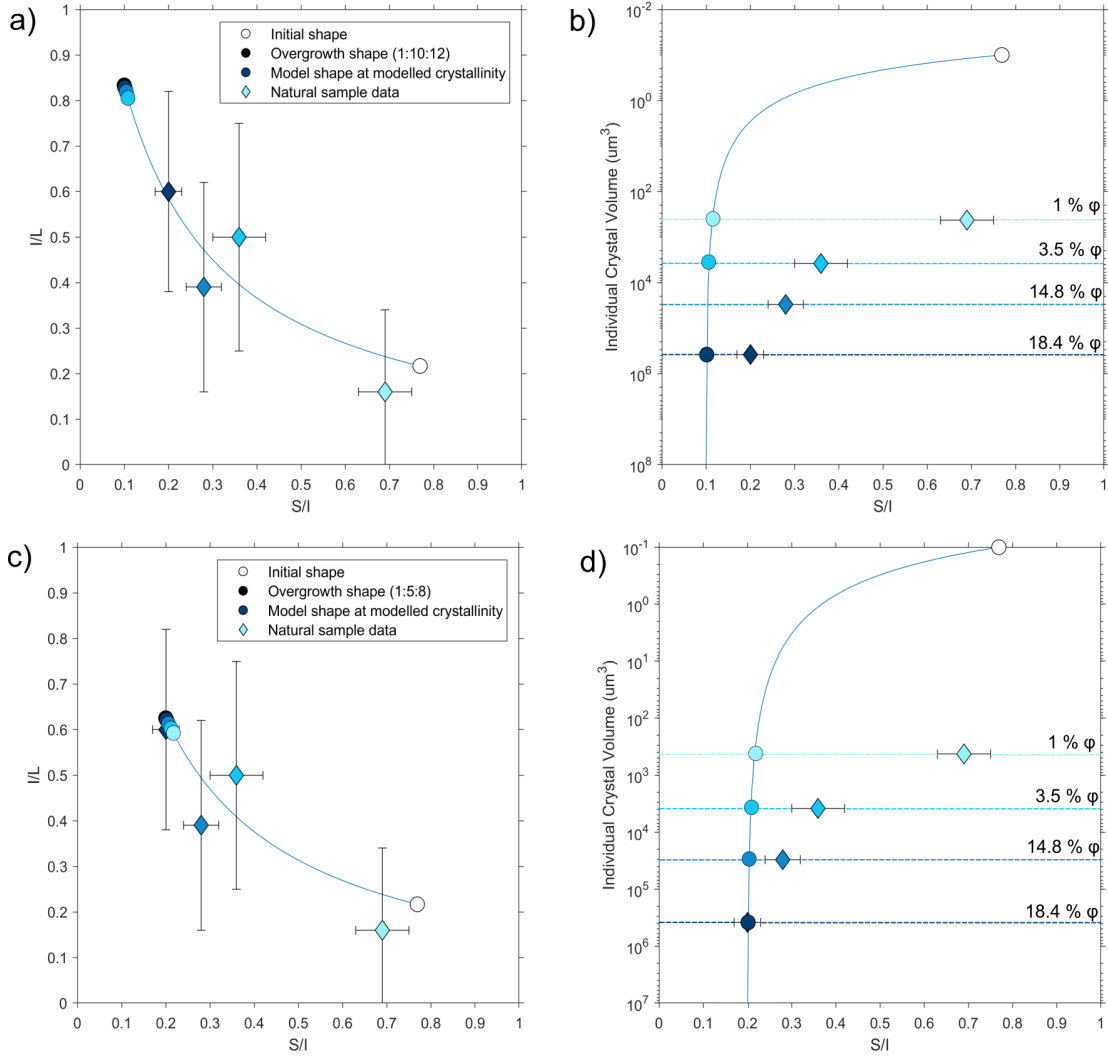


**Figure 6.3:** Approach 2: overgrowth of a prism to two steady-state shapes: 1:10:12 (a) - b)) and 1:5:8 (c) and d)), for four steps of crystallisation, reflecting the groundmass crystallinity of each plagioclase population. Natural plagioclase data are as in Figure 6.2. This approach cannot recreate the shape populations as in each step, the model crystal evolves to too low an  $S/I$  shape with a small increase in volume.

### Approach 3: Changing steady-state overgrowth shape

Previous approaches have demonstrated that shape evolution of the initial  $0.1 \mu\text{m}^3$  prism occurs with a small volume increase ( $10^{-1}$ - $10^2 \mu\text{m}^3$ ). Mangler et al. (2023) established that the threshold for attaining steady-state shape in experimentally grown plagioclase was  $\sim 100 \mu\text{m}^3$ . Any combination of melt crystallinity increase, initial crystal size and number density that results in the increase in individual model crystal volume exceeding  $\sim 100 \mu\text{m}^3$  will thus evolve the model crystal to the input overgrowth shape. Therefore, as the average crystal volume of each plagioclase population exceeds this threshold (Table 6.1), the only way to recreate the shape-size populations is to use the shape of each plagioclase population as the overgrowth shape. This approach essentially dictates that the steady-state overgrowth shape changes with each crystallisation step, illustrated in Figure 6.4. It progressively evolves from tabular ( $S/I = 0.2$ )

to prismatic ( $S/I = 0.7$ ) to reproduce increasingly smaller, higher  $S/I$  plagioclase populations.

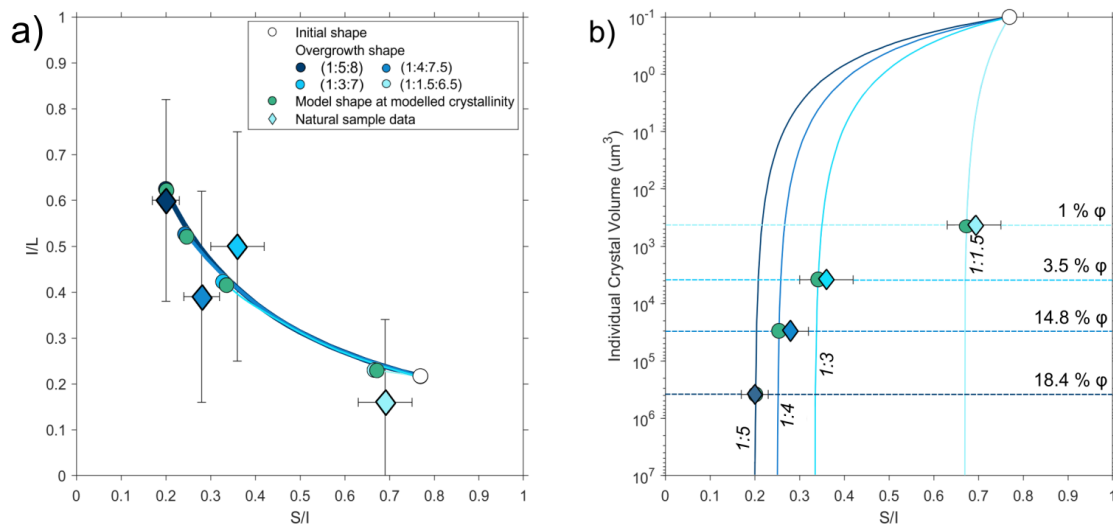


**Figure 6.4:** Approach 3: overgrowth of a prism to increasingly high  $S/I$  overgrowth shapes. Varying steady-state overgrowth shape to increasingly prismatic  $S:I:L$  can reproduce the plagioclase shape-size populations. See text for further explanation.

This approach might seem somewhat circular. However, Mangler et al. (2023) discovered that plagioclase morphology may be affected by an intermediate growth regime between interface-controlled and diffusion-limited growth, which is important when melt diffusivity is similar to interfacial reaction (growth) rates. In anisotropic crystal growth, where there are relative differences in interfacial reaction rates between faces, slower-growing crystal faces could be interface-controlled, while faster-growing faces are diffusion-limited. In this intermediate regime, crystal shape is therefore a function of the competing interface reaction kinetics and melt diffusivities. This is expressed as variation in euhedral morphology, as seen in experimentally grown plagioclase populations (Figure 6.5; here, variation in euhedral morphology is expressed as differences in  $S/I$ ). Relative growth rates of plagioclase grown in basaltic melts show a higher discrepancy between short and intermediate growth directions ( $S/I \approx 0.05$ ) than those grown in haplodacitic melts ( $S/I \approx 0.2$ ). Steady-state shape could therefore be dependent on melt diffusivity, evolving to higher  $S/I$  with increasingly silicic melt compositions.

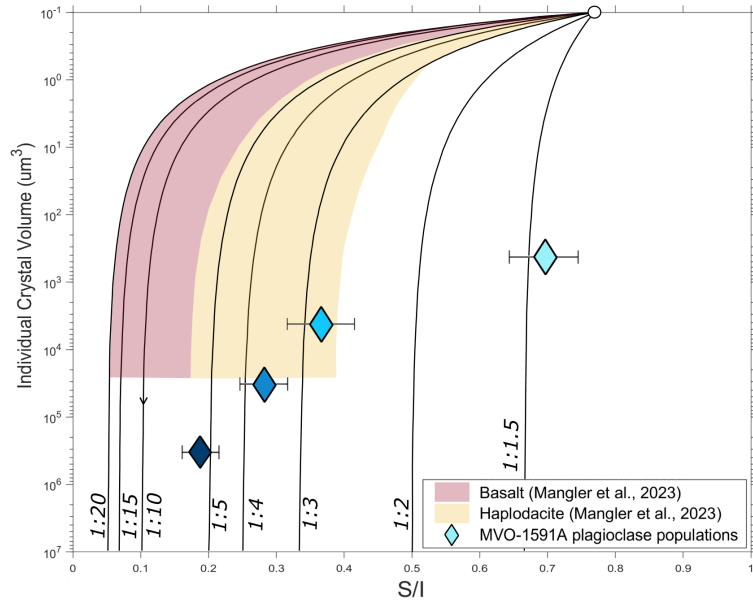


**Figure 6.5:** Comparison of experimental (Mangler et al., 2023) and mafic enclave (this study) plagioclase shape-size populations, with growth model curves defining model shape-size evolution from an initial  $0.1\mu\text{m}^3$  prism to a range of steady-state overgrowth shapes. Plagioclase grown in basaltic melt (red shading) evolve to lower  $S/I$  shapes than plagioclase grown in more silicic melt (yellow shading).

In our growth modelling, we required the steady-state overgrowth shape to evolve to increasingly high  $S/I$  with each crystallisation step in order to reproduce the plagioclase shape-size populations (Figure 6.4). This evolution in steady-state shape could have been driven by changing melt diffusivity. Initially, the intruding melt is basaltic, hydrous and  $\sim 1050^\circ\text{C}$  (Murphy et al., 2000). The bulk rock compositions of SHV mafic enclaves are between 48–57 wt%  $\text{SiO}_2$  (Plail et al., 2014; Christopher et al., 2014; Murphy et al., 2000; Zellmer et al., 2003a). Upon mingling with the cooler host andesite, the intruding melt quickly cools with groundmass plagioclase and other phases crystallising to form the diktytaxitic groundmass texture indicative of quench crystallisation (Bacon, 1986; Blundy & Sparks, 1992). With progressive crystallisation, melt evolves to increasingly silicic compositions, with residual glass in the enclaves being rhyolitic with 70–79 wt%  $\text{SiO}_2$  (Chapter 3; Plail et al., 2014; Murphy et al., 2000; Humphreys et al., 2010). Water will also be lost with progressive cooling and crystallisation, further reducing melt diffusivities. Therefore, it is conceivable that the evolution in residual melt composition within the mafic enclaves could drive a change in steady-state shape from tabular to prismatic, that could explain the plagioclase shape-size populations in the mafic enclaves (Figure 6.6). The largest, most tabular crystal population that is inferred to have nucleated first would likely attain a lower  $S/I$  steady-state shape than crystals nucleating later in increasingly silicic melt, reflected in the smaller populations being increasingly prismatic.

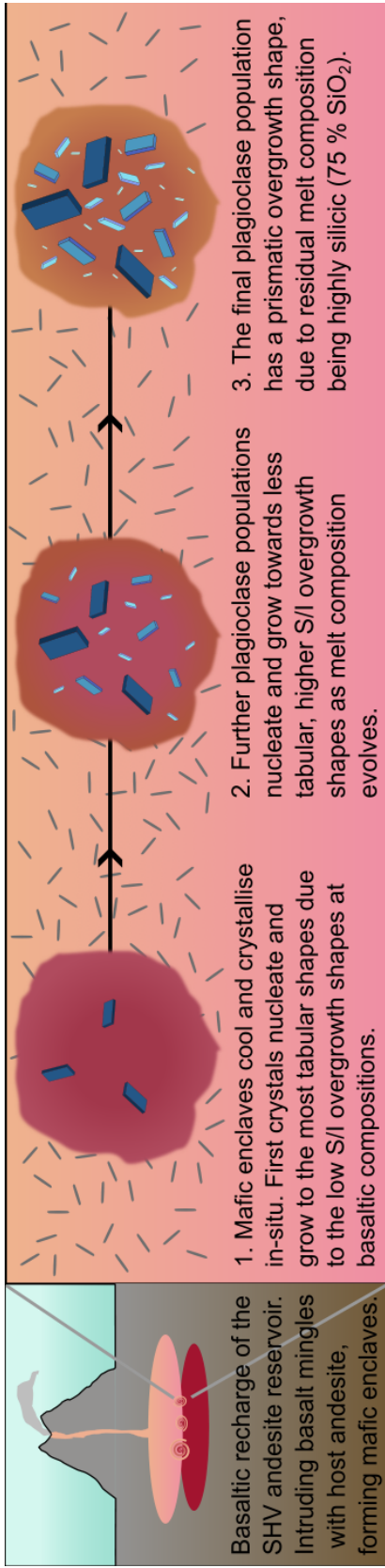


**Figure 6.6:** Groundmass plagioclase crystallisation in the mafic enclaves is driven by the mingling of hotter, more hydrous basaltic melt with cooler host andesite mush. Steady-state shapes change to higher *S/I* as melt composition evolves with cooling and crystallisation, producing increasingly small, prismatic plagioclase populations.

Are the proposed steady-state overgrowth shapes realistic? Steady-state shapes with relative growth rates of  $S/I \approx 0.2, 0.25$  and  $0.33$ , which are proposed to reproduce the three largest, most tabular plagioclase populations, fall within the range of shapes produced experimentally by Mangler et al. (2023) (Figure 6.5). These span the range from basaltic to silicic melts, with a systematic trend to more tabular shapes in more primitive melt, consistent with what is inferred here. However, no steady-state overgrowth shape greater than  $S/I \approx 0.38$  was observed. Reproducing the smallest, most tabular population requires a steady-state overgrowth shape of  $S/I \approx 0.66$ , which is not within error of plagioclase shape populations grown in even the most silicic compositions. Whilst not observed experimentally, the dependency of steady-state shape on melt diffusivity found in Mangler et al. (2023) suggests if diffusivity decreased further by melt evolving to more silicic compositions, steady-state shape should theoretically evolve to higher  $S/I$  (Figure 6.5). Whilst plagioclase were experimentally grown in haplodacite melt with 72.3 wt.%  $\text{SiO}_2$  and run under water-saturated conditions, the smallest plagioclase grown in the enclaves would have crystallised from more evolved melt ( $\sim 75$  wt.%) which had lost water from progressive cooling and crystallisation because these crystals nucleate last. The residual melt in the enclave therefore likely would have had lower melt diffusivity than the experiments by Mangler et al. (2023). Therefore, the high  $S/I$  steady-state shape required to reproduce the smallest, most prismatic population could be realistic.

An alternative explanation for the shape of the smallest, most prismatic population could be overestimation of the average crystal volume.  $W:L$  data from the  $<20 \mu\text{m}$  intersections were used to estimate average crystal volume. Whilst the influence of corner-cuts was explored in Chapter 5, it remains possible that some intersections are corner-cuts of a larger crystal population. An improvement on this method could be to calculate the intersection probability-distributions for each crystal population, to understand what percentage of each intersection size bin could be cuts of a larger crystal population (i.e, Sahagian & Proussevitch, 1998). Using even the highest relative growth rate observed in experimental work ( $S/I \approx 0.4$ ), the smallest plagioclase population ( $S/I = 0.69$ ) could only be reproduced if the average crystal volume had a magnitude of  $\sim 10^0 \mu\text{m}^3$ . The scaled dimension of a  $1 \mu\text{m}^3$  crystal of 1:1.45:9.20 (estimated shape of the smallest plagioclase population) would be  $0.42 \mu\text{m}:0.61 \mu\text{m}:3.90 \mu\text{m}$ . A population of this size would have intersections with a maximum length  $\sim 4 \mu\text{m}$ . The model crystal volume of  $\sim 10^0 \mu\text{m}^3$  is much smaller than the calculated average plagioclase volume of the smallest population ( $450 \mu\text{m}^3$ , Table 6.1). If the average volume is overestimated, perhaps due to a significant percentage of the 0-20  $\mu\text{m}$  intersections being corner-cuts, then maybe the smallest plagioclase are crystals that have not yet achieved steady-state shape. They could have been evolving towards an overgrowth shape with a relatively high relative growth rate, say  $S/I \approx 0.4$ , but did not reach steady-state shape due to a lack of available growth volume, having nucleated and grown last.

Another factor affecting the rate at which crystals approach their steady-state shape is the initial crystal volume (Mangler et al., 2022). The observed plagioclase shape-size populations can broadly be reproduced using a single steady-state overgrowth shape if the initial prism is sufficiently large (i.e.,  $\sim 100 \mu\text{m}^3$ ) (Figure 6.7). This is because shape evolution occurs

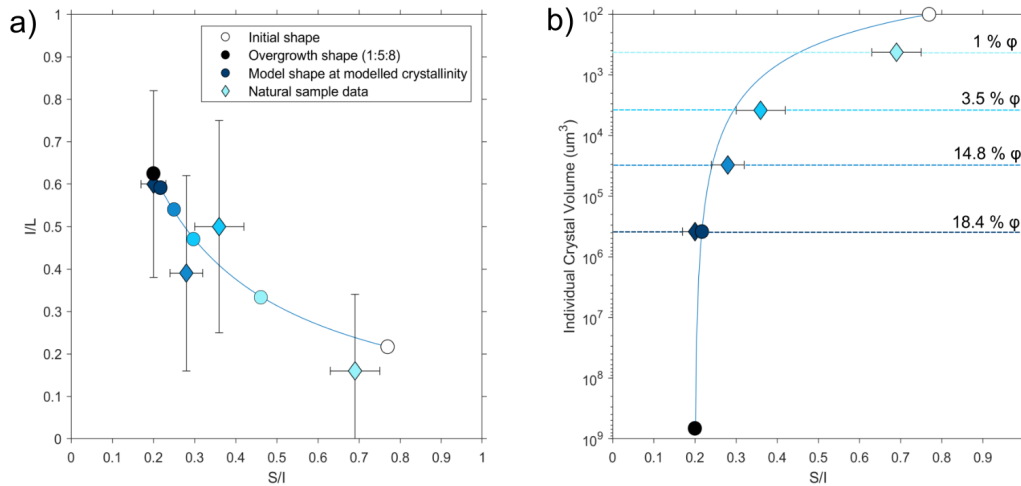


**Figure 6.7:** Overgrowth of a  $100 \mu\text{m}^3$  prism to a 1:5:8 steady-state overgrowth shape in the same application of the growth model as Approach 2 can reproduce the three largest observed plagioclase populations within uncertainty. It cannot reproduce the shape of the smallest, most prismatic population.  $100 \mu\text{m}^3$  is also an unrealistic size for a nucleating prism (see text).

quickly with increasing volume, as demonstrated in Approach 1 and 2. However, a  $100 \mu\text{m}^3$  initial prism is unrealistic. A 1:1.3:6 prism of  $100 \mu\text{m}^3$  volume would have scaled dimensions of  $2.34 \mu\text{m}:3.0 \mu\text{m}:14 \mu\text{m}$ , far too large for a nucleating prism. There is evidence for mechanical transfer of crystals between the mafic enclaves and the host andesite, including the inherited phenocryst population of the enclaves (Plail et al., 2014; Murphy et al., 2000) thought to occur upon mingling, and microlite transfer is known to occur from the enclave to host andesite upon enclave disaggregation (Humphreys et al., 2009). It therefore could be that a population of  $\sim 100 \mu\text{m}^3$  prismatic crystals from the host andesite may have been incorporated into the mafic enclave, and overgrown to the tabular shapes observed. However, the groundmass crystals show no textural evidence of disequilibrium similar to the inherited phenocryst population, so this is scenario is not realistic.

### 6.1.3 Limitations of the crystal growth model

The model effectively grows a single, isolated crystal in the melt. In reality, crystals continuously nucleate and grow, resulting in multiple shape-size populations reflecting changing magmatic conditions over time; the motivating principle of recent crystal shape-size studies. Applying the model in a step-wise crystallisation approach (Approach 2/3) attempted to address this limitation. This was useful to establish how plagioclase shape-size populations could be reproduced, and indeed the conditions under which they could not be reproduced. However, this approach effectively only models discrete nucleation and growth of crystal populations.

The growth model does not account for impingement and intergrowth. After Step 2, 33.2 % of the melt has crystallised to plagioclase. Groundmass amphibole and pyroxene crystallise alongside (Figure 3.1 and 3.2). At some crystallinity, impingement and intergrowth would occur, which could affect the resulting crystal shape (Holness, 2014). Section 4.2.1 illustrates the groundmass texture of MVO-1591A, with a significant degree of impingement and intergrowth.

An improvement on the growth model could be to account for the growth of other cuboids, perhaps by calculating when impingement is likely to occur for a certain number density of growing crystals randomly distributed in  $1 \text{ mm}^3$  of melt.

## 6.2 Groundmass crystal shapes in TRA10A

Unlike the other samples, groundmass plagioclase and amphibole in TRA10A displayed no change in shape with size (Chapter 3). Below we discuss why the plagioclase result departs from the observed trend of systematic change in shape with size in other enclaves, and the implications of the amphibole result.

### 6.2.1 Plagioclase

TRA10A plagioclase forms a single shape population with  $S/I = 0.48 (\pm 0.07)$  and an average crystal volume of  $\sim 200,000 \text{ }\mu\text{m}^3$ . As this exceeds the  $100 \text{ }\mu\text{m}^3$  threshold for development of a steady-state shape (Mangler et al., 2023), this suggests all plagioclase evolved to a singular steady-state shape, regardless of evolution in melt composition with enclave cooling. A steady-state shape of  $S/I = 0.5$  is far more equant than the tabular shape ( $S/I = 0.05\text{-}0.2$ , Mangler et al. (2023)) expected for plagioclase crystallising from an initially basaltic melt, and also exceeds the values in the most silicic experiments ( $S/I = 0.2\text{-}0.35$ , Mangler et al. (2023)) (Figure 6.5).

Is the single shape population a consequence of the intersection outlining? TRA10A is the coarsest-grained and most intergrown sample (Chapter 3), with irregular outlines possibly causing an inaccurate 3D shape estimate. However, Chapter 2.4 tested outlining approaches and found no significant difference in 3D shape estimate between outlining highly intergrown crystals exactly, or extrapolating and therefore estimating their shape. The single shape-size population is therefore thought to be an accurate result.

Impingement of growing crystals can lead to increasingly equant shapes due to cessation of growth of the fastest-growing face, forcing further growth to occur on the slower-growing faces (Holness, 2014). The first nucleating crystals in the enclave could have evolved towards tabular steady-states shapes, as for plagioclase in the other enclaves. Continued growth affected by impingement with other groundmass grains could have prevented further overgrowth of the fastest-growing face, stopping crystals from maintaining this tabular shape and instead forcing evolution towards more equant,  $S/I = 0.5$  shapes with further growth. Further nucleation in the increasingly silicic melt could produce crystals growing towards increasingly equant overgrowth shapes, regardless of the effect of impingement, because of the factors described above in Chapter 6.1.2. TRA10A has the coarsest-grained, highly intergrown groundmass (Figure 6.9), suggesting that impingement could have affected the largest crystal shapes.

Lindoo et al. (in prep) show that plagioclase shape is related to the dynamic undercooling of the melt over time, observing tabular crystals at high integrated undercooling and increasingly prismatic crystals at lower integrated undercooling. They suggest that the variation in euhedral shape is due to a change in growth mechanisms of different crystal faces arising from the changing undercooling conditions. The lack of prismatic plagioclase in TRA10A could therefore

be due to the enclave experiencing a lower degree of undercooling over time. The coarse-grained groundmass supports a low cooling rate, as there is a relatively low number density ( $\sim 500$  plagioclase intersections) of large groundmass plagioclase. The insulated interior of a large enclave could experience a low cooling rate. Whilst the mean diameter of the Type A enclaves characterised by Plail et al. (2014) was 2.3 cm, enclaves over 18 cm were measured, and the largest Phase V enclave observed to date is 26 cm diameter (Plail et al., 2017). Using Equation 2 below (Furlong et al., 1991), we model the cooling of a layered intrusion (i.e., a dike, here meant to approximate a buoyant plume of mafic magma rising into the host andesite and cooling).

$$T(x, t) = T_0 + \frac{\Delta T}{2} \left[ \operatorname{erf} \left( \frac{a - x}{(4\kappa t)^{1/2}} \right) + \operatorname{erf} \left( \frac{a + x}{(4\kappa t)^{1/2}} \right) \right] \quad (1)$$

$x$  = distance across enclave

$T$  = temperature

$t$  = time

$T_0$  = host andesite temperature (830 °C)

$\Delta T$  = temperature difference between host andesite and intruding mafic magma, where the initial temperature of the mafic magma is 1100 °C

$a$  = intrusion half-distance (13 cm)

$\kappa$  = thermal diffusivity (0.5e-6)

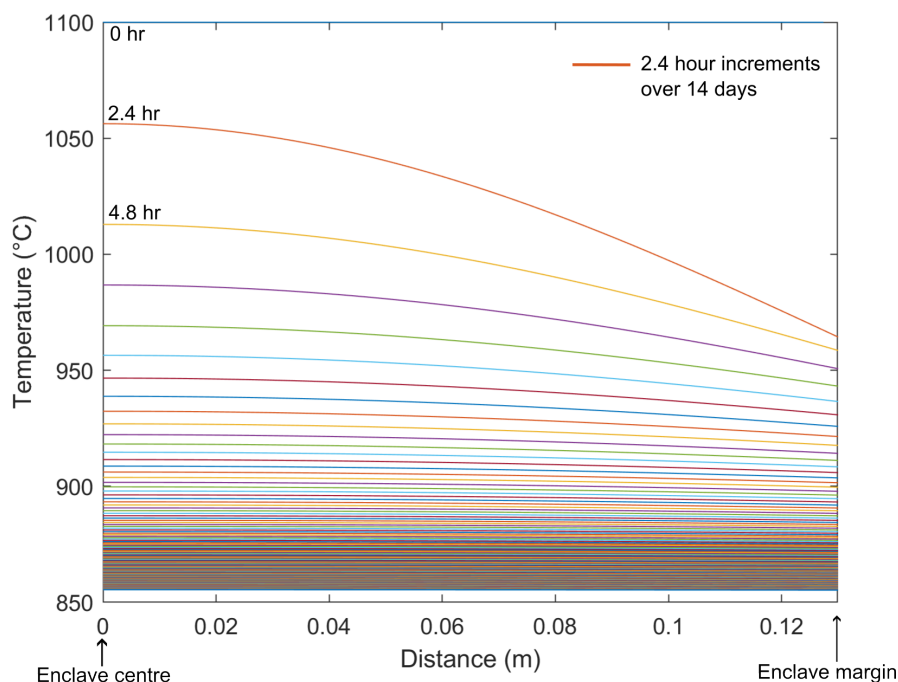


**Figure 6.8:** Cooling of a 26 cm diameter mafic enclave by thermal diffusion over a 14 day period. The margin initially cools more quickly than the insulated interior. They rapidly reach thermal equilibration, within 3 °C of each other 48 hours after mingling.

Figure 6.8 shows how temperature changes across an enclave of 26 cm diameter from centre to exterior margin over 14 days, in 2.4 hour increments. Instantly upon mingling at  $t = 0$ ,

the enclave is 1100 °C, the initial temperature of the mafic magma. Over time, the enclave quickly cools, faster at the margin than in the insulated interior. The mean cooling rate at the margin over the first 12 hours is 13.6 °C hr<sup>-1</sup>, whereas the interior has a slightly lower mean cooling rate of 12.0 °C hr<sup>-1</sup>. For an enclave of 26 cm diameter, the margin and interior reach thermal equilibration rapidly, within 3 °C of each other 48 hours after mingling. An interior of a larger enclave would cool at a slower rate. Whilst the largest enclave observed was only 26 cm diameter (Plail et al., 2017), larger enclaves could possibly form, but not be preserved in eruptive products because they disaggregate in the host andesite. Mechanical disaggregation of enclaves has been shown to occur in many systems (Martin et al., 2006; Tepley et al., 1999; Ruprecht et al., 2020). At SHV enclave disaggregation is evidenced by transfer of mafic microlites into the host andesite (Humphreys et al., 2009). Therefore, if the TRA10A section was the interior of a large enclave, following the findings of Lindoo et al. (in prep), the lower cooling rates experienced in the insulated interior could promote the development of tabular shapes, and explain the absence of prismatic shapes.

Mangler et al. (2024) demonstrated experimentally that plagioclase resorption reduces morphologies towards more equant, higher S/I shapes. This shape is maintained with further overgrowth. Resorption could therefore potentially explain plagioclase shape in TRA10A; is there textural evidence for resorption in this enclave? After Mangler et al. (2024), resorption is characterised as *surficial* (dissolution of crystal exteriors, producing rounded shapes) or *pervasive* (dissolution of crystal interiors, producing sieved textures). TRA10A contains large (2-3 cm) plagioclase with pervasive sieved interiors and clear calcic overgrowth rims, interpreted as inherited phenocrysts from the host andesite, not groundmass crystals (Murphy et al., 2000; Humphreys et al., 2009; Plail et al., 2014). All crystals displaying resorption features (red/orange outlines in Figure 6.9) were therefore discarded from outlining. However, upon reflection, some discarded crystals could be groundmass crystals displaying disequilibrium textures.

Orange outlines (Figure 6.9g-h) highlight discarded crystals due to their sieved, resorbed cores. However, these crystals have smaller intersections and less extensive sieving than the inherited plagioclase (Figure 6.9c) and texturally contribute to the diktytaxitic groundmass texture. These crystals could be re-interpreted as groundmass crystals that have undergone resorption. It should be noted that as these crystals were not outlined, they did not contribute to the plagioclase shape estimate. Even if they were included, it is unlikely this would have measurably changed the result as there are so few (~3 additional w:l measurements).

Regardless, evidence of plagioclase dissolution in the groundmass suggests that at least some crystals have growth histories more complex than simply crystallising in-situ upon mingling. Surficial resorption is more subtle, appearing as rounded cores (Figure 6.9i-j). This is clearer upon comparison to plagioclase with euhedral cores (Figure 6.9d-f). Other crystals possibly display evidence of surficial resorption in their interiors, but it is not certain due to the resolution

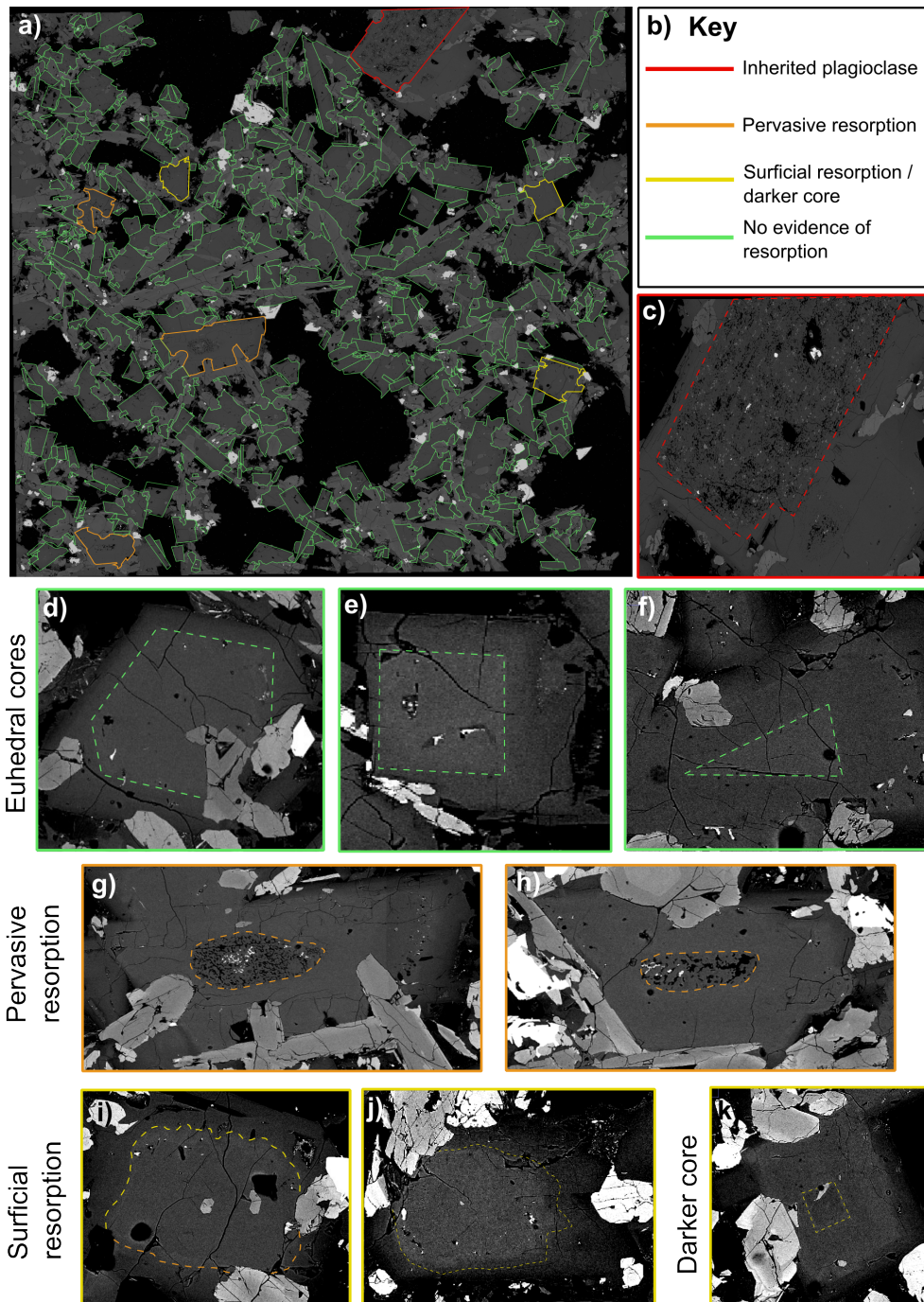


**Figure 6.9:** TRA10A groundmass plagioclase textures. **a)** Full BSE image outlined, with crystals colour-coded (**b)** by textural feature. **c)** Inherited plagioclase phenocryst. **d, e, f)** Groundmass plagioclase with clear euhedral cores and no evidence of resorption. **g, h)** Groundmass plagioclase with evidence of pervasive resorption. **i, j)** Groundmass plagioclase with possible surficial resorption. **k)** Groundmass plagioclase with a visibly darker core.

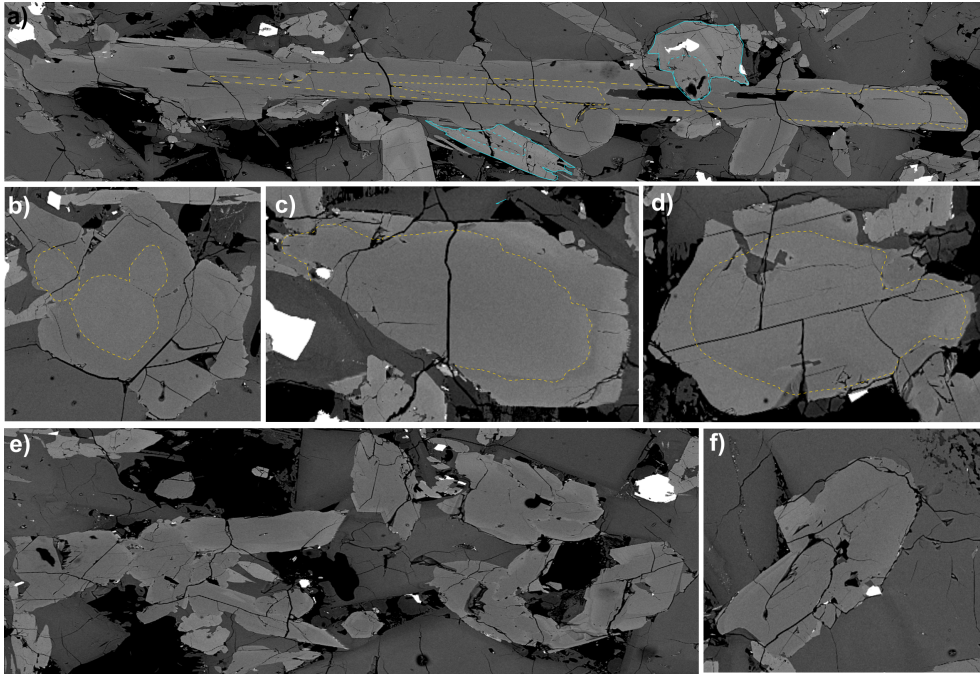


**Figure 6.10:** Complexity in mafic groundmass phases. **a)** Elongate amphibole crystal with complex, rounded zonation (yellow dashes). Intergrown clinopyroxene (blue) with complex zoning and rounded cores. **b,c,d)** Amphibole with lighter, rounded cores (yellow dashes). **e,f)** Amphibole is generally subhedral, with rounded outlines and often smooth contacts with plagioclase.

and contrast of the BSE stitch. Figure 6.9k highlights a groundmass plagioclase crystal with a distinct darker, equant core, further suggesting that some crystals have experienced complex growth histories. Variation in dissolution textures within the groundmass plagioclase, with some showing pervasive resorption and others surficial, is not unexpected as it has been demonstrated both experimentally and with comparison to natural samples that resorption events may not affect all crystals equally (Mangler et al., 2024). Textural complexity of other groundmass phases may further evidence the resorption suggestion. Amphibole displays complex zoning, often presenting as rounded cores (Figure 6.10a-d). Subhedral exteriors have rounded contacts with other crystals (Figure 6.10e,f). Clinopyroxene sometimes appears with rounded dark cores (Figure 6.10a).

Mafic enclaves are interpreted to form by quench crystallisation upon the mingling of two melts that are thermo-mechanically inhibited from mixing fully (e.g., Sparks & Marshall, 1986). Evidence of quench crystallisation includes the diktytaxitic groundmass texture and glassy margins between the host and enclave (Bacon, 1986; Murphy et al., 2000). The rationale of this study was that enclaves provide a simple crystallisation scenario in which to examine crystal shapes. However, groundmass crystals displaying disequilibrium features suggests that some crystals have more complex growth histories than simple quench crystallisation. This was recognised in Mangler et al. (2024), which reported that in quenched mafic inclusions from Mt St Helens Volcano, up to 37 % of crystals display surficial resorption. If some groundmass crystals did experience resorption, this could have reduced their morphologies towards more equant,

lower  $S/I$  shapes. Further growth would not restore the original, tabular shapes, which could be reflected in the single shape population estimate of  $S/I = 0.5$  for groundmass plagioclase in TRA10A. However, as the majority of plagioclase outlined appear to have euhedral cores, further investigation such as higher resolution BSE images of individual crystals is necessary to comment further.

### 6.2.2 Amphibole

TRA10A groundmass amphibole is a single shape population of  $S/I = 0.65 (\pm 0.06)$ . This shape estimate is realistic for amphiboles, which are known to have prismatic habits. The amphibole in this enclave is complicated texturally, with subhedral edges, rounded cores, and complex zonation (Figure 6.10). Plagioclase in TRA10A is also a single shape population. Amphibole appearing as chadacrysts trapped within plagioclase oikocrysts were outlined and measured, in an attempt to capture an earlier stage of crystal growth, following Higgins & Roberge (2003). However, fewer than 20 amphibole chadacrysts were outlined, an insufficient number for analysis with ShapeCalc, inhibiting comment on early amphibole shapes.

### 6.3 Orthopyroxene

Groundmass orthopyroxene in BEL1B-A was found to possibly have two shape populations: a smaller, more equant population of  $S/I = 0.71 (\pm 0.08)$  and a larger, more bladed population of  $S/I = 0.33 (\pm 0.05)$  (Chapter 3). It was inconclusive whether there are distinct shape populations or a single shape population across all sizes (Chapter 5.4). We apply the growth model to reproduce the two suggested size-shape populations, discussing the results in the context of recent work examining orthopyroxene tracht (Okumura et al., 2022; 2024).

#### Growth modelling

**Table 6.2:** Growth model inputs. Total crystallinity increase ( $\varphi_{\text{inc}}$ ) and volumetric number density ( $N_v$ ) after the textural characteristics of orthopyroxene populations in BEL1B-A. Constant parameters in all model runs include initial melt volume = 1 mm<sup>3</sup>, initial crystal volume = 0.1 μm<sup>3</sup> and initial crystal shape = 1:1.05:1.6.

Approach	Step	Population	$\varphi_{\text{inc}}$ (%)	$N_v$ (mm <sup>-3</sup> )	$V_{\text{inc}}$ (μm <sup>3</sup> )	Overgrowth shape	$\delta S/\delta I$
<b>Approach 1</b>	Run 1	n/a	5.1	6902	7389	1:10:25	0.1
<b>Approach 2</b>	Step 1	35 + μm	1.8	955	18,848	1:3:7.5	0.33
	Step 2	0-35 + μm	3.3	7846	4206	1:1.4:2.7	0.71

Approach 1 models the evolution of a 0.1 μm<sup>3</sup> equant crystal to a more bladed, lower  $S/I$  shape (Table 6.2). Like Approach 1 when modelling plagioclase growth, the average volumes of the orthopyroxene populations are much larger than the model cuboid at the same  $S/I$ , as overgrowth to steady-state shape occurs with a small volume increase (10<sup>-1</sup>-10<sup>2</sup> μm) (Figure 6.11). Again, as the average orthopyroxene volumes exceed 100 μm<sup>3</sup>, the only way to reproduce these populations is to use the shape of each orthopyroxene population as the overgrowth shape. Approach 2 therefore varies steady-state shape in the same way as in the plagioclase growth modelling. Changing steady-state shape from  $S/I \approx 0.33$  to 0.71 can reproduce both orthopyroxene shape-size populations (Figure 6.12).

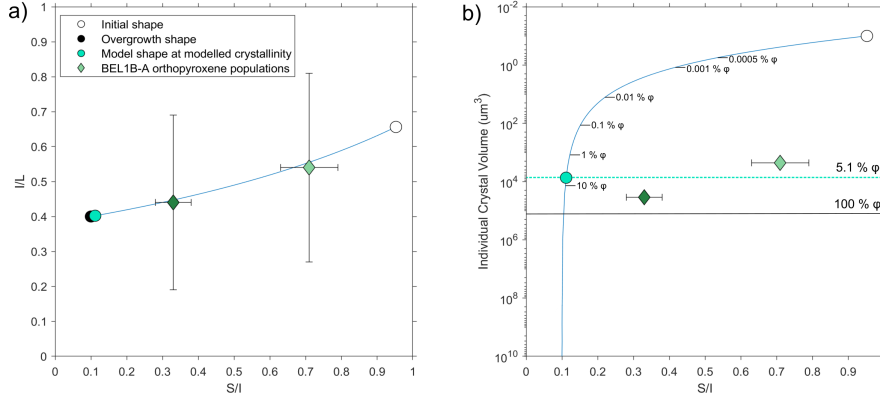


**Figure 6.11:** Approach 1: overgrowth of a  $0.1 \mu\text{m}^3$  equant crystal to a more bladed, lower  $S/I$  shape cannot recreate the orthopyroxene shape-size populations as evolution to steady-state shape occurs with a small volume increase.

In the plagioclase growth modelling, it was suggested that the change in steady-state shape to higher  $S/I$  could be driven by evolution in melt composition with enclave crystallisation. In theory, the same principles could apply to the orthopyroxene populations; changing melt diffusivity could be expressed as variation in euhedral crystal shape, reflected in the transition from large, bladed crystals to smaller, more equant morphologies. This speculation could benefit from a shape-size study of experimentally grown orthopyroxene populations like that of plagioclase in Mangler et al. (2024), as well as further clarity around if distinct shape populations even exist in the groundmass orthopyroxene (Chapter 5).

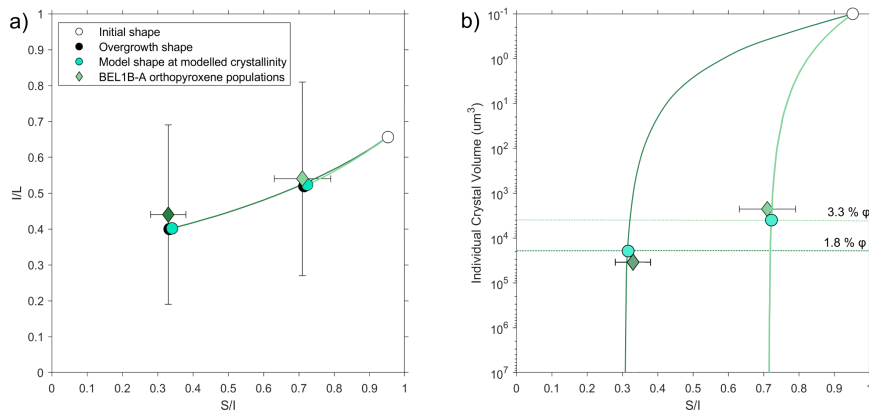


**Figure 6.12:** Approach 2: overgrowth of a  $0.1 \mu\text{m}^3$  equant crystal to two different steady-state shapes can reproduce the orthopyroxene shape-size populations. See text for further explanation.

Recent work (Okumura et al. 2022; 2024) has explored how pyroxene ‘tracht’ is affected by magmatic processes. ‘Tracht’ refers to the combination of crystallographic faces (Sunagawa, 2005). It is distinct from ‘habit’, which typically describes 3D aspect ratio or morphology (i.e., euhedral,  $S:I:L$ ). Okumura et al. (2022) conducted decompression experiments that demonstrated a systematic variation in pyroxene microlite tracht from octagonal to hexagonal as the degree of effective undercooling ( $\Delta T_{\text{eff}}$ ) increases. An examination of pyroxene microlites in

natural samples from the 2011 Shinmoedake eruption (Okumura et al., 2024) further explored this, suggesting that under high ( $\Delta T_{\text{eff}}$ ), the relative growth rates on one of the crystallographic faces becomes faster than those of the other prismatic faces until it disappears.

Our work aimed to establish if orthopyroxene displays a systematic variation in euhedral morphology with increasing size, which was ultimately inconclusive. The recent work examining tracht demonstrates that orthopyroxene can exhibit systematic variation in euhedral morphology, but it is not related to crystal size, with tracht change proposed to be driven by variation in  $\Delta T_{\text{eff}}$ . Undercooling conditions have long been recognised to affect crystal morphologies. The shift from the diffusion-limited growth regime producing anhedral morphologies (dendritic, skeletal, hopper) at high degrees of undercooling, to the interface-controlled growth regime producing euhedral shapes at lower degrees of undercooling has been extensively investigated (Lofgren, 1974; Hammer, 2008; Mollo & Hammer, 2017; Shea & Hammer, 2013). However, few studies have examined variation in euhedral morphology. Mangler et al. (2023) did not find a direct relationship between  $\Delta T_{\text{eff}}$  and plagioclase shape. Instead, as discussed, a dependency on melt diffusivity/composition was suggested. Okumura et al. (2022) recognised that melt composition impacted crystal shape where orthopyroxene grew in close proximity to plagioclase. These crystals displayed heptagonal tracht, whereas other crystals in the same sample that did not grow in proximity to plagioclase were octagonal. It was proposed after Mujin et al. (2017), that plagioclase crystallisation evolves the melt and results in an increase in  $\Delta T_{\text{eff}}$  for pyroxene (Figure 12b in Mujin et al., 2017). In contrast, Okumura et al. (2024) ruled out melt composition as the driver of tracht change. The pyroxene microlites in the most silica- and plagioclase-rich pumice are octagonal, whilst the most silica-poor pumice contained hexagonal microlites; the opposite observations would be expected if plagioclase crystallisation increasing  $\Delta T_{\text{eff}}$  for pyroxene was the driver of tracht change. They do recognise that melt composition may exert control over the threshold at which tracht change occurs, due the influence of melt diffusivity in anisotropic crystal growth (Okumura et al., 2024).

Okumura et al. (2024) used SR-XRCT scans to accurately reconstruct pyroxene microlite shape in 3D. Figure 6.13 compares their 3D reconstructions with our 3D shape estimates. There is no variation in shape, with all pyroxene microlites being prismatic (Okumura et al., 2024). Whilst both this population and our orthopyroxene shape estimate using the smallest intersections (0-35  $\mu\text{m}$ , light green diamond, Figure 6.13) are the same  $S/I$  ( $\sim 0.7-0.8$ ), and are likely within error of  $I/L$  due the difficulty in constraining  $L$  accurately, it is notable that the Okumura et al. (2024) shape estimates plot closer to the single shape population estimate than the 0-35  $\mu\text{m}$  estimate. This could support that our groundmass orthopyroxene is a single shape population. Okumura et al. (2024) do recognise that the pyroxenes in the high- $\text{SiO}_2$  ( $\sim 72$  wt.%) samples that experienced lower  $\Delta T_{\text{eff}}$  are more elongate than those in the low- $\text{SiO}_2$  samples ( $\sim 67$  %) that experienced greater  $\Delta T_{\text{eff}}$  (differences in  $I/L$  in Figure 6.13). This is not a significant difference in habit, but does demonstrate variation in euhedral habit within a single size population of pyroxenes. Similarly, Castro et al. (2003) reconstructed pyroxene microlites in 3D and found they exhibit a range of 3D aspect ratios from equant to prismatic, but this variation does not show an obvious correlation with crystal size. Even with variation in pyroxene shape noted

in Castro et al. (2003) and Okumura et al. (2024), none of their microlites display low  $S/I$  shapes like the bladed morphology of the largest orthopyroxene crystals suggested in this work (Chapter 3). This may not be expected as both examined microlites, but it is notable that a low  $S/I$  shape has not been noted elsewhere. This could potentially support the conclusion that there is a single prismatic population of orthopyroxene in BEL1B-A.

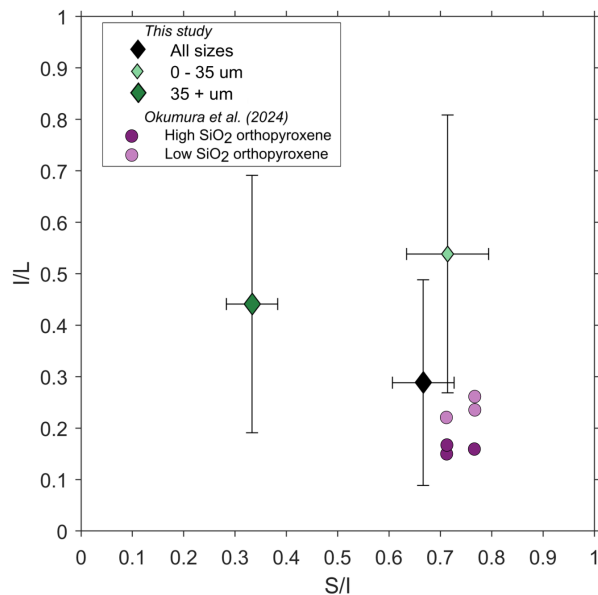


**Figure 6.13:** 3D shape estimates of orthopyroxene populations. All pyroxene microlites (purple circles, Okumura et al. (2024)) are prismatic, with orthopyroxene grown in low silica melt being slightly more elongate than those grown in higher silica melt. These microlites plot within error of the single-shape estimate for this study's orthopyroxene populations.

#### 6.4 Mafic enclave crystallisation at SHV

The mafic enclaves of SHV are ascribed to the mingling of hot ( $\sim 1050$  °C), hydrous basaltic melt with cooler ( $\sim 850$  °C) andesite upon intrusion of the mafic magma into the andesite mush at storage depths of 8-14 km (after Edmonds et al., 2016). The mafic enclaves are interpreted to have formed when molten. This is due to their diktytaxitic groundmass texture of framework plagioclase and the presence of chilled margins between the host andesite and enclave, textural features typical of rapid quench crystallisation in magmatic enclaves (Bacon, 1986; Murphy et al., 2000). The intrusion of mafic magma has long been recognised as a potential eruption trigger, as the addition of heat, mass and volatiles can potentially remobilise the host andesite (Didonna et al., 2019; Clyne, 1999; Devine et al., 1998). The exact dynamics and timescales of the magmatic interaction at SHV is debated. Groundmass textures in the mafic enclaves will reflect their history of crystallisation, and therefore can provide insights into the nature of mingling events.

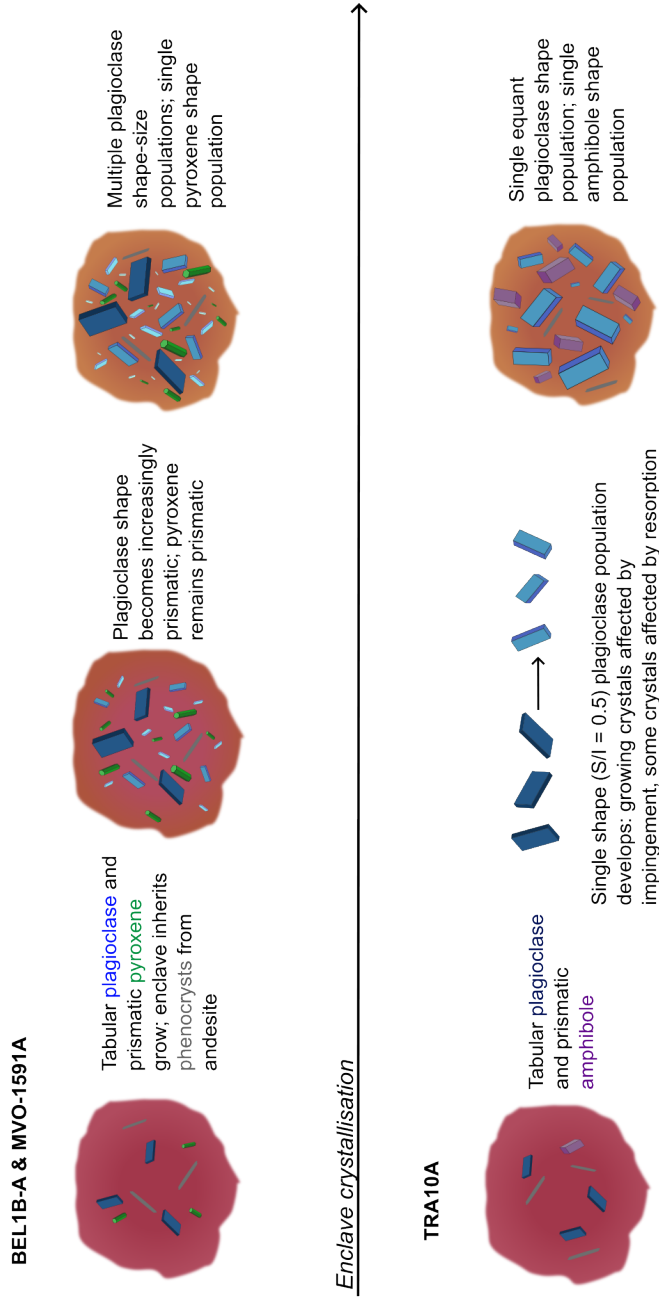
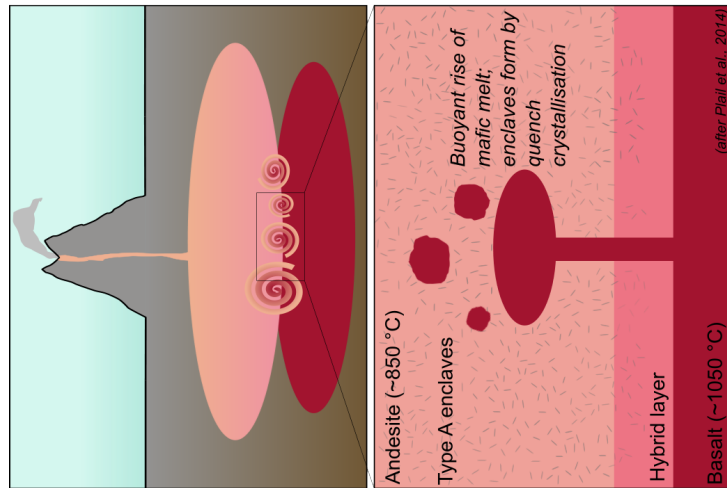


**Figure 6.14:** Intruding basaltic magma buoyantly rises as a plume into the host andesite (after Plail et al., 2014). Type A enclaves form at the plume margins by quench crystallisation, with little hybridisation between the mafic and silicic melts. See text for further explanation.

Plail et al. (2014) characterised Phase V enclaves as Type A, B or C based on geochemical and textural features. BEL1B-A, MVO-1591A and TRA10A were all classified as Type A enclaves (Chapter 3) due to the presence of high-Al groundmass amphibole, high vesicularity and abundant inherited phenocrysts. Type A enclaves are interpreted to form when the mafic magma rises into the host andesite as a buoyant plume. There is little hybridisation between the intruding melt and the silicic host, in contrast to Type B and C enclaves where formation is driven by the development of a hybrid layer at the mafic-silicic interface. The three enclaves studied here are therefore interpreted in line with this model, seen in Figure 6.14. The high cooling rate inferred from the quench crystallisation texture of the groundmass and the presence of chilled margins suggests these enclaves could have possibly formed at plume margins (Browne et al., 2006). Upon mingling, the mafic enclaves gain their inherited phenocrysts of disequilibrium-textured plagioclase, amphibole and orthopyroxene from the host andesite. Rapid undercooling induces crystallisation, with the first nucleated plagioclase growing to tabular forms in the initially basaltic melt. As melt composition evolves with progressive crystallisation, becoming increasingly silicic and losing water by volatile exsolution, the changing melt diffusivity pushes the steady-state overgrowth shape of plagioclase to increasingly high  $S/I$ . Later nucleating plagioclase therefore grow to progressively more prismatic shapes, reflected in the development of multiple shape-size populations in BEL1B-A and MVO-1591A (Figure 6.6; Figure 6.14). Groundmass orthopyroxene does not appear to change shape with size, producing a singular prismatic population. TRA10A, whilst still a Type A enclave, is texturally different to BEL1B-A and MVO-1591A due to its coarser-grained groundmass and single shape populations of groundmass plagioclase and amphibole. The coarser-grained and more equant plagioclase shapes could be due to a lower degree of undercooling promoting longer crystallisation times. The lack of multiple plagioclase populations was suggested to possibly reflect shape alteration due to impingement, evidenced by the highly intergrown and complex groundmass, or possibly resorption, evidenced by the presence of some sieved cores and dissolution surfaces in the groundmass plagioclase. This sample suggests that at least some mafic enclaves or crystals within have more complex growth histories than simple quench crystallisation, despite erupting in the same Phase of eruption. Further detailed geochemical work on groundmass crystals targeting mafic enclaves with diverse textures could provide insights into the dynamic nature of mingling processes at SHV.

## 7 Conclusions

The overarching goal of this work was to use groundmass crystal shape-size relationships in three mafic enclaves to gain insights into enclave crystallisation at SHV. The main aims were outlined in Chapter 1.2. Here, we outline the key findings of this work in the context of these aims, as well as the implications and further questions to be answered.

The three mafic enclaves were characterised texturally and geochemically using optical microscopy and SEM-EDS (Chapter 3). All three were categorised as Type A enclaves according to the framework of Plail et al. (2014), owing to the presence of groundmass amphibole, relatively high vesicularity, and chilled margins in two enclaves. Despite containing the same groundmass assemblage and all being Type A enclaves, there is clear textural diversity between samples. MVO-1591A and BEL1B-A are fine-grained with inherited phenocryst assemblages of plagioclase + amphibole + orthopyroxene, whereas TRA10A is a coarse-grained end-member with only inherited plagioclase. Geochemically, the studied groundmass phases of plagioclase and orthopyroxene, and the interstitial glass are not significantly different. However, the groundmass amphibole in BEL1B-A was significantly different to that of the other two samples and reported compositions (e.g., Plail et al., 2014), instead being similar in major element chemistry to that of the host andesite amphibole. These findings illustrate the diversity in mafic enclaves erupted within a single phase (Phase V), and therefore the range of crystallisation conditions upon mingling at depth. The implication is that any further work proposing a model for the mingling dynamics at SHV should account for this diversity in erupted products.

Crystal intersections were outlined and measured in order to convert the 2D intersection data into 3D shape-size estimates (Chapter 2.3). All three enclaves had an intergrown groundmass, with TRA10A having the most complex intergrowths between crystals. Multiple outlining and measurement approaches were tested to ensure that the final method would most accurately reflect the 2D intersection shapes and sizes, despite the complexity in groundmass texture. The detailed approach to collecting 2D measurements contributed to robust 3D shape-size estimates. This gave assurance when discussing the 3D shape-size results that these estimates, not an artefact of the outlining or measurement method, and instead were true shape-size reconstruction that could be discussed and interpreted in the context of magmatic processes at SHV.

Plagioclase in two enclaves was found to exhibit systematic change in shape with size, from prismatic (high  $S/I$ ) to tabular (low  $S/I$ ) with increasing size (Chapter 4.2). This is in agreement with the findings of Mangler et al. (2022; 2023). Statistical validation confirmed the plagioclase in both enclaves contains multiple shape populations, and that the smallest, most prismatic population could not be explained as corner-cuts of a larger, single-shape crystal population (Chapter 5.1 and 5.2).

The crystallisation conditions under which the observed plagioclase shape-size relationships could be reproduced were explored, applying an adapted crystal growth model (Chapter 6.1). It was found that varying steady-state overgrowth shape can reproduce the plagioclase shape-size populations. This is interpreted in the context of experimental work by Mangler et al.

(2023), where it was shown that plagioclase shape is sensitive to melt composition/diffusivity, with plagioclase grown in basaltic melt being lower  $S/I$  than those grown in more silicic melt. The change in steady-state shape to higher  $S/I$  values with smaller plagioclase populations is proposed to reflect changing melt diffusivity as the mafic enclaves cool and crystallise. Although, it is debated as to whether the relative growth rate of  $S/I$  necessary to reproduce the smallest, most prismatic population is realistic. An improvement to this approach would be to link the interstitial melt composition to semi-quantitatively define melt diffusivity, and then see if this fits within the anisotropic growth model of Mangler et al. (2023).

The crystal growth model is limited in its recreation of natural magmatic scenarios as it cannot model continuous nucleation and growth, nor does it account for the impacts of impingement. Here it was applied in a step-wise fashion with discrete intervals of nucleation and growth to reproduce the plagioclase populations. A more detailed model that could model how crystallinity, individual crystal shape and size evolve continuously would improve the applicability to natural samples, as would accounting for impingement at a certain crystallinity.

Plagioclase in TRA10A does not exhibit a systematic change in shape with size from prismatic to tabular, instead being a single shape of  $S/I = 0.48$ . Statistical validation confirmed it is a single-shape population. This diverges from the trend established by Mangler et al. (2022) and supported in MVO-1519A and BEL1B-A. Multiple factors were discussed that could have contributed to this observation, including impingement affecting crystal growth, which is likely in such a coarse-grained, intergrown sample. Textural disequilibrium features in the groundmass crystals such as sieved cores, rounded interiors and rounded crystal contacts suggest that at least some of these crystals have experienced complex growth histories beyond that of relatively simple and rapid quench crystallisation. The exact details of these more complex histories remains to be investigated, perhaps adding complexity to the existing models (i.e., Plail et al., 2017; Didonna et al., 2022) of mafic-silicic interactions at SHV. The plagioclase in TRA10A having experienced a lower cooling rate than those in the other two enclaves could have contributed to the development of larger, more equant crystals, perhaps in the insulated interior of an enclave. It was also suggested that TRA10A may have been a fragment of a larger enclave that disaggregated. The relationship between crystal shape and undercooling could therefore be applied to interrogate whether enclaves are ‘whole’ or disaggregated. A small enclave with large, equant crystals indicative of low cooling rates, lower than would be expected for the small size of the enclave, could possibly suggest that enclave represents the insulated interior of a larger enclave that disaggregated.

Groundmass orthopyroxene in BEL1B-A was shown to potentially contain two shape-size populations: a larger, more bladed population (lower  $S/I$ ), and a smaller, more equant population (higher  $S/I$ ) (Chapter 4.3.1). Statistical validation did not conclusively confirm that these populations are real, and instead suggested that the smallest population could be corner-cuts of larger, prismatic crystals (Chapter 5.4). Therefore, the groundmass orthopyroxene is interpreted to be a singular, prismatic shape population. The systematic evolution in shape with size observed in plagioclase has not been recreated for this silicate phase. However, orthopyroxene was only measured in one section of one enclave. Further work measuring euhedral pyroxene

of multiple sizes in rocks of different compositions and crystallisation conditions is necessary to make a definitive statement as to whether orthopyroxene undergoes a systematic evolution in shape with size. Moreover, recent work (Okumura et al. 2022; 2024) has demonstrated that pyroxene tracht is related to undercooling conditions and melt composition, demonstrating there is petrogenetic significance in pyroxene shape. Further work exploring tracht in other minerals could reveal whether there is a common growth process across all silicate phases.

Likewise, groundmass amphibole in TRA10A did not display a systematic evolution in shape with size, instead presenting as a single shape population that is relatively prismatic (Chapter 4.4.1). The amphibole, like some of the previously discussed plagioclase crystals, is texturally complex, with rounded cores, complex zonation and occasional overgrowths of clinopyroxene. As plagioclase in this sample was also a single shape population, and amphibole was only measured in one section of one sample, we are unable to make a definitive statement as to whether this silicate phase can display a systematic change in shape with size. Like the orthopyroxene, further work measuring more amphiboles in different rocks is necessary to conclude whether other silicate phases than plagioclase systematically evolve in shape with size, a feature that could be exploited in the interpretation of magmatic processes.

The mafic enclave groundmass crystal shape-size results were interpreted within the mingling model of Plail et al. (2014) (Chapter 6.4). The Type A enclaves of MVO-1519A and BEL1B-A form by rapid quench crystallisation upon the rise of a buoyant plume of the intruding mafic magma into the host andesite. The change in plagioclase shape with size reflects the evolution of melt composition as the enclave cools, crystallises and loses water by volatile exsolution. Orthopyroxene also crystallises, but does not also display a systematic change in shape that can be linked to changing magmatic conditions. The lack of multiple shape populations in Type A enclave of TRA10A highlights the textural diversity in enclaves from a single eruptive Phase, and the presence disequilibrium textures in some groundmass crystals suggests the crystallisation histories of at least some mafic enclaves are more complex than the quench crystallisation. Further work could quantitatively link crystal shape to melt composition in order to better understand the petrogenetic significance of plagioclase shape, which could possibly be used to track how melt diffusivity changes through time, or to better understand the timescales of mingling dynamics.

## 8 References

- Arganda-Carreras, I., Kaynig, V., Rueden, C., Eliceiri, K. W., Schindelin, J., Cardona, A., & Sebastian Seung, H. (2017). Trainable Weka Segmentation: A machine learning tool for microscopy pixel classification. *Bioinformatics (Oxford, England)*, *33*(15), 2424–2426. <https://doi.org/10.1093/bioinformatics/btx180>
- Arzilli, F., Polacci, M., La Spina, G., Le Gall, N., Llewellyn, E. W., Brooker, R. A., Torres-Orozco, R., Di Genova, D., Neave, D. A., Hartley, M. E., Mader, H. M., Giordano, D., Atwood, R., Lee, P. D., Heidelbach, F., & Burton, M. R. (2022). Dendritic crystallization in hydrous basaltic magmas controls magma mobility within the Earth's crust. *Nature Communications*, *13*(1), 3354. <https://doi.org/10.1038/s41467-022-30890-8>
- Aspinall, W. P., Miller, A. D., Lynch, L. L., Latchman, J. L., Stewart, R. C., White, R. A., & Power, J. A. (1998). Soufrière Hills eruption, Montserrat, 1995 - 1997: Volcanic earthquake locations and fault plane solutions. *Geophysical Research Letters*, *25*(18), 3397–3400. <https://doi.org/10.1029/98GL00858>
- Bacon, C. R. (1986). Magmatic inclusions in silicic and intermediate volcanic rocks. *Journal of Geophysical Research: Solid Earth*, *91*(B6), 6091–6112. <https://doi.org/10.1029/JB091iB06p06091>
- Barclay, J., Rutherford, M.J., Carroll, M.R., Murphy, M.D., Devine, J.D., Gardner, J., & Sparks, R.S.J. (1998) Experimental phase equilibria constraints on preemptive storage conditions of the Soufriere Hills magma. *Geophysical Research Letters*, *25*(18), 3437–3440. <https://doi.org/10.1029/98GL00856>
- Barclay, J., Herd, R. A., Edwards, B. R., Christopher, T., Kiddle, E. J., Plail, M., & Donovan, A. (2010). Caught in the act: Implications for the increasing abundance of mafic enclaves during the recent eruptive episodes of the Soufrière Hills Volcano, Montserrat. *Geophysical Research Letters*, *37*(19). <https://doi.org/10.1029/2010GL042509>
- Bennett, E.N., Lissenberg, C.J., & Cashman, K.V., (2019). The significance of plagioclase textures in mid-ocean ridge basalt (Gakkel Ridge, Arctic Ocean). *Contributions to Mineralogy and Petrology* *174*, 49 <https://doi.org/10.1007/s00410-019-1587-1>
- Blundy, J., & Cashman, K. (2008). Petrologic Reconstruction of Magmatic System Variables and Processes. *Minerals, Inclusions and Volcanic Processes*, *69*, 179–239.
- Browne, B., & Gardner, J. (2006). The influence of magma ascent path on the texture, mineralogy, and formation of hornblende reaction rims. *Earth and Planetary Science Letters*, *246*, 161–176. <https://doi.org/10.1016/j.epsl.2006.05.006>
- Browne, B.L., Eichelberger, J.C., Patino, L.C., Vogel, T.A., Dehn, J., Uto, K., & Hoshizumi, H., (2006). Generation of Porphyritic and Equigranular Mafic Enclaves During Magma Recharge Events at Unzen Volcano, Japan. *Journal of Petrology*, *47*(2), 301–328. <https://doi.org/10.1093/petrology/egi076>
- Brugger, C. R., & Hammer, J. E. (2010). Crystal size distribution analysis of plagioclase in

- experimentally decompressed hydrous rhyodacite magma. *Earth and Planetary Science Letters*, *300*(3), 246–254. doi: 10.1016/j.epsl.2010.09.046
- Brugger, C. R., & Hammer, J. E. (2015). Prevalence of growth twins among anhedral plagioclase microlites. *American Mineralogist*, *100*(2–3), 385–395. <https://doi.org/10.2138/am-2015-4809>
- Cashman, K. V. (1990). Textural constraints on the kinetics of crystallization of igneous rocks. *Reviews in Mineralogy and Geochemistry*, *24*(1), 259–314.
- Cashman, K. V. (1992a). Groundmass crystallization of Mount St. Helens dacite, 1980–1986: A tool for interpreting shallow magmatic processes. *Contributions to Mineralogy and Petrology*, *109*(4), 431–449. <https://doi.org/10.1007/BF00306547>
- Cashman, K. V. (1992b). Groundmass crystallization of Mount St. Helens dacite, 1980–1986: A tool for interpreting shallow magmatic processes. *Contributions to Mineralogy and Petrology*, *109*(4), 431–449. <https://doi.org/10.1007/BF00306547>
- Cashman, K. V. (2018). Chapter 10. Textural constraints on the kinetics of crystallisation of igneous rocks. In J. Nicholls & K. Russell (Eds.), *Modern Methods of Igneous Petrology: Understanding Magmatic Processes* (pp. 259–316). De Gruyter. <https://doi.org/10.1515/9781501508769-014>
- Cashman, K. V. (2020). Crystal Size Distribution (CSD) Analysis of Volcanic Samples: Advances and Challenges. *Frontiers in Earth Science*, *8*. <https://doi.org/10.3389/feart.2020.00291>
- Cashman, K. V., & Marsh. (1988a). Crystal size distribution (CSD) in rocks and the kinetics and dynamics of crystallization II: Makaopuhi lava lake. *Contributions to Mineralogy and Petrology*, *99*(3), 292–305. <https://doi.org/10.1007/BF00375363>
- Cashman, K. V., & Marsh, B. D. (1988b). Crystal size distribution (CSD) in rocks and the kinetics and dynamics of crystallization II: Makaopuhi lava lake. *Contributions to Mineralogy and Petrology*, *99*(3), 292–305. <https://doi.org/10.1007/BF00375363>
- Castro, J. M., Cashman, K. V., & Manga, M. (2003). A technique for measuring 3D crystal-size distributions of prismatic microlites in obsidian. *American Mineralogist*, *88*(8–9), 1230–1240. <https://doi.org/10.2138/am-2003-8-906>
- Christopher, T., Edmonds, M., Humphreys, M. C. S., & Herd, R. A. (2010). Volcanic gas emissions from Soufrière Hills Volcano, Montserrat 1995–2009, with implications for mafic magma supply and degassing. *Geophysical Research Letters*, *37*(19). <https://doi.org/10.1029/2009GL041325>
- Christopher, T., Humphreys, M. C. S., Barclay, J., Genareau, K., De Angelis, S. M. H., Plail, M., & Donovan, A. (2014). *Petrological and geochemical variation during the Soufrière Hills eruption, 1995 to 2010*. <https://doi.org/10.1144/m39.17>
- Clynne, M. A. (1999). A Complex Magma Mixing Origin for Rocks Erupted in 1915, Lassen Peak, California. *Journal of Petrology*, *40*(1), 105–132. <https://doi.org/10.1093/etroj/40.1.105>
- Coombs, M. L., Eichelberger, J. C., & Rutherford, M. J. (2003). Experimental and textural

- constraints on mafic enclave formation in volcanic rocks. *Journal of Volcanology and Geothermal Research*, 119(1), 125–144. [https://doi.org/10.1016/S0377-0273\(02\)00309-8](https://doi.org/10.1016/S0377-0273(02)00309-8)
- Delesse, M. A. (1847). Procédé mécanique pour déterminer la composition des roches – ScienceOpen. *Comptes Rendus de l'academie Des Sciences*, 25(544–545).  
<https://www.scienceopen.com/document?vid=622e8e04-0eab-49d7-871c-661e49aa4d78>
- Devine, J. D., Murphy, M. D., Rutherford, M. J., Barclay, J., Sparks, R. S. J., Carroll, M. R., Young, S. R., & Gardner, J. E. (1998). Petrologic evidence for pre-eruptive pressure-temperature conditions, and recent reheating, of andesitic magma erupting at the Soufriere Hills Volcano, Montserrat, W.I. *Geophysical Research Letters*, 25(19), 3669–3672.  
<https://doi.org/10.1029/98GL01330>
- Devine, J. D., Rutherford, M.J., Norton, G.E., & Young, S.R. (2003). Magma Storage Region Processes Inferred from Geochemistry of Fe-Ti Oxides in Andesitic Magma, Soufriere Hills Volcano, Montserrat, W.I. *Journal of Petrology*, 44(8), 1375–1400.  
<https://doi.org/10.1093/petrology/44.8.1375>
- Didonna, R., Costa, F., Handley, H., Turner, S., & Barclay, J. (2022). Dynamics and timescales of mafic–silicic magma interactions at Soufrière Hills Volcano, Montserrat. *Contributions to Mineralogy and Petrology*, 177(2), 28. <https://doi.org/10.1007/s00410-022-01891-z>
- Edmonds, M., Aiuppa, A., Humphreys, M., Moretti, R., Giudice, G., Martin, R. S., Herd, R. A., & Christopher, T. (2010). Excess volatiles supplied by mingling of mafic magma at an andesite arc volcano. *Geochemistry, Geophysics, Geosystems*, 11(4).  
<https://doi.org/10.1029/2009GC002781>
- Edmonds, M., Kohn, S.C., Hauri, E.H., Humphreys, M.C.S. & Cassidy, M., (2016). Extensive, water-rich magma reservoir beneath southern Montserrat. *Lithos*, 252–253, 216–233.  
<https://doi.org/10.1016/j.lithos.2016.02.026>
- Eichelberger, J. C. (1980). Vesiculation of mafic magma during replenishment of silicic magma reservoirs. *Nature*, 288(5790), 446–450. <https://doi.org/10.1038/288446a0>
- Elsworth, D., Mattioli, G., Taron, J., Voight, B., & Herd, R. (2008). Implications of magma transfer between multiple reservoirs on eruption cycling. *Science (New York, N. Y.)*, 322(5899), 246–248. <https://doi.org/10.1126/science.1161297>
- Furlong, K.P., Hanson, R.B., & Bowers, J.R., 1991. Chapter 10: Modelling thermal regimes. In D.M. Kerrick (Ed.), *Contact Metamorphism, Rev. Mineral*, 26, 437–505.
- Ginibre, C., Kronz, A., & Wörner, G. (2002). High-resolution quantitative imaging of plagioclase composition using accumulated backscattered electron images: New constraints on oscillatory zoning. *Contributions to Mineralogy and Petrology*, 142, 436–448.  
<https://doi.org/10.1007/s004100100298>
- Hammer, J. E., Cashman, K. V., Hoblitt, R. P., & Newman, S. (1999). Degassing and microlite crystallization during pre-climactic events of the 1991 eruption of Mt. Pinatubo, Philippines. *Bulletin of Volcanology*, 60(5), 355–380. <https://doi.org/10.1007/s004450050238>

- Hammer, J. E., & Rutherford, M. J. (2002). An experimental study of the kinetics of decompression-induced crystallization in silicic melt. *Journal of Geophysical Research: Solid Earth*, *107*(B1), ECV 8-1-ECV 8-24. <https://doi.org/10.1029/2001JB000281>
- Higgins, M. D. (1994). Numerical modeling of crystal shapes in thin sections: Estimation of crystal habit and true size. *American Mineralogist*, *79*(1–2), 113–119.
- Higgins, M. D. (1996a). Crystal size distributions and other quantitative textural measurements in lavas and tuff from Egmont volcano (Mt. Taranaki), New Zealand. *Bulletin of Volcanology*, *58*(2), 194–204. <https://doi.org/10.1007/s004450050135>
- Higgins, M. D. (1996b). Magma dynamics beneath Kameni volcano, Thera, Greece, as revealed by crystal size and shape measurements. *Journal of Volcanology and Geothermal Research*, *70*(1), 37–48. [https://doi.org/10.1016/0377-0273\(95\)00045-3](https://doi.org/10.1016/0377-0273(95)00045-3)
- Higgins, M. D. (2000). Measurement of Crystal Size Distributions. *American Mineralogist*, *85*, 1105–1116. <https://doi.org/10.2138/am-2000-8-901>
- Higgins, M. D. (2002a). A crystal size-distribution study of the Kiglapait layered mafic intrusion, Labrador, Canada: Evidence for textural coarsening. *Contributions to Mineralogy and Petrology*, *144*(3), 314–330. <https://doi.org/10.1007/s00410-002-0399-9>
- Higgins, M. D. (2002b). Closure in crystal size distributions (CSD), verification of CSD calculations, and the significance of CSD fans. *American Mineralogist*, *87*, 1244–1244. <https://doi.org/10.2138/am-2002-0118>
- Higgins, M. D., & Roberge, J. (2003). Crystal Size Distribution of Plagioclase and Amphibole from Soufrière Hills Volcano, Montserrat: Evidence for Dynamic Crystallization–Textural Coarsening Cycles. *Journal of Petrology*, *44*(8), 1401–1411. <https://doi.org/10.1093/petrology/44.8.1401>
- Holness, M. B. (2014). The effect of crystallization time on plagioclase grain shape in dolerites. *Contributions to Mineralogy and Petrology*, *168*(5), 1076. <https://doi.org/10.1007/s00410-014-1076-5>
- Humphreys, M. C. S., Christopher, T., & Hards, V. (2009). Microlite transfer by disaggregation of mafic inclusions following magma mixing at Soufrière Hills volcano, Montserrat. *Contributions to Mineralogy and Petrology*, *157*(5), 609–624. <https://doi.org/10.1007/s00410-008-0356-3>
- Humphreys, M. C. S., Edmonds, M., Christopher, T., & Hards, V. (2010). Magma hybridisation and diffusive exchange recorded in heterogeneous glasses from Soufrière Hills Volcano, Montserrat. *Geophysical Research Letters*, *37*(19), L00E06, doi:10.1029/2009GL041926.
- Humphreys, M., Edmonds, M., Plail, M., Barclay, J., Parkes, D., & Christopher, T. (2013). A new method to quantify the real supply of mafic components to a hybrid andesite. *Mineralogy and Petrology*, *165*, 191–215. <https://doi.org/10.1007/s00410-012-0805-x>
- Kent, A. J. R., Darr, C., Koleszar, A. M., Salisbury, M. J., & Cooper, K. M. (2010). Preferential eruption of andesitic magmas through recharge filtering. *Nature Geoscience*, *3*(9), 631–636.

<https://doi.org/10.1038/ngeo924>

Kirkpatrick, R. J. (1975). Crystal growth from the melt: A review. *American Mineralogist*, *60*(9–10), 798–814.

Larsen, J. F., Nye, C. J., Coombs, M. L., Tilman, M., Izbekov, P., & Cameron, C. (2010a). Petrology and geochemistry of the 2006 eruption of Augustine Volcano: Chapter 15 in *The 2006 eruption of Augustine Volcano, Alaska*. In *Professional Paper* (Nos. 1769–15; pp. 335–382). U.S. Geological Survey. <https://doi.org/10.3133/pp176915>

Laumonier, M., Scaillet, B., Pichavant, M., Champallier, R., Andujar, J., & Arbaret, L. (2014). On the conditions of magma mixing and its bearing on andesite production in the crust. *Nature Communications*, *5*(1), 5607. <https://doi.org/10.1038/ncomms6607>

Lofgren, G. (1974). An experimental study of plagioclase crystal morphology; isothermal crystallization. *American Journal of Science*, *274*(3), 243–273. <https://doi.org/10.2475/ajs.274.3.243>

Lofgren, G. E. (1983). Effect of Heterogeneous Nucleation on Basaltic Textures: A Dynamic Crystallization Study. *Journal of Petrology*, *24*(3), 229–255. <https://doi.org/10.1093/petrology/24.3.229>

Mangan, M. T. (1990). Crystal size distribution systematics and the determination of magma storage times: The 1959 eruption of Kilauea volcano, Hawaii. *Journal of Volcanology and Geothermal Research*, *44*(3), 295–302. [https://doi.org/10.1016/0377-0273\(90\)90023-9](https://doi.org/10.1016/0377-0273(90)90023-9)

Mangler, M. F., Humphreys, M. C. S., Wadsworth, F. B., Iveson, A. A., & Higgins, M. D. (2022). Variation of plagioclase shape with size in intermediate magmas: A window into incipient plagioclase crystallisation. *Contributions to Mineralogy and Petrology*, *177*(6), 64. <https://doi.org/10.1007/s00410-022-01922-9>

Mangler, M. F., Humphreys, M. C. S., Geifman, E., Iveson, A. A., Wadsworth, F. B., Brooker, R. A., Lindoo, A., & Hammond, K. (2023). Melt Diffusion-Moderated Crystal Growth and its Effect on Euhedral Crystal Shapes. *Journal of Petrology*, *64*(8), egad054. <https://doi.org/10.1093/petrology/egad054>

Mangler, M. F., Humphreys, M. C. S., Iveson, A.A., Cooper, K.M., Clynne, M.A., Lindoo, A., Brooker, R.A., Wadsworth, F.B., 2024. Crystal Resorption as a Driver for Mush Maturation: an Experimental Investigation, *Journal of Petrology*, *65*(9), egae088, <https://doi.org/10.1093/petrology/egae088>

Mangler, M. F. (2024b). *Crystal Shapes: Terminology, Counting Strategy, 2D-3D conversion*.

Marsh, B. D. (1988). Crystal size distribution (CSD) in rocks and the kinetics and dynamics of crystallization. *Contributions to Mineralogy and Petrology*, *99*(3), 277–291. <https://doi.org/10.1007/BF00375362>

Marsh, B. D. (1998). On the Interpretation of Crystal Size Distributions in Magmatic Systems. *Journal of Petrology*, *39*(4), 553–599.

<https://doi.org/10.1093/etroj/39.4.553>

Martel, C. (2012). Eruption Dynamics Inferred from Microlite Crystallization Experiments: Application to Plinian and Dome-forming Eruptions of Mt. Pelée (Martinique, Lesser Antilles). *Journal of Petrology*, 53(4), 699–725. <https://doi.org/10.1093/etrology/egr076>

Martin, V. M., Pyle, D. M., & Holness, M. B. (2006). The role of crystal frameworks in the preservation of enclaves during magma mixing. *Earth and Planetary Science Letters*, 248(3), 787–799. <https://doi.org/10.1016/j.epsl.2006.06.030>

Mock, A., & Jerram, D. A. (2005). Crystal Size Distributions (CSD) in Three Dimensions: Insights from the 3D Reconstruction of a Highly Porphyritic Rhyolite. *Journal of Petrology*, 46(8), 1525–1541. <https://doi.org/10.1093/etrology/egi024>

Muncill, G. E., & Lasaga, A. C. (1987). Crystal-growth kinetics of plagioclase in igneous systems; one-atmosphere experiments and application of a simplified growth model. *American Mineralogist*, 72(3–4), 299–311.

Murphy, M. D., Sparks, R. S. J., Barclay, J., Carroll, M. R., & Brewer, T. S., (2000). Remobilization of Andesite Magma by Intrusion of Mafic Magma at the Soufriere Hills Volcano, Montserrat, West Indies. *Journal of Petrology*, 41(1), 21–42. <https://doi.org/10.1093/etrology/41.1.21>

Murphy, M. D., Sparks, R. S. J., Barclay, J., Carroll, M. R., Lejeune, A.-M., Brewer, T. S., Macdonald, R., Black, S., & Young, S. (1998). The role of magma mixing in triggering the current eruption at the Soufriere Hills Volcano, Montserrat, West Indies. *Geophysical Research Letters*, 25(18), 3433–3436. <https://doi.org/10.1029/98GL00713>

Okumura, S. H., Mujin, M., Tsuchiyama, A., & Miyake, A. (2024). Crystal habit (tracht) of groundmass pyroxene crystals recorded magma ascent paths during the 2011 Shinmoedake eruption. *American Mineralogist*, 109(2), 325–338. <https://doi.org/10.2138/am-2022-8765>

Okumura, S. H., Okumura, S., & Miyake, A. (2022). Tracht change of groundmass pyroxene crystals in decompression experiments. *Journal of Mineralogical and Petrological Sciences*, 117(1), n/a. <https://doi.org/10.2465/jmps.211219> Jessica F. Larsen<sup>1</sup>, Christopher J. Nye<sup>2</sup>, Michelle L. Coombs<sup>3</sup>, Mariah Tilman<sup>1</sup>, Pavel Izbekov<sup>1</sup>, and Cheryl Cameron<sup>2</sup>

Pallister, J. S., Hoblitt, R. P., & Reyes, A. G. (1992). A basalt trigger for the 1991 eruptions of Pinatubo volcano? *Nature*, 356(6368), 426–428. <https://doi.org/10.1038/356426a0>

Pallister, J. S., Hoblitt, R. P., Meeker, G.P., Knight, R.J., Siems & D.F., (1996). Magma mixing at Mount Pinatubo: Petrographic and chemical evidence from the 1991 deposits. In *Fire and Mud: Eruptions and Lahars of Mount Pinatubo, Philippines* (C. G. Newhall & R. Punongbayan, pp. 687–732). University of Washington Press.

Plail, M., Barclay, J., Humphreys, M., Edmonds, M., Herd, R., & Christopher, T. (2014). Characterisation of mafic enclaves in the erupted products of Soufrière Hills Volcano, Montserrat 2009-2010. *Geological Society London Memoirs*.

- Plail, M., Edmonds, M., Woods, A. W., Barclay, J., Humphreys, M. C. S., Herd, R. A., & Christopher, T. (2018). Mafic enclaves record syn-eruptive basalt intrusion and mixing. *Earth and Planetary Science Letters*, *484*, 30–40. <https://doi.org/10.1016/j.epsl.2017.11.033>
- Randolph, A. D., & Larsen, M. A. (1971). *Theory of Particulate Processes*. New York Academic Press.
- Ruprecht, P., Simon, A. C., & Fiege, A. (2020). The Survival of Mafic Magmatic Enclaves and the Timing of Magma Recharge. *Geophysical Research Letters*, *47*(14), e2020GL087186. <https://doi.org/10.1029/2020GL087186>
- Rutherford, M., & Hill, P. (1993). Magma ascent rates from amphibole breakdown: An experimental study applied to the 1980–1986 Mount St. Helens eruptions. *Journal of Geophysical Research*, *981*. <https://doi.org/10.1029/93JB01613>
- Rutherford, M., & Devine, J. D. (2003). Magmatic Conditions and Magma Ascent as Indicated by Hornblende Phase Equilibria and Reactions in the 1995–2002 Soufrière Hills Magma. *Journal of Petrology*, *44*(8), 1433–1453. <https://doi.org/10.1093/petrology/44.8.1433>
- Ryan, G. A., Loughlin, S. C., James, M. R., Jones, L. D., Calder, E. S., Christopher, T., Strutt, M. H., & Wadge, G. (2010). Growth of the lava dome and extrusion rates at Soufrière Hills Volcano, Montserrat, West Indies: 2005–2008. *Geophysical Research Letters*, *37*(19). <https://doi.org/10.1029/2009GL041477>
- Salisbury, M. J., Bohron, W. A., Clynne, M. A., Ramos, F. C., & Hoskin, P. (2008). Multiple Plagioclase Crystal Populations Identified by Crystal Size Distribution and in situ Chemical Data: Implications for Timescales of Magma Chamber Processes Associated with the 1915 Eruption of Lassen Peak, CA. *Journal of Petrology*, *49*(10), 1755–1780. <https://doi.org/10.1093/petrology/egn045>
- Schindelin, J., Arganda-Carreras, I., Frise, E., Kaynig, V., Longair, M., Pietzsch, T., Preibisch, S., Rueden, C., Saalfeld, S., Schmid, B., Tinevez, J.-Y., White, D. J., Hartenstein, V., Eliceiri, K., Tomancak, P., & Cardona, A. (2012). Fiji: An open-source platform for biological-image analysis. *Nature Methods*, *9*(7), 676–682. <https://doi.org/10.1038/nmeth.2019>
- Shea, T., & Hammer, J. E. (2013). Kinetics of cooling- and decompression-induced crystallization in hydrous mafic-intermediate magmas. *Journal of Volcanology and Geothermal Research*, *260*, 127–145. <https://doi.org/10.1016/j.jvolgeores.2013.04.018>
- Sparks, R. S. J., & Marshall, L. A. (1986). Thermal and mechanical constraints on mixing between mafic and silicic magmas. *Journal of Volcanology and Geothermal Research*, *29*(1), 99–124. [https://doi.org/10.1016/0377-0273\(86\)90041-7](https://doi.org/10.1016/0377-0273(86)90041-7)
- Sparks, R. S. J., & Young, S. R. (2002). The eruption of Soufrière Hills Volcano, Montserrat (1995–1999): Overview of scientific results. In T. H. Druitt & B. P. Kokelaar (Eds.), *The Eruption of Soufrière Hills Volcano, Montserrat from 1995 to 1999* (Vol. 21, p. 0). Geological Society of London. <https://doi.org/10.1144/GSL.MEM.2002.021.01.03>

- Sparks, S. R. J., Sigurdsson, H., & Wilson, L. (1977). Magma mixing: A mechanism for triggering acid explosive eruptions. *Nature*, *267*(5609), 315–318. <https://doi.org/10.1038/267315a0>
- Streck, M. (2008). Mineral Textures and Zoning as Evidence for Open System Processes. *Reviews in Mineralogy & Geochemistry*, (*69*), 595–622. [10.2138/rmg.2008.69.15](https://doi.org/10.2138/rmg.2008.69.15).
- Sunagawa, I. (2005). *Crystals: Growth, Morphology, and Perfection*. pp. 295, Cambridge University Press, New York.
- Tepley, F. J., III, Davidson, J. P., & Clyne, M. A. (1999). Magmatic Interactions as Recorded in Plagioclase Phenocrysts of Chaos Crags, Lassen Volcanic Center, California. *Journal of Petrology*, *40*(5), 787–806. <https://doi.org/10.1093/petroj/40.5.787>
- Tepley, F. J., III, Davidson, J. P., Tilling, R. I., & Arth, J. G. (2000). Magma Mixing, Recharge and Eruption Histories Recorded in Plagioclase Phenocrysts from El Chichón Volcano, Mexico. *Journal of Petrology*, *41*(9), 1397–1411. <https://doi.org/10.1093/petrology/41.9.1397>
- Wadge, G., Voight, B., Sparks, R. S. J., Cole, P. D., Loughlin, S. C., & Robertson, R. E. A. (2014). Chapter 1 An overview of the eruption of Soufrière Hills Volcano, Montserrat from 2000 to 2010. *Geological Society, London, Memoirs*, *39*(1), 1–40. <https://doi.org/10.1144/m39.1>
- Zellmer, G. F., Hawkesworth, C. J., Sparks, R. S. J., Thomas, L. E., Harford, C. L., Brewer, T. S., & Loughlin, S. C. (2003a). Geochemical Evolution of the Soufrière Hills Volcano, Montserrat, Lesser Antilles Volcanic Arc. *Journal of Petrology*, *44*(8), 1349–1374. <https://doi.org/10.1093/petrology/44.8.1349>
- Zellmer, G., Sparks, R., Hawkesworth, C., & Wiedenbeck, M. (2003b). Magma Emplacement and Remobilization Timescales Beneath Montserrat: Insights from Sr and Ba profiles across plagioclase phenocrysts. *Journal of Petrology*, *FIX*
- Zellmer, G. F., Iizuka, Y., & Straub, S. M. (2024). Origin of Crystals in Mafic to Intermediate Magmas from Circum-Pacific Continental Arcs: Transcrustal Magmatic Systems Versus Transcrustal Plutonic Systems. *Journal of Petrology*, *65*(3), egae013. <https://doi.org/10.1093/petrology/egae013>

## A Appendix A: crystal growth model code

Here we present the crystal growth model code used in Chapter 6, adapted after Mangler et al. (2022). We also present the textural characteristics of plagioclase in MVO-1519A and orthopyroxene in BEL1B-A that were used to calculate model inputs.

### A.1 Crystal growth modelling MatLab code

```
%% Crystal Growth Model after Mangler et al., 2022
% Follows the same structure as Excel model
% Inputs are required in the 'User inputs' cell and the 'Crystal shape
  calculations' cell:

%% User inputs
ReferenceVolume = 1; % Reference volume of magma, mm^3

Xtlinity = 0.3626; % Total increase in crystallisation wanted for the
  reference volume of magma

NVxtl = 17510; % Volumetric number density of crystals

InitialIndividualXtlVolume = 0.1*10^-9; % Volume of a single crystal before
  overgrowth, mm^-3

%% Volume calculations

% Calculate total volume of crystals before overgrowth
InitialTotalXtlVolume = InitialIndividualXtlVolume * NVxtl;

% Calculate volume of magma remaining, accounting for volume of initial
  crystals
RemainingReferenceVolume = ReferenceVolume - InitialTotalXtlVolume;

% Calculate percentage of reference volume already crystallised, constituted
  by the initial crystal population
InitialXtlisation = (ReferenceVolume - RemainingReferenceVolume) * 100;

% Calculate crystallisation increase modelled, accounting for the initial
  crystallisation
XtlisationIncreaseModelled = (Xtlinity * 100) - InitialXtlisation;

% Calculate volume increase per crystal (if no nucleation)
Vincperxtl = ((RemainingReferenceVolume * 10^9) *
  (XtlisationIncreaseModelled / 100)) / NVxtl;

%% Crystal shape calculations

% Define initial crystal shape (INPUT HERE)
S_0 = 1;
I_0 = 1.3;
L_0 = 6;
```

```

% Calculate S/I and I/L of initial shape
S0_div_I0 = S_0/I_0;
I0_div_L0 = I_0/L_0;

% Calculate initial crystal scaling factor
syms F;
eqn = (InitialIndividualXtlVolume*10^9) == (S_0*F)*(I_0*F)*(L_0*F);
F_sol = double(solve(eqn, F, "Real", true));

% Scale initial crystal shape
Sscaled = S_0 * F_sol;
Iscaled = I_0 * F_sol;
Lscaled = L_0 * F_sol;

SI = Sscaled * Iscaled;
IL = Iscaled * Lscaled;
SL = Sscaled * Lscaled;

% Define overgrowth crystal shape (INPUT HERE)
deltaS = 1;
deltaI = 10;
deltaL = 12;

% Calculate S/I and I/L of overgrowth shape
S1_div_I1 = deltaS/deltaI;
I1_div_L1 = deltaI/deltaL;

%% Trigonometric calculations

BetaS = toDegrees("radians", (atan(deltaS/sqrt(deltaL^2+deltaI^2))));
BetaI = toDegrees("radians", (atan(deltaI/sqrt(deltaS^2+deltaL^2))));
BetaL = toDegrees("radians", (atan(deltaL/sqrt(deltaS^2+deltaI^2))));

% Generate model points between initial and overgrowth shape by solving for k
for range of I values
% Create an array of I values between the initial and overgrowth shape
S_div_I_values = S0_div_I0:-0.005:S1_div_I1;
values = [S_div_I_values, S1_div_I1];
I_values = 1./([S_div_I_values, S1_div_I1]);

% Calculate k values for array of I values
k_values = zeros(size(I_values)); % Array to store results of function

for i = 1:length(I_values)
    I2 = I_values(i);

    % Define the function to solve:
    fun = @(k) (Iscaled + 2*((sind(BetaI))*k)) / (Sscaled +
        2*((sind(BetaS))*k)) - I2;

```

```

% Solve for k numerically
k = fsolve(fun, 0);

k_values(i) = k;
end

DeltaS = sind(BetaS) * k_values;
DeltaI = sind(BetaI) * k_values;
DeltaL = sind(BetaL) * k_values;

SPrime = Sscaled + (2*DeltaS);
IPrime = Iscaled + (2*DeltaI);
LPrime = Lscaled + (2*DeltaL);

% Calculate new crystal shapes with progressive crystallisation
S_2 = SPrime./SPrime;
I_2 = IPrime./SPrime;
L_2 = LPrime./SPrime;

S2_div_I2 = S_2./I_2;
I2_div_L2 = I_2./L_2;

% Calculate volume change with progressive crystallisation
Vs = (1/3) * DeltaS .* (IL + sqrt(IL .* IPrime .* LPrime) + (IPrime .*
    LPrime));
Vi = (1/3) * DeltaI .* (SL + sqrt(SL .* SPrime .* LPrime) + (SPrime .*
    LPrime));
Vl = (1/3) * DeltaL .* (SI + sqrt(SI .* IPrime .* SPrime) + (SPrime .*
    IPrime));

TotalVolume = 2*Vs + 2*Vi + 2*Vl;

% Calculate crystallinity change with progressive crystallisation
xtlinity = ((TotalVolume*NVxtl)/(RemainingReferenceVolume*10^9))*100;

%% Modelled crystallisation increase
% Calculate the model shape at which the total volume of the crystal
    population creates the modelled crystallisation increase
% i.e., the value 'Total' (D46 on Excel sheet) is green.
% The volume of the model shape should equal the Vincperxtl value.

% Calculate k value required
syms k
eqn = Vincperxtl == (2*((1/3) * (sind(BetaI)*k) * (SL + sqrt(SL *(Sscaled +
    (2*(sind(BetaS)*k))) * (Lscaled + (2*(sind(BetaL)*k)))) + ((Sscaled +
    (2*(sind(BetaS)*k))) * (Lscaled + (2*(sind(BetaL)*k)))))) + (2*((1/3)
    * (sind(BetaS)*k)
    * (IL + sqrt(IL *(Iscaled + (2*(sind(BetaI)*k))) * (Lscaled +
    (2*(sind(BetaL)*k))))
    + ((Iscaled + (2*(sind(BetaI)*k))) * (Lscaled + (2*(sind(BetaL)*k)))))) +
    (2*((1/3) * (sind(BetaL)*k) * (SI + sqrt(SI *(Iscaled +
    (2*(sind(BetaI)*k))) * (Sscaled + (2*(sind(BetaS)*k)))) + ((Sscaled +

```

```

        (2*(sind(BetaS)*k))) * (Iscaled + (2*(sind(BetaI)*k))))));
k_sol = double(vpasolve(eqn, k));

DeltaS3 = sind(BetaS)*k_sol;
DeltaI3 = sind(BetaI)*k_sol;
DeltaL3 = sind(BetaL)*k_sol;

S3Prime = Sscaled + (2*DeltaS3);
I3Prime = Iscaled + (2*DeltaI3);
L3Prime = Lscaled + (2*DeltaL3);

% New crystal shape
S_3 = S3Prime/S3Prime;
I_3 = I3Prime/S3Prime;
L_3 = L3Prime/S3Prime;

S3_div_I3 = S_3/I_3;
I3_div_L3 = I_3/L_3;

% check VolumeInc = VIncperXtl
Vs3 = (1/3) * DeltaS3 * (IL + sqrt(IL * I3Prime * L3Prime) + (I3Prime *
    L3Prime));
Vi3 = (1/3) * DeltaI3 * (SL + sqrt(SL * S3Prime * L3Prime) + (S3Prime *
    L3Prime));
Vl3 = (1/3) * DeltaL3 * (SI + sqrt(SI * I3Prime * S3Prime) + (S3Prime *
    I3Prime));

TotalVolume3 = 2*Vs3 + 2*Vi3 + 2*Vl3;

CheckVolume3 = round(TotalVolume3, 4) == round(Vincperxtl, 4); % should match,
    ans = logical 1

xtlinity3 = ((TotalVolume3*NVxtl)/(RemainingReferenceVolume*10^9))*100;

Checkxtlinity3 = round(xtlinity3, 4) == round(XtlisationIncreaseModelled, 4);
    % should match, ans = logical 1

%% Plots: S/I against I/L, total volume, total crystallinity

figure

% S/I against I/L
subplot(1,3,1)
plot(S2_div_I2, I2_div_L2) % plots curve of change in shape with
    crystallisation
hold on
h1 = scatter(S0_div_I0, I0_div_L0,"MarkerFaceColor", "w",
    "MarkerEdgeColor","k", "Marker","o" ); % plot initial shape
h2 = scatter(S1_div_I1, I1_div_L1,"MarkerFaceColor", "k",
    "MarkerEdgeColor","k", "Marker","o" ); % plot overgrowth shape

```

```

h3 = scatter(S3_div_I3, I3_div_L3,"MarkerFaceColor", "#39B185",
    "MarkerEdgeColor","k", "Marker","o"); % plot xtlinity increase shape

% legend
legend([h1, h2, h3], "Initial shape", "Overgrowth shape", "Crystallisation
    increase modelled shape")

% format axes
box on
set(gca,"TickDir","out")
axis square
xlim([0 1])
ylim([0 1])
xticks(0.0:0.1:1.0)
xlabel("S/I")
ylabel("I/L")

% Plot S/I against total volume
subplot(1,3,2)
semilogy(S2_div_I2, TotalVolume + InitialIndividualXtlVolume*10^9);
set(gca, 'YDir', 'reverse')
hold on
h1 = scatter(values(1), InitialIndividualXtlVolume*10^9, "MarkerFaceColor",
    "w", "MarkerEdgeColor","k", "Marker","o"); % volume of initial shape
h2 = scatter(values(end), TotalVolume(end) + InitialIndividualXtlVolume*10^9,
    "MarkerFaceColor", "k", "MarkerEdgeColor","k", "Marker","o"); %
    volume of overgrowth shape
h3 = scatter(S3_div_I3, TotalVolume3 +
    InitialIndividualXtlVolume*10^9,"MarkerFaceColor", "#39B185",
    "MarkerEdgeColor","k", "Marker","o"); % volume of the xtlinity
    increase shape

% legend
legend([h1, h2, h3], "Initial shape", "Overgrowth shape", "Crystallisation
    increase modelled shape", 'Location', 'southeast')

% format axes
box on
set(gca,"TickDir","out")
axis square
xlim([0 1])
xticks(0.0:0.1:1.0)
xlabel("S/I")
ylabel("Individual Crystal Volume (um^3)")

% Plot S/I against total crystallinity
subplot(1,3,3)
semilogy(S2_div_I2, xtlinity + InitialXtlisation)
set(gca, 'YDir', 'reverse')
hold on
h1 = scatter(values(1), InitialXtlisation , "MarkerFaceColor", "w",
    "MarkerEdgeColor","k", "Marker","o"); % xtlinity of initial shape

```

```

h2 = scatter(values(end), xtlinity(end), "MarkerFaceColor", "k",
    "MarkerEdgeColor","k", "Marker","o"); % xtlinity of the overgrowth shape
h3 = scatter(S3_div_I3, xtlinity3 + InitialXtlisation,"MarkerFaceColor",
    "#39B185", "MarkerEdgeColor","k", "Marker","o"); % xtlinity of the xtlinity
    increase shape

% legend
legend([h1, h2, h3], "Initial shape", "Overgrowth shape", "Crystallisation
    increase modelled shape", 'Location', 'southeast')

% format axes
box on
set(gca,"TickDir","out")
axis square
xlim([0 1])
xticks(0.0:0.1:1.0)
xlabel("S/I")
ylabel("Crystallinity (%)")

```

## A.2 Textural characteristics

**Table A.1:** Textural characteristics of MVO-1591A, relevant to crystal growth modelling.  $\varphi_a$  = areal crystallinity;  $N_a$  = areal number density ( $\mu\text{m}^{-2}$ );  $S_n$  = characteristic crystal length ( $\mu\text{m}$ ),  $N_v$  = crystal volume density ( $\mu\text{m}^{-3}$ )  $A_{\text{xtl}}$  = average crystal intersection area ( $\mu\text{m}^2$ ),  $V_{\text{xtl}}$  = average crystal volume ( $\mu\text{m}^3$ ).

Parameter	Unbinned data	0-20 $\mu\text{m}$	20-40 $\mu\text{m}$	40-100 $\mu\text{m}$	100 + $\mu\text{m}$
$\varphi_a$	0.363	0.009	0.035	0.148	0.184
$N_a$ ( $\text{mm}^{-2}$ )	481	151	144	151	35
$S_n$ ( $\mu\text{m}$ )	27.5	7.5	15.6	31.2	72.8
$N_v$ ( $\text{mm}^{-3}$ )	1.75e+04	2.00e+04	9.2e+03	4.9e+03	4.8e+02
$A_{\text{xtl}}$ ( $\mu\text{m}^2$ )	754	56.4	245	974	5295
$V_{\text{xtl}}$ ( $\mu\text{m}^3$ )	20,701	423	3827	30,413	385,306

**Table A.2:** Textural characteristics of BEL1B-A, relevant to crystal growth modelling.

Parameter	Unbinned data	0-35 $\mu\text{m}$	35+ $\mu\text{m}$
$\varphi_a$	0.051	0.018	0.033
$N_a$ ( $\text{mm}^{-2}$ )	134.4	103	31
$S_n$ ( $\mu\text{m}$ )	19.5	13.2	32.6
$N_v$ ( $\text{mm}^{-3}$ )	6902.821	7845.8	955.1
$A_{\text{xtl}}$ ( $\mu\text{m}^2$ )	379.0235	173.2	1061.8
$V_{\text{xtl}}$ ( $\mu\text{m}^3$ )	7379.028	2280.1	34600.8